PHOTOCHEMICALLY AND THERMALLY CONTROLLED PHYSICAL PROPERTIES OF SELF-ASSEMBLED π–SYSTEMS

Thesis Submitted to AcSIR for the Award of the Degree of
DOCTOR OF PHILOSOPHY
in Chemical Sciences

AcSIR

By

SATYAJIT DAS

Registration No: 10CC14J39008

Under the guidance of

Prof. A. AJAYAGHOSH

CHEMICAL SCIENCE AND TECHNOLOGY DIVISION

**CSIR-NATIONAL INSTITUTE FOR INTERDISCIPLINARY
SCIENCE AND TECHNOLOGY (CSIR-NIIST)
THIRUVANANTHAPURAM-695019
KERALA, INDIA**

December, 2019

Dedicated to

Pabsat

DECLARATION

I hereby declare that the matter embodied in the thesis entitled: "**Photochemically and Thermally Controlled Physical Properties of Self-Assembled π–Systems**" is the result of the investigations carried out by me at the Photosciences and Photonics Section, Chemical Sciences and Technology Division, CSIR-National Institute for Interdisciplinary Science and Technology (CSIR-NIIST), Thiruvananthapuram, under the supervision of Prof. A. Ajayaghosh and the same has not been submitted elsewhere for the award of any other degree or diploma.

In keeping with the general practice of reporting scientific observations, due acknowledgement has been made wherever the work described is based on the findings of other investigators.

Satyajit Das

i

CERTIFICATE

*This is to certify that the work described in this Ph. D. thesis entitled **"Photochemically and Thermally Controlled Physical Properties of Self-Assembled π–Systems"** submitted by **Mr. Satyajit Das** to the Academy of Scientific and Innovative Research (AcSIR) in fulfilment of the requirements for the award of the **Degree of Doctor of Philosophy in Chemical Sciences** embodies original research work carried out by him under my supervision. I further certify that this work has not been submitted to any other University or Institution in part or full for the award of any degree or diploma. Research materials obtained from other sources have been duly acknowledged in the thesis. Any text, illustration, table etc., used in the thesis from other sources, have been duly cited and acknowledged.*

31·12·19

A. Ajayaghosh

(Supervisor)

(Satyajit Das)

ACKNOWLEDGEMENT

Satyajit Das

CONTENTS

Chapter 1 **Recent Progress in Supramolecular Organic Materials**
01–54

Chapter **2** Gel Phase Controlled [4+2] Diels–Alder Cycloaddition Reaction of a 9–Phenylethynyl Anthracene Derivative and its Luminescence Properties   55–92

List of Abbreviations

0,1,2,3D	Zero, One, Two, Three Dimensional
9-PEA	9-Phenylethynyl anthracene
Å	Angstrom
ACQ	Aggregation-caused quenching
ACN	Acetonitrile
AFM	Atomic force microscopy
AIE	Aggregation induced emission
Au	Gold
BEDO-TTF	Bis(ethylenedioxy)tetrathiafulvalene
BHJ	Bulk Herterojunction
BPOBP	[1,1':3',1″-terphenyl]-4,4″-diylbis(diphenylphosphine oxide
°C	Degree Celsius
C_3	Centre of rotation axis: A rotation by 360˚/3 that brings a three-dimensional body into an equivalent configuration
CB	Cucurbituril
CD	Circular Dichroism
CD	Cyclodextrin
CGC	Critical gelation concentration
c.a.	Calculated approximately
$CDCl_3$	Deuterated chloroform
COF	Covalent Organic Framework
CIE	International Commission on Illumination
CIA	Calixarene induced aggregation
CO_2	Carbon dioxide
δ	Chemical shift
Da	Dalton
DPP	Diketopyrrolopyrrole
D-A-D	Donor-acceptor-donor
D-A	Diels-Alder

DNA	Deoxyribo nucleic Acid
DMSO	Dimethyl sulfoxide
DLS	Dynamic light scattering
DSC	Differential scanning calorimetry
et al.	*Et allii/alia*
ESIPT	Excited-state intramolecular proton transfer
EML	Emitting layer
ETM	Electron transporting material
EL	Electroluminescence
ε	Molar extinction coefficient
α_{agg}	Fraction of aggregates
Φ_F	Fluorescence quantum yield
FT-IR	Fourier-transform infrared spectroscopy
FF	Fill factor
eV	Electronvolt
G'	Elastic storage modulus
G"	Elastic loss modulus
h	Hour
H-bond	Hydrogen bond
HBC	Hexabenzocoronene
HPS	Hexaphenylsilole
HOMO	Highest occupied molecular orbital
HPLC	High performance liquid chromatography
HTM	Hole transporting materials
HRMS	High resolution mass spectrometry
Hz	Hertz
H_D	Hydrodynamic diameter
ICT	Intramolecular charge transfer
IR	Infrared
ITO	Indium tin oxide
I-V	Current–voltage
J_{sc}	Short circuit current

JAF	*J*-aggregate formation
K	Kelvin
λ_{abs}	Wavelength of absorption
λ_{ex}	Wavelength of excitation
λ_{em}	Wavelength of emission
L_{max}	Luminescence maxima
LUMO	Lowest unoccupied molecular orbital
LC	Liquid Crystalline
LEC	Light-emitting electrochemical cells
LCST	Lower critical solution temperature
LD	Linear dichroism
L-B	Langmuir-Blodgett
M	Molar
M^+	Molecular ion peak
MALDI-TOF	Matrix-assisted laser desorption-Time of flight
MOF	Metal-organic frameworks
μ	Transition dipole moment
μM	micromolar
μm	micrometre
kJ	kilo Joule
mol	Mole
mmol	millimole
mL	millilitre
min	minutes
mW	milliwatt
mA	milliampere
MCH	Methyl cyclohexane
η	Viscosity
NIR	Near-infrared
nm	Nanometer
NMR	Nuclear magnetic resonance
NDI	Naphthalene diimide

NP	Nanoparticle
OD	Optical density
OLED	Organic light emitting diode
OFET	Organic field effect transistor
OSC	Organic solar cell
OPV	Oligo(p-phenyleneethynylene)
OPE	Oligo(phenyleneethynylene)
pH	Hydrogen ion concentration at logarithmic scale
pK_a	Acid dissociation constant at logarithmic scale
PAM	Poly-α-methylstyrene
PCP	Porous coordination polymers
PET	Photoinduced electron transfer
PCE	Power conversion efficiency
Pd	Palladium
Pt	Platinum
PC$_{71}$BM	[6,6]-Phenyl C$_{71}$ butyric acid methyl ester
PBI	Perylene bisimide
PEG	Polyethylene glycol
P–N	Pyridinium-Naphthalene
PDMS	Polydimethylsiloxane
PVCz	Poly(9-vinylcarbazole)
PL	Photoluminescence
PVMe	Polyvinyl methyl ether
ppm	Parts per million
RET	Resonance-energy transfer
RIR	Restricted intramolecular rotations
rt	Room temperature
s	Seconds
SAM	Self-assembled monolayer
SB2	9,9'-(5'-(4-(3,6-di-tert-butyl-9H-carbazol-9-yl)phenyl)-[1,1':3',1"-terphenyl]-4,4"-diyl)bis(3,6-di-tert-butyl-9H-carbazole)
SHG	Solar heat gain

Si	Silicon
SOF	Supramolecular organic framework
T	Temperature
TEM	Transmission electron microscopy
TICT	Twisted Intramolecular Charge Transfer
T_{film}	Film forming temperature
TEA	Triethylamine
TLC	Thin layer chromatography
THF	Tetrahydrofuran
T_{cloud}	Cloud temperature
UV-Vis	Ultraviolet-visible
V	Voltage
V_{oc}	Open circuit voltage
WAXS	Wide angle X-ray scattering
wt%	Weight percentage
XRD	X-ray diffraction

PREFACE

Development of π–conjugated supramolecular systems has gained tremendous interest over the years, owing to their superior and tuneable optoelectronic properties, synthetic feasibility, facile processability, etc. In this context, various strategies for controlling the spatiotemporal self–organization of chromophores leading to unprecedented morphologies, properties and applications, have been extensively explored. Over the past one and a half decades, our group has also been actively working in the area of molecular self–assembly and fine tuning their optoelectronic properties for multifarious applications.[1] From the beginning of my scientific pursuit at CSIR–National Institute for Interdisciplinary Science and Technology, I was involved in the design, synthesis and related investigations of a few light and heat responsive supramolecular π–conjugated organic molecules. With an objective of translating the expertise acquired by our group in this field into responsive smart systems, we chose a few designed photoactive anthracene derivatives and dipole variable oligo(phenyleneethynylene) based π–conjugated systems for detailed investigations. Such building blocks have been extensively explored for lighting, photovoltaics and smart materials applications. Among these supramolecular systems, the photo- and thermo-responsive chromophoric assemblies of extended π–molecular systems are promising candidates for real world applications.

In the present thesis, **Chapter 1** briefly introduces the structure-properties relationship of π–conjugated functional materials and provides insights into their self-assembly, with particular focus on morphologies and functional properties of the resulting supramolecular systems. Subsequently, recent developments in stimuli-responsive chromophores and their self-assembly for different applications are discussed.

In **Chapter 2**, we have explored the potential of the supramolecular gel phase of a 9-phenylethynylanthracene derivative and selectively directed its photocycloaddition reaction to form the corresponding *anti*-[4 + 2] photoadduct in exceptionally high yield. Further, these compounds were used as emitters to fabricate organic light emitting diodes. While the monomer and the photoadduct exhibited blue photoluminescence, the latter exhibited white electroluminescence (x, y = 0.33, 0.32)

in the presence of a hole transporting agent. The formation of an electroplex between the photoadduct and the hole-transporting material could be the probable reason for the additional band in the EL spectrum leading to a near-perfect white light emission.[2]

The design and studies of an amphiphilic liquid π-system, exhibiting LCST behavior within the tropical temperature range, is described in **Chapter 3**. The amphiphile, upon *anti*-[4 + 2] photocycloaddition, transformed into a bolaamphiphile having an LCST phase transition at low concentration and lower temperatures as compared to the parent molecule. We fabricated smart window prototypes to control solar light and heat transmission, by sandwiching the aqueous solutions of the amphiphilic molecule between sealed glass panels. These windows exhibited transparency below 29 $^{\circ}$C with >92% visible light transmission. However, above 32 $^{\circ}$C, the window turned opaque and blocked >80% of the solar radiation. Similar results, but with a neutral white opacity switching, could be achieved using the photoadduct at lower concentrations near room temperature. Thus, one of the widely studied classical photoreaction has been used for the design of dynamic windows that can modulate light and heat transmission, with tremendous implications in energy saving, aesthetics and glare reduction.[3]

In the final chapter, **Chapter 4**, we demonstrated the preparation of macroscopic free-standing films, synchronized with supramolecular polymerization and LCST phase transitions in a monophasic solvent medium. Our findings provide a rare example to achieve free standing film formation in a single-phase medium, which is distinctly different from existing film processing techniques such as solvent evaporation or interfacial processes. The realization of macroscopic films *via* a thermally assisted self-assembly process within a monophasic medium is expected to open up opportunities for further developments in thin film fabrication with the help of supramolecular chemistry of stimuli- responsive molecules.[4]

References

1. (a) Functional π-gelators and their applications: Sukumaran Santhosh Babu, Vakayil K Praveen, Ayyappanpillai Ajayaghosh *Chem. Rev.* **2014***, 114,* 1973-2129. (b) Stimuli-responsive Supramolecular Gels - Chapter 7: Rakesh K. Mishra, **Satyajit**

Das, Balaraman Vedhanarayanan, Gourab Das, Vakayil K. Praveen and Ayyappanpillai Ajayaghosh; **2018**, ISBN:978-1-78801-111-2.

2. Supramolecular Gel Phase Controlled [4 + 2] Diels–Alder Photocycloaddition for Electroplex Mediated White Electroluminescence: **Satyajit Das**, Naoki Okamura, Shigeyuki Yagi, and Ayyappanpillai Ajayaghosh: *J. Am. Chem. Soc.*, **2019**, *141*, 5635–5639.

3. Thermoresponsive Molecules for Controlled Heat and Light Transmission Windows and Applications Thereof: Ayyappanpillai Ajayaghosh, **Satyajit Das**, Soman Suraj, Asok Adersh, Shankar Pooppanal Sreejith: (Indian Patent Application No:- **201911052506**; Patent Cooperation Treaty (PCT) Application, **2019**) and manuscript under preparation.

4. Thermally Assisted Supramolecular Film Formation within a Monophasic Solvent Medium. **Satyajit Das**, Rajasekaran Thirumalai, and Ayyappanpillai Ajayaghosh (Manuscript under Preparation)

Recent Progress in Supramolecular Organic Materials
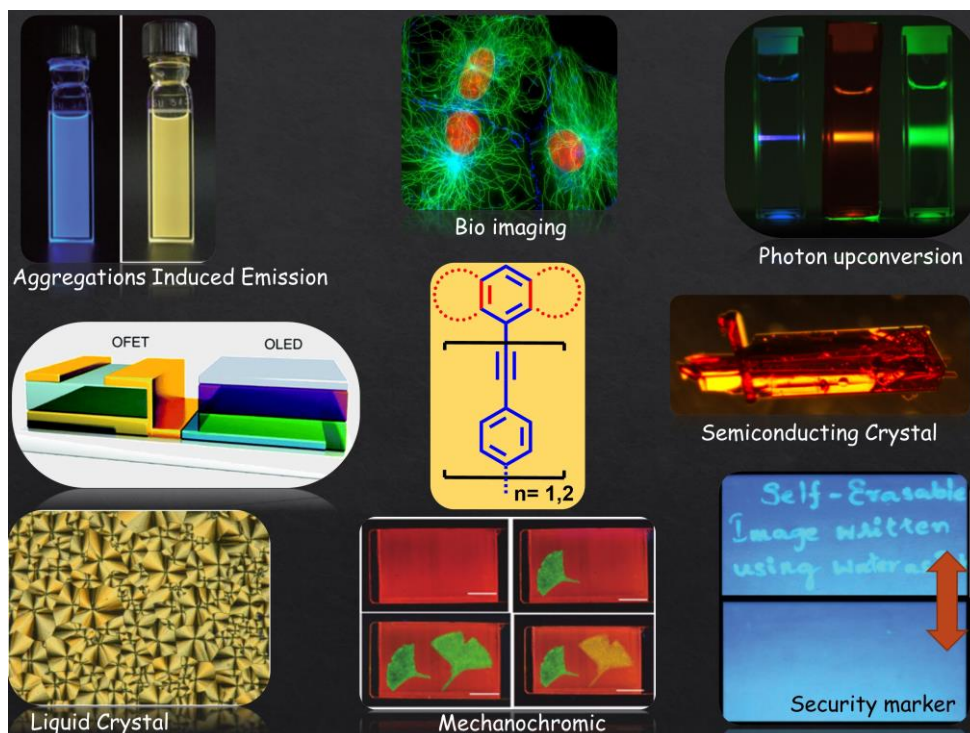
1.1. Abstract

Supramolecular self-assembly refers to the molecular organization via non-covalent interactions by virtue of different chemical functionalities that attributes order and unique properties to the system. Creation of such ordered assemblies and modulation of their properties have been achieved using structural modification, synthetic variations and controlled environmental conditions. Recent advances in supramolecular approaches have unambiguously impacted different realms of science - from synthetic organic chemistry to devices and drug delivery. Supramolecular chemistry provides a versatile tool to design functional materials by inducing unique properties and morphologies for multifarious applications. This chapter provides a brief introduction to the recent developments in π–conjugated

functional molecules and their self-assembly to form soft materials with intriguing properties. An overview on stimuli responsive materials derived from amphiphilic π–conjugated molecules and their applications are also detailed. An outline of the present thesis is provided towards the end of the chapter.

1.2. Introduction

Supramolecular chemistry has been paying a pivotal role in various scientific advancements made in the past few decades.[1] Pioneering works in this field by several stalwarts are well-recognized at the highest level, the latest being the 2016 Nobel prize jointly awarded to Prof. Sauvage, Sir Stoddart and Prof. Feringa for their contributions to the development of molecular machines.[2] Majority, if not all, of the developments in supramolecular chemistry derived inspirations from nature. Creative human minds orchestrated the development of a large number of self-assembled materials for multifarious applications.[3] New generation materials developed using supramolecular approaches offer high level of complexity blended with superior properties.[4] Emergence of supramolecular materials has witnessed an advent in materials science by virtue of the unprecedented control over their unique properties and morphologies. A predictive but reliable approach to molecular engineering can facilitate the development of materials with pre-defined properties. Supramolecular strategies synchronized with multi-disciplinary synthetic approaches across the borders of chemistry, physics, biology and computation, offer creative and ingenious opportunities for the development of responsive and adaptive functional materials.[5]

Small molecule based extended π-systems have recently been gaining momentum as preferred semiconductor materials, especially for solution processable thin film devices. The comparably lower command over the performance and reproducibility of several polymer-based devices stems from their structural defects, polydispersity and purity of the active material with rather poor batch-to-batch reproducibility. This issue has been addressed to a large extent, by employing conjugated small molecule

based supramolecular materials. Molecular self−assembly thus offers a unique strategy for the realization of new and engineered functional materials with superior properties and applications without the need for extensive chemical modifications in the structural backbone of the monomers and oligomers.[6]

In this chapter, we discuss the recent developments in the synthesis and applications of functional supramolecular materials, with particular emphasis on stimuli-responsive amphiphilic molecular assemblies and their tunable electro-optical and morphological characteristics.

1.3. Functional Supramolecular Materials

Functional supramolecular materials are of profound interest for a variety of applications because of their potential in realizing novel technologies. The *de novo* preparation of complex and large structures via conventional covalent synthesis is often demanding and time consuming. In contrast, supramolecular chemistry offers a wider opportunity to create distinct and hierarchically well-ordered materials with precise functional properties under shorter reaction times. Over the past few decades, the self-assembly of small molecules has proven to be an extremely useful tool in the development of well-defined nanostructured materials.[7]

Supramolecular materials, formed via non-covalent linkages between monomeric building blocks, replicate several key characteristics of covalent polymers via strong, directional and reversible molecular interactions. The dynamic non-covalent nature of the supramolecular bonds in these materials is critical to directing their self-assembly from the (sub)nano to macro scales, modulating their conformation and imparting specific functions.[8] A large number of functional supramolecular materials reported over the years have spanned multifarious applications due to their fascinating optical, electrical, optoelectronic, magnetic and biochemical properties.[9] Engineered supramolecular materials with intriguing attributes such as self-healing ability and stimuli-responsive chemistry have attracted the attention of several research groups to explore them as potential candidates for innately smart and

adaptive functional materials.[10] Structural diversity offered by numerous permutations and combinations of different monomers along with the dynamic reversibility of non-covalent interactions undoubtedly manifest supramolecular polymers as one of the materials of choice for next-gen technologies.[11] One pivotal challenge in the extended applications of most supramolecular polymers emanates from their moderate chemical and mechanical robustness; however, quite a few supramolecular polymers with stability *akin* to covalent polymers have emerged over the past few years.[12]

Several riveting properties commensurate with extended covalent systems are now accomplished using non-covalent supramolecular materials. The responsive and adaptive characteristics of such supramolecular systems are rarely achieved using their covalent counterparts. The synthetic evolution of supramolecular polymers is rather complex compared to conventional covalent systems. Most of the reported supramolecular materials are obtained via self-assembly at the molecular level, thereby facilitating facile formation and deformation of bonds.[13] A plethora of supramolecular materials have thus emerged with specific and fascinating applications.[14] Significantly, molecular self–assembly offers a unique strategy to enhance or tune the optical and electronic properties of a large number of π– conjugated systems. 1D, 2D or 3D supramolecular architectures can be constructed using π–conjugated systems by the interplay of various non–covalent interactions such as ionic, van der Waals, solvophobic, coordination and H-bonds.[15] 'Bottom up' approaches combined with the dynamic nature of aggregates provides access to modulate the size and shape in the nano– and meso-scopic regimes. Supramolecular chemistry thus offers a unique platform for the discovery of new functional systems as well as improvized application of existing domains.[16]

1.4. Supramolecular Chemistry: The World of Non-covalent Interactions

Molecular self-assembly, driven by non-covalent interactions particularly predominant in biological systems, offers a great tool for engineering nanoscopic architectures.[17] These non-covalent bonds can either be attractive or repulsive intermolecular forces, that are resposible for the formation of supramolecular arrays. The different classes of possible interactions are (i) electrostatic interactions (ionic or dipole interactions), (ii) H-bonding, (iii) $\pi-\pi$ interactions/stacking, (iv) van der Waals forces, (v) solvent interactions and (vi) London forces. In traditional organic/polymer chemistry, the covalent bonding between atoms is the key to form ordered materials, whereas supramolecular chemistry makes use of non-covalent interactions between molecules to build hierarchical structures. Covalent bonds generally have a bond energy in the range of 100-400 kJ/mol, whereas supramolecular interactions are usually much weaker, and range from 4-5 kJ/mol for vdW forces, up to 120 kJ/mol for H-bonds and ~250 kJ/mol for coulombic interactions (**Table 1.1**). These individually weak but collectively strong interactions result in stable and complex molecular architectures with a high degree of selectivity, directionality and tunability.

Table 1.1. The strength of non-covalent forces compared with that of the covalent bond.

TYPE OF INTERACTION	STRENGTH (KJ/MOL)
Covalent bond	100-400
Coulomb	250
Hydrogen bond	4-120
Ion –Dipole	50-200
Dipole-Dipole	5-50
Cation-π	5-80
$\pi-\pi$ stacking	4-20
Solvent effects	4-40
van der Waals forces	<5

5

H-Bonding is a specific dipole-dipole interaction with a high degree of directionality, defined geometry and specificity. H-Bonds are frequently observed in nature, e.g. folding of proteins, substance recognitions by enzymes and double helical structure of DNA.[18] The $\pi-\pi$ stacking is a weak electrostatic interaction between aromatic rings or conjugated bonds whereas the van der Waals forces occur between a negatively charged $\pi-$electron cloud and a positivly charged $\sigma-$framework of an adjacent molecule. van der Waals attraction helps in compromising the electrostatic $\pi-\pi$ repulsions between two π-clouds, leading to better $\pi-\pi$ stacking interactions. However, the relative orientation of two interacting molecules depends on the electrostatic repulsion between two electron rich $\pi-$systems.[19]

Improvised performance and applications of organic supramolecular materials demand control over molecular organization and morphology. Hence, supramolecular $\pi-$conjugated systems possess huge potential for practical applications owing to their ability to form highly directional and dynamic molecular assemblies. Though direct correlations between the molecular structure, packing, and the morphology of supramolecular assemblies is not yet elucidated completely, the interplay of non-covalent interactions in adjusting the packing parameters of such systems is highly desirable. Despite being formed through weak intermolecular interactions, such materials exhibit properties comparable or superior to covalent organic polymers and the design and synthesis of supramolecular architectures is often temed *non-covalent synthesis*.[20-21]

1.4.1. Hydrogen Bonding and $\pi-\pi$ Stacking: The Favorites in Supramolecular Assemblies

The advantages of H-bonding and $\pi-\pi$ stacking stem from their tunable strength, directionality and specificity. The strength of a single H-bond is defined by the acidity of the hydrogen donor group and basicity of the acceptor group. Among various non–covalent interactions, H–bonding is predominantly used for

constructing supramolecular architectures owing to its high binding affinity, selectivity and directional nature. Intermolecular H-bonding has been extensively used to control the self-assembly, solid state morphology and functional properties of supramolecular assemblies. For instance, several reports have demonstrated the role of H–bonding in the supramolecular self-assembly of π–conjugated systems leading to better transport properties due to the availability of continuous and extended percolation pathways. H-Bonding, in cooperation with other non-covalent forces, particularly π−π stacking and van der Waals interactions, offers molecules to self-organize to form stable supramolecular architectures with control over shape and properties.

π−π-Interaction represents a special case of non-covalent binding between large π–conjugated surfaces. Electrostatic attractions between electron-rich and electron-poor π–surfaces can also influence the possibilities for π–stacking. Several modes of stacking (cofacial, slipped, face-to-face or face-to-edge) operate in π-conjugated supramolecular materials and may be tuned *via* different processing conditions.[22] Recently, a perylene bisimide dye based self-organised liquid crystals *via* careful engineering of non-covalent chemical functionalities, leading to controlled H-bonding and π−π interactions was reported by Würthner and co-workers.[23] Lateral H-bonding and slip stacked π–stacking of molecule **1** resulted in strongly coupled *J*-aggregated hexagonal columnar packing, whereas the control molecule **2** afforded columnar packing through weakly coupled cofacial helical π–stacking (**Figure 1.1**).

1.5. Supramolecular Assemblies of Chromophoric π-Systems

Chromophores are molecules that are colored and absorb light to undergo various excited state processes. Several such chromophoric systems have been used as building blocks for the design of functional supramolecular materials. In this context, extended π-systems have been exploited to create stimuli-responsive materials resulting in the modulation of the optoelectronic properties. As a result, a

7

large number of small molecule based supramolecular materials have been reported to exhibit superior optoelectronic performance especially in OSCs and OFETs.[24-26] This section provides an overview on the various aspects of supramolecular chromophoric assemblies. The following sections will elaborate on the aggregation behavior in chromophoric assemblies, their photophysical characteristics and morphological diversity.
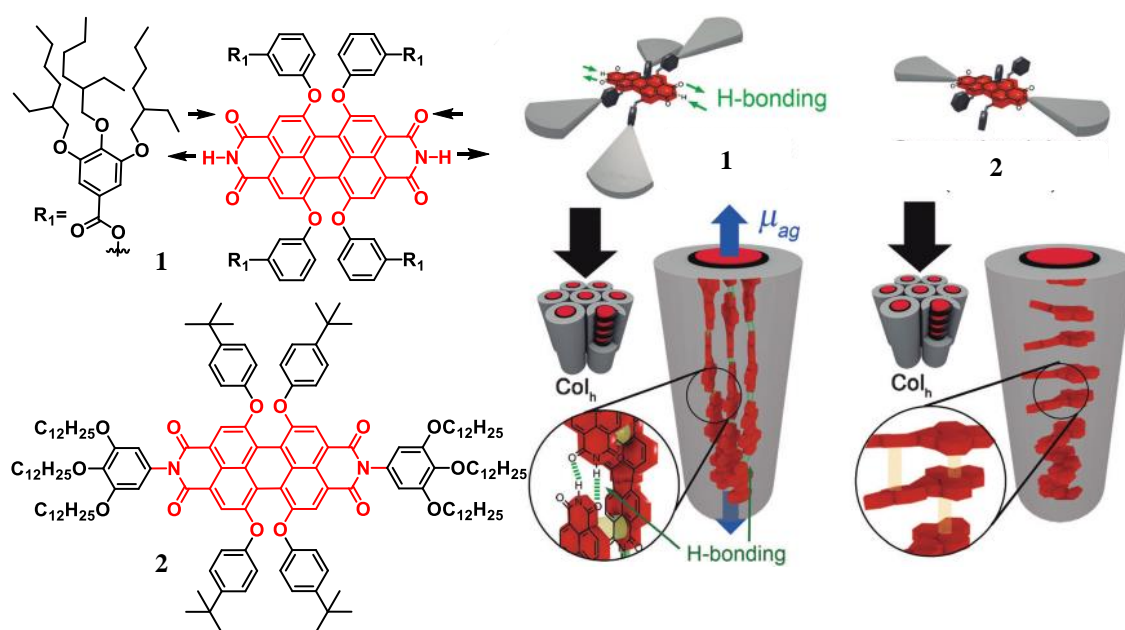
Figure 1.1. Chemical structures of the PDI derivative **1** and control molecule **2** and their H-bonding and $\pi-\pi$ stacking assisted hexagonal columnar molecular self-assembly.[23]

1.5.1. *H-* and *J-* Aggregates

The structure-optical property relationship in molecular aggregates have gained tremendous attention in supramolecular chemistry. Distinct changes in absorption have been observed for aggregates as compared to their monomeric solutions. Aggregates with a certain absorption band shifted to a longer wavelength (bathochromic shift) with respect to the monomer absorption are called as *J*-type aggregates.[17b] Aggregates with absorption bands shifted to a shorter wavelength (hypsochromic shift) with respect to the monomer band, are called *H*-aggregates that exhibit, in most cases, low or no fluorescence (**Figure 1.2**). [27-29]

As f'' and f' are non-zero,
both transitions are allowed

$2f$

f''

f'

$2f$

Monomer H-type Dimer Oblique-type Dimer J-type Dimer
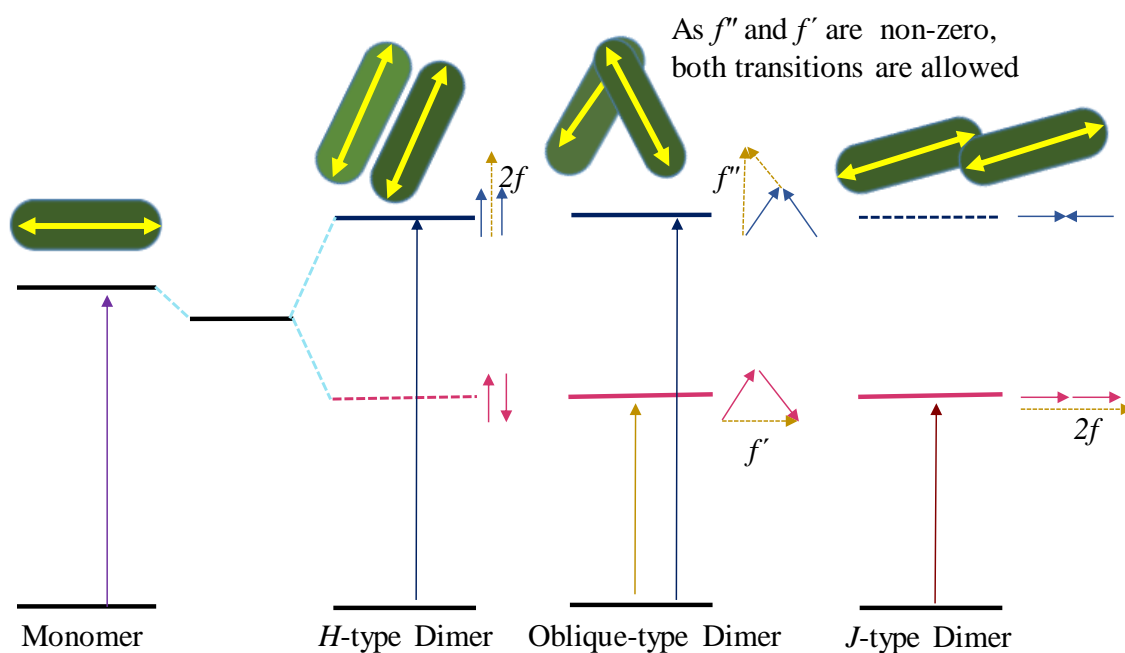
Figure 1.2. Schematic representation of typical *H*–, Oblique, and *J*–type dimers for a π–conjugated molecule and the corresponding effects in the UV–vis absorption spectra. Allowed transitions are depicted in solid arrows (transition dipole moment μ($2f$) > 0), and dashed lines represent the forbidden ones (μ($2f$) = 0).

Recently, Würthner *et al.* have demonstrated the fine tuning of *J*-and *H*-type molecular aggregates in a core-shell hexagonal liquid crystal (**Figure 1.3a,b**).[30] A donor-acceptor dyad comprising of perylenebisimide decorated with four bithiophene arms in its periphery (**3** and **4**) can undergo theromotropic liquid crystalline (LC) phase transition at 230 °C. In their hexagonal columnar LC domains, PBI cores were found to be assembled *via* lateral H-bonding and π−π stacking. As a result, *J*-type packing with a bathochromic shift in the PBI absorption spectrum was observed in the film state (**Figure 1.3c**). Due to the jacketing of PBI aggregates, the peripheral units were forced to assemble in an *H*-type fashion with a hypsochromic shift in the absorption maxima. Such a packing was further confirmed by WAXS diffraction pattern. The hexagonal columnar aggregates in their film state showed very weak fluorescence, indicating fast electron transport from bithiophenes to the PBI core.
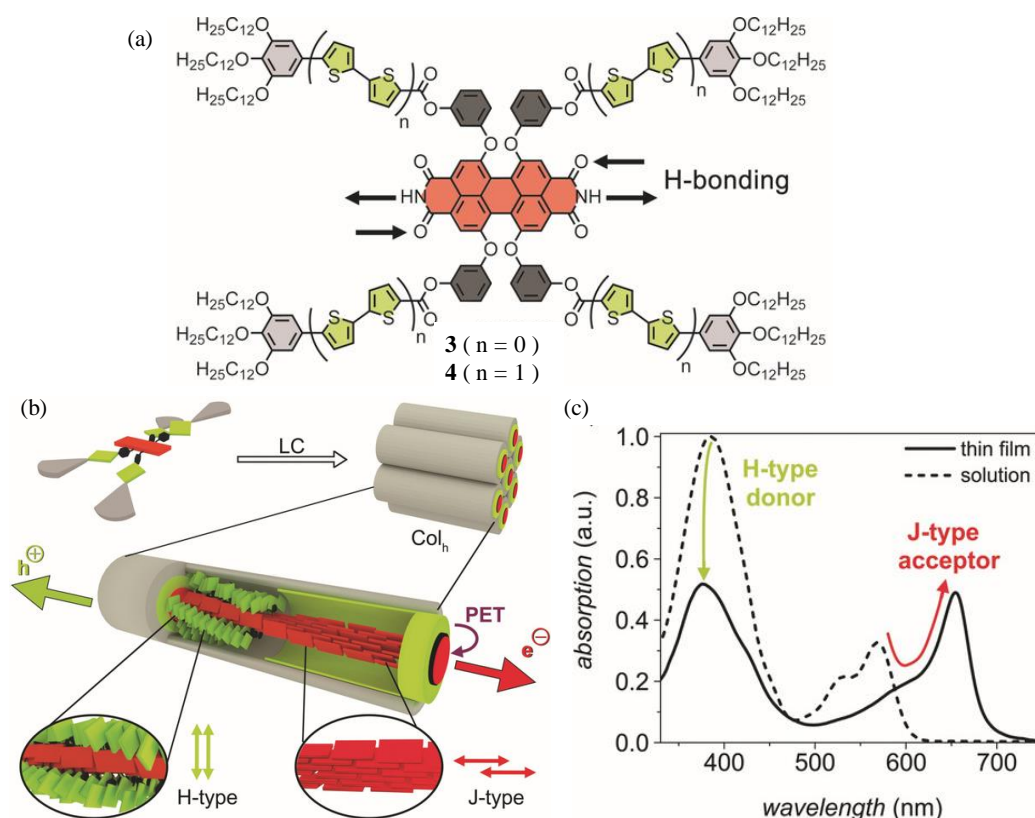
Figure 1.3. (a) Chemical structures of the PBI derivatives **3** and **4**. **(b)** Molecular agrrangements in the hexagonal liquid crystalline phase showing H-bonding and $\pi-\pi$ stacking driven *J*-type aggregates of the PBI core whereas as the peripheral bithiophene units aggregate in *H*-type fashion. **(c)** Absorption spectra of *H*- and *J*- type aggregates.[30]

1.5.2 Aggregation Induced Emission (AIE) and Aggregation Caused Quenching (ACQ)

AIE is a photophysical phenomenon in which luminogens are non-emissive in their molecular form and are induced to emit via aggregate formation. Hexaphenylsilole (HPS) is one of the well-investigated AIE chromophores (**Figure 1.4**). On the other hand, the phenomenon of luminophores that are emissive in their monomeric state in solution and tend to exhibit emission quenching, partially or completely, upon aggregation, is known as aggregation-caused quenching (ACQ).[31] Typically, the π-π stacking interactions between the aromatic rings of adjacent luminophores prompt the formation of an excimer that decay or relax back to the ground state *via* a non-

radiative pathway, resulting in ACQ. A prototypical example for ACQ fluorophore is fluorescein (**Figure 1.4**).
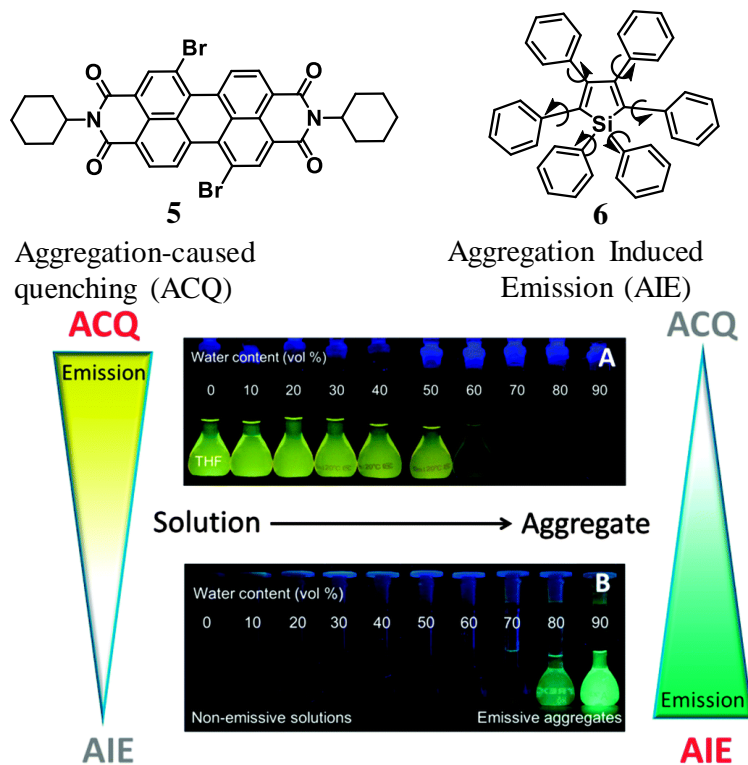
Figure 1.4. Schematic representation of aggregation caused quenching of molecule **5** and aggregation induced emission of molecule **6**.

AIE molecules generally contain polycyclic as well as multiple aromatic rings.[32] Moreover, most of them emit blue or green light, while red AIE emitters are relatively rare. AIE fluorogens have been extensively used for molecular detection and cell imaging. Mechanistic pathways behind this process are associated with either or a combination of restricted intramolecular rotations (RIR), excited-state intramolecular proton transfer (ESIPT), twisted intramolecular charge transfer (TICT) and *J*-aggregate formation (JAF).[33]

1.5.3. Morphological Distinction in Supramolecular Assemblies

Self-assembly of π-conjugated small molecules allows their organization into well-defined supramolecular architectures with distinct morphological features.

Supramolecular ordering of carefully designed building blocks in a three dimensional space leads to intricate molecular assemblies with defined morphologies and desired functional properties. Control over morphology at the molecular level further facilitates the fine-tuning of bulk properties and functionalities at the macroscopic level. For instance, the morphology of the active layer plays a decisive role in determining the efficiency of a device platform through optimum nanophase segregation and extended percolation pathways with high carrier mobility. The relatively low performance of small molecule-based devices is generally ascribed to their curtailed carrier percolation pathways arising from inadequate interconnectivity within the active layers, that unanimously underlines the significance of morphologies in such device architectures.[34] Our group has extensively investigated the morphology-properties relationship of oligo(*p*-phenyleneethynylene) derived assemblies.[12] These molecules generally undergo gelation in non-polar solvents with fibril-like morphology. However, it has been observed that, there is a correlation between the molecular length and their molecule-substrate interaction in dictating the final morphology. Similarly, concentration plays a crucial role in altering the assembled structures. For instance, at a lower concentration, compound **7** formed a vesicular structure, whereas **8** and **9** exhibited morphologies similar to entangled fibers and spiral structures, respectively (**Figure 1.5**). The morphology of such exotic superstructures were further controlled by tuning the humidity and temperature of the aliquot solutions.[35]

1.6. Extended π–Systems-based Supramolecular Gelators

Gels, in general, refer to a dilute cross-linked networked system exhibiting no flow in the steady state. Supramolecular assemblies of π–systems under the influence of various non-covalent interactions lead to gel formation. Though several parameters affect the process of gelation, nature of solvent(s) is a crucial factor. Polarity, functional groups, hydrophobicity/hydrophilicity, viscosity etc. decide the properties of the resultant gel. Several prior reports on supramolecular aggregation

and gelation have enabled researchers to design gelators *via* the incorporation of structural features that are known to promote aggregation.
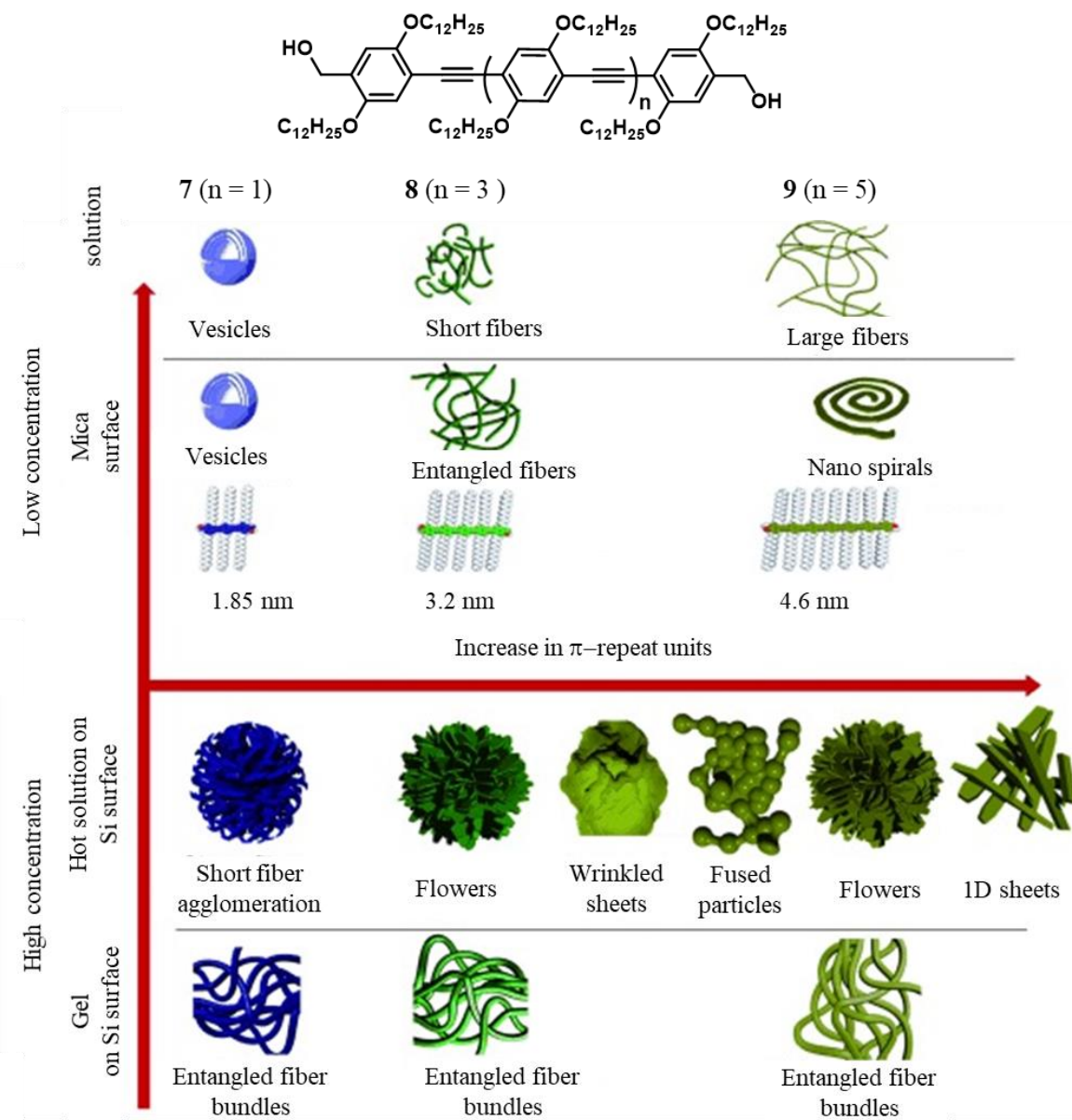
Figure 1.5. Effect of conjugation length of gelators on morphological properties of three different oligo (*p*-phenyleneethynylene) derivatives **7-9**.[35]

This class of supramolecular materials exhibit distinct properties induced by self-assembly, leading to diverse architectures. Gelation is normally observed when a homogeneous solution obtained by heating in a suitable solvent, is cooled to room temperature or below. Super saturation-mediated nucleation and growth is believed

to be the basic driving force behind the gel nanostructure formation.[36] Our group has extensively worked on the design and synthesis of several OPV derived organogelators capable of modulating their optical band gaps. For example, the emission of gelators **10-12** was found to depend on the end-group functionality (**Figure 1.6**). These molecules provide a lucid instance for a system, where the donor–acceptor groups are tailored symmetrically on to the extended backbone for fine-tuning the properties of the resulting gels.[37]

Light driven self-assembly of organogelators utilizing photoinduced *cis-trans* isomerization of azobenzene is well documented in literature.[38] In a recent work, Liu *et al.* explored the dual stimuli-responsive behavior of azobenzene–cholesteryl $\pi-$gelator **13** (**Figure 1.6b**)[38b] that underwent thermally reversible gelation in xylene. However, the gel irreversibly transformed into the corresponding sol upon exposure to UV light. Fernandez *et al.* reported the influence of metal coordination on stimuli-responsive behavior of the $\pi-$gelator **14** containing an azo moiety with pyridyl ligands that enabled response towards both light and metal coordination.[38c] Molecule **14**, in methyl cyclohexane, self-assembled into long twisted fibers and dissembled into short rods upon photoirradiation. However, Pd (II) complexation induced a strong cooperative assembly to form thin and long fibers with a slip stacked molecular packing leading to gelation, that upon UV irradiation, transformed into thin rod like structures (**Figure 1.6c**). Supramolecular interactions facilitate the organization of small molecules having rigid $\pi-$surfaces and flexible functional groups into network-like structures with a mesophasic domain (**Figure 1.7b**).[39a] Triphenylene derivatives (**15**) can undergo gelation with a liquid crystalline polynomial orientation.[39b] Diring *et al.* have reported that incorporation of chemical functionalities at different positions of a pyrene core (molecules **16-17**) facilitate H-bonding and van der Waals interactions, leading to gelation and a stable mesophasic behavior with distinct photoluminescence properties.[40]
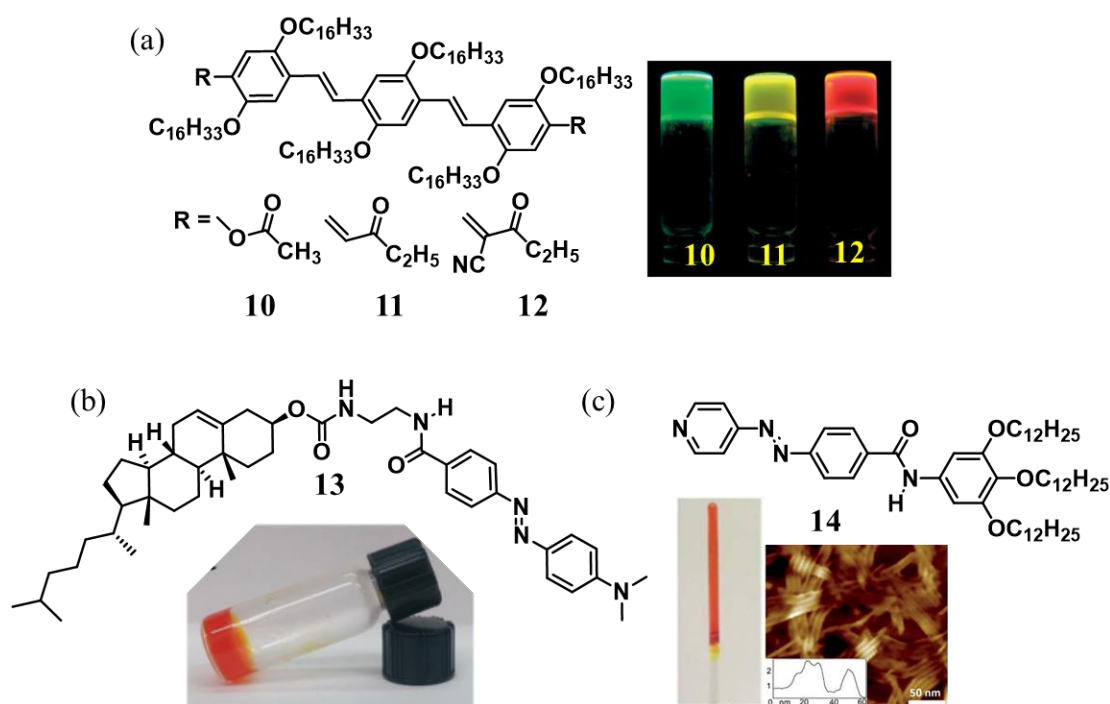
Figure 1.6. (a) The chemical structure of organogelators **9-11** (left) and photographs of the corresponding gels under UV light (right). (**b**) Structure of the dual responsive azobenzene–cholesteryl π–gelator **13**. The photograph of the corresponding gel is also shown. (**c**) Chemical structure of organogelator **14** with azo and pyridyl moieties that exhibited Pd (II) coordination driven light induced gel-to-sol transformation concomitant with a distinct morphological transformation.

Furthermore, gels were found to be potential candidates for the fabrication of field effect transistors with good bulk charge carrier mobility. Pereze *et al.* have synthesized a conjugated molecule **18**, with two bulky benzyloxy ether moieties as end groups. Compound **18** was found to undergo gelation in decane as well as in cyclohexane *via* a columnar π-stacked packing, leading to fibril-like nanostructures. A liquid crystalline phase transition was also observed at 59 °C with a *schlieren-*type texture. Both the LC phase and the gel state exhibited aggregation induced emission (**Figure 1.7e**).[41] Highly luminescent borondipyrromethene (F-Bodipy) templated supramolecular assembly of compound **19** formed a robust gel with fibril-like nanostructures in nonane via multiple non-covalent H-bonding interactions. Compound **19** also displayed a long temperature range thermotropic liquid

crystalline phase transition ranging from 25.1 °C to 213.7 °C, with a columnar mesophase and pseudo-fan shaped textures.[42]
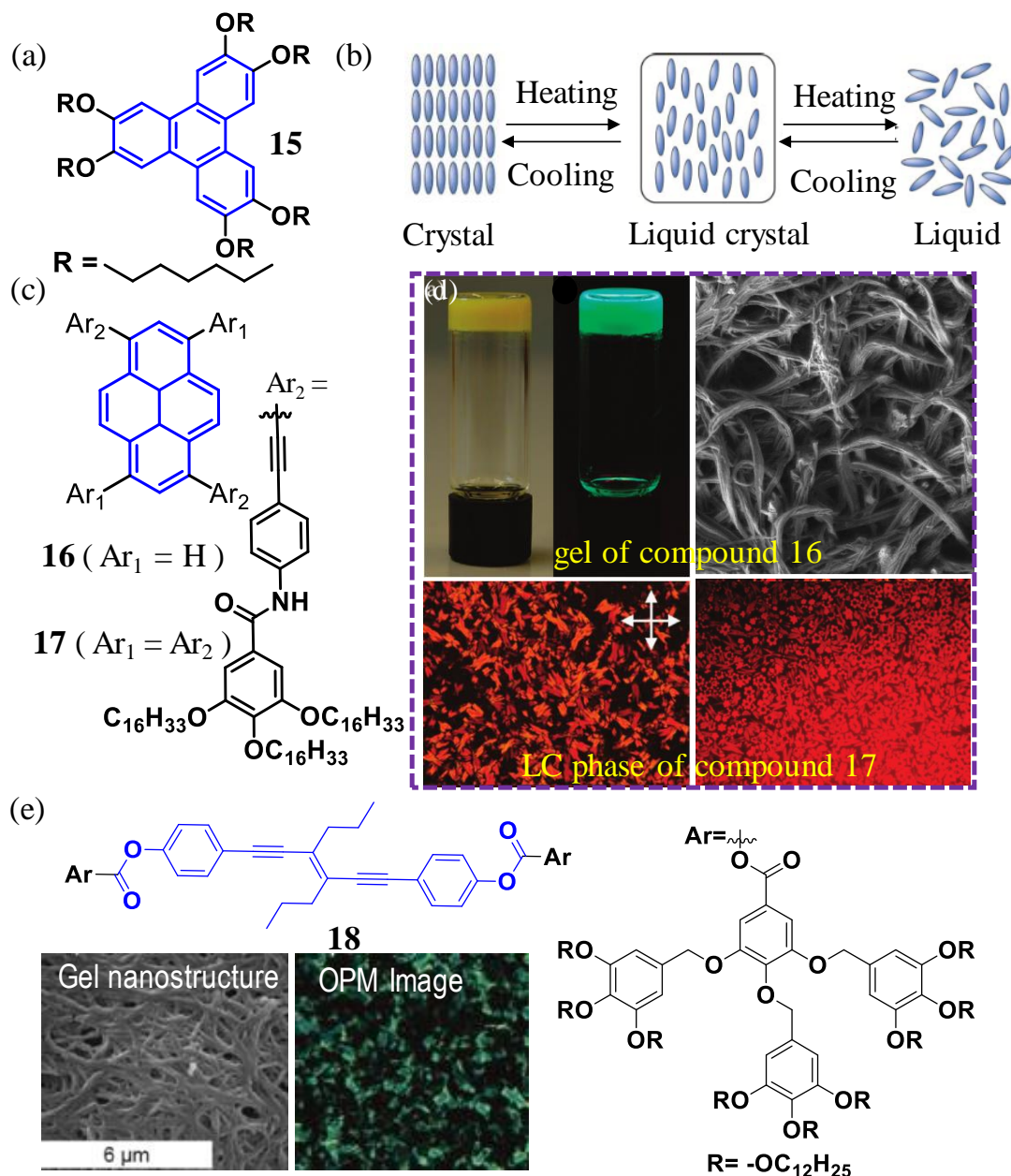
Figure 1.7. (a) Chemical structure of the triphenylene derivative **15** that exhibits both gelation and LC phase. **(b)** Distinction of the thermotropic LC state from liquid and solid crystalline states. **(c,d)** Structures of the pyrene derivative **16**–**17** exhibiting gelation and a stable mesophase in the temperature range of 20-200 °C respectively. **(e)** Chemical structure of the mesogen **18** that exhibited aggregation induced blue emission upon gelation in decane and its thermotropic LC phase transitions.

The gel state of compound **19** was found to be highly emissive with an yellowish-orange emission under 365 nm UV light illumination (**Figure 1.8a**). However, during mesophasic transitions, a bathochromic shift in fluorescence was observed from yellow-green to orange-red. Recently, it was reported that knocking off a peripheral side alkyl chain from a C_3 symmetric π-conjugated oligo(p-phenylenevinylene) derivative **20** can transform liquid crystalline molecules with a hexagonal columnar mesophase into gels in toluene and *n*-decane. Interestingly, the removal of the middle alkyl chain (compound **22**) did not result in either gelation or liquid crystalline behavior (**Figure 1.8b**).[43]

Ajayaghosh and co-workers have reported on the partial energy transfer from an oligo(*p*-phenylenevinylene) donor **23** (which in turn was a weak gelator) to a red emissive dopant **25**, resulting in white light emission with CIE coordinates (0.31, 0.35).[44] A strong gelator with the same π−core (**24**) afforded only red emission due to efficient energy transfer between the donor and the acceptor (**Figure 1.9a**). Similar energy transfer mechanisms could further be applied to achieve white light emission from linearly fused acenes (**Figure 1.9b**). The white light emission, in this case, originated from a combination of two energy transfer processes - an intermolecular energy transfer between the blue emissive anthracene **26** to the green emissive tetracene **27** and an intramolecular energy transfer between the green and red-emitting tetracenes **27** and **28**. Controlled energy migration from anthracene to teracence was shown to result in white light emission. Interestingly, the incorporation of single molecule white light emitters into a physical gel can also result in a white light emitting gel.[45] Recently, Ma *et al.* have reported single molecule white light emission from a bifunctional D-A-D system **29**, comprising of a pyridinium-naphthalene (P-N) unit attached to coumarin at both ends. In an aqueous medium, a self-folded state was observed via tandem hydrophobic effect and π−π stacking, resulting in a donor-acceptor charge transfer complex (**Figure 1.9d**).
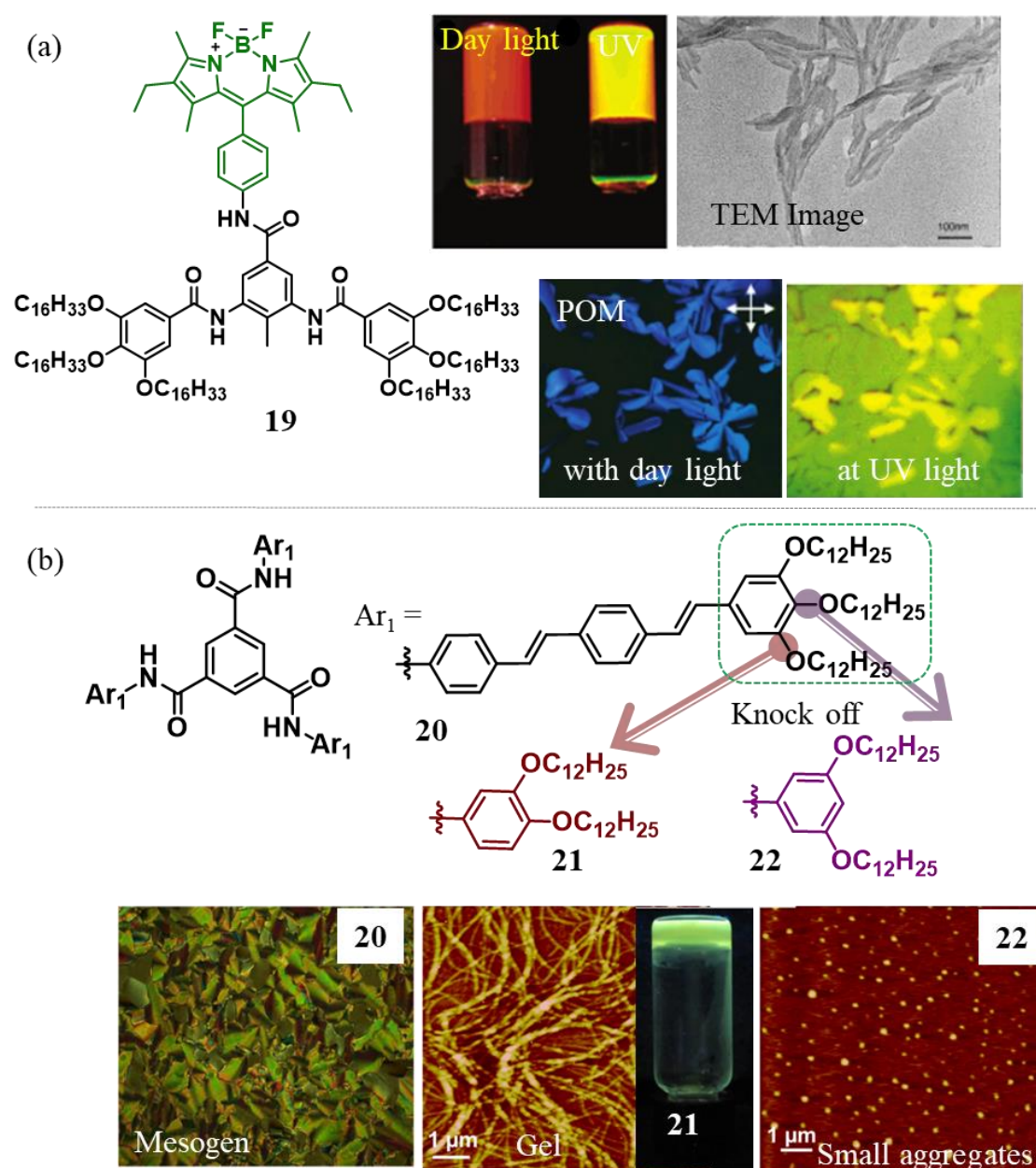
Figure 1.8. (a) Chemical structure of the Bodipy-based gelator **19** that formed highly emissive gels with a fibril like morphology. The gelator also exhibited thermotopic liquid crystalline phase transition at 212 °C.[42] **(b)** Chemical structures of the C_3 symmetric oligo(phenylenevinylene) derivatives **20**- **22**, obtained by knocking off peripheral alkyl chains. Compound **20** was found to exhibit a mesophase at 250 °C, whereas compound **21** is a gelator, and **22** was not found to form a gel nor exhibit a mesophase.[43]
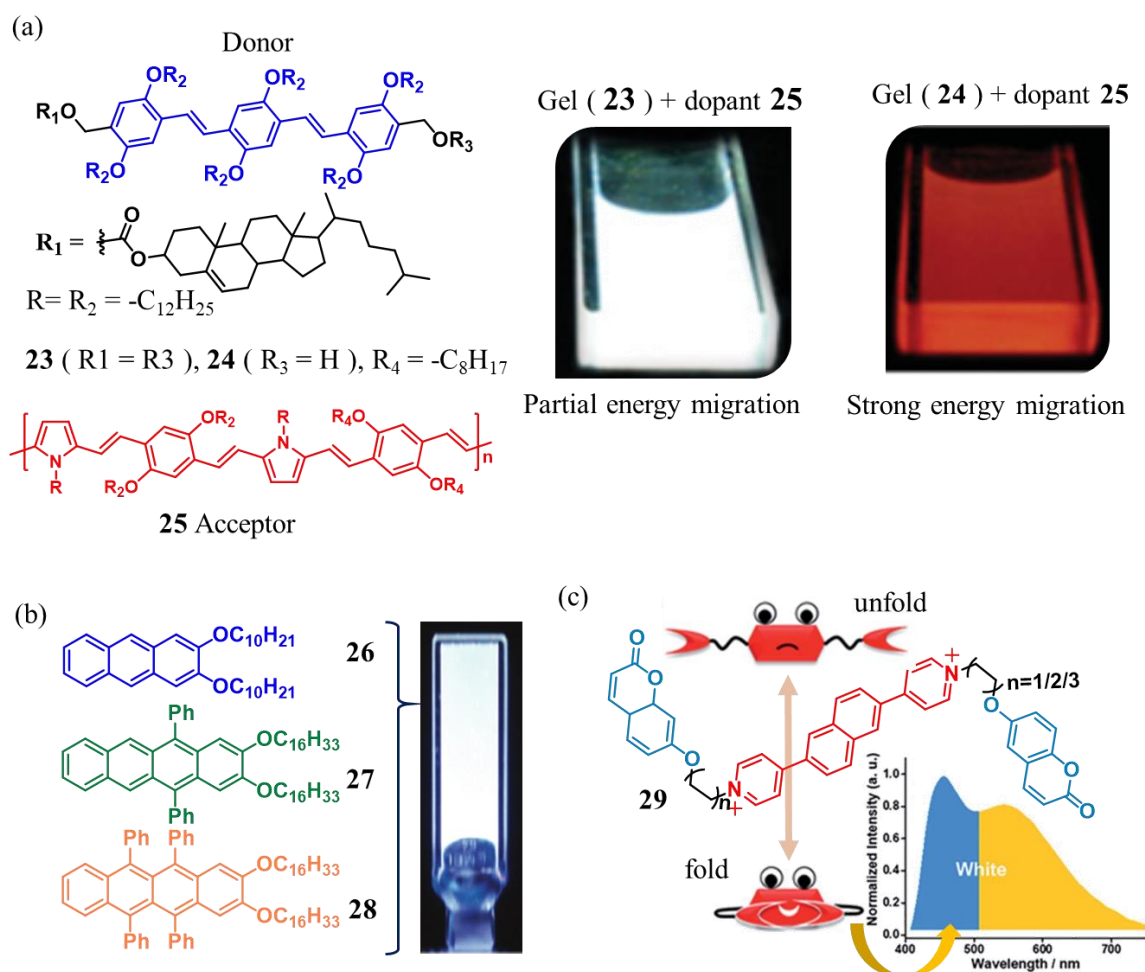
Figure 1.9. (a) Molecular structures of the weak gelator **23** and the strong gelator **24**. Due to weak supramolecular interactions between the gelator units, compound **23** showed white emission (left) in presence of the dopant **25**, whereas strong organogel of compound **24** resulted in a red emission only (right).[44] **(b)** Chemical structures of blue-emitting anthracene **26**, and green and red emitting tetracenes **27** and **28,** respectively.[45] **(c)** Chemical structure of a white emitting molecule **29** and its controlled folding and unfolding charge transfer complexes.[46]

The folding was found to enhance the ICT emission leading to pure white light. A white light emitting hydrogel was obtained by doping an agarose gelator medium with the molecular system.[46] Würthner and co-workers have reported the formation of a red organogel using a perylene bisimide (PBI) derivative **30** (**Figure 1.10a**). When the linear alkyl chain was replaced by a branched one (**31**), the formation of a 'dark green, almost black' organogel was observed.[47a]

(a)

30 R = C₁₂H₂₅

31 R=

530 nm

Both H and J type aggregates

493 nm

463 nm

430 nm

620 nm

70 min
35 min
17 min
9 min
5 min

Formation of black gel

(b)

32

Δλ = 20 nm   Δλ = 140 nm

H   J

PDMS
DPP-Amide
PDMS-DPP
-Amide

NIR

Vis
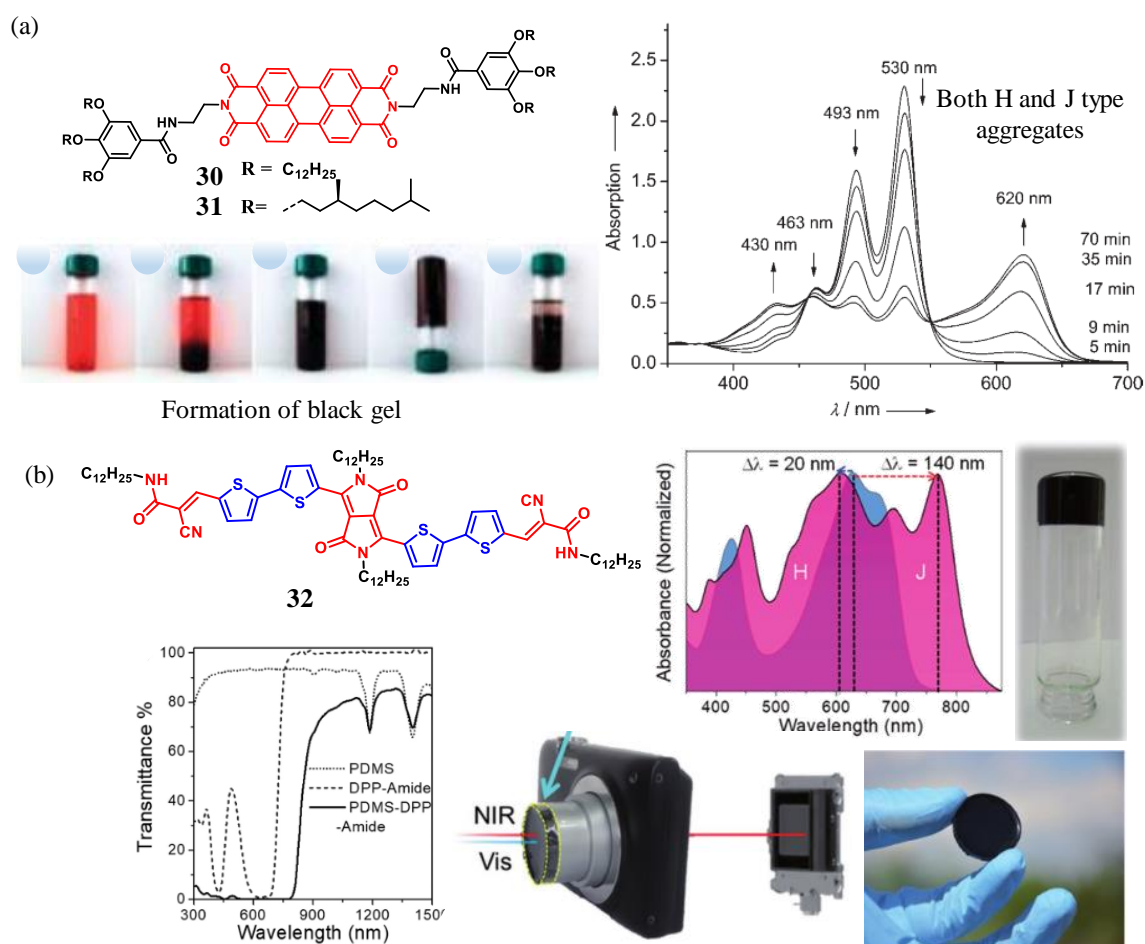
Figure 1.10. (a) Molecular structure of the PBI organogelators **30** and **31**. Images showing the time dependent gelation of **30** in *S*–limonene (0.3 mM). Time–dependent absorption spectra monitoring the gelation of **30** after heating followed by cooling is also shown. Packing model for *H*–type (**31**, top) and *J*–type (**30**, bottom) aggregates.[9] **(b)** Molecular structure of a diketopyrrolopyrrole based organogelator **32**, with a panchromatic absorption have been demonstrated as an NIR-transmitting filter for night surveillance applications. Photographs of the gel and the filter are also shown.[48]

Spectroscopic studies revealed that, in a hot solution of **31**, the large PBI π−cores under the influence of H-bonds formed both *J*- and *H*-type aggregates leading to a panchromatic absorption. However, only a few PBI derivatives have exhibited the simultaneous presence of *H*- and *J*-type molecular aggregates in their assembled state.[47b]

Taking advantage of supramolecular *H*- and *J*-type aggregates and their hypsochromic-bathochromic absorption bands, a diketopyrrolopyrrole (**32**) based supramolecular black gel was reported, which is visibly opaque and NIR transparent,

due to a broad absorption spanning the whole visible region owing to internal charge transfer from its donor to acceptor moieties.[48] The black molecular aggregates were further incorporated to a polydimethylsiloxane (PDMS) matrix to fabricate a free standing optical filter, capable of exclusively filtering UV-vis light and transmitting only NIR light. A customized camera equipped with the aforementioned optical filter was used for night surveillance, and security and forensic related applications (**Figure 1.10b**).

1.7. Self-Assembled Chromophores for Device Applications

Self-assembled functional materials have been explored for various optoelectronic applications in devices and related technologies.[49] Owing to their intrinsic π–conjugation and facile synthetic possibilities and tunable microscopic supramolecular structures and morphologies, chromophoric molecular assemblies are materials of choice for developing semiconductors,[50] light harvesters,[51] pigments[52] and chromogenic materials including electrochromics and thermochromics.[53] Inferior mechano-chemical robustness of small molecules has led to the selective adoption of supramolecular semiconductors for optoelectronic applications.[54] However, supramolecular materials, when compared to conventional covalent polymers, have reversible and adaptive properties.[55] Unlike in classical polymers, the building blocks in supramolecular materials are held together through various non–covalent interactions that enable the possibility for the self–rectification of packing defects during their formation. Nevertheless, supramolecular self-assembly achieved via molecular design and fine-tuning the environmental conditions provides an unprecedented opportunity to dynamically regulate thin film morphology, molecular orientation and their tailored properties. The defined and directed molecular arrangement in these supramolecular materials combined with optimum nanophase segregation and tunable band gaps lead to preferential pathways for the percolation of electrons and holes with high mobility and enhanced life times, thereby furnishing high photoconversion efficiencies and superior performance parameters. A judicious combination of molecular engineering, supramolecular self-

assembly, processing methodologies and device optimization holds the key towards harnessing the potential of self-assembled materials for next generation optoelectronic devices. Directed self-assembly of small molecules with predictable self-organization, leading to specific morphologies and selective electron and energy transfer offers ample opportunities for researchers working in the field of supramolecular optoelectronic materials.[56] The following sections describe selected examples of supramolecular assemblies as active materials for solar light harvesters, and in devices such as solar cells, field effect transistors and electrochromics.

1.7.1. Solar Light Harvesters

Several pioneering efforts have underlined the significance of supramolecular materials for artificial light harvesting applications. Synthetic analogues of the light-harvesting supramolecular system mainly comprise of scaffolds such as porphyrin arrays, biopolymeric assemblies and quantum dots. Very recently, Adams and co-workers have reported a two component multi-chromophoric peptide linked hydrogel, wherein the controlled assembly with self-sorted 1D nanostructures (**33-35**) was found to generate a localized energy gradient (**Figure 1.11a**).[57] However, the corresponding co-assembly did not exhibit any such electron transfer behavior. In another report, by taking advantage of the host-guest assembly, Yang *et al.* have prepared a water dispersible anthracene based donor and acceptor systems **36** and **37** as guests in combination with a pillar[5]arene host.[58] A polymeric chain formed by inclusion complexation led to photoinduced energy transfer from the donor to the acceptor (**Figure 1.11b**).
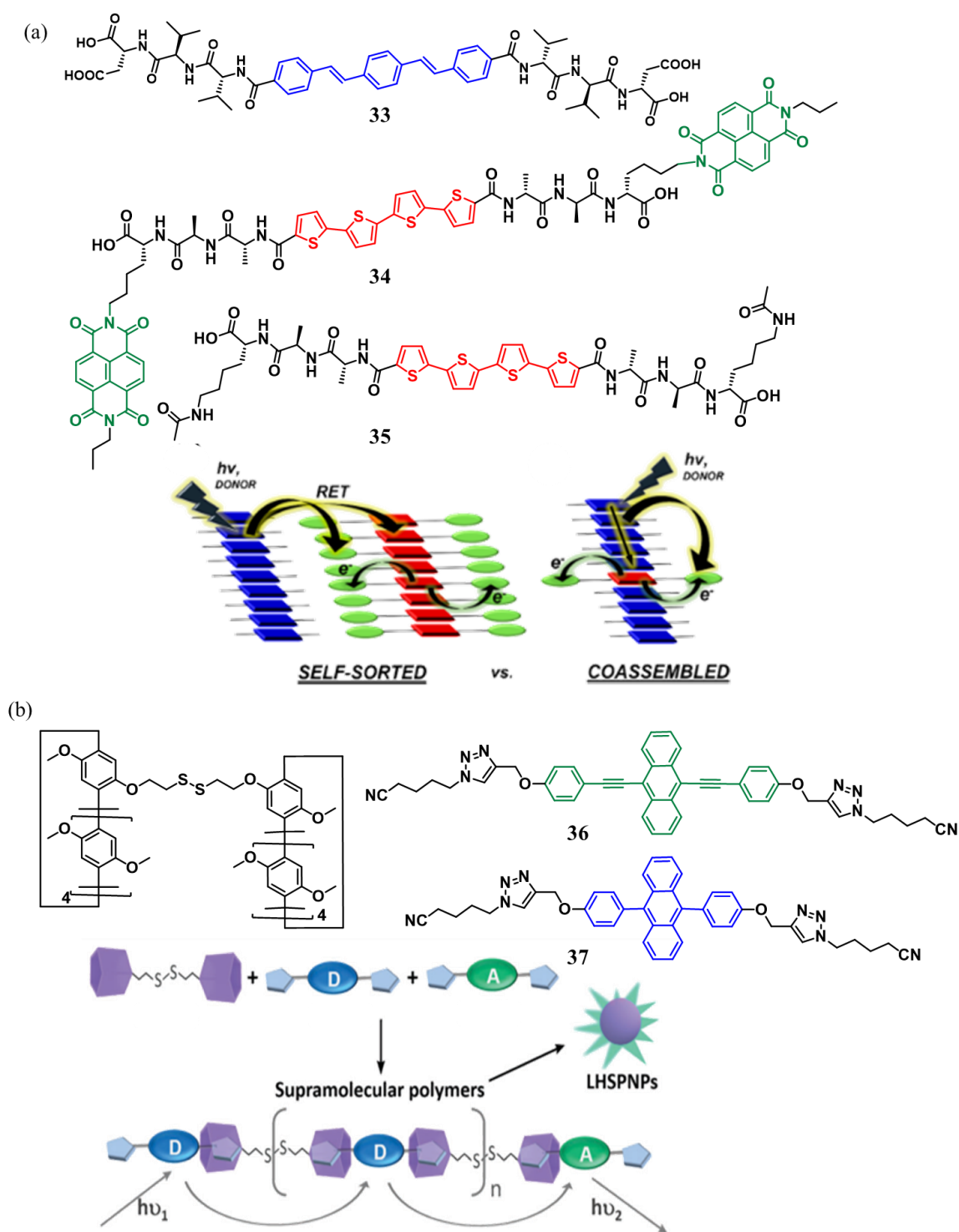
Figure 1.11. (a) Molecular structures of peptides appended π-scaffolds **33**-**35** and a schematic representation of resonance-energy transfer (RET) and electron-transfer process within a two component self-sorted and randomly assembled systems.[57] **(b)** Chemical structures of disulfide-bridged bis-pillararene and the guest molecules **36** and **37** and the light-harvesting properties of their supramolecular polymeric nanoparticles.[58]

1.7.2. Field Effect Transistors and Solar Cells

Owing to their lower cost, light weight and synthetic flexibilities, organic semiconductors are preferred over their silicon counterparts for application in field effect transistors. Among various kinds of molecules used so far, there has always been a strong tendency to use non-fullerene based self-assembled low band gap donor-acceptor systems comprising of strong solar light absorbing organic chromophores in organic transistors and bulk-heterojunction (BHJ) cells.[59] The common approach towards these kinds of self-assembled structures involves D-A-D scaffolds with molecular π−conjugated systems.[60] The controlled self-assembly of such materials has been shown to provide optimized morphologies with better device performance.[61a] Würthner and co-workers have extensively investigated self-assembled merocyanine, perylene bisimide, squaraine and other π−conjugated molecules with different chemical functionalities for photovoltaic applications.[62b] Several optimized processes have been used for the controlled self-assembly of such chromophores. One such technique is solution shearing.[62] OTFTs fabricated from solution sheared selenium squaraine bearing dodecyl substituents (**40**) exhibited a maximum hole mobility of 0.45 cm^2 V^{-1} s^{-1}, which is by far the highest value reported for squaraine based systems (**Figure 1.12a**). Zhu and co−workers have developed a few diketopyrrolopyrrole (DPP) based small molecules, that in their self-assembled state exhibited excellent electron mobility up to 0.55 cm^2 V^{-1}s^{-1}.[63] Our group has reported a supramolecular 2D assembly via a controlled anisotropic arrangement of DPP derivatives (**41**) for the fabrication of organic field-effect transistors with high fluorescence quantum yield and anisotropic charge carrier properties (**Figure 1.12b**).[64] The DPP based amphiphile assembled into 2D sheets in both an organic non-polar solvent and water. The sheets obtained from water was more ordered with an edge-on organization, having a high charge carrier mobility in a direction parallel to the microwave electric field vector. Recently, Mateo-Alonso and co-workers have demonstrated a unique technique to achieve facile processability and better performance in field-effect transistors. Drop casting the sol

phase of the peropyrene π-gelator **42** resulted in a well ordered network structure while resting at room temperature (**Figure 1.12c**).[65]
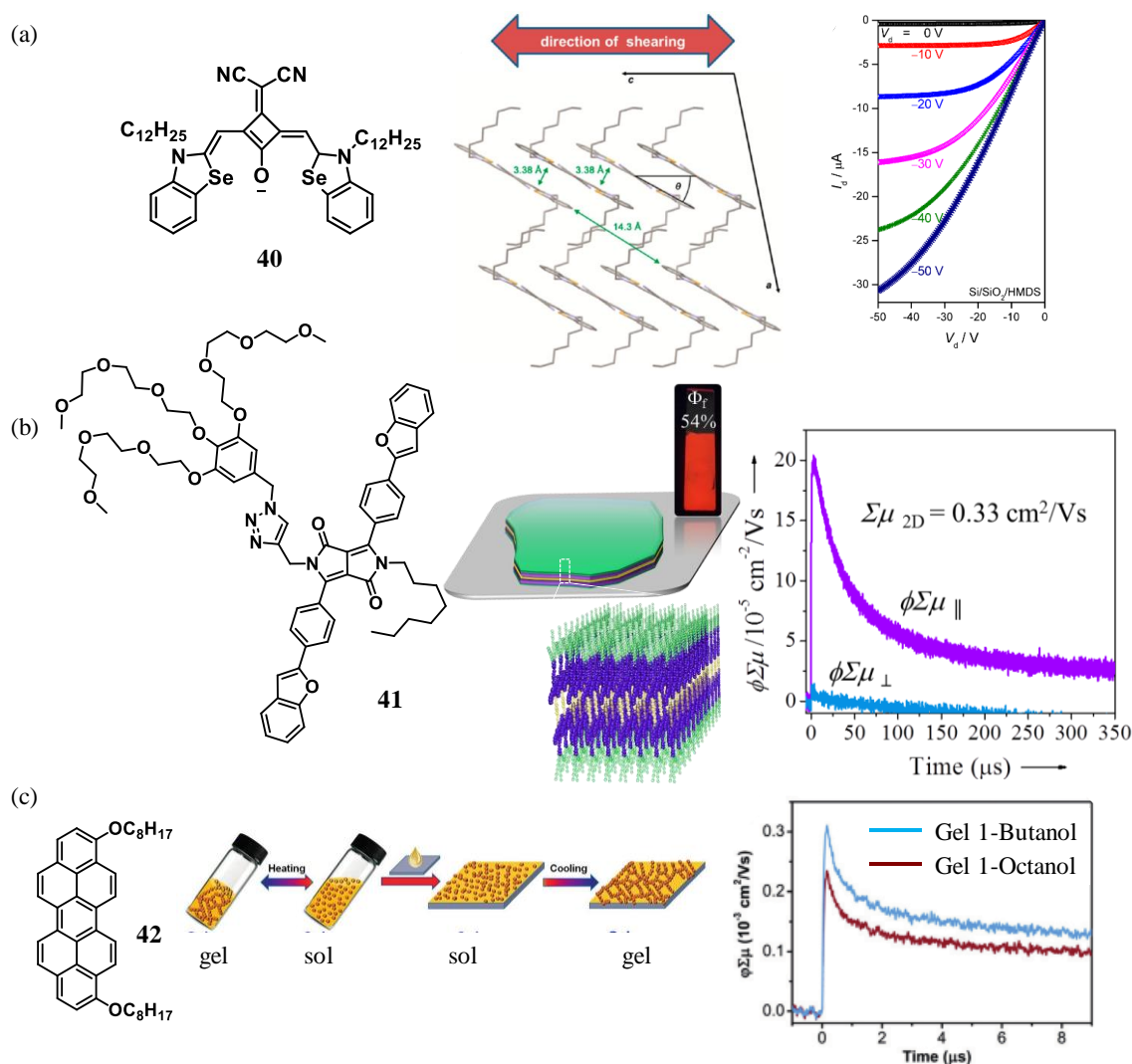
Figure 1.12. (a) Chemical structure of the squaraine dye **40**, and a representation of the self-assembled structure prepared by solution-shearing. The characteristics of a fabricated bottom-gate, top-contact OTFTs is also shown.[62] **(b)** Chemical structure of the D-A type DPP amphiphile **41** and a representation of its ordered nanostructure with high crystallinity and anisotropic charge carrier mobility.[64] **(c)** Chemical structure of the dialkoxylated peropyrene **42** and the sol–gel processing method for device fabrication. The corresponding enhanced charge carrier mobility is also shown.[65]

As a result, an enhanced charge carrier mobility was achieved. Fréchet and co–workers have introduced π–stacking motifs at the terminals of small molecules **43-**

47 to have an end–to–end self–assembly (**Figure 1.13a**).[66] Among different motifs, pyrene is known to have the maximum propensity to readily undergo π–stacking.

43 (n = 1) ; **44** (n = 2)

45: R= 2-ethylhexyl

46: R= 2-ethylhexyl

47: Ar = 1-pyerene
R= 2-octyldodecyl
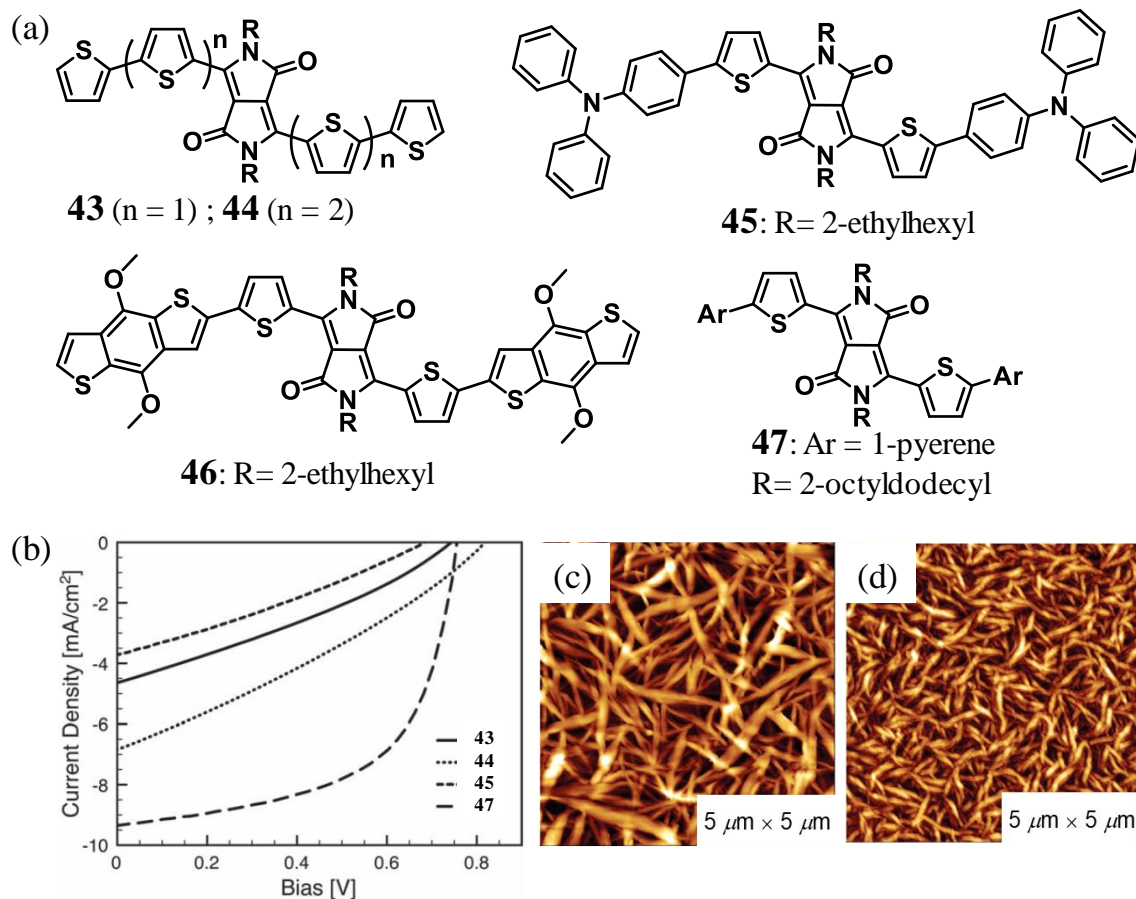
Figure 1.13. (a) Chemical structures of the DPP derivatives **43-47**. **(b)** Characteristic *J–V* curves of organic solar cells fabricated with **43**, **44**, **45** and **47** (AM 1.5 G, 100 mW cm^{-2}). AFM images of films spun-cast from ~0.01 M solutions of **(c) 43** and **(d) 44** on silicon substrates.[66]

The derivatives **43-47** exhibited broad absorption in the film state and hence were used as donors in BHJ solar cells. Active layer of the OSCs were fabricated using PC$_{71}$BM as an acceptor in different blend ratios and maximum PCE of 4.1% was obtained when the derivative **46** was used as the donor (**Figure 1.13b**). The high PCE of the device is attributed to the high J_{SC} value arising from the high crystallinity of the films is promoted by the interplay of the end groups (**Figure 1.13 c, d**).

1.7.3. Electrochromic Devices

Self-assembled materials with stimuli responsive properties can be utilized in devices that reversibly change color or transparency with external stimuli, such as a voltage, light, heat etc. Electrochromic materials undergo change in color/transparency up on application of electric voltage.[67a] Such materials find applications in sensors, smart glass, optical devices etc.[67b] Many inorganic metal oxides based electrochromic materials are well explored. In this context, organic materials have been gaining attention owing to their synthetic feasibility, processability, color tunability and high optical contrast.
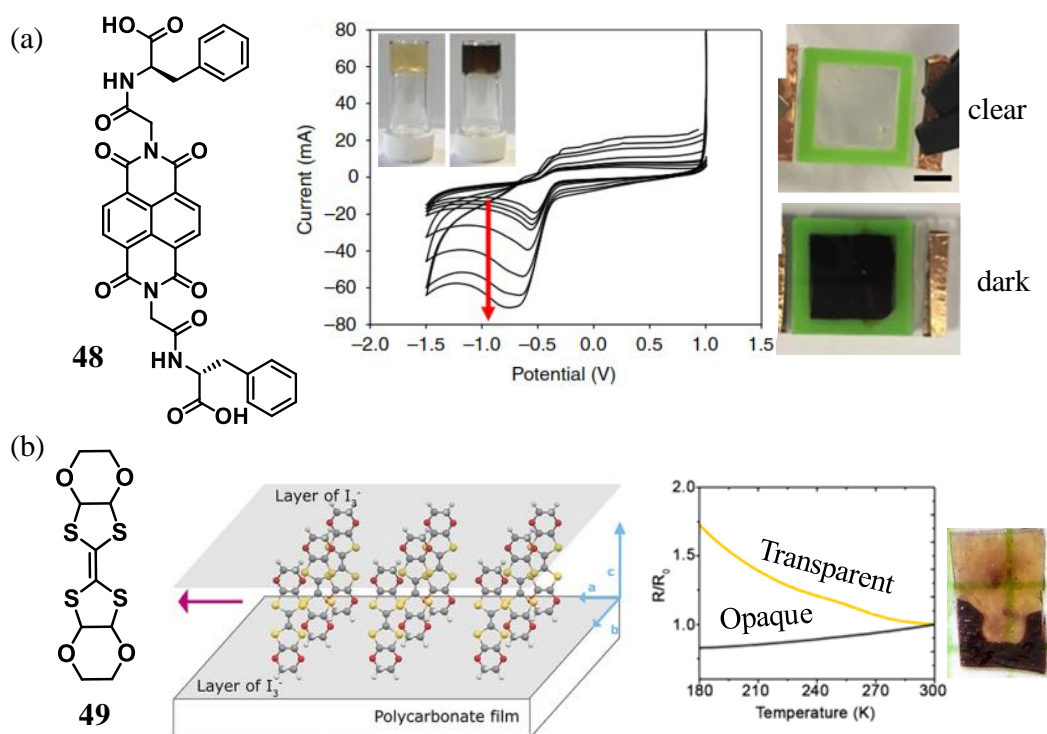
Figure 1.14. (a) Chemical structure of the molecule **48** (left). The electrochemical response (CV) and colorimetric changes upon applying voltage (scan rate of 0.02 to 0.8 V/s), to the gel sandwich device exhibiting stimuli responsive behavior are also shown (right). The photographs of the corresponding hydrogel are also shown.[68] **(b)** Molecular structure of **49** (left), a representation of the supramolecular bilayer film and the corresponding electrochromic device characteristics (right).[69]

Draper and co-workers have fabricated smart windows using a naphthalene diimide NDI (**48**) derived photo- and electrochromic supramolecular gel that exhibited a tunable color from transparent to black and *vice-versa* in response to on applied voltage.[68] In the neutral state of NDI, the gel appeared colorless, which on oxidation turned black (**Figure 1.14a**). The reversible changes in color was observed for many cycles without any degradation. Similarly, using a two dimensionally organized organic molecular metals (BEDO-TTF)$_{2.4}$I$_3$ [BEDO = bis(ethylenedioxy)tetrathiafulvalene) **49**, Daniels *et. al.* have fabricated an electrochromic device that changed color upon electric stimulation (**Figure 1.14b**).[69]

1.8. Supramolecular Amphiphilic Assemblies

Self-organization of amphiphilic molecules is commonly observed in biological systems. For example, the cell membrane is comprised of self-assembled lipid bilayers. Supramolecular chemists, over the past few decades, have been in pursuit of new classes of synthetic amphiphiles that may mimic self-assembly characteristics of native biologically relevant counterparts.[9d] In this context, amphiphilic π−conjugated molecules are of prime significance for creating functional supramolecular materials of different shape and dimensionality, by fine tuning their solvophilic and solvophobic interactions.[70]

Self-assembly of molecules based on ethylene oxide chains have been shown to form water-soluble supramolecular structures. The design and synthesis of such molecular amphiphiles are practically not limited to any particular π−system. Generally, amphiphilic systems consist of a hydrophobic segment and a hydrophilic part. Amphiphilic building blocks can be broadly classified into four classes based on their size, and shape of the hydrophobic π−segment and hydrophilic chain (**Figure 1.15**): (i) linear amphiphiles, (Eg: compound **50**)[71a] (ii) facial amphiphiles, (Eg: compounds **51**)[71b] (iii) bolaamphiphiles, (Eg: compound **52**)[71c] and (iv) disc-like amphiphiles, (Eg: compound **53**).[71d]
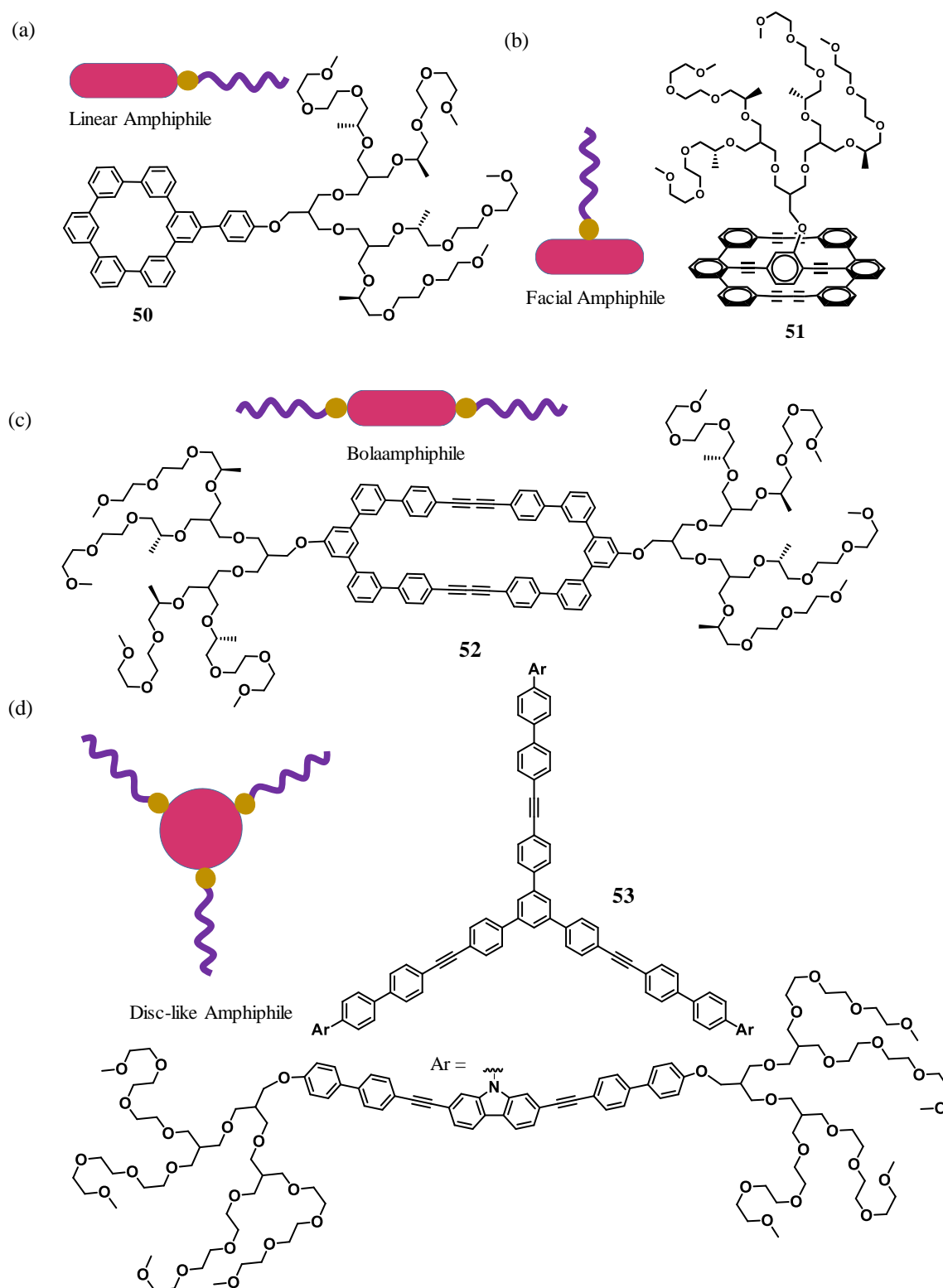
Figure 1.15. Classification of amphiphilic building blocks based on their size, and shape of the hydrophobic π-segment and hydrophilic chain. Molecular structures and schematic representations of **(a)** linear amphiphile **50**, **(b)** facial amphiphile **51**, **(c)** bolaamphiphile **52**, and **(d)** disc-like amphiphile **53**.

Depending on the molecular structure, processing methodology, concentration, stimuli, solvent, environment etc, π−conjugated amphiphiles self-assemble into a wide variety of superstructures. The formation of such aggregates is mainly governed by non-covalent interactions with water molecules.[72]

Construction of 0D assemblies of supramolecular units has mostly been aimed at delivering efficient light harvesters, multivalent molecular recognition units, catalytic systems and templates for the synthesis of various types of materials. Typical examples of 0D supramolecular scaffolds are spherical particles. Fujita *et. al.* have reported a bent bidentate ligand **54** with a glycol chain attached,[73a] that self-assembled into hollow spherical cuboctahedral nano-objects in the presence of Pd^{2+} (**Figure 1.16a**). Self-sorted 0D assembly of oligo(phenyleneethynylene) (OPE)-based amphiphilic molecules, turned into 1D assembly,[73b] which eventually led to gelation in a polar protic solvent. Similarly, Pt-coordinated rectangular shaped bolaamphiphiles **55-57** resulted in a self-assembled structure with size variations roughly in the range of 2.9 to 6.0 nm (**Figure 1.16b**).[73c] Das *et al.* have reported the aggregation behavior of the amphiphile **58** in water-DMSO mixtures, wherein self-organization into small spherical particles with green emission was observed upon gradual increase in the amount of water.[74] In 99% water, the 30-80 nm sized particles emitted at 495 nm ($\tau_{av} = 2.10$ ns, **Figure 1.16c**). The water responsive spherical nanoparticles obtained from amphiphilic molecules **59 - 60** displayed reversible emission color change from blue to cyan upon contact with water (**Figure 1.16d**).[75] This property has been exploited for creating security labels for the protection of currency and valuable documents. However, such reversible changes in emission was not observed for compound **60**. Park *et al.* have investigated the morphology and aggregation induced emission properties of aqueous assemblies of the rod-coil amphiphile **61** having a PEGylated α-cyanostilbene skeleton.[76] Due to the rigid hydrophobic skeleton, the amphiphile **61** in water, self-organized into spherical nanostructures with size 27.6 ± 4.9 nm (**Figure 1.16e**).
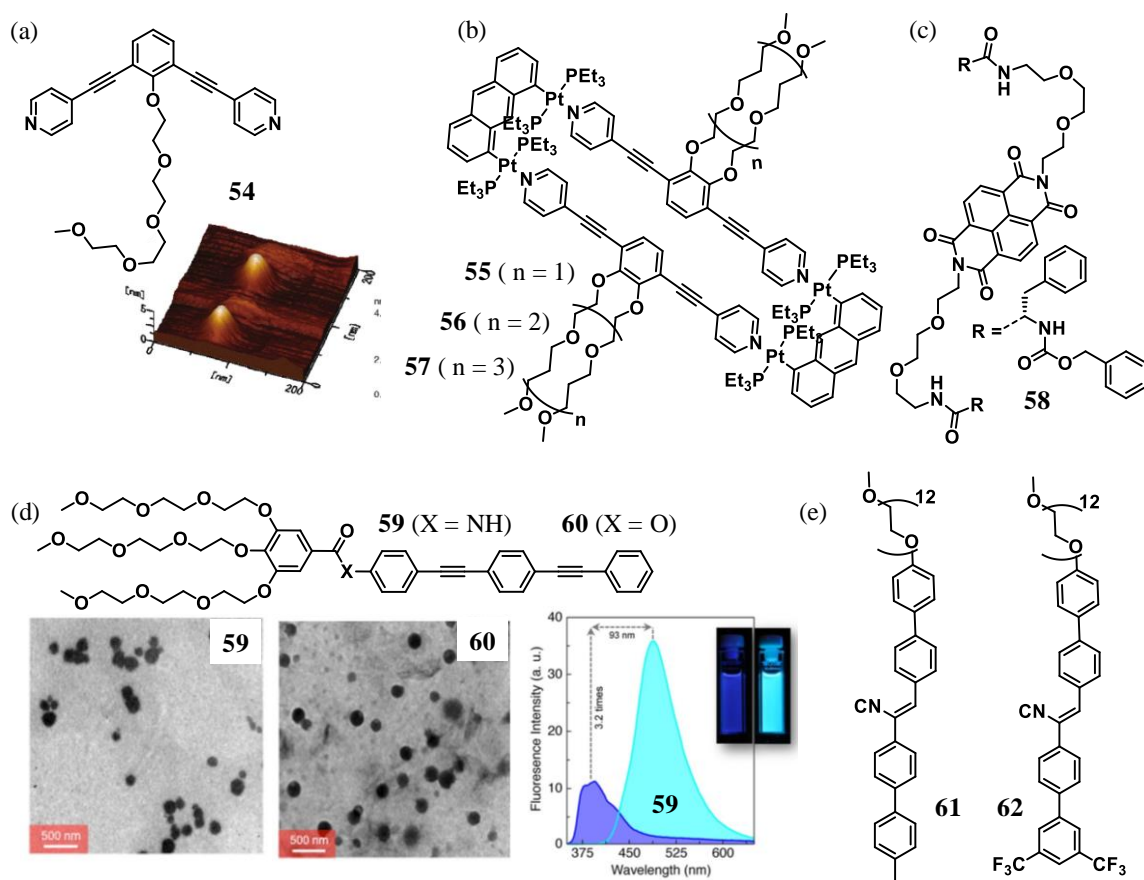
Figure 1.16. (a) Chemical structure of the amphiphilic molecule **54** and the 4-5 nm sized structures formed upon Pt coordination with 24 units of compound **54**. **(b)** Molecular structure of Pt coordination driven supramolecular rectangular amphiphiles **55**-**57** having different glycol chains. **(c)** Molecular structure of the amphiphile **58** that formed green emitting spherical nanoparticles in DMSO-water mixture. **(d)** Chemical structures of amphiphiles **59**-**60** and their self-organized spherical nanoparticles in water-THF mixtures. The corresponding fluorescence change is also shown. **(e)** Molecular structures of the amphiphiles **61** and **62** that formed spherical aggregates in water and rods in water-THF (v/v = 9:1) mixtures.

The isotropic spherical nanostructures emit cyan color with λ_{max} at 500 nm. However, simple variations in chemical functionalities, for instance, incorporation of $-CF_3$ groups (**62**), transformed the morphology of the aqueous aggregates into anisotropic 1D nanofibers. The self-organization of molecule **62** was facilitated by strong $\pi-\pi$ and electrostatic C–F---H–Ar interactions.

Supramolecular structures with specific dimensions could be constructed from designed monomers via the interplay of several non-covalent forces such as H-bonding and π−π stacking. Schenning and co-workers have reported a nucleic acid appended oligo(p-phenylenevinylene) bolaamphiphile **63**,[77] that could be anchored to complementary hydrogen bonding units to form two component 1D supramolecular structures (**Figure 1.17a**). The preferred morphologies for π−amphiphiles with 1D supramolecular structures are rods, fibrils, or nanotubes. Ghosh *et al.* have synthesized unsymmetrical amphiphiles by varying H-bonding units such as amide (**64**) and ester (**65**) groups. The amide **64** formed hydrogels with long fibrillar supramolecular morphologies (**Figure 1.17b**),[78] whereas the ester **63** with spherical micellar structures was not found to form gels. Sanchez *et al.* have reported a C_3 symmetric OPE amphiphilic system, which organized into multidimensional structures such as hollow vesicles, planar networks or rod-like objects depending on the nature of the solvents used. Particularly in benzene, 1D rod like structures were observed.[79a] In another report, Pt complexation with a linear amphiphile **68** transformed itself into a gelator bolaamphiphile with 1D rod like nanostructures (**Figure 1.17d**).[79b] Very recently, Cui and co-workers have reported a π−conjugated hydrophobic system as an active supporter to create 0D spherical aggregates with 6.5 nm diameter, which was later transformed into 1D rods and 1D filaments.[80a] Similarly, in a recent study, Zhang *et al.* have reported a seeded supramolecular assembly of diketopyrrolopyrrole (DDP) based bolaamphiphiles **66** and **67** in water. DPP **66** was found to form 1D nanofibers *via* H-bonding and π−π interactions (**Figure 1.17c**).[80b] Taking advantage of variable H-bonding subunits, Ghosh and co-workers have demonstrated the formation of supramolecular nanostructures of NDI-based amphiphiles (**Figure 1.17e**). The amide linked amphiphiles **69** formed fibrils via slipped H-bonded packing, whereas the hydrazide linked amphiphile **70** and the molecule **71** without any H-bonding moieties exhibited rigid vesicle and micelle structures, respectively.[81]
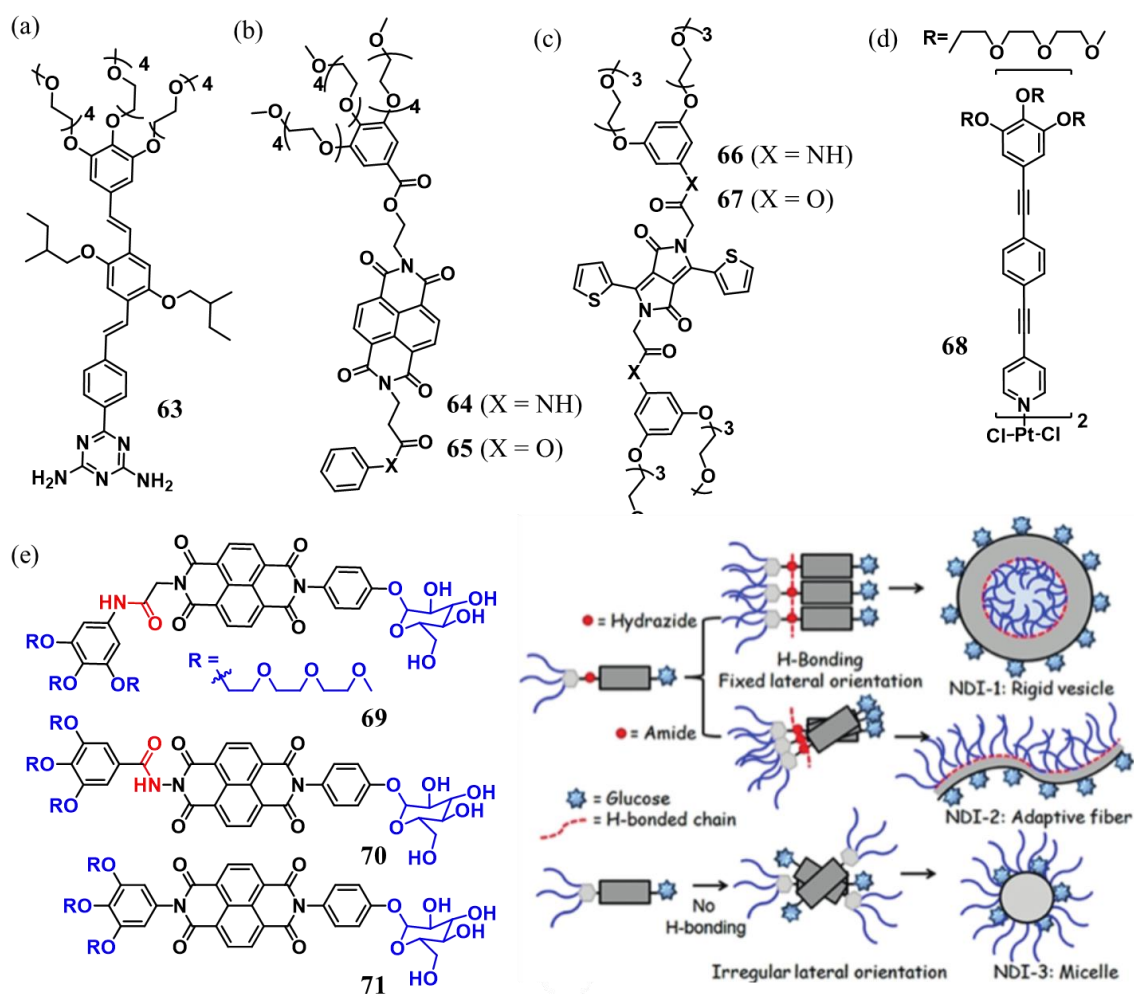
Figure 1.17. Molecular structures of **(a)** OPV based amphiphile **63**, **(b)** NDI based bolaamphiphiles **64** (amide) and **65** (ester) with variable H-bonding units, **(c)** DPP based amphiphiles **66-67** that underwent seeded supramolecular polymerization in aqueous medium, **(d)** the linear amphiphile **68** and **(e)** the NDI based amphiphiles **69-71** with variations in non-covalent functionalities. The corresponding nanoscopic structures formed upon self-assembly are shown.

Extensive investigations by Meijer and co-workers have demonstrated the temperature and concentration dependent pathway complexity of 1D supramolecular growth process involving chiral discotic molecules **72**-**73** (**Figure 1.18a,b**).[82] Aida and co-workers have exploited the amphiphilic assembly of hexabenzocoronene (HBC) **74** for the generation of conductive self-assembled nano-tubular structures (**Figure 1.18c**).[83] For instance, nanotubes from oligo(ethylene glycol) appended HBC were found to be completely debundled and

monodispersed in water. Lee *et al.* have investigated the morphological transformations in the amphiphilic co-assembly of molecules **75** and **76**. Upon increasing the concentration of **76**, a co-assembly comprising of smaller toroid like supramolecular nanostructures was observed.
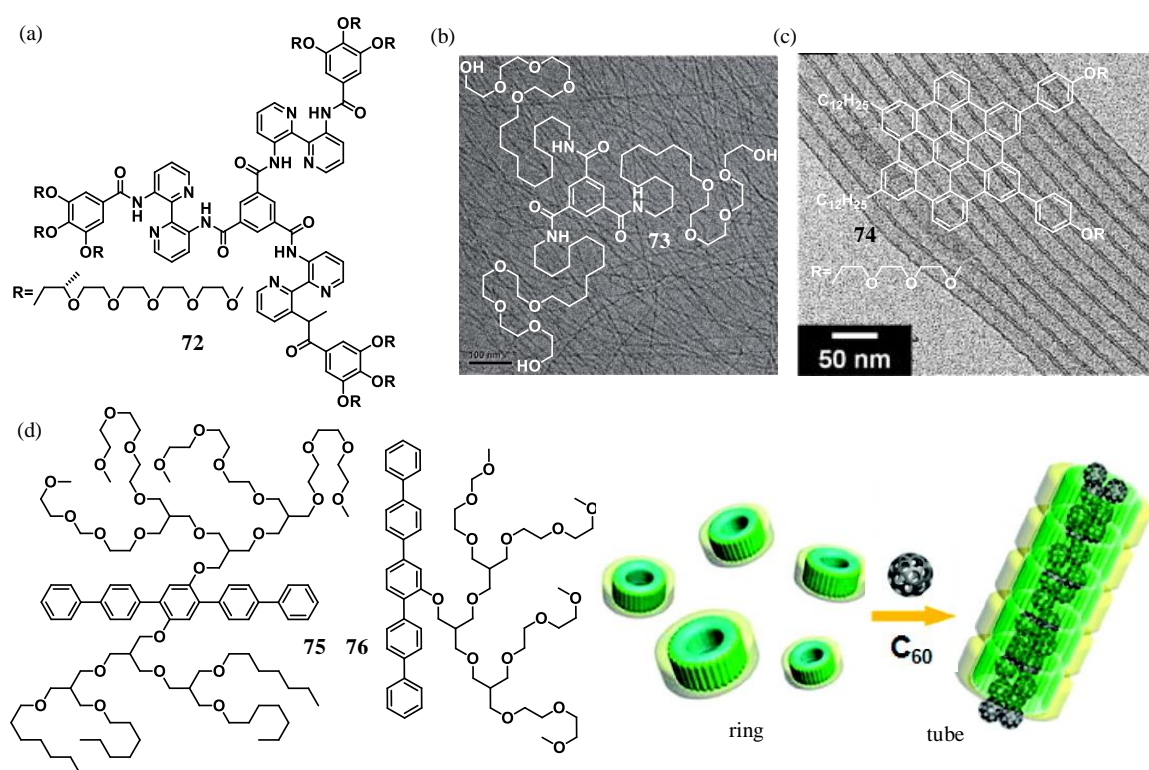
Figure 1.18. (a) Chemical structure of the amphiphilic molecule **72**. **(b)** Structure and TEM image of the fibril morphology of C_3 symmetric amphiphile **73**. **(c)** Structure of hexabenzocoronene based amphiphile **74** and its instantaneous 1D growth into a tubular morphology. **(d)** Molecular structures of the dendritic amphiphiles **75**-**76** and a schematic illustration of the transformation of toroids to 1D tubes in presence of fullerene.

Interestingly, the introduction of fullerene into those toroids resulted in the formation of 1D tubes. The transformation of toroids to tubes is best explained by one dimensional self-stacking of supramolecular rings (**Figure 1.18d**). George and co-workers have synthesized an amphiphilic oligo(*p*-phenylenevinylene) (OPV) derivative **77**, that formed free standing nanosheets in water with enhanced hole mobility (**Figure 1.19a**).[85] Lee *et al.* have demonstrated the formation of 2D supramolecular films using amphiphilic assemblies *via* 2D dynamic lateral growth

of the amphiphile **78** (**Figure 1.19b**).[86a] Upon corannulene inclusion, it transformed into a bucky-ball structure within a span of 30 days. The dimeric micelles without corannulene instantaneously grew only in *x-y* directions, however, curved corannulene induced distortion in the molecular array, that over time transformed into micelles. Very recently, the same group reported an enantiomer sieving 2D membrane that exclusively captured a single enantiomer from a racemic solution. The chiral molecule **79** was found to form chiral pores via dimeric stacking and allowed only a particular enantiomer to pass through (**Figure 1.19c**).[86b] A similar design strategy involving an isomeric amphiphile in the *cis* and *trans* forms was also used to demonstrate morphological distinction in supramolecular assemblies.[86c] While the *cis*-conformer **80** afforded stable static 2D sheets *via anti*-parallel packing at room temperature, the *trans*-conformer **81** produced a dynamic 2D nanostructure, that at room temperature rolled up into a tubular structure and unrolled reversibly at a higher temperature (**Figure 1.19d**).

Three dimensional ordering of molecules and scaffolds are commonly seen in coordination assemblies such as MOFs (metal-organic frameworks) and PCPs (porous coordination polymers).[87] 3D assemblies often result from hierarchical growth of either 1D or 2D molecular assemblies. Kim *et al.* have reported an unusual temperature-dependent LCST phase transition in multiple derivatives of crown ether substituted bezenetricarboxamide. The crown ether derivatives formed a three dimensional hierarchical structure under equilibrium conditions. In another report, Lee and co-workers have synthesized a polyether dendritic amphiphile **82** that forms vesicles (100 nm size) in water (**Figure 1.20a**).[88a] Later, Kim *et al.* have reported the influence of stiffness of the π-core of the molecule **83** on its 3D morphological transformations (**Figure 1.20b**).[88b] Rigid macrocycles factionalized with hydrophilic ether chains are excellent candidates for the construction of 3D nanostructures. Flat aromatic subunits of **84** were found to stack with a face-to-face interaction resulting in vesicular morphology (**Figure 1.20c**).[88c] Similarly, a co-assembly of two PBI based amphiphiles **85-87** also formed vesicular structures with

a pH responsive molecular uptake affinity and tunable emission properties (**Figure 1.20d**).[89]
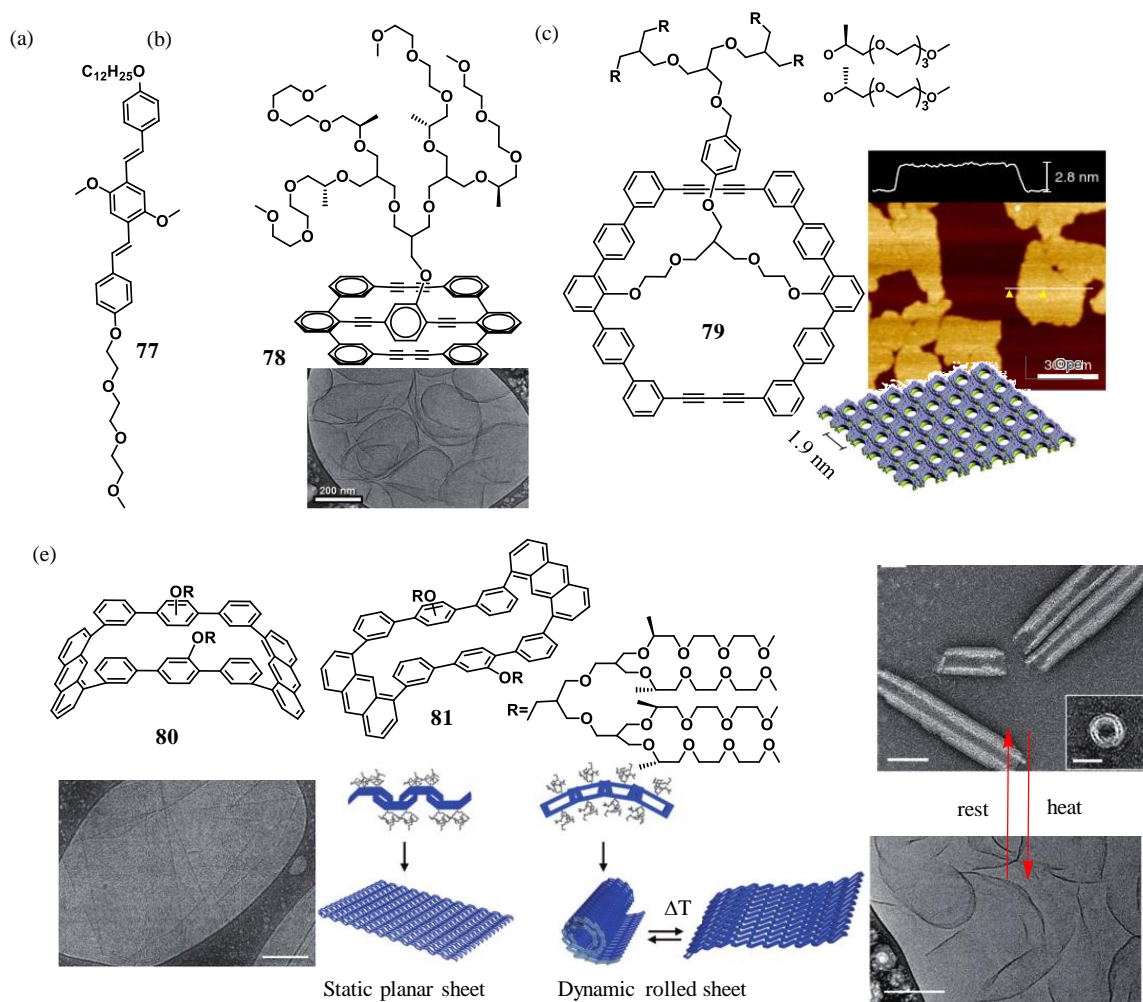
Figure 1.19. (a) Chemical structure of the amphiphile **77** that formed supramolecular sheets with high charge carrier mobility. **(b,c)** Molecular structures of facial amphiphiles, **78**-**79** that formed 2D sheets in water medium. **(d)** Molecular structures of amphiphilic *cis* and *trans*-isomers **80**-**81** that formed stable 2D sheets and tubular structures due to thermally reversible rolling of sheet and exfoliation at high temperature, respectively.

Percec and co-workers have reported a strong emitting dendritic amphiphile **87** (**Figure 1.20e**) that existed as monomer in ethanol and self-assembled when injected into buffered water. Morphological investigations confirmed the formation of nanometer sized multi-lamellar onion-like red emitting 3D supramolecular vesicular dendrimersomes.[90]
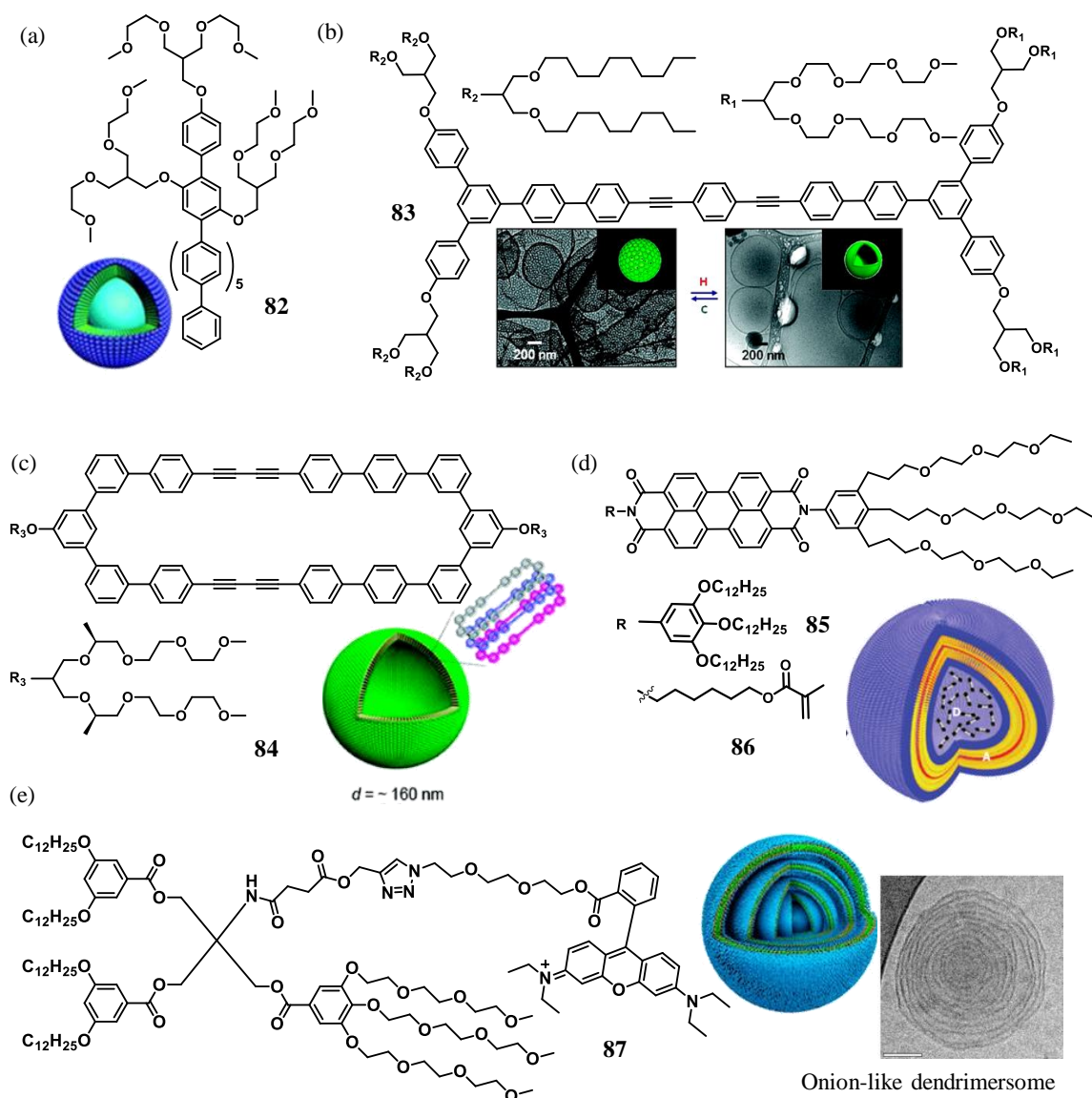
Figure 1.20. Chemical structure of **(a)** the amphiphile **82**, that formed vesicles with a size of 100 nm, **(b)** dumbbell shaped molecule **83** having thermoresponsive vesicular nanostructure, **(c)** amphiphile **84** with rigid macromolecular $\pi-$core that assembled into large vesicles due to face-to-face staking, **(d)** PBI based amphiphiles **85** and **86** with a pH responsive molecular uptake capability and **(e)** Rhodamine-B labeled janus dendrimer **87** that self-assembled into onion-like dendrimersome.

1.8.1. Stimuli-responsive Amphiphilic Assemblies

Recent research in the area of supramolecular amphiphiles are focused towards the development of stimuli responsive smart materials. Large number of molecules with different structural diversity have been tested for their response to various stimulus.

Small amphiphilic molecules with PEGylated moieties have been exploited to create such materials that are responsive to their environmental temperature. In this context, Lee *et al.* have reported thermoresponsive nematic gels *via* careful modulation of the chemical structures of the compounds **88** and **89**. They were found to supramolecularly organize into entangled nanofibers having diameter of ~9 nm and several micrometers in length, under a mutually parallel allignment.[91a] The opaque gel formed at 30 °C was reversibly transformed into its sol upon cooling to 10 °C (**Figure 1.21a**).

In thermally assisted supramolecular polymerization, the dormant state of monomeric units can be activated with heat to undergo polymerization. Lee and co-workers have recently suggested heat-stress to be a trigger for supramolecular polymerization of synthetic toroidal aggregates into helical chains. In the dormant state of the amphiphilic assembly of **90**, the dehydration of the exterior polyether chains at 50 °C disturbed the eclipsed packing and transformed into a slipped packing.[91b] As a result, the hydrophobic cross-sectional area of the globules increased. The slipped conformational changes with inherent kinetic stability allowed a living supramolecular polymerization, leading to spiral chains within a span of four days. However, upon cooling back to room temperature, the helical chain depolymerized into static toroids (**Figure 1.21b**). Photoresponsive amphiphilic molecular building blocks are potential candidates for creating stimuli-responsive smart materials. Matsuda *et al.* have reported a light triggered reversible dynamic motion of amphiphilic assembly concomitant with a morphological transformation. The amphiphilic assembly of a photochromic diarylethene in its open form **91** exhibited colorless micro-spherical structures. Upon UV irradiation, the diarylethene core transformed into the closed form **92**, with a change in its color and morphology leading to dark violet fiber-like structures. The reversal to the initial stage was achieved upon visible light irradiation (**Figure 1.22a**).[92a]

(a)

88 (n = 1)
89 (n = 2)

Heating

Cooling

ΔT

4.5 nm

(b)

R= S
R

90

Self-assembly

Static toroid

Energy

Inactive

Active

Heat treat
(50 °C , 20 min)

Active toroid

Growth
(25 °C)

Static toroid

Helical chain

Dissipation

1 day   2 day   3 day   4 day
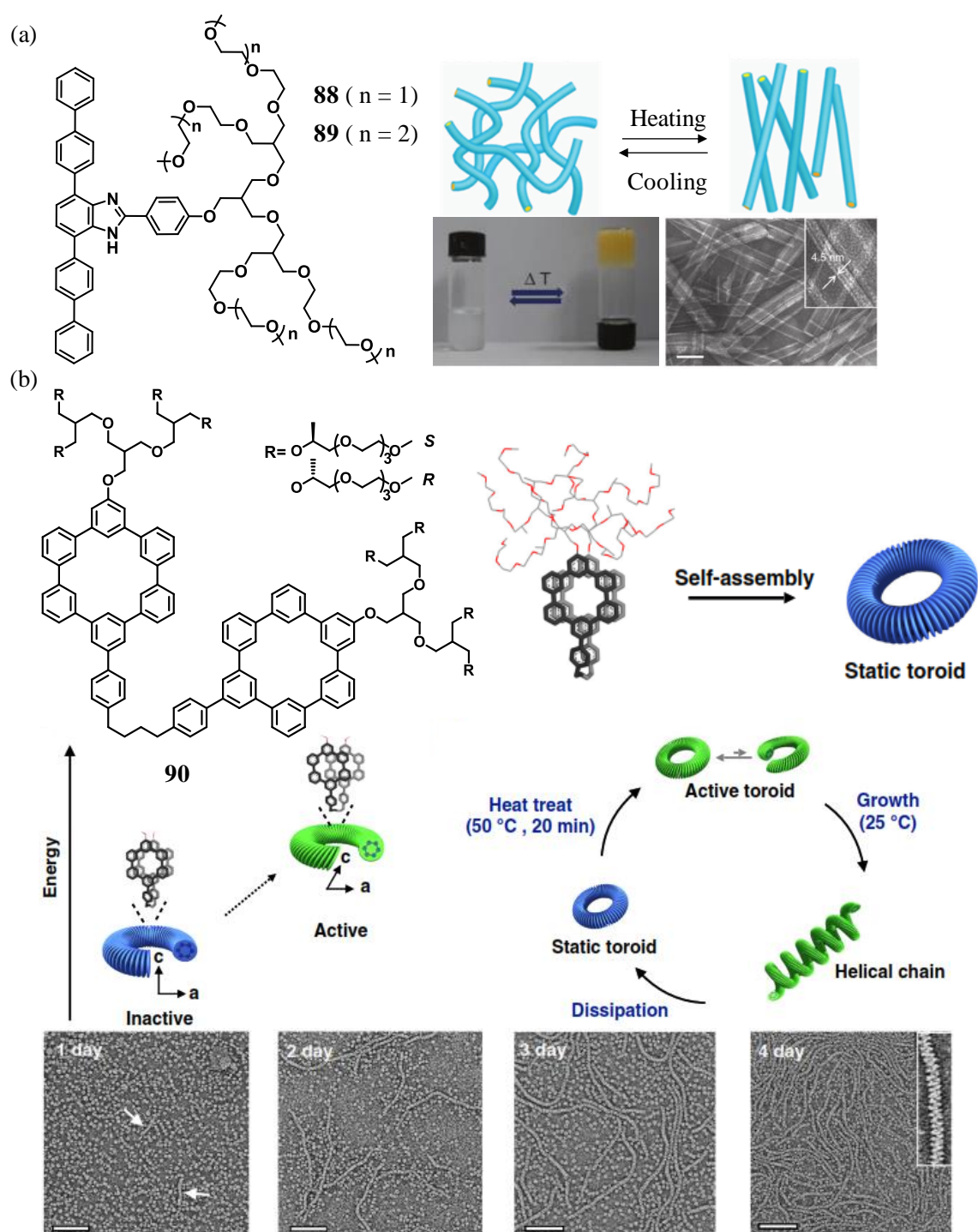
Figure 1.21. (a) Structure of amphiphiles **88** and **89** exhibiting thermoresponsive sol-gel transformation. **(b)** Chemical structure of the macrocycle **90**, which self-assembled into static toroids at room temperature in water. Upon thermal activation, spontaneous helical polymerizations occurred and reversibly transformed back to static toroid via depolymerization upon cooling to room temperature.
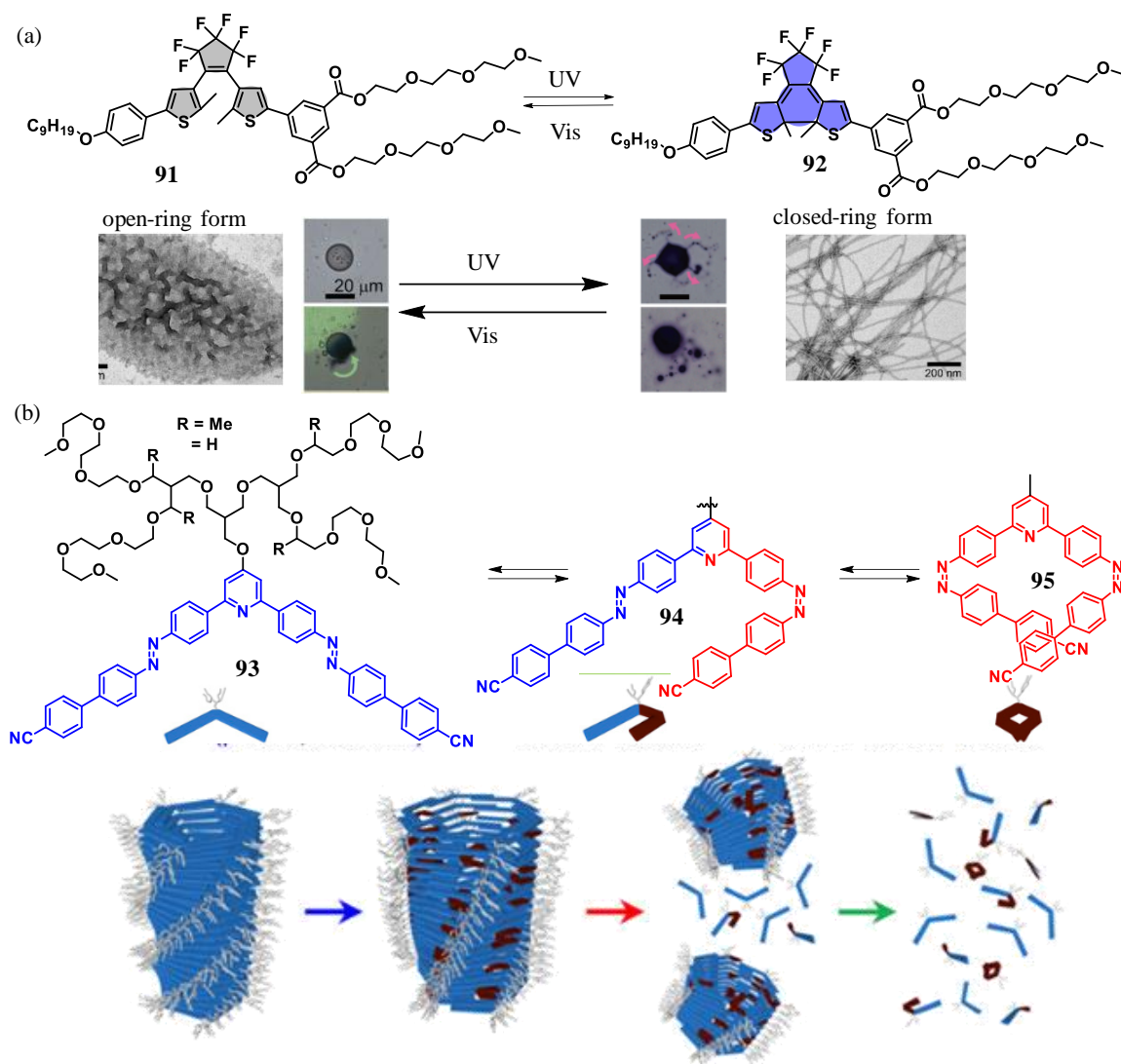
Figure 1.22. a) Chemical structure and reversible photochromic transformation of an amphiphilic diarylethene from its open ring structure **91** to the closed form **92**, along with a concomitant morphological variation. The supramolecular assembly of the open structured oil-like droplets featured a spherical morphology, whereas the closed form had fibrilar structures. **(b)** Chemical structure of the photoresponsive chiral building block in its all *trans* state, **93,** *trans-cis* state **94** and all *cis* state **95** featured a nano-tubular morphology, which upon light induced reversible transformation to mono (**94**) and all *cis* (**95**) forms leading to the destruction of its assembled structure.

Taking advantage of a photoresponsive azo-group, Pavan and co-workers have demonstrated a switchable supramolecular tubular morphology in a water soluble

chiral amphiphile **93** upon photoirradiation. Upon light illumination beyond a threshold strain, the tubes disassembled into individual molecules.[92b]
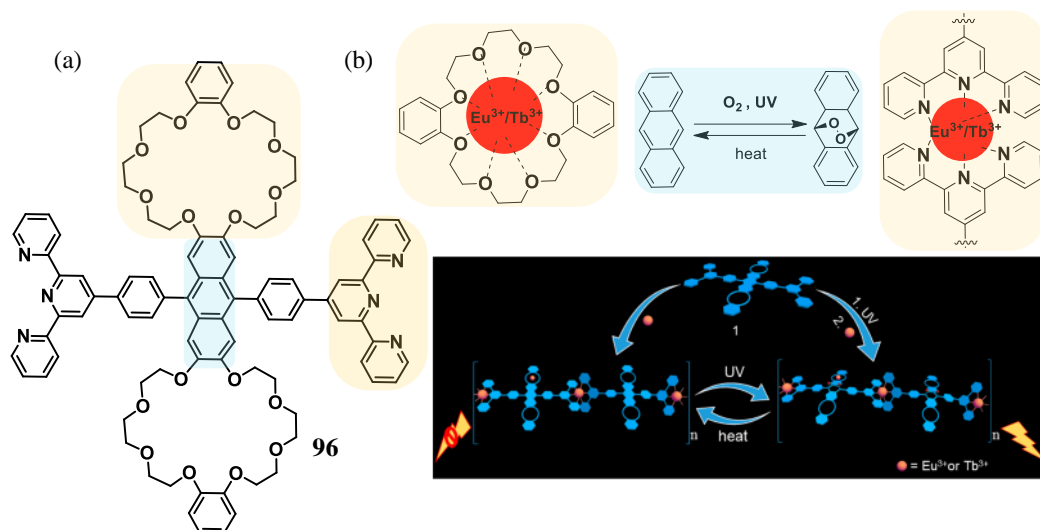
Figure 1.23. (a) Chemical structure of the amphiphile **96** and **(b)** the corresponding oxygen photoaddition and lanthanide coordination.

Recently, Liu *et al.* reported the tunable luminescence behavior of a self-assembled anthracene system *via* photoreaction and coordination of lanthanides. The 9,10-diphenylanthracene derivative **96** has an excited state that matches the first excited state of certain lanthanides. Therefore, it can undergo photoaddition with oxygen with a turn ON fluorescence, when Tb^{3+} and Eu^{3+} bind to the terpyridine groups. Heat induced deoxygenation turned OFF the lanthanide luminescence.[93]

Another class of exciting materials are the electroactive amphiphiles comprising of redox-switchable functional groups. Several reports on electroactive amphiphilic assemblies have explored the twin possibilities of switching the structural features simultaneous with their functional behavior.[94] The structural change can be from a self-assembled state to discrete monomers, or to more complex structures. Usually, such amphiphiles consist of well-investigated ferrocene or tetrathiafulvalene based redox active groups. Very recently, a PDI based supramolecular amphiphile **97** was reported to undergo chemical reduction in the presence of $Na_2S_2O_4$ to compound **98** that in prescence molecular O_2 got reversed to the neutral form. An equilibrium was

proposed to exist between the monomeric units and the self-assembled *H*-type aggregates of the amphiphile **97**.[95a] Oxidation of **98** followed by an internal structural rearrangement enabled nucleation and growth, thereby facilitating a side to side fused assembly with time. The ordered *H*-type packing was shown to transform into a slipped *J*-type arrangement, which led to precipitation overnight.
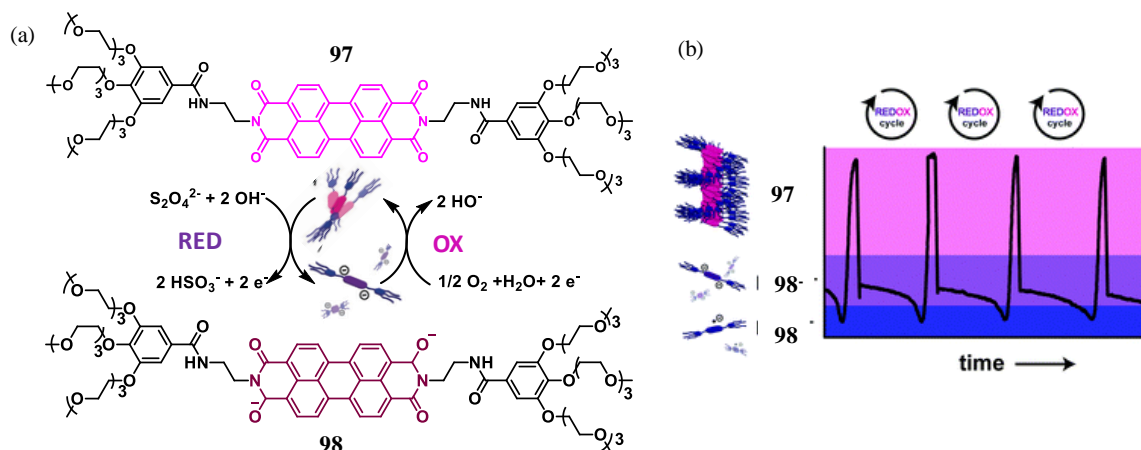
Figure 1.24. (a) Molecular structures of the PDI derivatives **97**–**98** and the mechanism of redox processes involved in their mutual interconversion and **(b)** the corresponding reversible redox cycles.

Apart from effecting a simple on/off response, it is further possible to control the overall morphology of the assemblies by altering their redox states. Some particularly attractive examples are based on the oligoaniline **99**, that upon redox switching, transformed its morphology between vesicles and puck-like micelles (**Figure 1.25a**).[96] Stupp and coworkers have reported charge transfer complexation based ferroelectric materials using an acceptor **101** and a donor **102**, that showed spontaneous electric polarization and can be reversed by the application of an external electric field (**Figure 1.25b**). Such materials are of potential interest for application in sensors, photonic crystals and energy efficient memories.[97]

Lee and coworkers have synthesized a number of amphiphilic units armed with polyether chains leading to differently sized and shaped supramolecular assemblies. The co-assembly of a pyridine-based molecule **103** in its cationic and neutral forms was shown to encapsulate double standard DNA via electrostatic non-covalent interactions, facilitated by the counter ionic charge distribution of DNA and the

molecules.[98] The pyridine subunits upon protonation led to an increase in the electrostatic interactions between the molecule and the encapsulated helical DNA. As a result, the pore size of tubular nanostructure was reduced leading to the inversion of the helical structures of DNA. It is important to note that such processes, in nature, are found to be reversible with deprotonation (**Figure 1.26a**).
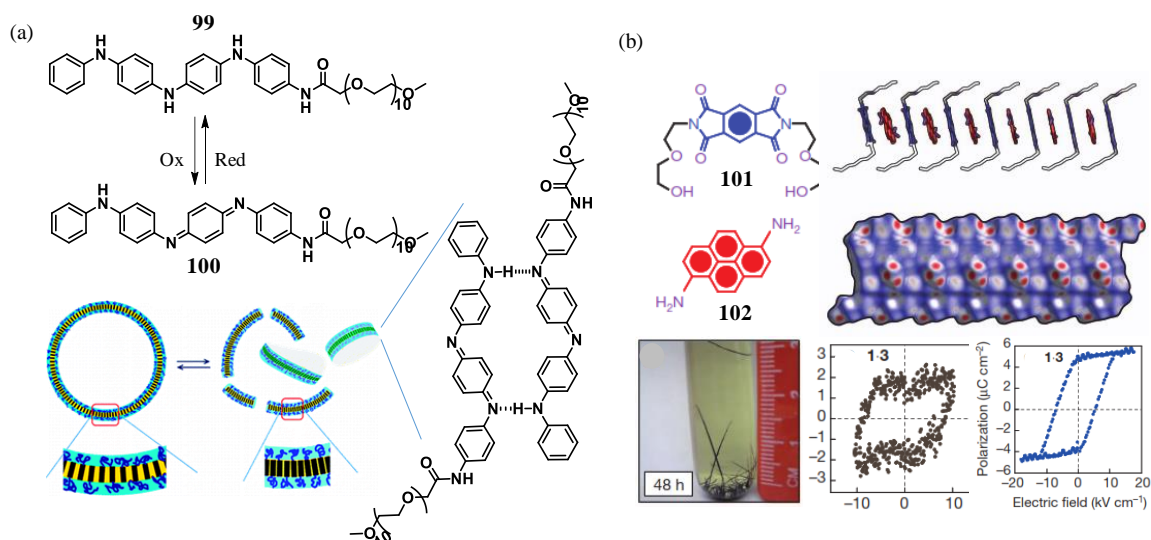
Figure 1.25. (a) Molecular structures of the voltage responsive amphiphiles **99** and **100** and a schematic representation of redox switching between vesicles and puck-like micelles. **(b)** Molecular structures of the acceptor **101** and the donor **102** forming room temperature ferroelectric supramolecular charge transfer complexes. Images show the hirschfeld effect of the grown crystal and polarizations hysteresis.

The same group also developed dynamic 2D materials via the interplay of protonation induced electrostatic interactions between two amphiphiles. The amphiphile **104** bearing protonation active pyridine moieties, in its deprotonated state, formed self-sorted nano-tubular structures with 2D sheets of **105** at pH 7.4.[99] Protonation of pyridine in **104** led to the disassembly of the tubular structures into nano-rings, however electrostatic interactions afforded the formation of 2D network heterostructures at pH 5.5.

π-Conjugated molecular assemblies with tunable luminescence properties under the influence of an external mechanical stimulus are potential candidates for

application in sensors and imaging devices.[10] The rational design of mechanoresponsive amphiphiles depends on the dipolar characteristics of π-conjugated systems. In this context, Yagai *et al.* have reported an OPV system **106** with a didodecylamino group at one end and a tri(ethylene glycol) ester group at the other end, that exhibited multiple color states *via* a controlled molecular self-assembly.[100]
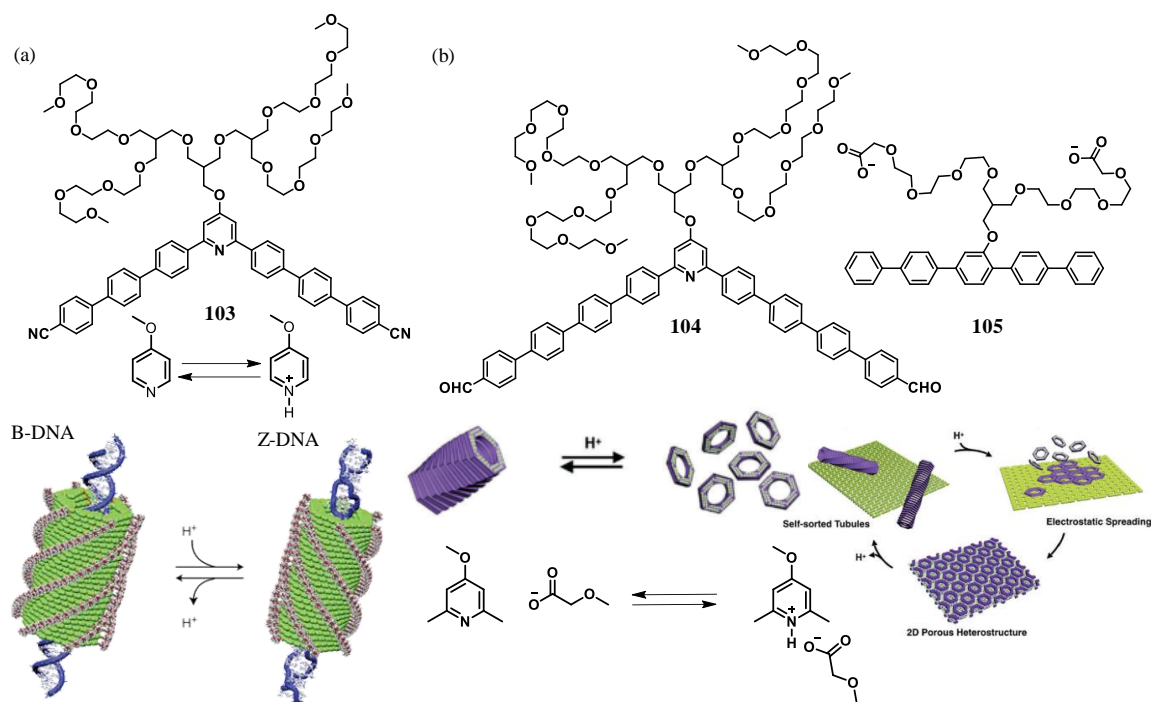
Figure 1.26. (a) Chemical structure of the molecules **103** and helicity inversion of DNA with the amphiphilic assembly triggered by protonation and deprotonation of the pyridine core. **(b)** Molecular structures of compounds **104**-**105** and the corresponding pH responsive reversible disassembly of tubules leading to the formation of 2D hetero networks between macrocycles of **104** and 2D sheets of **105**.

A yellow emitting thin film obtained by the drop casting of an aqueous acetonitrile solution changed to a fluidic material with an orange emission upon gentle pressing. It further changed to yellowish green followed by a green emissive crystalline state under rubbing and annealing at 50 °C, respectively (**Figure 1.27a**).

π-Conjugated amphiphiles with rigid π−cores and flexible hydrophobic segments were found to exhibit different supramolecular structures and physicochemical properties depending on several factors such as concentration, experimental conditions, etc. For instance, mechanochromic behavior was imparted to the amphiphilic aqueous assembles of the anthracene derivative **107** by changing its core to pyrene (**108**).[101]
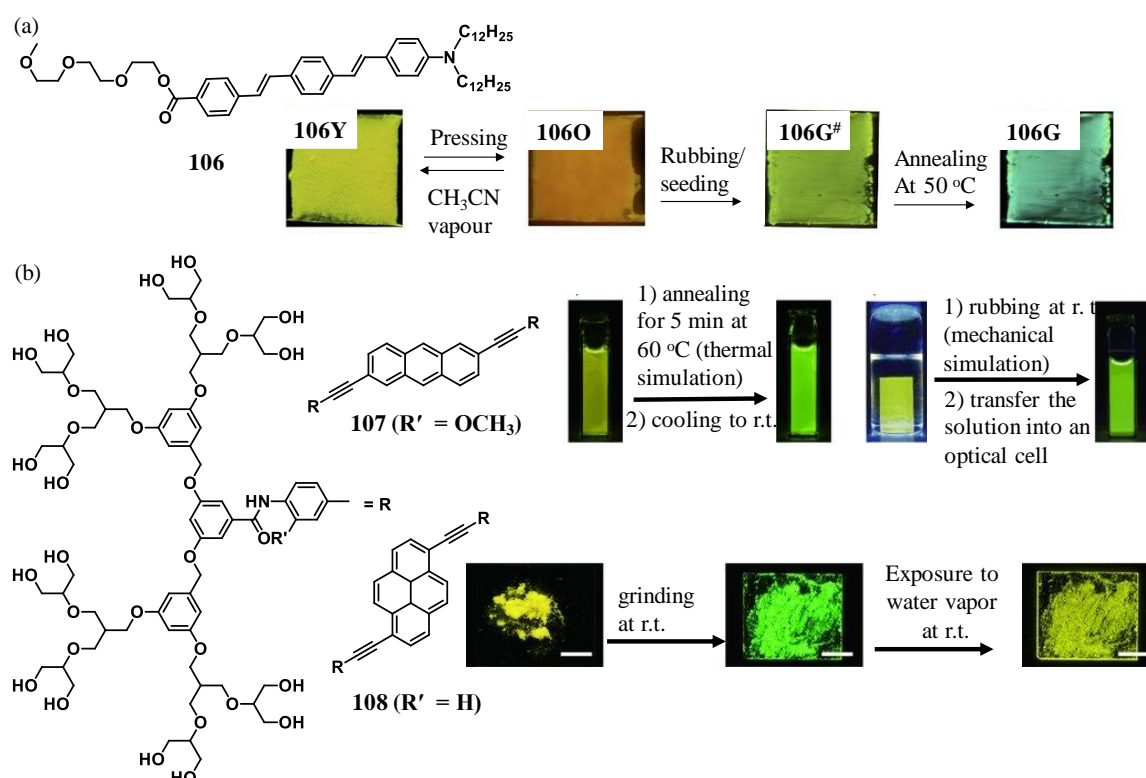
Figure 1.27. Molecular structure of **(a)** the amphiphile **106** that, as a thin film, exhibited multi-step stimuli-responsive fluorescence changes, and **(b)** the anthracene and pyrene derivatives **107**-**108**. The mechano-humidity sensing and mechanical grinding response are also shown.

The supramolecular assembly of **107** exhibited a yellow to green emission change grinding or heating in water. On the other hand, the pyrene based amphiphile **108** responded to both mechanical stimulus and humidity in its solid state. Both the amphiphiles formed micellar structures with diameters 5 nm and 10 nm, respectively, in water. The mechanical properties of the assemblies of the pyrene derivative **108** is best explained using the concept of excimer formation.[102] The yellow emissive excimer in solid state transformed into non-excimeric green

emissive self-assembled structures upon grinding and regained its yellow emission upon exposure to water vapor (**Figure 1.27b**).

1.9. Objectives and Methodologies of the Present Work

The present thesis deals with a systematic study of the synthesis, self−assembly and electronic properties of a few rationally designed supramolecular organic functional materials based on π−systems. We synthesized a few anthracene and phenyleneethynylene based photo and thermos-responsive systems, and investigated their stimuli responsive self-assembly with respect to the mechanism, properties and applications of the resultant supramolecular architectures. Modulation of geometry controlled Diels-Alder photoreaction of anthracenes, controlling the transparency of molecular solutions via self-assembly mediated thermoresponsive behavior and formation of free standing films in a monophasic solvent was achieved through various supramolecular interactions involving specifically designed chromophoric systems. Although, nanoscopic and macroscopic investigations on the supramolecular growth of an amphiphilic assembly is well documented in literature, exact understanding behind the observed changes in properties, say the film formation in a monophasic medium, is still in its infancy.

With the above objectives in mind, we synthesized H-bonding motifs linked anthracene and phenyleneethynylene based π–conjugated molecules with an expectation to restrict their π–core interactions inside confined environments as in a gel medium. With this objective, in **Chapter 2**, we report on a geometrically locked molecular environment inside a gel medium that provided access to stereoselective [4 + 2] Diels-Alder photocycloaddition reaction in high yields. Such photoadduct has distinctly different photo- and electroluminescence properties unlike its parent system. We further attempted to utilize similar photocycloaddition reactions to manipulate the thermoresponsive properties of an amphiphilic system utilizing their *via* LCST phase transitions as reported in **Chapter 3**. The near room temperature thermoresponsive nature of the molecules was further exploited to fine tune light

and heat transmission properties of their aqueous solutions aiming at the development of smart windows. In the final chapter (**Chapter 4**), we demonstrate thermally assisted supramolecular film formation properties of the co-assembly of two dipole-varied amphiphiles inside a single phase solvent. Thermally assisted copolymerization resulted in the growth of free-standing films within a homogeneous aqueous medium. Detailed insights on the work described in the various chapters was achieved by the systematic characterization of the morphological features, optical properties and related behavior using various experimental and instrumental techniques.

1.10. References

(1) (a) Lehn, J.-M.; *Supramolecular Chemistry*; Winheim, Germany, **1995**. (b) Steed, J. W.; Atwood, J. L. *Supramolecular Chemistry*; Wiley: Chichester, **2000**.

(2) The Nobel Prize in Chemistry 2016–Advanced Information. Nobelprize.org. Nobel Media AB 2014. Web. October 6, 2016.

(3) (a) Kay, E. R.; Leigh, D. A.; Zerbetto, F. *Angew. Chem. Int. Ed.* **2007**, *46*, 72. (b) Erbas-Cakmak, S.; Leigh, D. A.; McTernan, C. T.; Nussbaumer, A. L. *Chem. Rev.* **2015**, *115*, 10081.

(4) (a) Brunsveld, L. ; Folmer, B. J. B.; Meijer, E. W. Sijbesma, R. P.; *Chem. Rev.* **2001**, *101*, 4071. (b) Whitesides, G. M.; Grzybowski, B. *Science* **2002**, *295*, 2418. (c) Kato, T. *Science* **2002**, *295*, 2414. (d) Aida, T.; Meijer, E. W.; Stupp, S. I. *Science* **2012**, *335*, 813.

(5) (a) Kim, H.-J.; Kim, T.; Lee, M. *Acc. Chem. Res*. **2011**, *44*, 72. (b) Görl, D.; Zhang, X.; Würthner, F. *Angew. Chem. Int. Ed.* **2012**, *51*, 6328. (c) Grzybowski, B. A.; Stone, H. A.; Whitesides, G. M. *Nature* **2000**, *405*, 1033. (d) Prins, L. J.; Reinhouldt, D. N.; Timmerman, P. *Angew. Chem. Int. Ed.* **2001**, *40*, 2382.

(6) (a) Lehn, J.-M. *Science* **1985**, *227*, 849. (b) Lehn, J.-M. *Angew. Chem.***1988**, *100*, 91.

(7) Piepenbrock, M.-O. M.; Lloyd, G. O.; Clarke, N.; Steed, J. W. *Chem. Rev.* **2010**, *110*, 1960.

(8) Hoeben, F. J. M.; Jonkheijm, P.; Meijer, E. W.; Schenning, A. P. H. J. *Chem. Rev.* **2005**, *105*, 1491.

(9) (a) Hamley, I. W. *Angew. Chem. Int. Ed.* **2003**, *42*, 1692. (b) Shimizu, T.; Masuda, M.; Minamikawa, H. *Chem. Rev.* **2005**, *105*, 1401. (c) Palmer, L. C.; Stupp, S. I. *Acc. Chem. Res.* **2008**, *41*, 1674; (d) Rosen, B. M.; Wilson, C. J.;   Wilson, D. A.; Peterca, M.; Imam, M. R.; Percec, V. *Chem. Rev.* **2009**, *109*, 6275.

(10) Sagara, Y.; Yamane. S.; Mitani, M.; Weder, C.; Kato, T. *Adv. Mater.* **2016**, *28*, 1073.

(11) Reinhoudt, D. N. *Supramolecular Materials and Technologies*: Wiley, **1999**

(12) Babu, S. S.; Praven, V. K.; Ajayaghosh, A. *Chem. Rev.* **2014**, *114*, 1973.

(13) Ludlow, R. F.; Otto, S. *Chem. Soc. Rev.*, **2008**, *37*, 101.

(14) Hamilton, A. D. *Supramolecular Control of Structure and Reactivity*; Wiley, **2008**.

(15) Ariga, K.; Hill, J. P.; Lee, M. V.; Vinu, A.; Charvet, R.; Acharya, S. *Sci. Technol. Adv. Mater.* **2008**, *9*, 014109.

(16) (a) Görl, D.; Zhang, X.; Würthner, F. *Angew. Chem. Int. Ed.* **2012**, *51*, 6328. (b) Hoeben, F. J. M.; Jonkheijm, P.; Meijer, E. W.; Schenning, A. P. H. J. *Chem. Rev.***2005**, 105, 1491.

(17) (a) Ajayaghosh, A.; Praveen, V. K.; Vijayakumar, C. *Chem. Soc. Rev.* **2008**, *37*,109. (b) Würthner, F.; Kaiser, T. E.; Saha-Möller, C. R. *Angew. Chem. Int. Ed.* **2011**, *50*, 3376; (c) Yagai, S. *Bull. Chem. Soc. Jpn.* **2015**, *88*, 28.

(18) Berg, J. M.; Tymoczko, J. L.; Stryer, L. *Biochemistry*, 6th Ed., W. H. Freman &Co., New York, **2006**.

(19) Hunter, C. A.; Sander, K. M. *J. Am. Chem. Soc.* **1990**, *112*, 5525.

(20) Beer, P. D.; Gale, P. A.; Smith, D. K. *Supramolecular Chemistry*, Oxford, **1999**.

(21) Prins, L. J.; Reinhoudt, D. N.; Timmerman, P. *Angew. Chem. Int. Ed.* **2001**, *40*, 2382.

(22) Rivnay, J.; Mannsfeld, S. C.; Miller, C. E.; Salleo, A.; Toney, M. F. *Chem. Rev.* **2012**, *112*, 5488.

(23) Herbst, S.; Soberts, B.; Leowanawat, P.; Lehmann, M.; Wutthner, F. Angew. Chem. Int. Ed. **2017**, *56*, 1.

(24) Anthony, J. E. *Chem. Rev.* **2006**, *106*, 5028.

(25) Hains, A. W.; Liang, Z.; Woodhouse, M. A.; Gregg, B. A. *Chem. Rev.* **2010**, *110*, 6689.

(26) Mas-Torrent, M.; Rovira, C. *Chem. Rev.* **2011**, *111*, 4833.

(27) Kasha, M. *Radiation Research* **1963**, *20*, 55.

(28) Kasha, M.; Rawls, H. R.; Ashraf El-Bayoumi, M. *Pure Appl. Chem.* **1965**, *11*, 371.

(29) Kistler, K. A.; Pochas, C. M.; Yamagata, H.; Matsika, S.; Spano, F. C., *J. Phys. Chem. B* **2012**, *116*, 7786.

(30) Hecht, M.; Schlossarek, T.; Stolte, M.; Lehmann, M. *Angew. Chem. Int. Ed.* **2019**, *58*, 12979.

(31) Le Bras, L.; Chaitou, K.; Aloise, S.; Adamo, C.; Perrier, A. *Phys. Chem. Chem. Phys.,* **2019**, *21*, 46.

(32) Luo, J.; Xie, Z.; Lam, J. W. Y.; Cheng, L.; Chen, H.; Qiu, C.; Kwok, H. S.; Zhan, X.; Liu, Y.; Zhu, D.; Tang, B. Z. *Chem. Commun*. **2001**, 1740.

(33) Chen, L.; Lin, G. W.; Peng, H. R.; Ding, S. Y.; Luo, W. W.; Hu, R. R.; Chen, S. M.; Huang, F.; Qin, A. J.; Zhao, Z. J.; Tang, B. Z. *Mater. Chem. Front.* **2017**, *1*, 176.

(34) (a) Chen, Z. J.; Lohr, A.; Saha-Möller, C. R.; Wűrthner, F. *Chem. Soc. Rev.* **2009**, *38*, 564 – 584 (b) Babu, S. S.; Mçhwald, H.; Nakanishi, T. *Chem. Soc. Rev.* **2010**, *39*, 4021. (c) Babu, S. S.; Prasanthkumar, S.; Ajayaghosh, A. *Angew. Chem. Int. Ed.* **2012**, *51*, 1766.

(35) Gopal, A.; Varghese, R.; Ajayaghosh, A. *Chem. - Asian J.* **2012**, *7*, 2061.

(36) (a) Fages F, ed. *Low Molecular Mass Gelators: Design, Self-Assembly, Function*. **2005**, Berlin/Heidelberg, Ger.:Springer-Verlag. (b) Weiss R, Terech P, eds. *Molecular Gels: Materials with Self-Assembled Fibrillar Networks*. **2006**, Dordrecht,Neth.: Springer. (c) Weiss, R. G. eds. *Molecular Gels: Structure and Dynamics*, **2018**, RSC publisher, UK

(37) Ajayaghosh, A.; Praveen, V. K.; Srinivasan, S.; Varghese, R. *Adv. Mater.* **2007**, *19*, 411.

(38) (a) Rajaganesh, R.; Gopal, A.; Mohan Das, T.; and Ajayaghosh, A. *Org.Lett.*, **2012**, *14*, 748. (b) Kuo, S.-Y.; Liu, C.-Y.; Balamurugan, R.; Zhang, Y.-S.; Fitriyani, S.; Liu, J. H. *New J. Chem.*, **2017**, *41*, 15555. (c) Kartha, K. K.; Allampally, N. K.; Politi, A. T.; Prabhu, D. D.; Ouchi, H.; Albuquerque, R. Q.; Yagai, S.; Fernandez, G. *Chem. Sci.,* **2019**, 10, 752.

(39) (a) Yildirim, A.; Sentker, K.; Smales, G. J.; Pauw, B. R.; Huber, P. and Schonhals, A. *Nanoscale Adv*., **2019**,*1*, 1104. (b) Iqbal, S.; and Khan, A. A. *RSC Adv.* **2019**, *9*, 6335-6345.

(40) Diring, S.; Cameral, F.; Donnio, B.; Dintzer, T.; Toffanin,S.; Capelli, R.; Muccini, M.; Ziessel, R. *J. Am. Chem. Soc.* **2009**, *131*, 18177.

(41) Perez, A.; Serrano, J. L.; Sierra, T.; Ballesteros, A.; Saa, D. D.; Barluenga, J. *J. Am. Chem. Soc.* **2011**, *133*, 8110.

(42) Cameral, F.; Bonardi, L.; Schmutz, M.; Ziessel, R. *J. Am. Chem. Soc.* **2006**, *128*, 4548.

(43) Sandeep, A.; Praveen, V.K.; Rao, D. S.; Prasad, S. K.; Ajayaghosh, A. *ACS Omega* **2018**, *3*, 4392.

(44) Vijayakumar, C.; Praveen, V. K.; Ajayaghosh, A. *Adv. Mater.* **2009**, *21*, 2059.

(45) Giansante, C.; Raffy, G.; Schafer, C.; Rahma, H.; Kao, M.; Olive, A. G. L.; Guerzo, A. D. *J. Am. Chem. Soc*. **2011**, *133*, 316.

(46) Li, D.; Hu, W.; Wang, J.; Zhang, Q.; Cao, X.; Ma, X.; Tian, H. *Chem. Sci.* **2018***, 9,* 5709.

(47) (a) Würthner, F.; Bauer, C,; Stepanenko, V.; Yagai, S. Adv. Mater. **2008**, *20*, 1695. (b) Ghosh, S.; Li, X. Q.; Stepanenko, V.; Wurthner, F. *Chem. Eur. J.* **2008**, *14*, 11343.

(48) Ghosh, S.; Cherumukkil, S.; Suresh, C. H.; Ajayaghosh, A. *Adv. Mater.* **2017**, 1703783.

(49) Li, H.; Choi, J.; Nakanishi, T. *Langmuir* **2013**, *29*, 5394.

(50) Würthner, F.; Meerholz, K*. Chem.—Eur. J.* **2010**, *16*, 9366.

(51) Otsuki, J. *J. Mater. Chem. A*, **2018**,*6*, 6710.

(52) Würthner F. *Acc. Chem. Rec.* **2016**, *49*, 868.

(53) Würthner, F.; Saha-Möller, C. R.; Fimmel, B.; Ogi, S.; Leowanawat, P.; Schmidt, D. *Chem. Rev.* **2016**, *116*, 962.

(54) (a) Mutai, T.; Satou, H.; Araki, K. *Nat. Mater.* **2005**, *4*, 685. (b) Lott, J.; Ryan, C.; Valle, B.; Johnson, J. R.; Schiraldi, D. A.; Shan, J.; Singer, K. D.; Weder, C. *Adv. Mater.* **2011**, *23*, 2425.

(55) Bisoyi, H. K.; Li, Q. *Chem. Rev.* **2016**, *116*, 24, 15089.

(56) Hirai, M.; Tanaka, N.; Sakai, M.; Yamaguchi. S. *Chem. Rev.* **2019**, *119*, 8291.

(57) Ardona, H. A. M.; Draper, E. R.; Citossi, F.; Wallace, M.; Serpell, L. C.; Adams, D. J.; Tovar, J. D. *J. Am. Chem. Soc.* **2017**, *139*, 8685.

(58) Sun, C.-L.; Peng, H.-Q.; Niu, L.-Y.; Chen, Y.-Z.; Wu, L.-Z.; Tung, C.-H.; Yang, Q.-Z. *Chem. Commun.*, **2018**, *54*, 1117.

(59) Lu, L.; Zheng, T.; Wu, Q.; Schneider, A. M.; Zhao, D.; Yu , L. *Chem. Rev.*, **2015**, *115* , 12666.

(60) Siram, R. B. K.; Stephen, M.; Ali, F.; Patil, S. *J. Phys. Chem. C.* **2013**, *117*, 9129.

(61) (a) Zhu, X.; Tang, W.; Bi, P.; Yan, L.; Wang, X.; Wong, W.-K.; Hao, X.; Ong, B. S. Zhu, X.; *J. Mater. Chem. A*, **2018**, *6*, 14675. (b) Lv, A.; Stolte, M.; Wurthner, F. *Angew. Chem. Int. Ed.* **2015**, *54*, 10512.

(62) Gsanger, M.; Kirchner, E.; Stolte, M.; Burschka, C.; Stepanenko, V.; Pflaum, J.; Wurthner, F. *J. Am. Chem. Soc.* **2014**, *136*, 2351.

(63) Lin, G.; Qin, Y.; Zhang, J.; Guan, Y–S; Xu, H.; Xu, W.; Zhu, D.; *J. Mater. Chem. C*, **2016**, *4*, 4470.

(64) Ghosh, S.; Philips, D. S.; Saeki, A.; Ajayaghosh, A. *Adv. Mater.* **2017**, 1605408.

(65) Abadia, M. M.; Antonicelli, G.; Saeki, A.; Alonso, A. M. *Angew. Chem.Int. Ed.* **2018**, *130*, 8341.

(66) Lee, O. P.; Yiu, A. T.; Beaujuge, P. M.; Woo, C. H.; Holcombe, T. W.; Millstone, J. E.; Douglas, J. D.; Chen M. S.; Fréchet, J. M. J. *Adv. Mater.* **2011**, *23*, 5359.

(67) (a) Mortimer, R. J. *Annu. Rev. Mater. Res.* **2011**, *41*, 241. (b) Rosseinsky, D. R.; Mortimer, R. J. *Adv. Mater.* **2001**, *13*, 783.

(68) Gonzalez, L.; Liu, C.; Dietrich, B.; Su, H.; Sprousles, S.; Cui, H.; Honecker, D.; Adams, D. J.; Draper, E. R. *Commun Chem.*, **2018** *1*, 77.

(69) Suarez, D.; Steven, E.; Laukhina, E.; Gomez, A.; Crespi, A.; Mestres, N.; Rovira, C.; Choi, E. S.; Jaume, V. *NPJ Flex Electron.* **2018**, *2*, 29

(70) Thota, B. N. S.; Urner, L. H.; Haag, R. *Chem. Rev.* **2016**, *116*, 2079.

(71) (a) Shen, B.; He, Y.; Kim, Y.; Wang, Y.; Lee, M. *Angew. Chem. Int. Ed.* **2016**, *55*, 2382. (b) Kim, Y.; Lee, M. *Chem. - Eur. J.* **2015**, *21*, 5736. (c) Kim, J.-K.; Lee, E.; Kim, M.-C.; Sim, E.; Lee, M. *J. Am. Chem. Soc.* **2009**, *131*, 17768−17770. (d) Moon, K.-S.; Lee, E.; Lee, M. *Chem. Commun.* **2008**, 3061.

(72) Zhou, Y.; Yan, D. *Angew. Chem., Int. Ed.* **2004**, *43*, 4896.

(73) (a) Tominaga, M.; Suzuki, K.; Murase, T.; Fujita, M.; *J. Am. Chem. Soc.* **2005**, *127*, 11950. (b) Mayoral, M. J.; Rest, C.; Schellheimer, J.; Stepanenko V.; Ferna´ndez, G. *Chem. – Eur. J.*, **2012**, *18*, 15607. (c) Northrop, B. H.; Glocker, A.; Stang, P. J. *J. Org. Chem.* **2008**, *73*, 1787.

(74) Choudhury, P.; Das, K.; Das, P. K. *Langmuir* **2017**, *33*, 4500.

(75) Thirumalai, R.; Mukhopadhyay, R.; Praveen, V.; Ajayaghosh, A. *Sci. Rep.*, 2015, 9842.

(76) Shin, S.; Gihm, S. H.; Park, C. R.; Kim, S.; Park, S. Y. *Chem. Mater.* **2013**, *25*, 3288.

(77) Janssen, P. G. A.; Vandenbergh, J. ; van Dongen, J. L. J.; Meijer E. W.; Schenning, A. P. H. J. *J. Am. Chem. Soc.,* **2007**, *129*, 6078.

(78) Rajdev, P.; Chakraborty, S.; Schmutz, M.; Mesiniand, P.; Ghosh, S. *Langmuir*, **2017**, *33*, 4789.

(79) (a) Fernandez, G.; Garcia, F.; Sanchez, L. *Chem. Commun.,* **2008**, 6567. (b) Rest, C.; Mayoral, M. J.; Fucke, K.; Schellheimer, J. Stepanenko, V.; Fernandez, G. *Angew. Chem. Int. Ed.* **2014**, *53*, 700.

(80) (a) Su, H.; Wang, F.; Wang, Y.; Cheetham, A. G.; Cui, H. *J. Am. Chem. Soc.* **2019**, *141*, 17107. (b) Song, B.; Wei, H.; Wang, Z.; Zhang, X.; Smet, M. Dehaen, W. *Adv. Mater.*, **2007**, *19*, 416.

(81) Sikder, A.; Ray, D. S.; Aswal V. K.; Ghosh, S. *Angew. Chem., Int. Ed.* **2019**, *58*, 1606.

(82) (a) Kulkarni, C.; Meijer, E. W.; Palmans, A. R. A. *Acc. Chem. Res.* **2017**, *50*, 1928. (b) Lafleur, R. P. M.; Lou, X.; Pavan, G. M.; Palmans, A. R. A.; Meijer, E. W. *Chem. Sci.* **2018**, *9*, 6199.

(83) (a) Hill, J. P.; Jin, W.; Kosaka, A.; Fukushima, T.; Ichihara, H.; Shimomura, T.; Ito, K.; Hashizume, T.; Ishii N.; Aida, T. *Science*, **2004**, *304*, 1481. (b) Jin, W.; Yamamoto, Y.; Fukushima, T.; Ishii, N.; Kim, J.; Kato, K.; Takata, M.; Aida, T. *J. Am. Chem. Soc.* **2008**, *130*, 9434.

(84) Lee, E.; Kim, J. K.; Lee, M. *J. Am. Chem. Soc*. **2009**,*131*, 18242.

(85) Narayan, B.; Senanayak, S. P.; Jain, A.; Narayan, K. S.; George, S. J. *Adv. Funct. Mater.* **2013**, *23*, 3053.

(86) (a) Kim, Y.; Lee, M.; *Chem. -Eur. J.* **2015**, *21*, 5736. (b) Sun, B.; Kim, Y.; Wang, Y.; Wang, H.; Kim, J.; Liu, X.; Lee, M. *Nat. Mater.*, **2018**, *17*, 599. (c) Wang, Y.; Kim, Y.; Lee, M. *Angew. Chem. Int. Ed.* **2016**, *55*, 13122.

(87) Ishiwari, F.; shoji, Y. and Fukushima, T. *Chem. Sci.,* **2018**, *9*, 2028.

(88) (a) Yoo, Y. S.; Choi, J. H.; Song, J. H.; Oh, N. K.; Zin, W. C.; Park, S.; Chang, T.; Lee, M. *J. Am. Chem. Soc.* **2004**, *126*, 6294. (b) Kim, J.-K.; Lee, E.; Lim, Y.; Lee, M. *Angew. Chem., Int. Ed.* **2008**, *47*, 4662. (c) Kim, J.-K.; Lee, E.; Kim, M.-C.; Sim, E.; Lee, M. *J. Am. Chem. Soc.* **2009**, *131*, 17768.

(89) Zhang, X.; Rehm, S.; Safont-Sempere M. M.; Wűrthner, F. *Nat. Chem.* **2009**, *1*, 623.

(90) Xiao, Q.; Rubien, J. D.; Wang, Z.; Reed, E. H.; Hammer, D. A.; Sahoo, D.; Heiney, P. A.; Yadavalli, S. S.; Goulian, M.; Wilner, S. E.; Baumgart, T.; Vinogradov, S. A.; Klein, M. L.; Percec, V. *J. Am. Chem. Soc.* **2016**, *138*, 12655.

(91) (a) Haung, Z. ; Lee, H. ; Kang, S-K. ; Nam, J.-M. ; Lee M. *Nat. Commun.* **2011**, *2*, 459 (b) Shen, B.; Zhu, Y.; Kim, Y.; Zhou, X.; Sun, H.; Lu, Z.; Lee, M. *Nature Commun.* **2019,** *10*, 1080.

(92) (a) Higashiguchi, K.; Taira, G.; Kitai, J.-I; Hirose, T.; Matsuda, K. *J. Am. Chem. Soc.* **2015**, *137*, 2722. (b) Fredy, J. W.; Mendez-Ardoy, A.; Kwangmettatam, S.; Bochicchio, D.; Matt, B.; Stuart, M. C. A.; Huskens, J.; Katsonis, N.; Pavan, G. M.; Kudemac, T. *Proc. Nat. Acad. Sci.* **2017**, *114*, 11850.

(93) Zhou, Y.; Zhang, H.-Y. Zhang, Z.-Y.; Liu, Y. *J. Am. Chem. Soc.* **2017**, *139*, 7168.

(94) Townsend, E. J.; Alotaibi, M.; Mills, B. M.; Watanabe, K.; Seddon, A. M.; Faul, C. F. J. *ChemNanoMat.* **2018**, *4*, 741.

(95) Leira-Iglesias, J.; Sorrenti, A.; Sato, A.; Dunne, P. A.; Hermans, T. M. *Chem. Commun.*, **2016**, *52*, 9009.

(96) Kim, H.; Jeong, S.-M.; Park, J.-W. *J. Am. Chem. Soc.* **2011**, *133*, 5206.

(97) Tayi, A. A.; Shveyd, A. K.; Sue, A. C.-H.; Szarko, J. M.; Rolczynski, B. S.; Cao, D.; Kenedy, T. J.; Sarjeant, A. A.; Stern, C. L.; Paxton, W. F.; Wu, W.; Dey, S. K.; Fahrenbach, A. C.; Guest, J. R.; Mohseni, H.; Chen, L. X.; Wang, K. L.; Stoddart, F. J.; Stupp, S. I. *Nature*, **2012**, *488*, 485.

(98) Kim, Y.; Li, H.; He, Y.; Chen, X.; Ma, X.; Lee, M. *Nature Nanotech,* **2017**, *12,* 551.

(99) Liu, X.; Li, H.; Kim, Y.; Lee, M. *Chem. Commun.* **2018**, *54*, 3102.

(100) Yagai, S.; Okamura, S.; Nakano, Y.; Yamauchi, M.; Kishikawa, K.; Karatsu, T.; Kitamura, A. Ueno, A.; Kuzuhara, D.; Yamada, H.; Seki, T.; Ito, H. *Nat. Commun.* **2014**, *5*, 4013.

(101) Sagara, Y.; Komatsu, T.; Terai, T.; Ueno, T.; Hanaoka, K.; Kato, T.; Nagano, T. *Chem. Eur. J.* **2014**, *20*, 10397.

(102) Sagara, Y.; Komatsu, T.; Ueno, T.; Hanaoka, K.; Kato, T.; Nagano, T. *Adv. Funct. Mater.* **2013**, *23*, 5277.

Gel Phase Controlled [4 + 2] Diels-Alder Cycloaddition Reaction of a 9-Phenylethynyl Anthracene Derivative and its Luminescence Properties
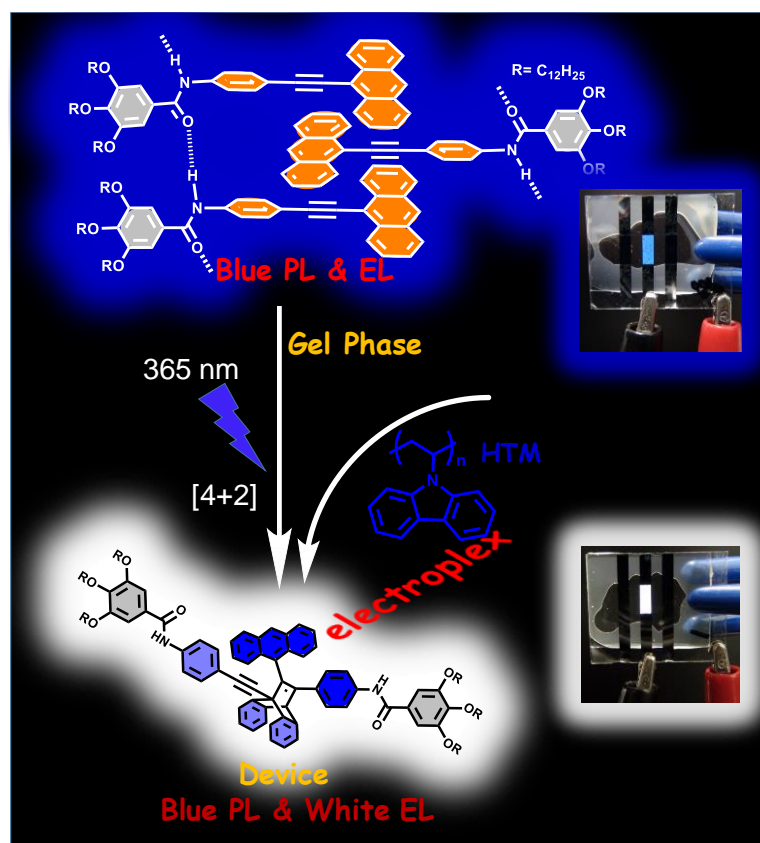
2.1. Abstract

Diels-Alder photocycloaddition of 9-phenylethynylanthracene is a classical reaction resulting in multiple [4 + 2] and [4 + 4] cycloaddition products in solution, which can be controlled to form specific products by creating a restricted environment. We have exploited supramolecular gel chemistry of a 9-phenylethynylanthracence derivative to specifically yield the anti-[4 + 2] adduct in >90% yield. The photocycloadduct which was identified as the anti-isomer exhibited similar photo- and electroluminescence with a blue emission having CIE chromaticity of x = 0.16

and y = 0.16. However, the chromaticity could be significantly modulated by constructing an organic light emitting device with the photocycloadduct, using a carbazole based hole transporting host, which resulted in blue photoluminescence and white electroluminescence with CIE chromaticity of 0.33, 0.32. This observation not only highlights the use of molecular assembly and gel chemistry to achieve the otherwise difficult to obtain photoproducts but also underlines their potential use in optoelectronic devices.

2.2. Introduction

Chemical reactions within confined states of molecular systems have several advantages over solution phase reactions, typically for yielding regio- and stereospecific reaction products, that are otherwise difficult to achieve.[1] For example, in crystalline solids, reactants are mostly confined within the lattices, acquiring accurately defined orientations and positions. Therefore, depending on such defined spatio-temporal arrangements, certain stereospecific chemical reactions that are otherwise unfavorable in solution phase, are easily achieved.[2-3] Several small molecules and metal-organic caged systems have been shown to act as templates to direct light-induced cycloaddition reactions. Photochemical [2+2] cycloaddition reaction in porous coordination polymers (PCP) have emerged as a tool to synthesize regiospecific products of stilbene derivatives. Haynes *et.al.* have reported a multi-stimuli responsive PCP with a temperature induced phase transition leading to controlled photocycloaddition of 1,4-bis[2-(4-pyridyl)ethenyl]benzene.[4] The ligand comprised of two olefinic bonds that are photoactive even inside the PCP structures. In this PCP, the two ligands could be stacked either out-of-phase or in-phase, resulting in the formation of one or two cyclobutane rings during cycloadditions. As a result, selective formation of either of the isomeric photocycloadducts are possible (**Figure 2.1**). The same group have also reported a cadmium (II) based PCP that produced different isomeric structures of [2+2] photoadduct under irradiation with UV light, depending on the solvent guest molecules present in the porous structure. The simple solvent exchange process led

to different stacking of ligand, with either an in-phase or an out-of-phase orientation.[5]
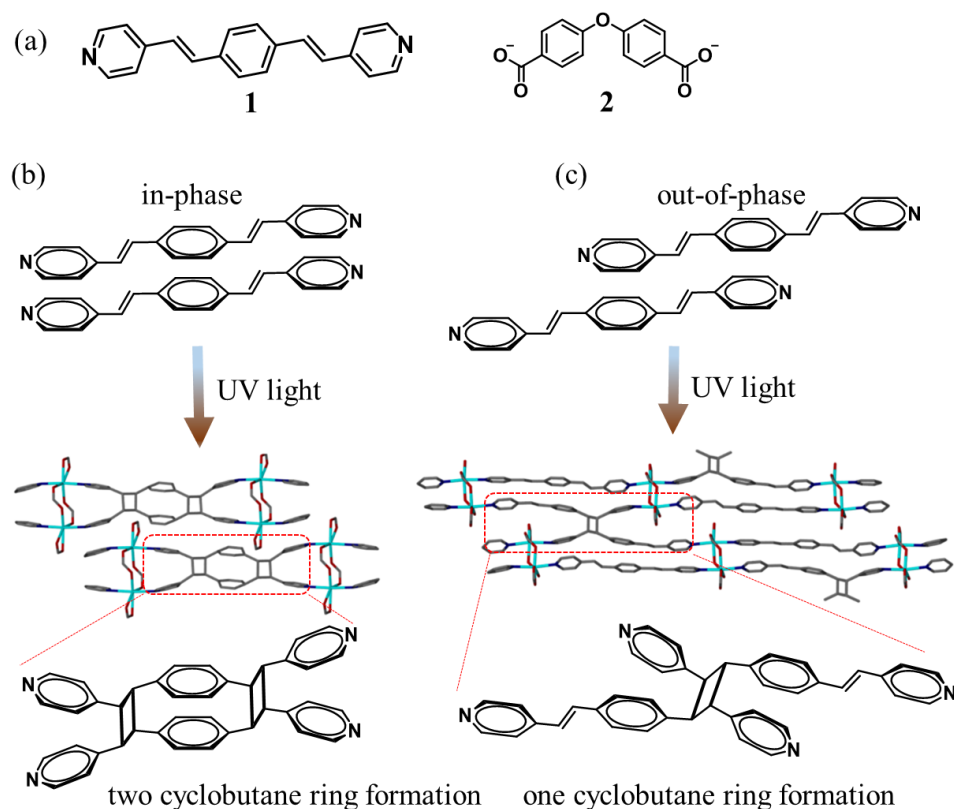
Figure 2.1. (a) Chemical structure of 1,4-bis[2-(4-pyridyl)ethenyl]benzene **1** and 4,4'-oxybis(benzoic acid) **2**. (**b**) In-phase and (**c**) out-of-phase alignment of **1**, resulting in the formation of the photocycloadduct containing two cyclobutane rings and one cyclobutane ring inside the Cd (II) porous coordination polymers, respectively.

Similarly, a defined crystalline state can provide a template to direct the [2 + 2] Diels-Alder photocycloaddition of stilbene derivatives. A co-crystal of 1,3 dihydroxybenzene and bis (4-pyridyl)ethylene (4,4´-bpe) **3** with a H-bond directed assembly allowed the two ethylene moieties to undergo a cycloaddition reaction (**Scheme 2.1a**).[5b] Further, the U-shaped naphthalene dicarboxylic acid **4** that formed a H-bonded dimer with two pre-organized C=C bonds for a photodimerization assisted formation of [2 + 2] photoadducts exclusively (**Scheme 2.1b**).[6,7]
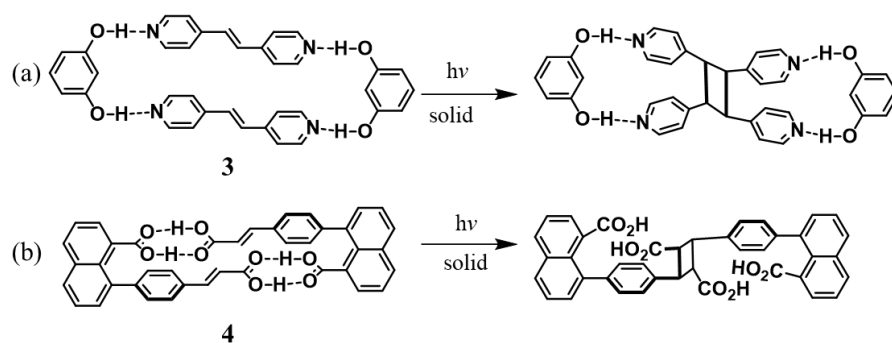
Scheme 2.1. Chemical structure of **(a)** the co-crystal of **3** that led to a template directed [2 + 2] photodimerization in the solid state and **(b)** the 'U'-shaped di-acid **4**, wherein the H-bonded molecular geometric constraint formed the dimer with ~100% *ee* upon photoirradiation.

Another classical example for photocycloaddition is the Diels-Alder reaction of anthracene and its derivatives,[8] leading to the formation of *anti* and *syn* isomers of [4 + 4] photocycloadducts in the absence of oxygen (**Scheme 2.2**).[9] Stereochemical control in Diels-Alder reactions can be achieved via supramolecular approaches. Ishida *et al.* demonstrated an enantioselective reversible photoreaction of the anthracene derivative **7** in a thermoresponsive metastable liquid crystalline phase (**Scheme 2.3**). The enantioselective photoreaction was achieved at higher temperatures, when the liquid crystalline salt of **6** and **7** was irradiated with UV light. A photodimer of (+) isomer (*anti*^HH) was formed with high enantioselectivity (+86% *ee*). However, photocycloaddition of an aged sample afforded the corresponding (-) isomer (*anti*^HH, -94% *ee*).[10]
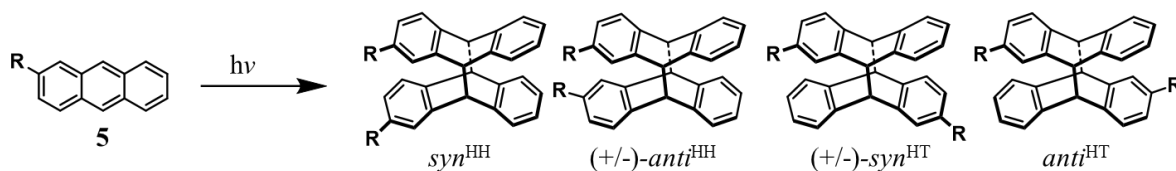
Scheme 2.2. Possible chemical structures of [4 + 4] photodimers of 2-substituted anthracene **5**.

Taking advantage of the inclusion complexation of cyclodextrin and cucurbitril units, Inoue and co-workers were able to control the stereochemical photoreaction of anthracene appended with γ-CD (**8**). Compound **8** formed a dimeric (2:1)

supramolecular inclusion complex in an antiparallel orientation inside γ-CD, forming *anti*[HT] and *syn*[HT] dimers upon photoirradiation with >320 nm light. The 2:1 inclusion complex of cucurbit[8]uril with a head-to-head organization of the two anthracene cores, resulted in light induced *anti*[HH] and *syn*[HH] dimer formation (**Figure 2.2**).[11]
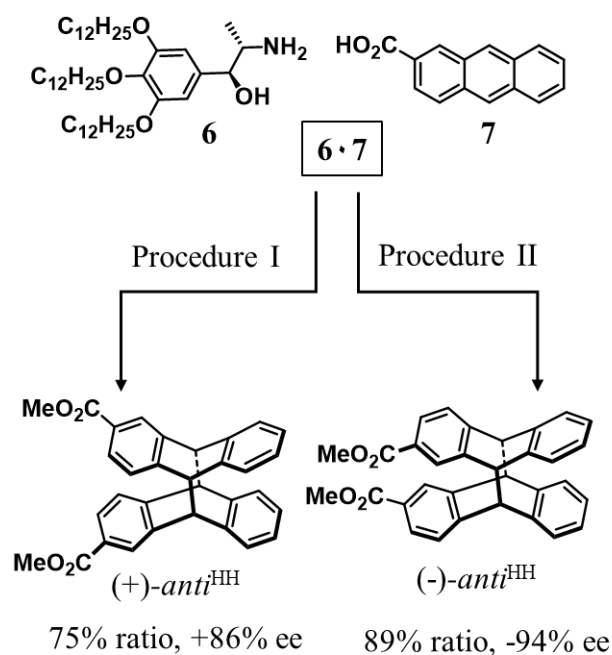
Scheme 2.3. Supramolecular control of enantioselective photodimer formation of the anthracene derivative **7**. The salt **6·7** was melted and annealed at 45 °C for <1 min (procedure I) or for 20 h (procedure II), photoirradiated with UV/vis light (λ > 380 nm), and methylated with Me_3SiCHN_2 offering high yield of (+)-*anti*[HH] in procedure-I and (-)-*anti*[HH] in procedure-II.

9-Phenylethynylanthracene (9-PEA) can undergo light triggered bimolecular Diels-Alder cycloaddition reaction in the absence of molecular oxygen. As a result, it can produce four stereochemical cycloadducts (**Scheme 2.4**).[12] Due to the presence of the triple bond at 9-position, it can also act as a diene for D-A reaction. Therefore, in contrast to unsubstituted anthracene derivatives, 9-PEA derivatives afford both [4 + 4] and [4 + 2] cycloaddition reaction resulting in [4 + 2]-*anti*, [4 + 2]-*syn*, [4 + 4]-*syn* and [4 + 2]-*anti* cycloaddition products. Though these products are allowed by selection rules, the unfavorable geometries enable only [4 + 2]-*anti (64%)* and [4 +

4]-*anti* (23%), thereby minimizing the formation of [4 + 2]-*syn* and [4 + 4] *syn* products.[13]
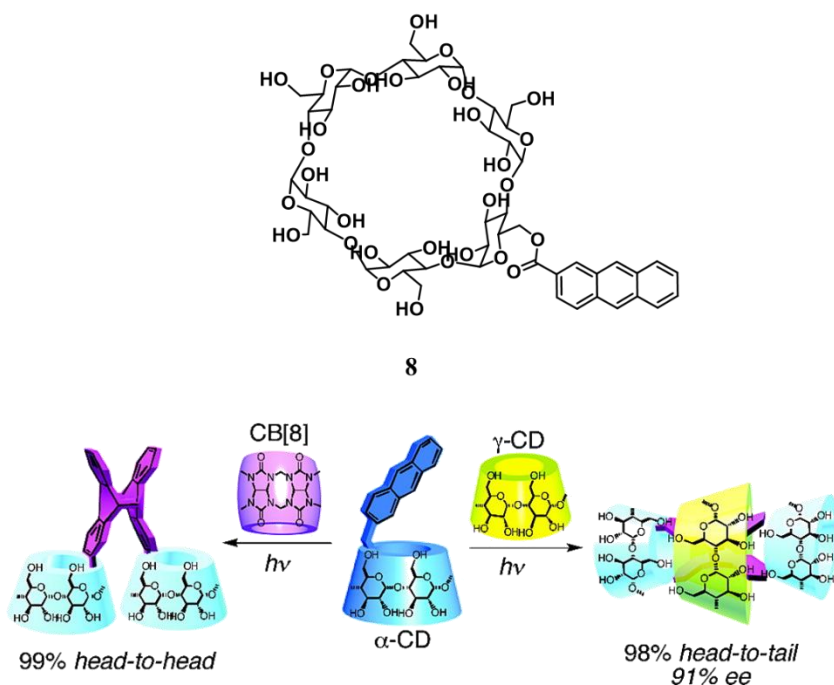
Figure 2.2. γ-Cyclodextrin (γ-CD) and cucurbit[8]uril (CB[8]) assisted controlled stereochemical photocycloaddition of α-Cyclodextrin (α–CD) labeled anthracene **8**.
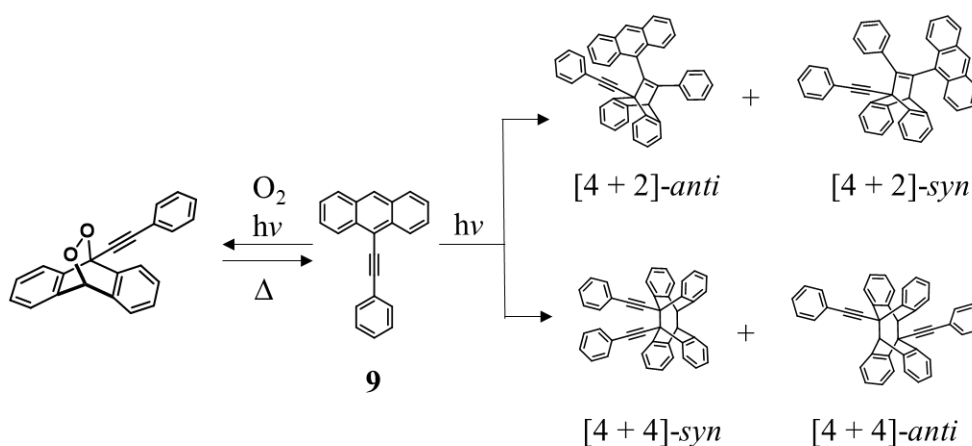
Scheme 2.4. Photoreaction of 9-phenylethynylanthracene **9** (9-PEA), either with oxygen (left) or with itself (right). The bimolecular photocycloaddition of **9** can yield both [4 + 2] or [4 + 4] products.

However, Weiss and coworkers have demonstrated that energetically unfavorable [4 + 4]-*syn* dimer can be specifically obtained via the immobilization of 9-

phenylethynyl derivatives of anthracene on gold surface[14] (**Figure 2.3a**). Formation of a self-assembled monolayer (SAM) of the anthracene derivative **10** on gold surfaces afforded a photoinduced [4 + 4] D-A reaction that is otherwise difficult to achieve in solution. Such photochemical transformation of **10** was favored due the geometry locked positioning and the restricted free rotation of the triple bond. Later, Klajn *et.al.* also reported the biomolecular reaction of anthracene derivatives confined to nanoparticle surfaces by manipulating the length of the linkers (**10**-**12**) or by exploiting the curvature of Pd nanoparticles *via* tuning the particle size (**Figure 2.3b**).[15] Recently, Yashima *et al.* were able to direct the photocycloaddition of 9-phenylethynylanthracene *via* salt-bridge formation. This template-directed cycloaddition reaction afforded 30-60 fold higher yields when compared to the solution state.[13b] However, majority of these reports are limited to the demonstration of the synthesis of selective products on designed surfaces, wherein scale up and practical applications are limited.
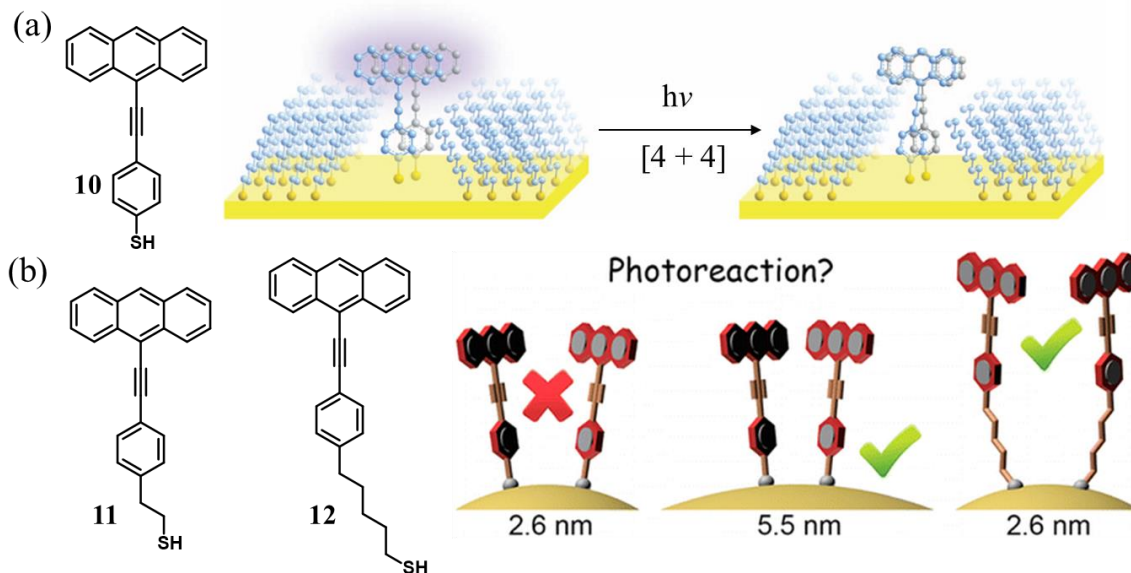
Figure 2.3. (a) Chemical structure of the anthracene derivative **10** (left) and the schematic representation of its controlled [4 + 4] photoreaction on an Au{111} surface. **(b)** Chemical structures of ethynylanthracenes **10-12** and their bimolecular photoreaction possibilities confined to the surfaces of nanoparticles that can be manipulated by varying the linker length, as well as by the curvature of the NPs**.**

Molecular self-assembly leading to supramolecular polymerization and gelation of organic molecules is an ideal approach to achieve molecular confinement.[16] Supramolecular gels have been shown to be a suitable medium for crystallization of molecules.[16d] H-Bonding and π–stacking in the gel state is advantageous over the corresponding solution state to direct chemical reactions towards stereospecific products in high yields.[17] Shinkai and co-workers have reported a binary gelator comprising of the molecules **13** and **7** (**Figure 2.4a**), that formed a gel in cyclohexane (**Figure 2.4b**). The binary gel upon photoirradiation with UV light over 120 min, formed (+/-)-*anti*[HH] adduct with a significant enantiomeric.[17a]
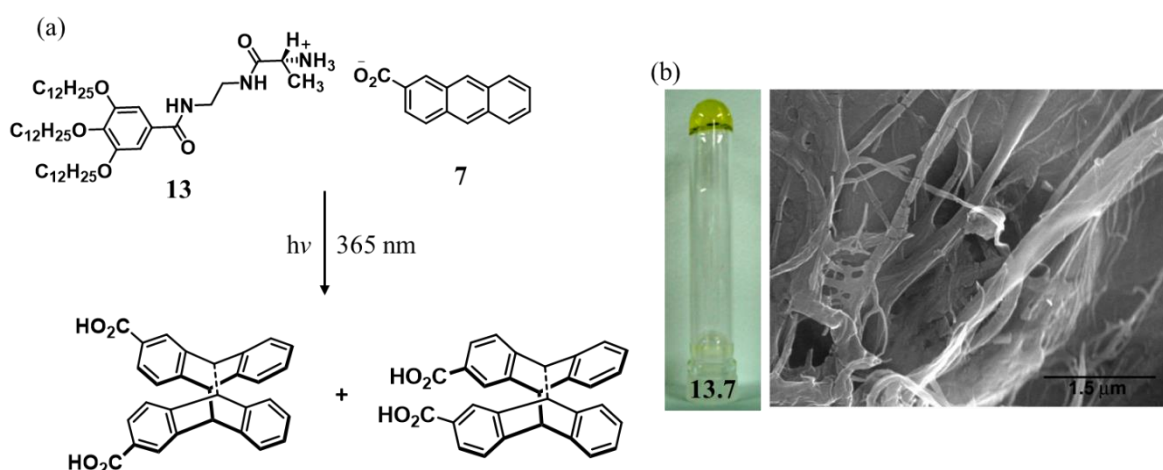
Figure 2.4. (a) Chemical structures of the molecules **13** and **7**. Upon UV irradiation with 365 nm light, *anti* head-to-head photodimers were formed. **(b)** The photograph of the binary gel in cyclohexane (left) and TEM image showing a fibril-like morphology (right).

Single molecular white light emission is a topic of current interest in displays and lighting applications.[18] There are a few reports on photoluminescent white light emission from single molecules.[19] However, single molecular white electroluminescence is rarely observed except for certain Pt-complex based dendrimeric electroluminescent emitters.[20] Electromer and electroplex formation either among or between the emitting species and the hole transporting materials has been reported to result in white electroluminescence.[21] Such electrically excited complexes, *akin* to excimers observed in the case of photoluminescence, have long

wavelength mixed emission, providing balanced color coordinates required for the white light emission. The principles of molecular self-assembly and gel chemistry can be used to control Diels-Alder photocycloaddition to achieve a specific product in high yield, and can be further used for fabricating white light emitting devices, by allowing chromaticity modulations required for simultaneous red-green-blue (RGB) emission.

In this context, taking advantage of the room temperature photochemical transformation of highly reactive pentacene derivative **14**, De Costa and co-workers have fabricated third generation light-emitting electrochemical cells (LEC) with tunable chromaticity. The [4 + 4] Diels-Alder photocycloaddition of **14** led to the formation of anthracene derivatives with shorter wavelength emission (**Figure 2.5a-d**). As a result, chromaticity of the LEC changed when an aged solution of **14** was used for device fabrication. With a pure solution of **14,** deep red emission with CIE coordinates x = 0.69, y = 0.31 was observed. However, upon photocycloaddition over several days, a warm white emission with CIE coordinates of x = 0.36, y = 0.38 and a luminance of 10 cd m^{-2} was achieved (**Figure 2.5e**).[22]

In this chapter, we exploited the supramolecular gel chemistry of a 9-phenylethynylanthracene derivative to specifically yield the [4 + 2] cycloadduct. The photocycloadduct was identified as the *anti*-isomer with a blue emission. The photo- and electroluminescence were found to be similar (blue) with CIE chromaticity of (x, y) = (0.16, 0.16). However, the photoadduct exhibited different photo- and electroluminescence. A significant chromaticity modulation was observed in an organic light emitting device fabricated from the photocycloadduct, using a carbazole based hole transporting host. While the photoadduct also exhibited blue photoluminescence, white light emission with CIE chromaticity of (x, y) = (0.33, 0.32) was observed under electrical stimulation. This observation not only highlights the use of molecular assembly and gel chemistry to achieve the otherwise difficult to obtain photoproducts but also underlines their potential use in optoelectronic device fabrication.
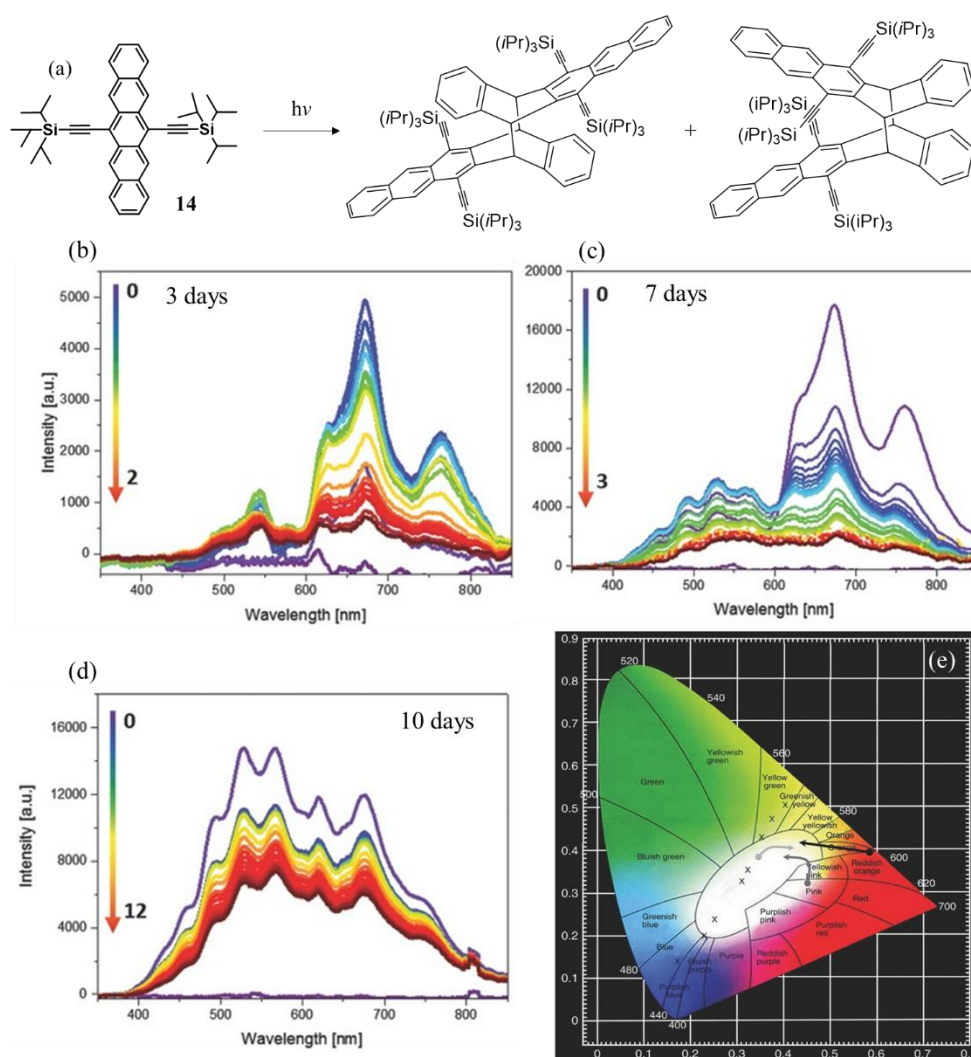
Figure 2.5. (a) Chemical structure and photoinduced chemical modification of **14**. EL spectral evolutions of the device fabricated with **(b)** 3, **(c)** 7, and **(d)** 10 days aged solutions of **14** containing the photodimers. **(e)** Respective changes in the CIE coordinates of the fabricated LEC devices.

2.3. Results and Discussion

2.3.1. Synthesis of the Anthracene Derivative 25

The π–extended photoactive 9-phenylethynylanthracene derivative **25** has been synthesized by a multistep synthetic procedure involving alkylation, condensation, hydrolysis and Sonogashira-Hagihara coupling reactions (**Scheme 2.5**). The iodo derivative **20** and the anthracene derivative **24** were synthesized using already reported procedures.[15] The final product **25** was obtained via a Pd catalyzed

Sonogashira cross-coupling between the compounds **20** and **24**. All the intermediates and the final compound were purified and characterized by nuclear magnetic resonance spectroscopy (NMR) and high–resolution mass spectroscopy (HRMS).
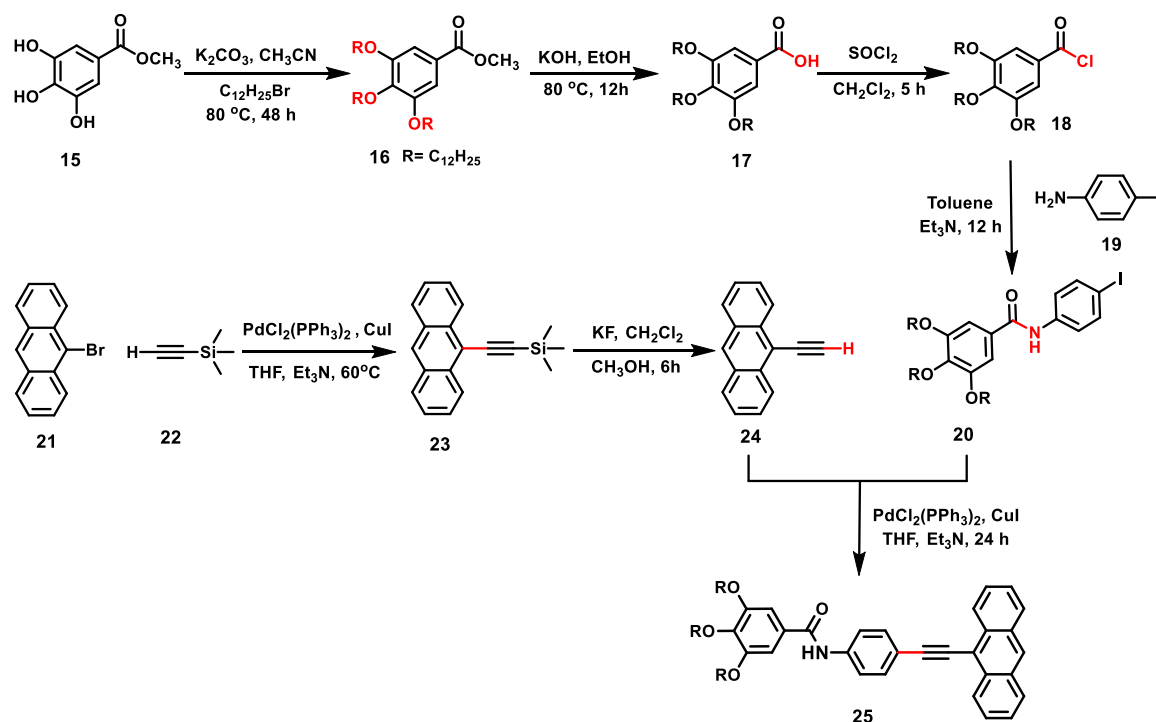
Scheme. 2.5. Synthetic protocol adopted for the synthesis of compound **25**.

The chemical structure of molecule **25** was confirmed *via* ^{1}H NMR spectral analysis (CDCl$_3$, 500 MHz, 25 °C) as shown in **Figure 2.6**. The anthracene protons were found to resonate in the aromatic region, with the peaks corresponding to the most de-shielded protons, H$_b$ and H$_a$, appearing at 8.66 (doublet) and 8.44 (singlet) ppm, respectively. The H$_e$ and H$_c$/H$_d$ protons appeared respectively at 8.03 ppm (doublet) and 7.77 ppm (quartet). The amide proton, H$_h$ resonated as a broad singlet at 7.86 ppm. The peaks corresponding to the phenyl protons (H$_g$, H$_f$) ortho to the triple bond were found to appear as triplets, respectively at 7.60 and 7.52 ppm. The phenyl protons H$_i$, belonging to the second benzene ring, were found to have a chemical shift of 7.07 ppm and appeared as a singlet. The remaining six alkoxy protons, H$_j$ appeared as characteristic peaks resonating at 4.05 ppm. Peaks corresponding to all

the carbon atoms were found in the ^{13}C NMR spectrum. The existence of a chemical species corresponding to the expected structure of compound **25** (calcd. mass for the molecular formula of **25**: 950.4223, experimentally found: 951.3864, correlating to an [M+H]$^+$ species) was further corroborated by high resolution mass spectrometry. The complete characterization data is provided in the experimental section.
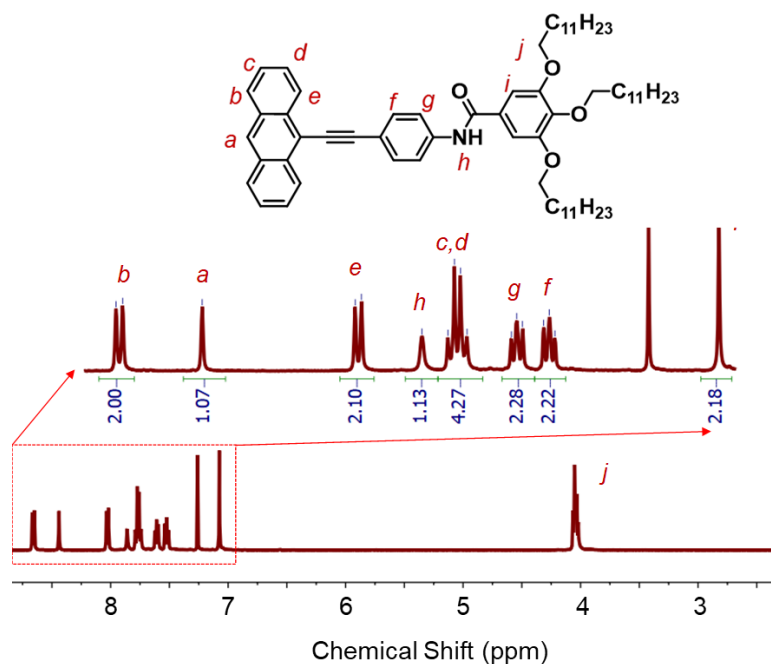
Figure 2.6. Chemical structures and ^{1}H NMR spectrum of compound **25** in CDCl$_3$ (500 MHz, 25 ^{o}C). The protons are labelled in red (*a-j*). The inset shows the expanded region of the spectrum corresponding to the aromatic protons.

2.3.2. Photophysical Characterization

The 9-phenylethylanthracene derivative **25** was designed to exhibit solvent dependent aggregation behavior and its photophysical properties were studied in both solution and aggregated states (**Figure 2.7a,b**). Typical monomer absorption profile was observed in chloroform (*c* = 3.33 μM) with characteristic bands corresponding to an anthracene core at 429, 406, 386 and 365 nm. A slight bathochromic shift in these peaks was observed in comparison to simple anthracene, due to the extended conjugation through a triple bond at the 9-position. At a concentration of 3.33 μM in methyl cyclohexane (MCH), the compound **25** was

found to aggregate via H-bonding and the absorption spectrum showed a corresponding hypsochromic shift of 4 nm in comparison to the monomeric absorption in chloroform (**Figure 2.7a**).
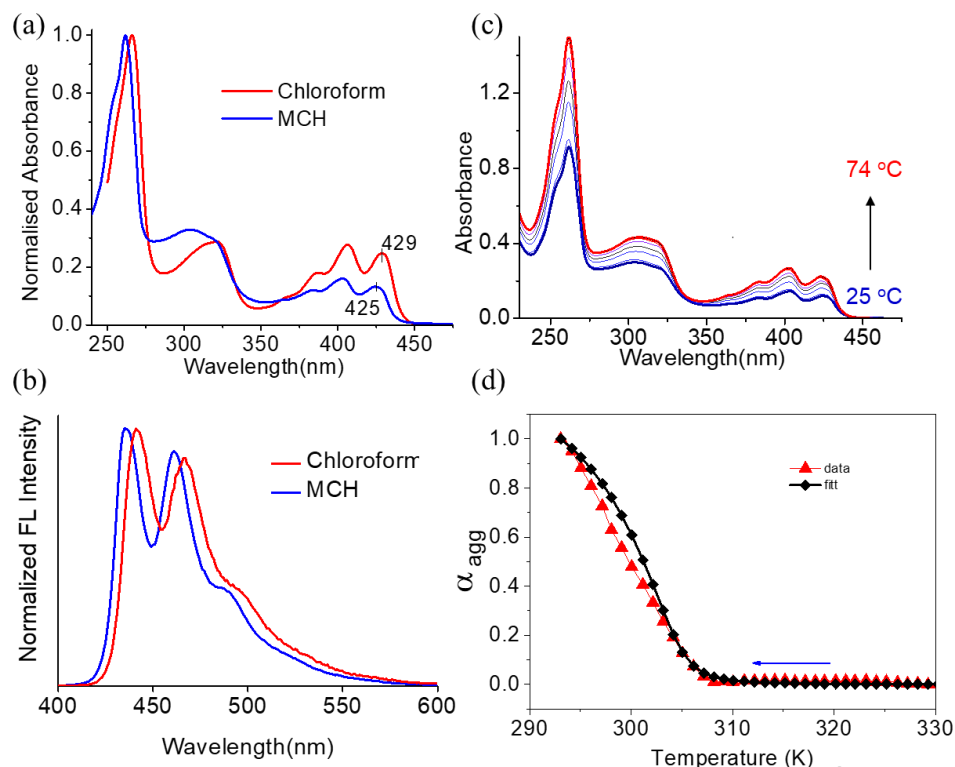
Figure 2.7. Normalized **(a)** absorption and **(b)** emission spectra of compound **25** in chloroform (red, monomeric state) and methyl cyclohexane (MCH, blue, aggregated state). **(c)** Temperature dependent absorption spectra of the gel in MCH (diluted to a concentration of 1 x 10^{-5} M). **(d)** Plot of the fraction of aggregates, α_{agg} vs temperature at concentration of 3.3 µM in MCH indicating cooperative assembly pathway.

The emission spectra of compound **25** was found to appear as mirror images of its structured chromophore absorption profiles due to similar transitions during absorption and emission involving the vibrational energy levels corresponding to the S_1 and S_0 states. Consequently, a 4 nm hypsochromic shift was observed in fluorescence spectra in MCH (aggregated state) when compared to the monomeric emission (chloroform) (**Figure 2.7b**). The fluorescence quantum yield in chloroform was 0.79 with a lifetime of 2.91 ns (single exponential decay).

Temperature dependent absorption profiles of the aggregates of compound **25** in MCH confirmed an increase in absorption intensity with increase in temperature in the range 25-74 °C. Plots of the fraction of aggregate (α_{agg}) against applied temperature could be fitted to a cooperative self-assembly pathway. The thermodynamic parameters were calculated using a nucleation-elongation model for the self-assembly in MCH. The enthalpy of nucleation of the assembly (ΔH_{nucl}) was found to be -9.0 kJ/mol and the elongation temperature was 303 K (**Table 2.1**).

Table 2.1. Thermodynamic parameters for the self-assembly of **25** in MCH (c = 3.3 μM) obtained using the nucleation-elongation model

ΔH [kJ mol^{-1}]	ΔS [kJ mol^{-1} K^{-1}]	T_e [K]	ΔH_{nucl} [kJ mol^{-1}]	K_1 [mol^{-1}]	K_2 [mol^{-1}]	s
-149.14	-0.3877	302.77	-0.900	8.645×10^3	3.102×10^5	2.786×10^{-2}

2.3.3. Gelation

The compound **25** was soluble in chloroform. However, it has a high propensity towards molecular aggregation in less polar solvents, due to the presence of the amide units and extended π–surface. A stable gel was formed due to the H–bonding and π–π stacking interactions in methyl cyclohexane, at a critical gelator concentration (CGC) of 11.9 mg/mL at 298 K (**Figure 2.8a**). The gelator (1.2 mg/100 μL) was initially dissolved in MCH by heating and the solution was slowly cooled back to room temperature, under sonication for about 2 min to afford a gel. The gel was found to have sonication-induced reversibility under heating-cooling cycles. The gel behavior was confirmed by rheological measurements. For example, the storage (G′) and the loss (G″) moduli were constant as a function of the applied angular frequency. The value of G′ was one order of magnitude higher than that of G″, indicating the strong viscoelastic nature of the gel (**Figure 2.8b**). Fourier transform infrared (FTIR) measurements of the xerogel revealed a broad N–H stretching band at 3261 cm^{-1} with a hypsochromic shift of 23 cm^{-1} as compared to

the parent compound **25** (3284 cm^{-1}), that is further indicative of H–bonding in the gel state (**Figure 2.8c**).
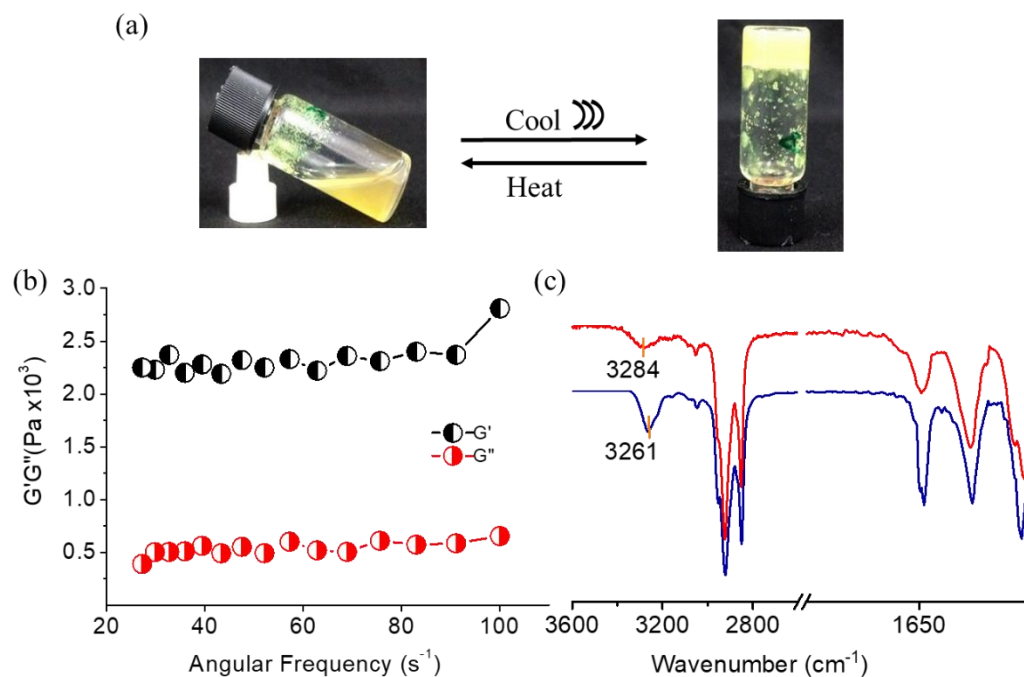
Figure 2.8. (a) Photographs showing reversible gelation of **25** in MCH (11.9 mg/mL). **(b)** Rheological behavior of the gel. **(c)** FTIR spectrum of compound **25** in chloroform (red) and the xerogel (Blue).

2.3.4. Morphology and Packing Analysis of the Gel Obtained from Compound 25

Atomic force microscopy (AFM) and transmission electron microscopy (TEM) analyses of the gel revealed the existence of supramolecular tape like structures (**Figure 2.9a,b**). The average height of the structures was found to be 5.2 nm (**Figure 2.9c**). X-ray diffraction (XRD) of the xerogel exhibited diffraction patterns corresponding to *d*-spacing of 47.9, 21.5 and 12.5 Å (**Figure 2.10a**). The first three peaks followed a reciprocal relationship with a near 1:2:4 ratio, corresponding to a multidimensional lamellar packing. The diffraction peaks corresponding to 3.82 and 4.20 Å are indicative of strong π-stacking and long range ordered intermolecular H-bonding, respectively.
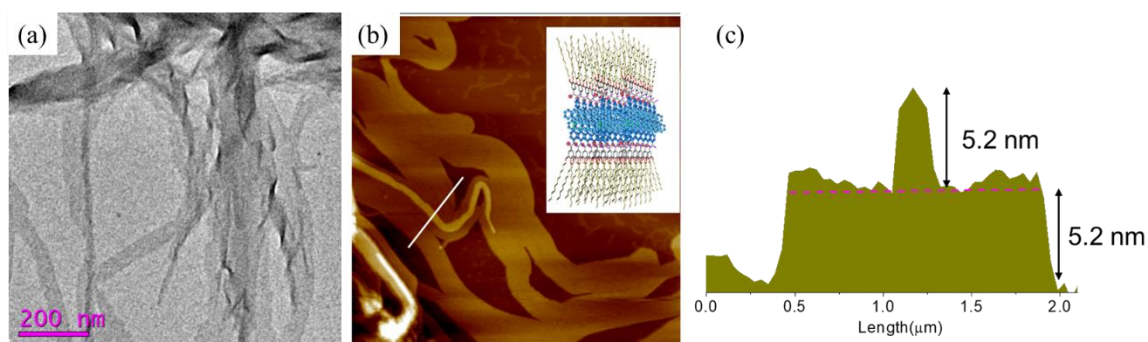
Figure 2.9. (a) TEM image of the gel obtained from **25** in MCH. **(b)** AFM image of the self-assembled molecule **25** in MCH and **(c)** the corresponding height profile obtained from AFM.
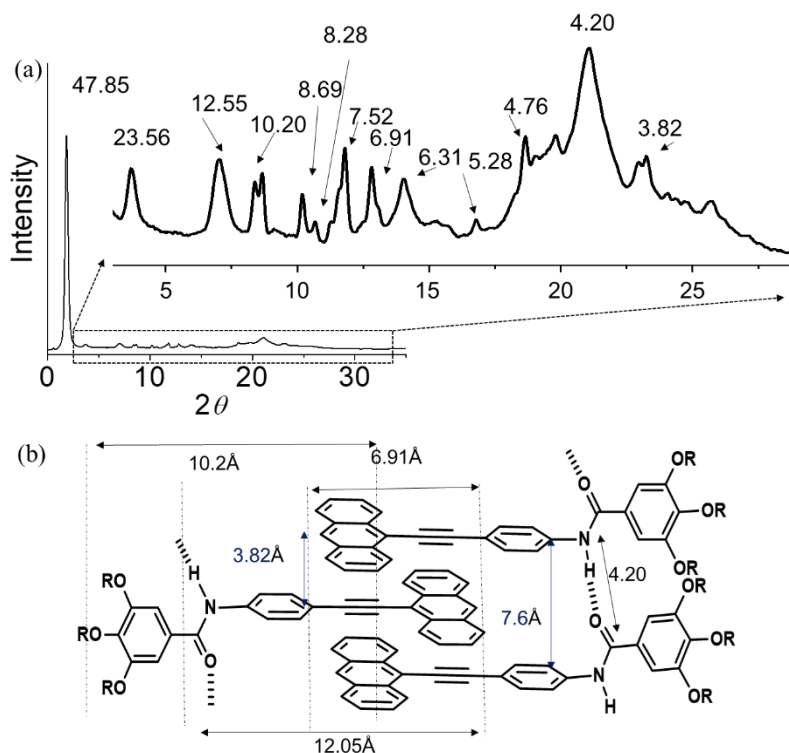
Figure 2.10. (a) X-ray diffraction (XRD) pattern obtained for the xerogel of compound **25** in MCH. The inset shows the zoomed-in area of the pattern. **(b)** The probable spatial arrangement of the molecule **25** in its self-assembled state with the anthracene moiety of one molecule overlapping with the triple bond of another molecule.

The diffraction peaks corresponding to 8.69, 8.28, 7.49, 6.91, 6.31, 5.80, and 5.28 Å represent the interdigitated arrangement of the H-bonded supramolecular assembly, where the anthracene moiety of one molecule is overlapping with the

triple bond of another molecule (**Figure 2.10b**). Such molecular organization in gel phase was further evident from temperature-controlled absorption changes in 230-260 nm region. The absorption band corresponding to ^1B_b transition dipole of anthracene, parallel to the molecular axis and not being polarized *via* aggregation, was found to remain nearly unsplit (**Figure 2.11a,b**).[23] The emission spectra of the gel was found to be very similar to that of the aggregates in MCH (**Figure 2.11c**). As expected, the steady state fluorescence spectrum of the gel did not exhibit any excimeric emission,[24] which was confirmed by time correlated single photon counting experiment. The fluorescence decay profile of the gel was fitted with a bi-exponential decay having lifetime values of 1.95 and 4.00 ns (**Figure 2.11d**).
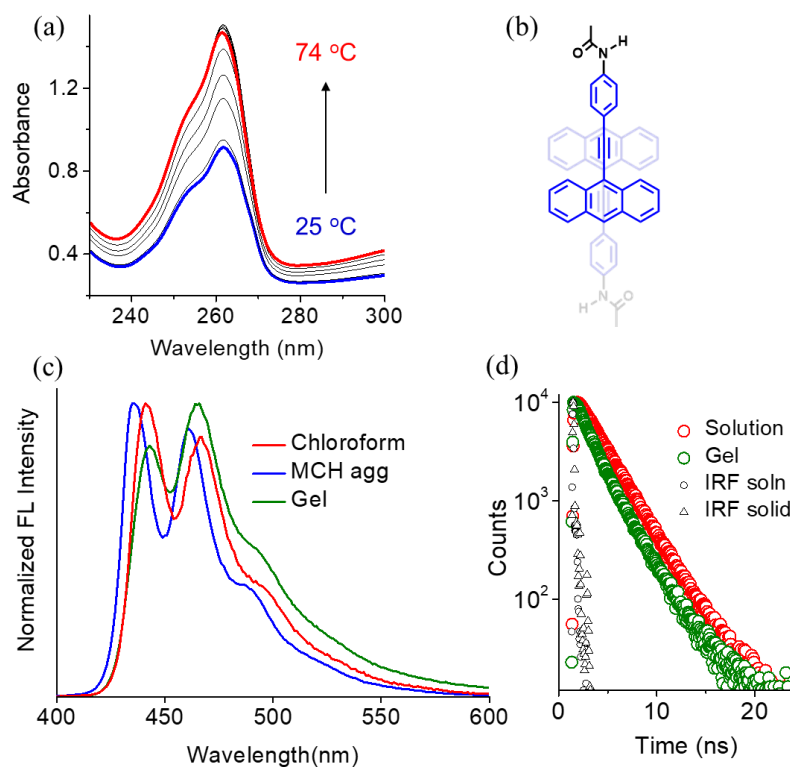
Figure 2.11. (a) Temperature dependent absorbance of the compound **25** in MCH in the range of 230-300 nm, corresponding to ^1B_b transition dipole of anthracene parallel to the molecular axis **(b)**. **(c)** Emission spectra of compound **25** in solution (chloroform, red), aggregated (MCH, blue) and gel (green) states. **(d)** Lifetime decay profiles in solution (red) and gel (green) states (λ_{ex} = 375 nm).

2.3.5. Photoirradiation in the Gel State

Room temperature stable gel of the compound **25** was taken in an ultraviolet transparent container and irradiated with 365 nm light for 20 h. A gel to sol transformation was observed and was confirmed by the inversion of the container (**Figure 2.12a**). MALDI-TOF analysis of the photoirradiated gel confirmed the existence of a chemical species of molecular mass 1926.11, that correlates to the corresponding [4 + 2] cycloadduct (**Figure 2.12b**).
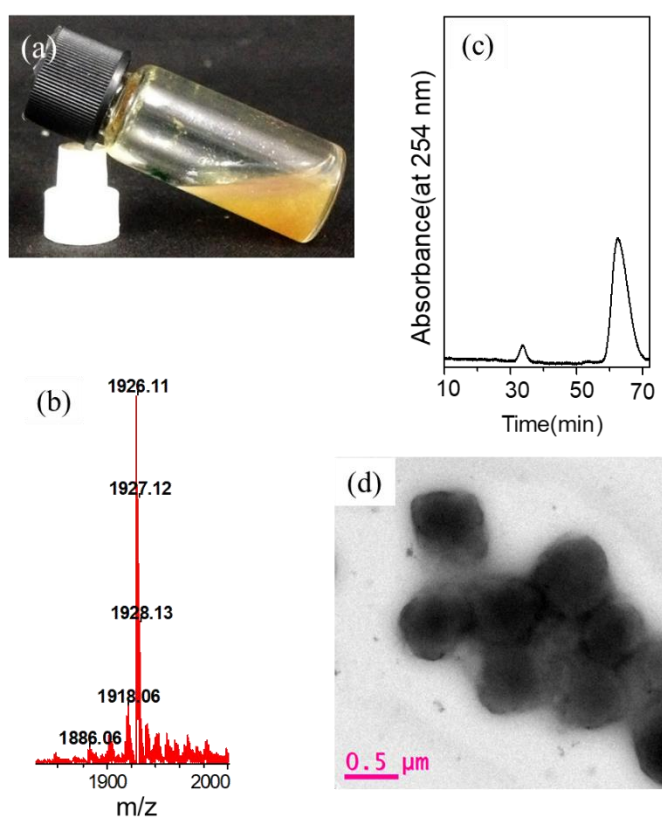
Figure 2.12. (a) Photographs showing the gel and **(b)** the MALDI-TOF spectrum of photoirradiated gel. **(c)** HPLC chromatogram of photoirradiated gel. **(d)** TEM images after photoirradiation.

HPLC profile of the irradiated solution showed a major peak corresponding to a 91% photoconversion of the starting compound (**Figure 2.12c**). TEM analyses of the photoadduct showed ill-defined particle like morphology, justifying the destruction of the one-dimensional H-bonded assembly of the gel phase (**Figure 2.12d**). This observation was further confirmed by the XRD analysis of the gel after

photoirradiation, which showed a decrease in the number of diffraction peaks. After photoirradiation, the solvent was removed using a rotary evaporator at a set temperature <35 °C. ^{1}H NMR (CDCl$_3$, 500 MHz, 25 °C) profile of the residue suggested 90-92% yield of the *anti*-[4 + 2] photoadduct. Photoirradiation with >420 nm light for 48 h also resulted in *anti*-[4 + 2] cycloadduct, which indicated that molecular packing does not allow for any other mode of cycloaddition (**Scheme 2.6**).
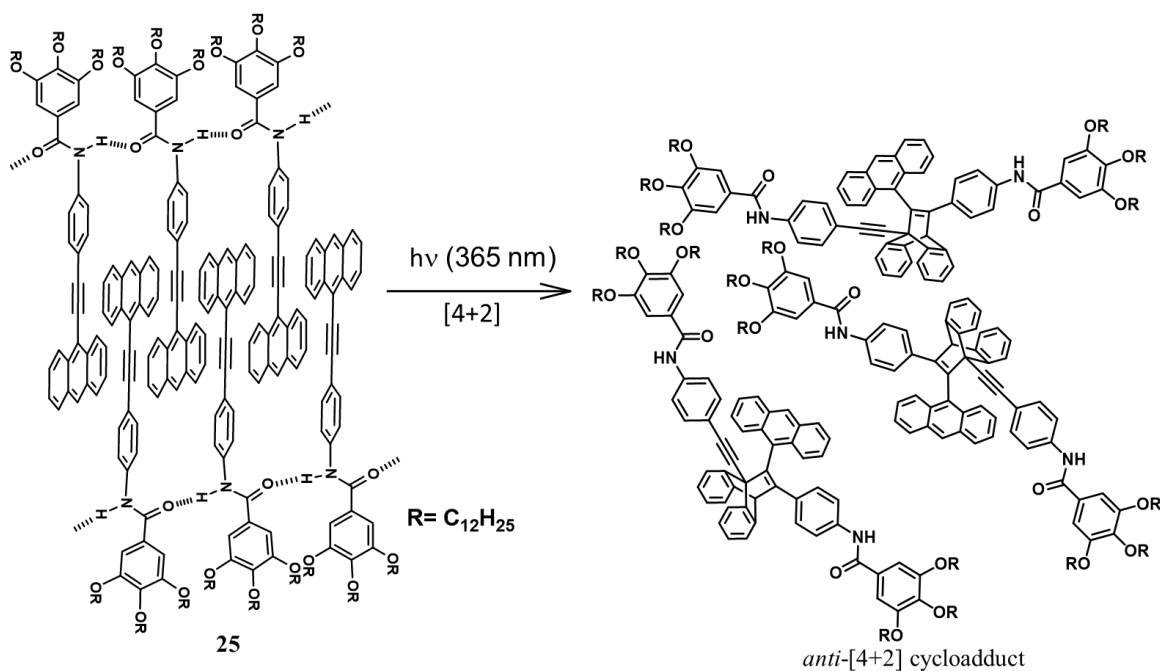
Scheme. 2.6. Photoinduced transformation of the self-assembled gelator **25** The possible spatial molecular arrangement of compound **25** in the gel state that facilitates the preferred formation of *anti-*[4 + 2] cycloadduct is shown.

The structure of the photoadduct was unambiguously confirmed by ^{1}H NMR and NOESY spectra that confirmed the formation of *anti*-[4 + 2] product with the middle ring of anthracene covalently linked with triple bond of a second molecule (**Figure2.13a-c**). In the ^{1}H NMR spectrum of the photoadduct, the proton '20' appeared as a singlet at a chemical shift of 5.74 ppm, corroborating its loss of aromaticity upon cycloaddition (**Figure 2.13a**). The two amide protons (protons 6

and 25) were found to resonate at two different chemical shifts, that is indicative of the formation of the cycloadduct.
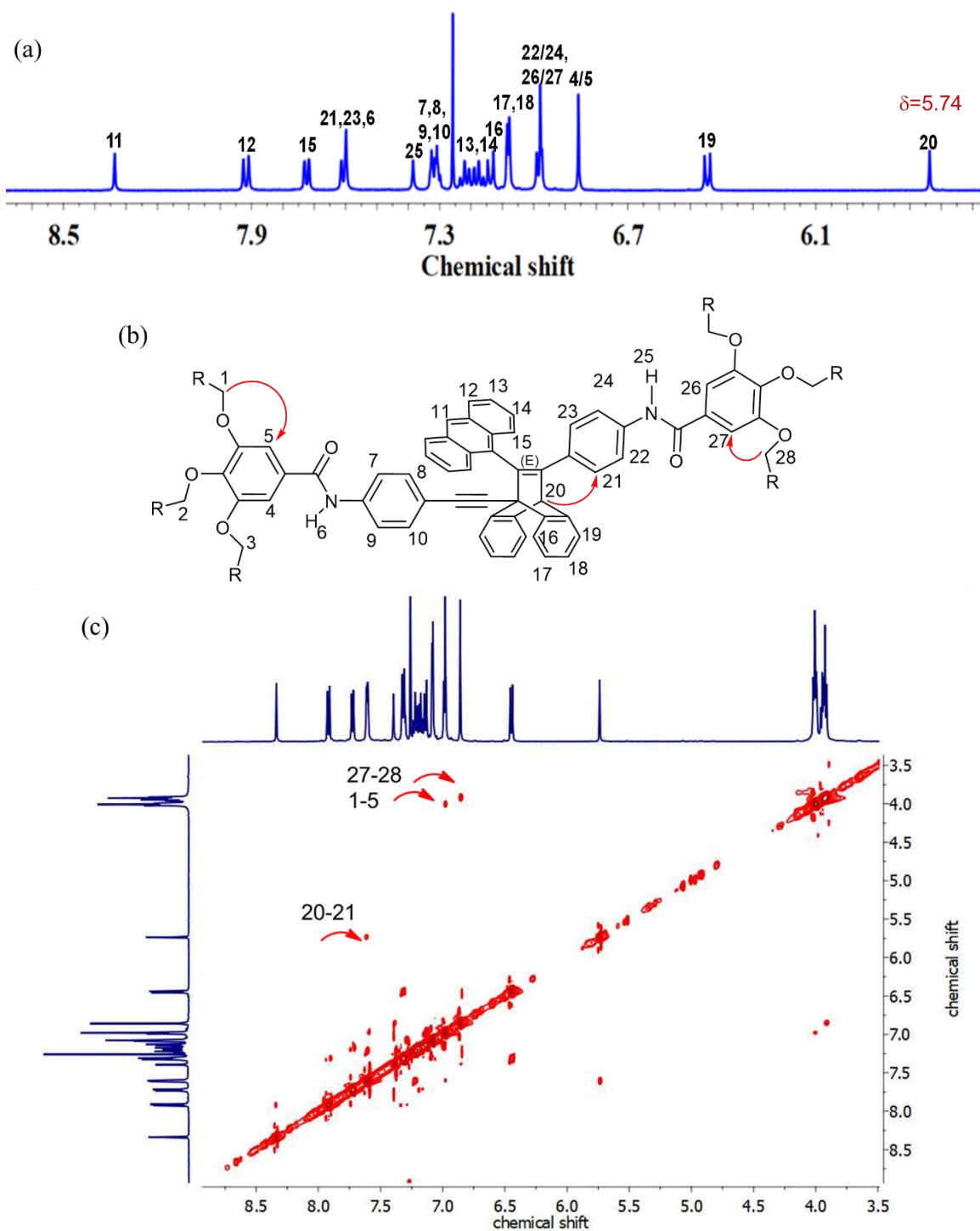
Figure 2.13. ^{1}H NMR spectrum of the purified photoadduct in CDCl$_3$ at 500 MHz. **(b)** The *anti*-confirmation of the [4 + 2] cycloadduct. The corresponding spatial interactions between the protons are shown by red arrows. **(c)** NOESY spectrum showing the interaction between protons 1 and 5, protons 20 and 21 and protons 26 and 27.

The NOESY NMR spectrum confirmed spatial interaction of proton '20' with proton '21', that confirms the formation of the *anti*-[4 + 2] product (**Figure 2.13c**). The stereochemistry of the photoadduct features an *anti*-conformation of the double bond as shown in **Figure 2.13b**. However, the xerogel and solution state photoreactions showed low conversion and less stereoselective cycloaddition. While low stereoselectivity was observed for the photoadduct in solution state (**Figure 2.14a**), photoirradiation of the xerogel barely afforded any cycloadduct (**Figure 2.14b**).
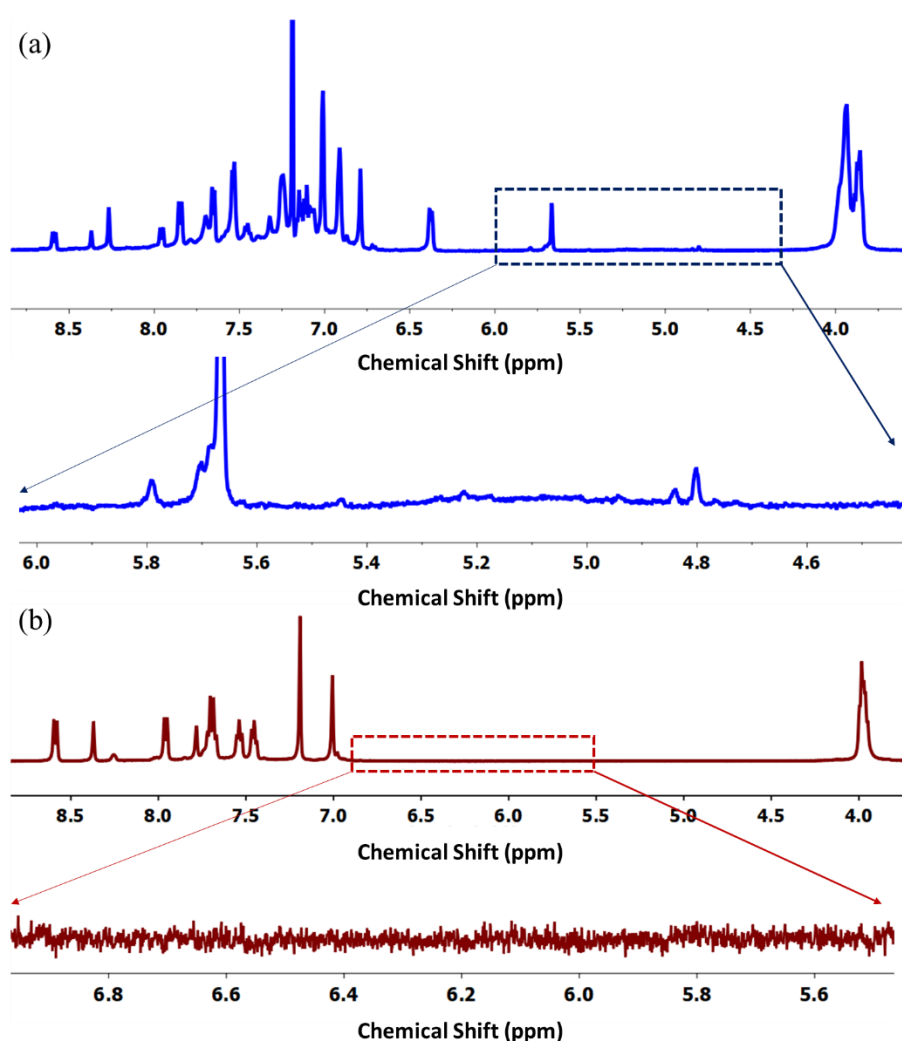
Figure 2.14. Partial ^{1}H NMR (500 MHz, CDCl$_3$) spectra of photoirradiated **25** in **(a)** solution and **(b)** xerogel states, indicating less stereoselectivity in the formation of photoadduct in the solution state and nearly no formation of the photoadduct in the xerogel state. The zoomed area where the peak corresponding to the de-aromatized proton should appear in the cycloadduct are also shown for **(a)** and **(b)**.

The FTIR spectra showed significant changes in the vibrational bands of the photoadduct as compared to its parent compound **25**. The cycloaddition product has an asymmetric triple bond acting as a linker between sp^3 and sp^2 carbon atoms with a stretching frequency of 2359 cm^{-1} that is 2 cm^{-1} higher than the triple bond stretching frequency in the parent derivative **25**. Similarly, a noticeable change was observed in the carbonyl C=O ($\Delta v_{C=O}$ = +2 cm^{-1}) and amide N-H (Δv_{N-H} = +19 cm^{-1}) stretching frequencies. Upon photoirradiation, H-bonded N-H stretching frequency of the gel (v_{N-H} = 3261 cm^{-1}) shifted to a higher value (3279 cm^{-1}) which is close to that of compound **25** (3284 cm^{-1}). The steric geometry of the photoadduct disturbs the assembly of the molecule resulting in the dissolution of the gel.

2.3.6. Photophysical Characteristics of the Cycloadduct

Comparison of the absorption and emission features of the photoadduct in chloroform (3.3 μM) with those of the parent compound **25** is shown in **Figure 2.15a,b**. The absorption spectrum of the photoadduct exhibited the appearance of two relatively less intense bands at 393 and 373 nm and an intense band at 299 nm, simultaneous with the disappearance of the characteristic bands (429 and 406 nm) of compound **25**. The compound **25** exhibited two intense emission peaks at 450 and 475 nm, whereas the photoadduct showed an emission with maximum at 440 nm. The fluorescence quantum yields of compound **25** and the photoadduct were 0.79 and 0.57, respectively. The fluorescence lifetime analysis of compound **25** and its photoadduct in chloroform exhibited a single exponential decay with lifetime values of 2.91 and 4.28 ns, respectively (**Figure 2.15c**). Cyclic voltammetry (**Figure 2.15d**) suggested a better stabilization of the HOMO of the photoadduct (E_{HOMO} = -5.54 eV) as compared to the parent compound **25** (E_{HOMO} = -4.79 eV). This stabilization is attributed to the reduction in extended π-conjugation upon photocycloaddition. Similar effects were also observed in the comparison of the E_{LUMO} of the photoadduct (-2.59 eV) and compound **25** (-1.98 eV) (**Table 2.2**).
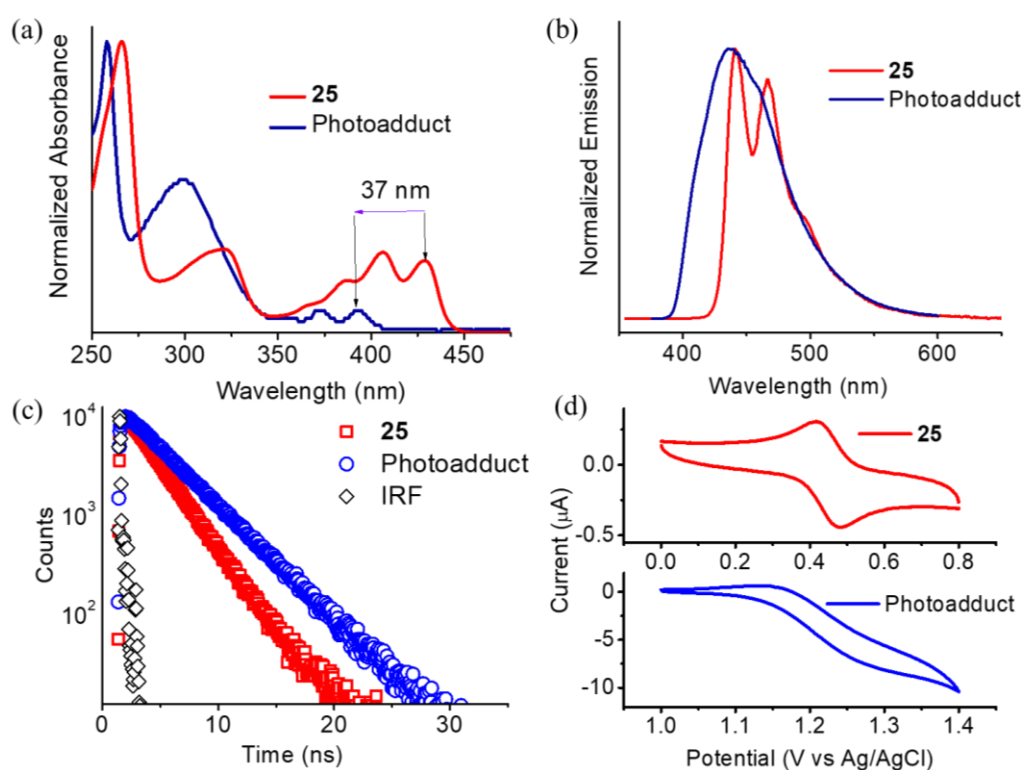
Figure 2.15. Comparative properties of **25** (red) and photoproduct (blue): **(a)** absorption, **(b)** emission, **(c)** fluorescence lifetime decay profiles in chloroform and **(d)** cyclic voltammograms in dichloromethane.

Molecular orbital calculations also suggested that, upon photocycloaddition, the electron density got localized on to the anthracene core and was not extended throughout the molecule (**Figure 2.16**).

Table 2.2. Absorption data and HOMO-LUMO energy levels of the compound **25** and its photoadduct.

Compound	λ_{abs} [nm]	E_{gap} [eV]	$E_{1/2}$ [V]	E_{LUMO} [eV]	E_{HOMO} [eV]
25	266, 323, 366, 386, 406, 429	2.81	0.449	-1.98	-4.79
Photoadduct	258, 299, 360, 373, 393	2.95	0.740	-2.59	-5.54
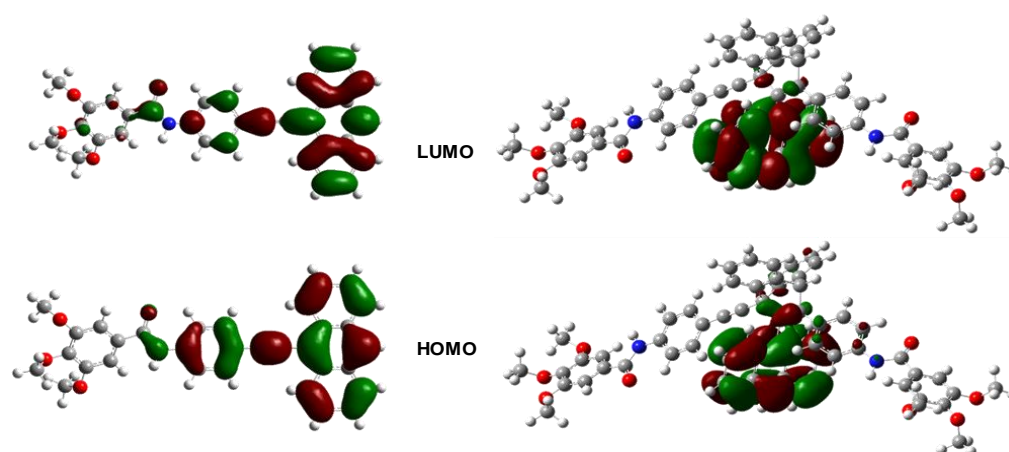
Figure 2.16. Theoretically calculated molecular orbitals of compound **25 (**R = methyl**)** (left) and the photoadduct (R = methyl) (right); HOMO (down), LUMO (top) using B3LYP 6-31G(d).

2.3.7. Electroluminescence of Compound 25 and its Photoadduct

The electroluminescent device characteristics of the parent compound **25** was investigated by fabricating solution processed single layer organic light emitting devices.[25] The emitting layer (EML) comprised of the gelator **25**, carbazole derivatives PVCz or SB2[26] as the hole transporting materials (HTM) and an oxadiazole derivative PBD as the electron transporting material (ETM). PVCz was a better HTM than SB2 as indicated by the higher L_{max} value of the devices with the former (**Table 2.3**).

Table 2.3. Device characterization data for compound **25** and its photoadduct.

Emitter	HTM	ETM	l_{EL} (nm)	L_{max} (cd m^{-2}) [@V]	EQE$_{max}$ (%) [@V]	CIE (x,y)
25	PVCz	PBD	448, 474	1244 [16.5]	0.71 [11.5]	(0.16,0.16)
	SB2	PBD	446, 468	231 [14.5]	0.3 [7.5]	(0.16,0.13)
Photoadduct	PVCz	PBD	445,473, 573	344.7 [16]	0.35 [11.5]	(0.28,0.25)
	SB2	PBD	443, 461, 560	127.5 [16]	0.3 [8]	(0.33,0.32)

The intensity of the EL spectra of both compound **25** and the photoadduct increased upon increasing the applied voltage, however, the structure of the spectra remained unchanged, while using PVCz or SB2 as the hole transporting material (**Figure**

2.17a-d). The CIE coordinates for the devices fabricated from compound **25** using PVCz (0.16, 0.16) or SB2 (0.16, 0.13) remained almost constant at any applied voltage (**Figure 2.17a,b_insets**). However, voltage dependent changes in the chromaticity coordinates were observed when the photoadduct was used as the emitter (**Figure 2.17c,d_insets**).
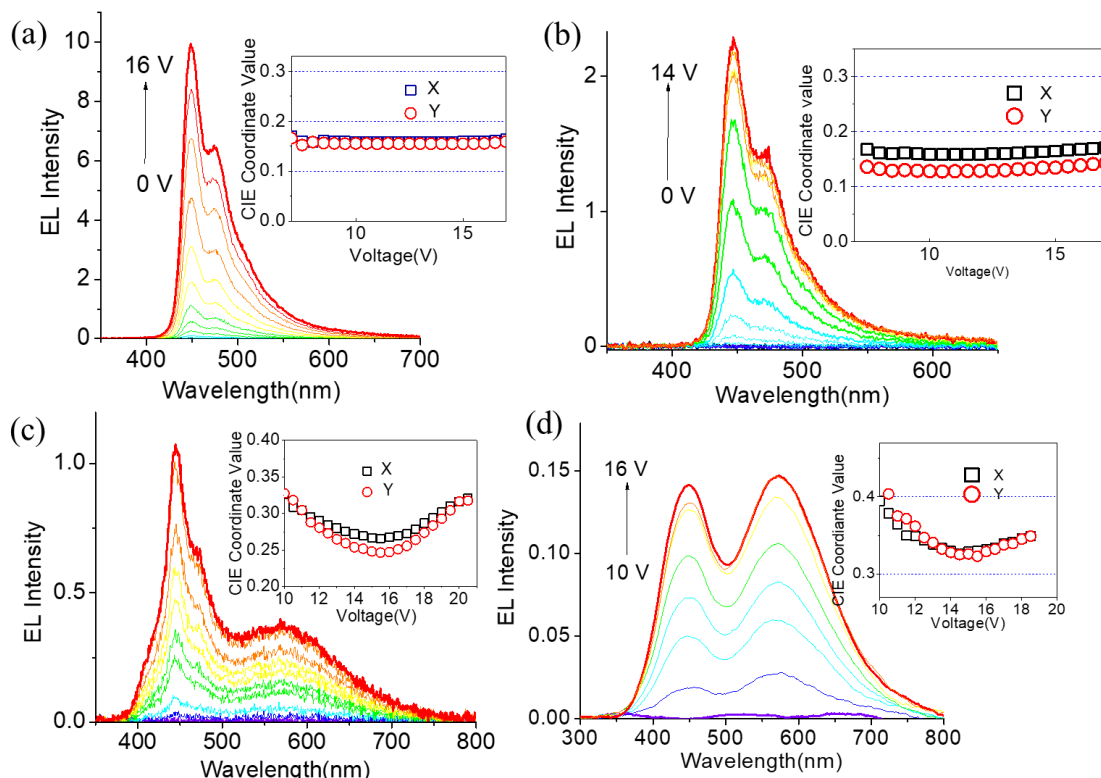
Figure 2.17. Electroluminescence spectra at different voltages for **(a)** compound **25** + PVCz device, **(b)** compound **25** + SB2 device, **(c)** photoadduct + PVCz device and **(d)** photoadduct + SB2 device (inset: change in the CIE (x,y) values with voltage).

The L_{max} obtained for the **25**+PVCz was 1244 cd/m^2 at 16.5 V, and 231 cd/m^2 for **25**+SB2 at 14.5 V (**Figure 2.18a**). In both cases, blue EL with CIE coordinates of (0.16, 0.16) and (0.16, 0.13), respectively, were obtained (**Figures 2.18c, 2.19a,c**). Interestingly, the device fabricated using the photoirradiated gel with PVCz (or SB2) as EML and PBD as ETM exhibited broad EL spectra emitting between 400-750 nm, with maxima at 445 and 573 nm (**Figure 2.18d**), resulting in white electroluminescence (**Figure 2.19b**). The performance of the PVCz based device

was better when compared to that with SB2 (**Figure 2.18b**). When SB2 was used as HTM, the CIE coordinates of the white light emission was x = 0.33, y = 0.32, indicating high color purity. On the other hand, the value of the CIE coordinates was x = 0.28, y = 0.25 when PVCz was used as the HTM (**Figure 2.19b,c**).
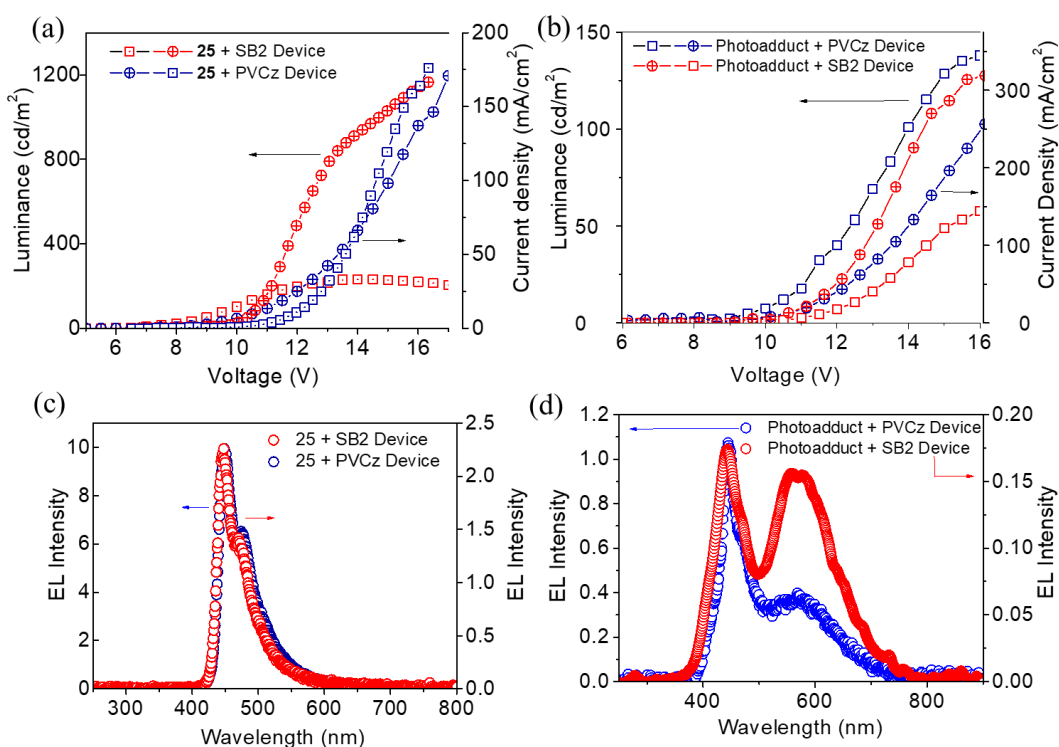
Figure 2.18. Device characteristics (luminance and current density vs voltage plot) of **(a) 25** and **(b)** the photoadduct. Electroluminescence spectra of OLED fabricated from **(c) 25** and **(d)** photoadduct as emitter with SB2 (red) and PVCz (blue) as hole-transporting materials.

2.3.8. Electroplex Characterization

For a deeper understanding of the origin of the white electroluminescence, the EL and the PL spectra of the devices fabricated with the gelator **25** before and after photoirradiation using PVCz and SB2 as the HTM were compared (**Figure 2.20a-d**). Both EL and PL spectra of the gelator before photoirradiation were comparable, and exhibited a blue emission with maxima at 450 and 470 nm. Similarly, the PL spectra of the devices fabricated using the photoadduct and both PVCz and SB2 as HTM showed blue emission with λ_{max} at 450 nm. A shoulder band was also observed at 475 nm. However, in addition to the sharp emission at 450 nm, a broad emission

at 600 nm was observed in the EL spectra of the photoadduct in both cases (**Figure 2.20b,d**). Notably the intensity of the broad 600 nm emission was less when PVCz was used as the HTM.
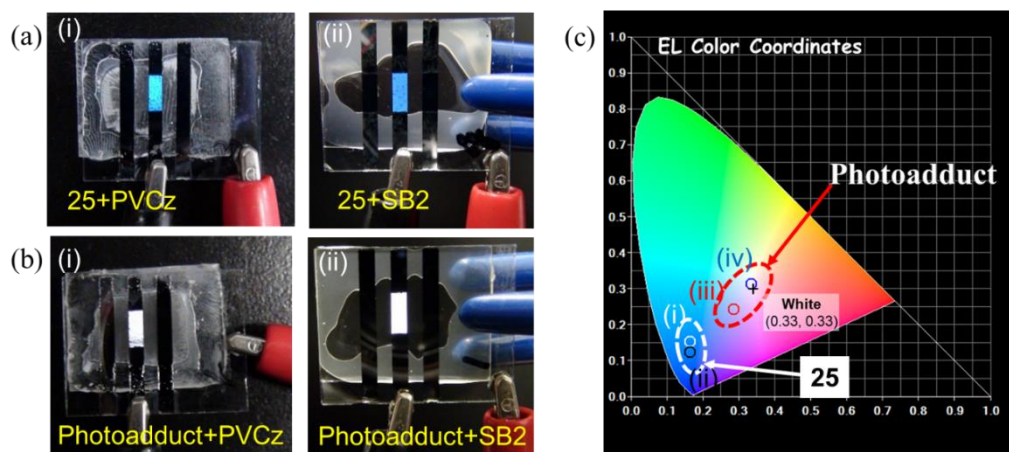
Figure 2.19. Photographs of the electroluminescent devices fabricated from **(a)** compound **25** (i: PvCz as HTM and ii: SB2 as HTM) and **(b)** the photoadduct (i: PvCz as HTM and ii: SB2 as HTM). **(b)** EL color coordinates of the devices fabricated from compound **25** and the photoadduct.
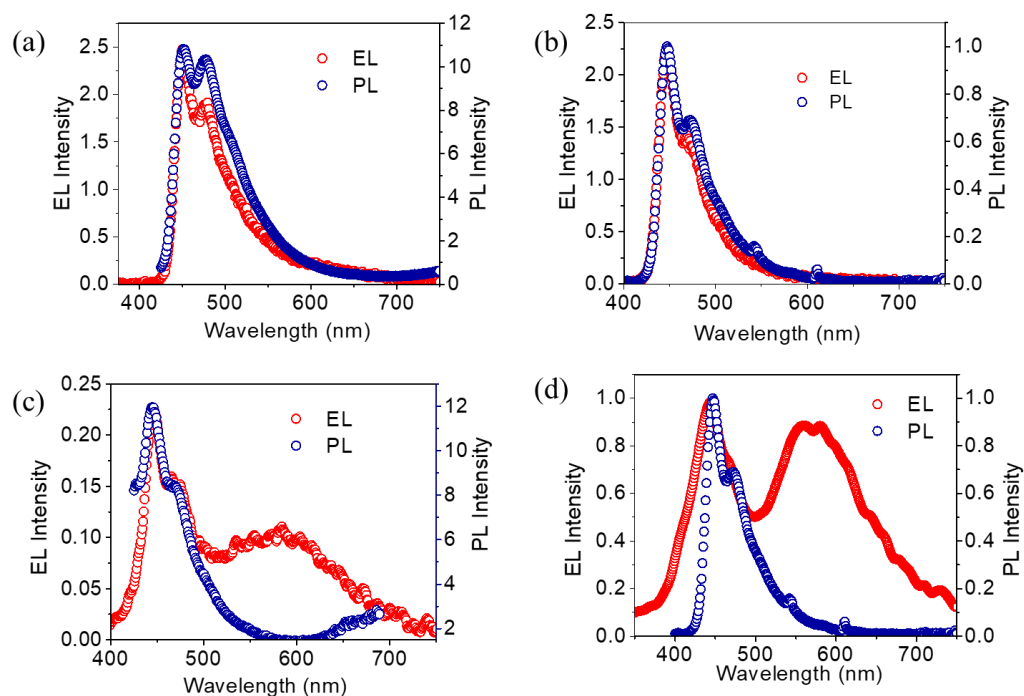
Figure 2.20. Comparative PL and EL spectra of devices made of **(a)** 25 + PVCz**, (b)** 25 + SB2, **(c)** photoadduct + PVCz, and **(d)** photoadduct + SB2.

Since the PL emission of the photoirradiated gelator was blue, we expected a similar emission characteristic for the EL spectrum as well. Instead, we observed an electrogenerated white light emission, which may not be the property of the photoadduct alone. Furthermore, film state absorption of EML did not show any new band in the presence of the photoadduct (**Figure 2.21**), which is a clear indication for the absence of any ground state charge transfer complex between the emitter and the HTM.
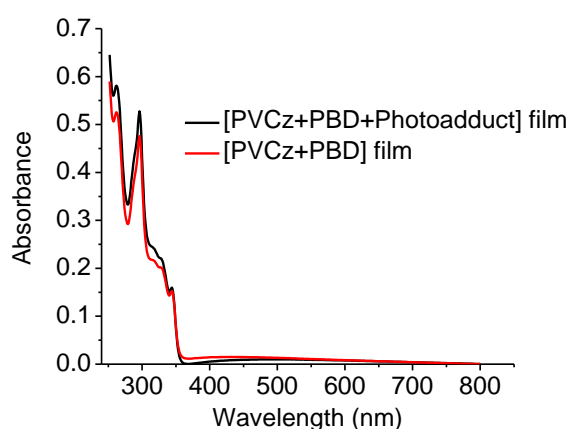
Figure 2.21. Comparative solid-state absorption spectra of model films of EML with and without photoadduct, indicating the absence of any new band corresponding to charge transfer complexes.

Therefore, the green and red emission components required for the white emission must have generated through the interaction between the photoadduct and the transporting materials under the applied electric field. Probably, an electron transfer from the HTM to the photoadduct could generate an excited complex called electroplex, similar to a photoexcited exciplex (**Figure 2.22**). Such an emission by the electrically excited electroplex can be visible only in an EL spectrum and not in the photoexcited PL spectrum.[27] The energy levels of the electroplex will be lower than that of the singlet excited state of the photoadduct (**Figure 2.22a**). This electroplex (photoadduct$^-$ + HTM$^+$) formation is in analogy with previous reports and should be responsible for the green-to-red emission along with the blue emission of the photoadduct, leading to the white light emission (**Figure 2.22b**).[21,28]
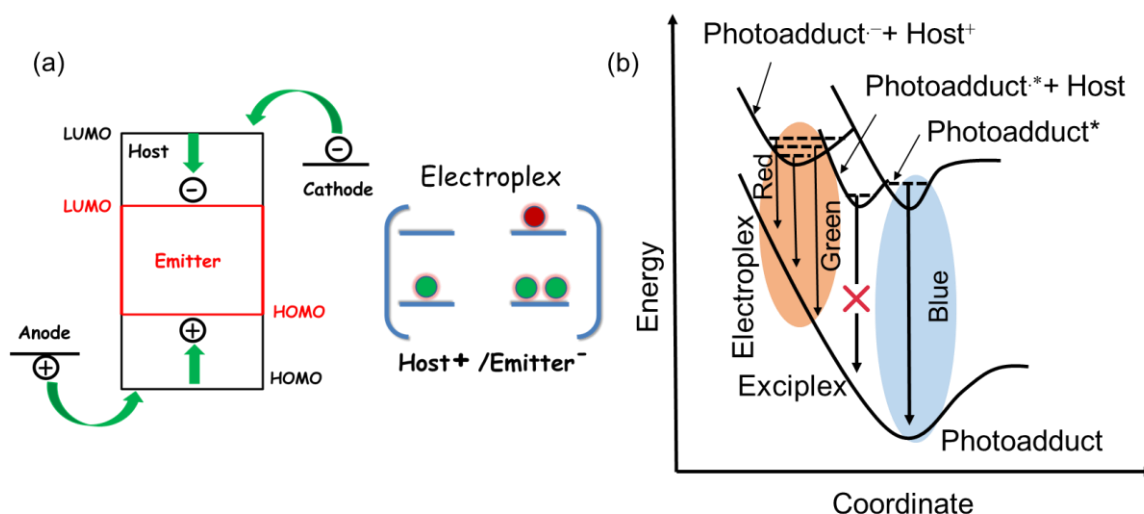
Figure 2.22. (a) Schematic representation of the electronic configuration in molecular orbitals of the electroplex host/emitter. **(b)** Proposed energy profiles for the electroluminescence response of the photoadduct, exciplex, and electroplex.

To establish the electroplex formation between the emitter and the HTM, we fabricated devices by mixing them together with an electron transporting layer ([1,1':3',1″-terphenyl]-4,4″-diylbis(diphenylphosphine oxide), BPOBP)[29] separately coated in solution processed double layer devices (**Figure 2.23a**).
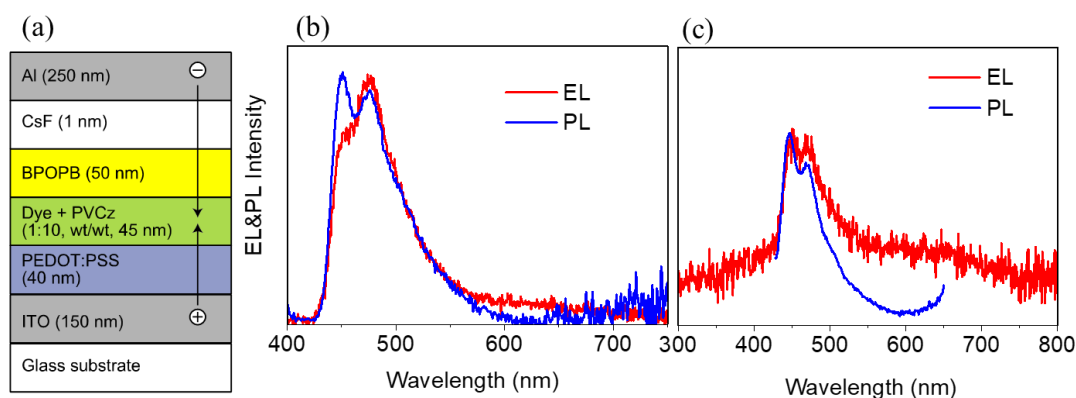
Figure 2.23. (a) Fabrication of multilayer OLEDs, where BPOPB was used as the electron transporter and the emitting layer consisted of the parent compound **25** or its photoadduct that was mixed with the hole transporting materials (PVCz). The corresponding PL and EL spectra of multilayered OLEDs with **(c)** compound **25** and **(d)** the photoadduct.

As expected, the device with the emitter **25** showed blue emission, whereas the device made out of the photoirradiated gel exhibited white light emission,

underlining the electroplex formation between the photoadduct and the carbazole based compounds (**Figure 2.23b,c**). The emitters are responsible for electroplex formation with HTM, that is further confirmed by fabricating a device with 9-phenylethylanthracene (9-PEA) and its [4 + 2] photoadduct. The devices fabricated from 9PEA and either PVCz or SB2 as HTM exhibited similar photo- and electroluminescence with a blue emission (**Figure 2.24a**), whereas the use of the corresponding photoadduct as emitter resulted in blue photoluminescence and bluish-white electroluminescence, wherein an electroplex emission was clearly visible in the 500-700 nm region of the EL spectrum (**Figure 2.24b**).
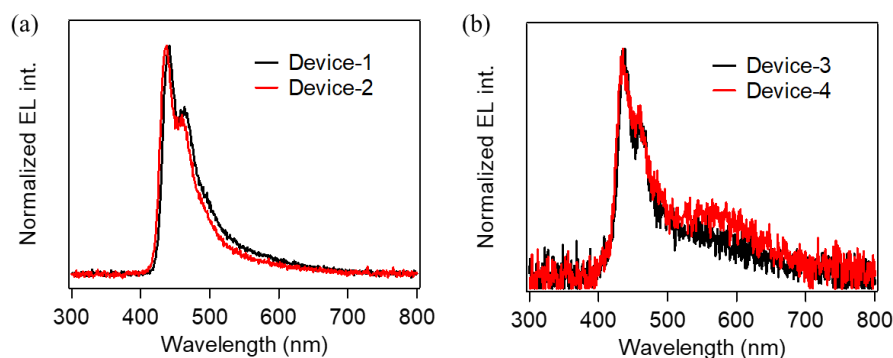
Figure 2.24. (a) Normalized EL intensity of Device-1 (9PEA + PVCz) and Device-2 (9PEA + SB2) and **(b)** that for Device-3 (9PEA dimers + PVCz) and Device-4 (9PEA dimers + SB2).

2.4. Conclusion

In conclusion, the molecular assembly of the molecule **25** at its supramolecular gel phase creates enough confinement to selectively yield the [4 + 2] photocycloadduct. Light emitting devices fabricated from the gelator **25** exhibited a blue emission, whereas the device fabricated with the photo-irradiated gelator showed a white electroluminescence. The generation of the green and red emission required for white luminescence is explained on the basis of an electroplex formation between the photocycloadduct and the hole transporting material within the device structure under an applied electric potential. This report highlights the role of H-bonded supramolecular assembly and gelation of functional molecules to achieve exclusive photoproduct formation for their further use in photonic device application.

2.5. Experimental Section

2.5.1. Materials and Methods

General procedures: All chemicals were purchased from Sigma Aldrich, Alfa Aesar and TCI and used without further purification. PVCz, PEDOT:PSS (Clevios P CH 8000), PBD, Cesium fluoride (CsF) and aluminium (Al) were purchased from commercial suppliers (Sigma Aldrich Co., Heraeus GmbH, Luminescence Technology Corp., Wako Pure Chemical Industries, Ltd. and the Nilaco Co. respectively). PVCz was reprecipitated in THF and dried under vacuum prior to use. BPOPB was synthesized according to a reported procedure.[29] Moisture and oxygen sensitive reactions were performed under dry argon/nitrogen atmosphere. Merck silica gel plates on aluminum sheets were used for performing thin layer chromatography (TLC). Column chromatography was carried out using 100-200 mesh silica gel. Solvents used for carrying out the reactions were distilled and stored under an anhydrous atmosphere. K_2CO_3 was activated by heating at 300 ºC for 4 h. Anhydrous sodium sulfate (Na_2SO_4) was used for drying the organic extracts. HEIDOLPH rotary evaporator was used for the removal of solvents under reduced pressure. The purchased HPLC grade solvents were used for gelation, spectroscopic studies and device fabrication.

^{1}H and ^{13}C NMR measurements were performed in chloroform-d_6, with an internal standard TMS (δ = 0 ppm for ^{1}H and δ = 77 ppm for ^{13}C) on a Bruker Avance 500 (^{1}H: 500 MHz; ^{13}C: 125 MHz) spectrometer. FT-IR measurements were performed in SHIMADZU IR Prestige21 FTIR Spectrometer using KBr. Matrix-assisted laser desorption ionization time-of-flight (MALDI-TOF) mass spectra were performed on an AXIMA-CFR PLUS (SHIMADZU) MALDI-TOF mass spectrometer. High-resolution mass spectra were obtained from a JEOL JSM 600.

UV–Vis Electronic Absorption and Emission Spectral Measurements: A Shimadzu UV-2600 Spectrophotometer and a SPEX-Fluorolog FL-1039 Spectrofluorimeter have been used for UV-vis and fluorescence

measurements respectively. Temperature variable absorption experiments were performed using a 0.1 cm quartz cuvette on a Shimadzu UV-2600 Spectrophotometer.

Transmission Electron Microscopy (TEM): TEM imaging was performed on a JEOL-JEM0310 microscope with an accelerating voltage of 100 kV. The samples were prepared by drop casting over a carbon coated copper grid. TEM images were obtained without staining.

Atomic Force Microscopy (AFM): AFM images were recorded at ambient conditions using a Nanocut instrument operating under tapping mode. Micro-fabricated TiN cantilever tips with a resonance frequency of 299 kHz and a spring constant of 20-80 Nm^{-1} was used. Samples were prepared by drop casting the sample over silicon wafer at defined concentrations.

Electrochemical measurements: Cyclic voltammetric measurements were carried out in dichloromethane containing 0.1 M tetra-*n*-butyl ammonium hexafluorophosphate as supporting electrolyte. The experiments were performed in a single compartment cell with a three electrode setup consisting of a glassy carbon working electrode, a Pt counter electrode, and a Ag/Ag$^+$ quasi reference electrode. The dichloromethane was distilled prior to use. Before performing the electrochemical measurements, the solution was bubbled with N$_2$, and the N$_2$ atmosphere was maintained in the head space of the cell during the course of the experiment.

Wide–angle X–ray Scattering (WAXS): Wide–angle X–ray Scattering measurements were performed on a XEUSS 2D SAXS/WAXS system using a Genix microsource from Xenocs operated at 50 kV and 0.3 mA. The Cu Kα radiation ($\lambda =$ 1.54 Å) was collimated with a FOX2D mirror and two pairs of scatterless slits from Xenocs. Xerogel of **25** and the photoadduct were placed directly into the sample holder.

General procedure for fabrication of solution-processed OLEDs: We followed a previously reported procedure for the fabrication of OLEDs.[30]

Fabrication of Monolayer OLED: The anode substrate (pre-patterned ITO glass) was washed with an aqueous detergent solution under ultra-sonication, and then with distilled water, acetone, chloroform, hexane and 2-propanol. ITO layer was treated with UV-O$_3$ for 10 minutes PEDOT:PSS (40 nm) was then coated using a spin-coater, then dried at 115 °C for 1 h. For preparation of the EML, a mixture of PVCz, PBD and **25** or the photoadduct in dry toluene (with a ratio of **25** : PBD : PVCz or SB2 = 0.5 mg : 1.5 mg : 5 mg) was filtered through a 0.2 mm Millex-FG filter (Millipore), then spin-coated over the PEDOT:PSS layer under inert atmosphere. Subsequently, electron injection layer (CsF, 1.0 nm) and cathode (Al, 250 nm) were vacuum deposited on the EML under a base pressure of ca. 1 x 10^{-4} Pa. In order to protect from air and moisture, the device was sealed with a glass cap and encapsulated with a UV-curing epoxy resin under inert conditions. The emitting pixel was 10 mm^2 (2 x 5 mm). The fabrication of device was performed inside a glovebox filled with dry argon.

Fabrication of Multilayer OLEDs: The cleaning of pre-patterned ITO glass substrate and spin coating of PEDOT:PSS were performed as described in the previous section. For fabrication of an EML, a mixture of PVCz, and **25** or the photoadduct in dry toluene (**25** or Photoadduct: PVCz = 0.641 mg : 6.41 mg in 0.7 mL) was filtered through a 0.2 mm Millex-FG filter (Millipore). The obtained stock solution was spin-coated onto the PEDOT:PSS layer under an argon atmosphere and annealed at 120 °C for 1 h. Thereafter, BPOBP (10.5 mg) in 2-propanol (1.5 mL) was spin-coated and annealed at 80 °C for 10 min. A similar procedure as described in the previous section was followed for vacuum deposition of CsF (1 nm), Al (250 nm) and sealing with glass cap by UV-curing epoxy resin.

2.5.2. Synthesis and Characterization

Synthesis of N-(4-(anthracen-9-ylethynyl) phenyl)-3,4,5-tris (dodecyloxy) benzamide (25):

Compound **20** (0.138 mmol), Pd(PPh$_3$)$_2$Cl$_2$ (10 mol%), and CuI (10 mol%) were taken in a pre-dried two neck round bottom flask and was degassed under high vacuum. Argon purging and vacuum treatments were performed thrice. A solvent mixture comprising of trimethylamine and THF (1:1, v/v) was degassed with argon for 20 minutes and 10 mL was added to the reaction mixture. 9-Ethynylanthracene **24** (0.150 mmol), dissolved 10 mL degassed solvent mixture (TEA/THF), was added and stirred at room temperature in the dark. Completion of the reaction was monitored by TLC. After the removal of the solvent under reduced pressure, chloroform was added to the residue and filtered through celite. The crude product was then purified by column chromatography on silica gel (100-200 mesh) using chloroform: methanol (98:2) as eluent.

Yield: 75%; **^{1}H NMR (500 MHz, CDCl$_3$)**: δ = 8.66 (d, 2H, J = 9 Hz), 8.44 (s, 1H), 8.03 (d, 2H, J = 8.5 Hz), 7.86 (s, 1H), 7.77 (q, 4H, J = 8 Hz), 7.61 (t, 2H, J = 7.5 Hz), 7.52 (t, 2H, J = 7.5 Hz), 7.08 (s, 2H), 4.07-4.02 (m, 6H), 1.86-1.81 (m, 4H), 1.79-1.74 (m, 2H), 1.52-1.46 (m, 6H), 1.27-1.22 (m, 48H), 0.90-0.87 (t, 9H) ppm.

^{13}C NMR (125 MHz, CDCl$_3$): δ = 165.00, 153,34, 138.24, 132.58, 132.53, 131.23, 129.65, 128.72, 127.65, 126.60, 125.71, 119.88, 119.88, 119.44, 117.36, 105.90, 100.57, 100.00, 86.19, 73.61, 69.55, 31.96, 31.94, 30.35, 29.72, 2.68, 29.66, 29.38, 26.10, 22.70, 14.13 ppm.

HRMS: Molecular formula (C$_{65}$H$_{91}$NO$_4$) Calcd.: 950.4223, found = 951.3864 [M+H]$^+$.

FT-IR (KBr): ν = 3263.55, 3049.45, 2920.23, 2850.79, 2358.94, 2196.92, 1645.28, 1581.63, 1514.12, 1492.90, 1467.83, 1427.32, 14402.25, 1384.89, 1336.67, 1309.67, 1290.38, 1240.23, 1217.08, 1178.51, 1120.64, 1010.69, 956.69, 881.47,

840.97, 827.47, 779.24, 759.95, 734.88, 675.08, 655.79, 640.37, 613.36, 551.64, 532.35, 453.27, 408.91 cm^{-1}.

Synthesis of the Photoadduct

Room temperature stable gel of **25** was taken in a UV transparent container and subjected to photoirradiation using UV light (λ_{max} = 365 nm) for 20 h. Complete transformation of the gel to sol was observed. The sol was then dried using a rotary evaporator maintained at a water bath temperature <35 °C. The photoirradiation resulted in an almost exclusive *anti*-[4 + 2] cycloaddition product, which indicated that molecular packing does not allow for any other mode of cycloaddition.

^{1}H NMR (500 MHz, CDCl₃): δ = 8.34 (s,1H), 7.93 (d, 2H, J = 8.5Hz), 7.73 (d, 2H, J = 7.5 Hz), 7.61 (d, 2H, J = 7.5 Hz), 7.60 (s,1H Hz) 7.39 (s, 1H), 7.32-7.30 (m, 4H), 7.23-7.16 (m, 4H), 7.14 (d, 2H, J = 8.5 Hz) 7.09 (d, 2H, J = 6.8 Hz), 6.99-6.97 (m, 4H), 6.86 (s, 2H), 6.46 (d, 2H, J = 8.5 Hz), 5.74 (s, 1H), 4.02-3.99 (m, 6H), 3.96-3.91 (m, 6H), 1.82-1.78 (m, 4H), 1.77-1.68 (m, 8H), 1.48-1.40 (m ,12H), 1.27-1.25 (m, 96H), 0.90-0.86 (m, 18H) ppm.

^{13}C NMR (125 MHz, CDCl₃): δ = 165.36, 153.26, 153.15, 145.31, 144.66, 144.16, 141.40, 133.01, 132.13, 131.38, 130.57, 128.33, 127.08, 126.81, 119.45, 119.11, 105.78, 105.61, 100.00, 73.59, 69.37, 58.35, 31.93, 30.32, 29.71, 29.68, 29.65, 29.61, 29.40, 29.36, 26.08, 22.69, 14.12 ppm.

FT-IR (KBr): ν = 3282.84, 3051.39, 2924.08, 2852.72, 2360.87, 2341.58, 1647.21, 1581.63, 1512.19, 1494.83, 1465.90, 1425.39, 1404.18, 1334.74, 1238.29, 1209.37, 1116.78, 1012.63, 885.33, 842.89, 781.17, 752.24, 734.88, 719.44, 669.29, 650.01, 601.79, 540.06, 460.98, 418.55 cm^{-1}.

2.6. References

(1) (a) Yoshizawa, M.; Klosterman, J. K.; Fujita, M. *Angew. Chem. Int. Ed.* **2009**, *48*, 3418. (b) Ramamurthy, V.; Sivaguru, J. *Chem. Rev.* **2016**, *116*, 9914.

(2) Ariel, S.; Askari, S.; Scheffer, J. R.; Trotter, J. *J. Org. Chem.* **1989**, *54*, 4324.

(3) Sakamoto, M.; Takahashi, M.; Fujita, T.; Watanabe, S.; Iida, I.; Nishio, T.; Aoyama, H. *J. Org. Chem.* **1993**, 58 (13), 3476.

(4) Claassens, I. E.; Barbour L. J.; Haynes D. A. *J. Am. Chem. Soc.* **2019**, *141*, 11425.

(5) (a) Aakeröy, C. B.; Salmon, D. J. *Cryst. Eng. Comm.,* **2005**, 439. (b) Claassens, I. E.; Nikolayenko, V. I.; Haynes, D. A.; Barbour, L. J. *Angew. Chem., Int. Ed.* **2018**, *57*, 15563.

(6) Feldman, K. S.; Campbell, R. F. *J. Org. Chem.* **1995**, *60*, 1924.

(7) Aoyama, Y.; Endo, K.; Anzai, T.; Yamaguchi, Y.; Sawaki, T.; Kobayashi, K.; Kanehisa, N.; Hashimoto, H.; Kai, Y.; Masuda, Y. *J. Am. Chem. Soc.* **1996**, *118*, 5562.

(8) (a) Becker H.-D. *Chem Rev.* **1993**, *93*, 145. (b) Bouas-Laurent, H.; Castellan, A.; Desvergne, J.-P.; Lapouyade, R. *Chem. Soc. Rev.* **2000**, *29*, 43.

(9) (a) Aubry, J.-M.; Pierlot, C.; Rigaudy J.; Schmidt, R. *Acc. Chem. Res.*, **2003**, *36*, 668. (b) Fudickar, W.; Linker, T. *J. Am. Chem. Soc.*, **2012**, *134*, 15071. (c) Nakamura, A; Inoue,Y. *J. Am. Chem. Soc.,* **2003***, 125,* 966. (d) Fukuhara, G.; Kazuhiro I., Kawanami, Y.; Tanaka, H., Mori, T.; Inoue Y. *J. Am. Chem. Soc.*, **2015**, *137*, 15007.

(10) Ishida, Y; Matsuoka, Y.; Kai, Y.; Yamada, K.; Nakagawa, K.; Asahi, T.; Saigo, K. *J. Am. Chem. Soc.* **2013**, *135*, 6407.

(11) Yang, C.; Mori, T.; Origane, Y.; Ko, Y. H.; Selvapalam, N.; Kim, K.; Inoue, Y. *J. Am. Chem. Soc.* **2008**, *130*, 8574.

(12) Becker, H. D.; Andersson, K. *J. Photochem.* **1984**, *26*, 75.

(13) (a) Tanabe, J.; Taura, D.; Ousaka N.; Yashima E. *Org. Biomol. Chem.* **2016**, *14*, 10822. (b) Becker H.-D.; Andersson, K. *J. Photochem.*, **1984**, 26, 75.

(14) (a) Kim, M.; Hohman, J. N.; Cao, Y.; Houk, K. N.; Ma, H.; Jen K.-Y. A.; Weiss, P. S. *Science*, **2011**, *331*, 1312. (b) Zheng, Y. B.; Payton, J. L.; Song, T.-B.; Pathem, B. K.; Zhao, Y.; Ma, H.; Yang, Y.; Jensen, L.; Jen, A. K.-Y.; Weiss, P. S. *Nano Lett.* **2012**, *12*, 5362.

(15) Zdobinsky, T.; Maiti, P. S.; Klajn, R. *J. Am. Chem. Soc.*, **2014**, *136*, 2711.

 (16) (a) Babu, S. S.; Praveen, V. K.; Ajayaghosh A. *Chem. Rev.* **2014**, *114*, 1973. (b) Jones, C. D.; Steed, J. W. *Chem. Soc. Rev.,* **2016**, *45*, 6546. (c) Nair, V. S.; Mukhopadhyay, R. D.; Saeki, A.; Seki, S.; Ajayaghosh, A. *Sci. Adv*. **2016**, *2*, e1600142.

(17) (a) Dawn, A.; Fujita, N.; Haraguchi, S.; Sada, K.; Shinkai, S. *Chem. Commun.*, **2009**, *0*, 2100. (b) Dawn, A.; Shiraki, T.; Ichikawa, H.; Takada, A.; Takahashi, Y.; Tsuchiya, Y.; Lien, L. T. N.; Shinkai, S. *J. Am. Chem.Soc.* **2012**, *134*, 2161.

(18) Ying, L.; Ho, C.-L.; Wu, H.; Cao Y.; Wong, W.-Y. *Adv. Mater.* **2014**, *26*, 2459.

(19) (a) Chen, Y.-H.; Tang, K.-C.; Chen, Y.-T.; Shen, J.-Y.; Wu, Y.-S.; Liu, S.-H.; Lee, C.-S.; Chen, C.-H. Lai, T.-Y.; Tung, S.-H.; Jeng, R.-J.; Hung, W.-Y.; Jiao, M.; Wu, C.-C.; Chou P.-T. *Chem. Sci.* **2016**, *7*, 3556. (b) Xu, B.; Wu, H.; Chen, J.; Yang, Z.; Yang, Z.; Wu, Y.-C.; Zhang, Y.; Jin, C.; Lu, P.-Y.; Liu, S.; Xu, J.; Aldred, M. *Chem. Sci.*, **2017**, *8*, 1909.

(20) (a) Liu, Y.; Nishiura,M.; Wang,Y.; Hou. Z. *J. Am. Chem. Soc.* **2006***, 128,* 5592. (b) Okamura, N.; Maeda, T.; Fujiwara, H.; Soman, A.; Unni, K. N. N.; Ajayaghosh, A.; Yagi, S. *Phys. Chem. Chem. Phys.*, **2018**, *20*, 542. (c) Okamura, N.; Egawa, K.; Maeda, T.; Yagi, S. *New J. Chem.*, **2018**, *42*, 11583.

(21) (a) Berggren, M.; Gustafsson, G.; Inganäs, O.; Andersson, M. R.; Hjertberg, T.; Wennerström, O. *J. Appl. Phys.* **1994**, *76*, 7530. (b) Li, J. Y.; Liu, D.; Ma, C.; Lengyel O.; Lee C.-S. Tung, C.-H.; Lee S. *Adv. Mater*. **2004**, *16*, 1538. (c) Wen, L.; Li, F.; Xie, J.; Wu, C.; Zhen, Y.; Chen, D.; Xu, S.; Guo, T.; Qu, B.; Chen, Z.; Gong, Q. *J. Lumin.* **2011**, *131*, 2252. (d) Luo, D.; Li, X.-L.; Zhao, Y.; Gao, Y.; Liu, B. *ACS Photonics,* **2017**, *4*, 1566.

(22) Weber, M. D.; Adam, M.; Tykwinski, R.R.; Costa, R. D. *Adv. Funct. Mater.* **2015**, *25*, 5066.

(23) Ando, Y.; Sugihara, T.; Kimura, K.; Tsuda, A. *Chem. Commun.*, **2011**, *47*, 11748.

(24) Sugino, M.; Araki, Y.; Hatanaka, K.; Hisaki, I.; Miyata, M.; Tohnai, N. *Cryst. Growth Des.* **2013**, *13*, 4986.

(25) Shigehiro, T.; Yagi, S.; Maeda, T.; Nakazumi, H.; Fujiwara, H.; Sakurai, Y. *J. Phys. Chem. C.* **2013**, 117, 532.

(26) Okamura, N.; Funagoshi, H.; Ikawa, S.; Yagi, S.; Maeda, T. *Mol. Cryst. Liq. Cryst.* **2015**, *621*, 59.

(27) Zhao, Z.; Xu, B.; Yang, Z.; Wang, H.; Wang, X.; Lu, P.; Tian, W. *J. Phys. Chem. C.* **2008**. *112,* 8511.

(28) (a) Wei, M.; Gui, G.; Chung, Y.-H.; Xiao, L.; Qu, B.; Chen, Z. *Phys. Status Solidi B.,* **2015**. *252,* 1711. (b) Shin, D.-M. *J. Nanosci. Nanotechnol.* **2010**, *10*, 6794. (c) Liu, J.; Chou, S.-Y.; Tong, K.; Luan, X.; Zhao, F.; Pei, Q.; Li, H. *J. Phys. Chem. C.* **2017**, *121*, 10112. (d) Li, J.; Xu, Z.; Zhang, F.; Zhao, S.; Song, D.; Zhu, H.; Song, J.; Wang, Y.; Xu, X. *Solid-State Electronics* **2010**, *54*, 349.

(29) Aizawa, N.; Pu, Y. J.; Watanabe, M.; Chiba, T.; Ideta, K.; Toyota, N.; Igarashi, M.; Suzuri, Y.; Sasabe, H.; Kido, J. *Nat. Commun.* **2014**, *5*, 5756.

(30) Okamura, N.; Nakamura, T.; Yagi, S.; Maeda, T.; Nakazumi, H. Fujiwara, H.; Koseki, S. *RSC Adv*. **2016**, 6, 51435.

Chapter 3

Lower Critical Solution Temperature (LCST) Modulation of Amphiphilic π-Systems by Photocycloaddition for Controlled Transmission of Solar Radiation
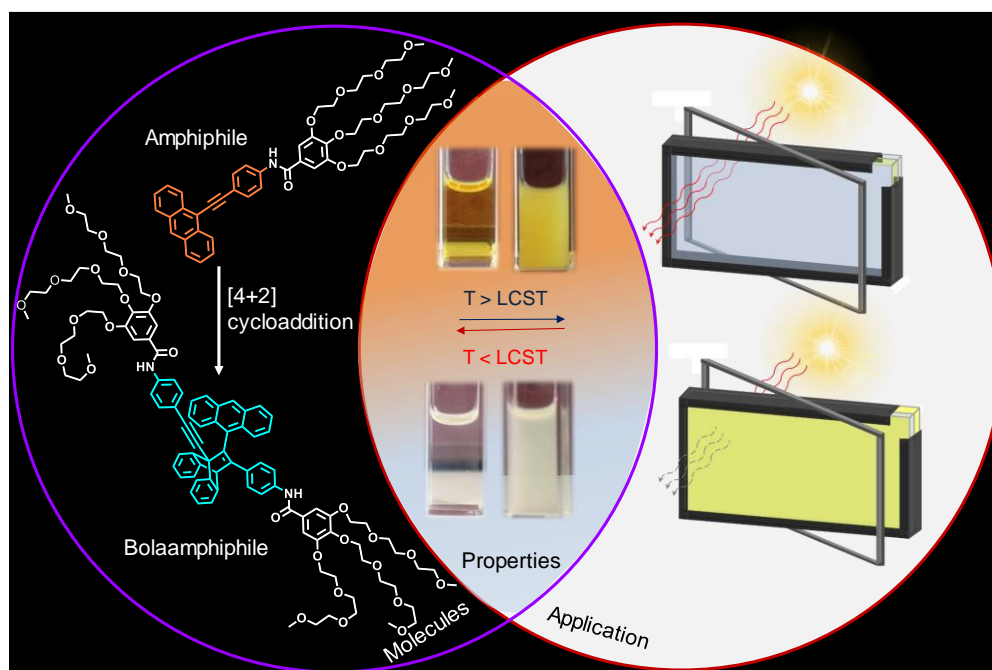
3.1. Abstract

Residential buildings in the tropical regions consume huge amount of energy for maintaining indoor temperature. Energy inefficiency and solar radiation induced indoor heating in the architectural sector is attributed to the energy loss through windows. Therefore, the development of low-cost and scalable responsive smart materials exhibiting controllable light and heat transmission for application in smart windows is a prerequisite towards effectively managing indoor energy consumption. Herein, we report the design and study of an amphiphilic liquid π-system having an LCST based thermoresponsive behavior in the range 27-32 °C at a minimum concentration of 0.25 mM. This molecule upon photoirradiation at 365 nm yielded the [4 + 2] photocycloadduct which is a bolaamphiphile that exhibited LCST

behavior at a lower temperature range of 24-27 °C and at a minimum concentration of 6 μM. The lowered LCST behavior of the photocycloadduct at ~42 times lower concentration when compared to that of the parent molecule is of advantage for the fabrication of near room temperature responsive dynamic windows. As a proof-of-concept, we fabricated smart window prototypes by sandwiching the aqueous solutions of the amphiphilic molecule between two parallel glass panels. The prototypes fabricated from the amphiphile exhibited transparency below 29 °C with >92% visible light transmittance. However, above 32 °C, the window turned opaque and blocked >80% of the solar radiation. The photoadduct exhibited a lower LCST transition temperature of 24 °C, below which ~90% transparency was achieved and transmission of light was blocked upto 64% at temperatures above the LCST. Variable temperature DLS correlation coefficient analysis of the molecules before and after photoirradiation revealed the formation of globular particles of 760 nm and 845 nm respectively, above their LCST transition, causing the visible and near infrared solar radiation to scatter off, thereby reducing the indoor heating effect. Thus, one of the extensively studied classical photoreaction has been used for the design of smart windows that can modulate light and heat transmittance, with implication in energy saving and management.

3.2. Introduction

Innovations in stimuli-responsive smart materials is of contemporary interest for the construction of energy efficient devices and buildings. One such example is dynamic windows that control light transmission in response to the ambient conditions and user demands. In this context, materials exhibiting lower critical solution temperature (LCST), that exhibit changes in transparency in response to temperature, have attracted immense attention.[1] In addition to the modulation of light transmission, molecular systems that exhibit LCST transitions are particularly attractive because, the insoluble aggregates formed above the LCST can be used as nano/microenvironments for catalysis[2,3], drug delivery[4], ion/logic gates[5,6], bacterial aggregation[7], photoresists[8] and sensors[9]. A majority of LCST materials reported till

date are polymeric in nature, as exemplified by poly (*N*-isopropylacrylamide) (PNIPAM), that displays an LCST transition around 32 °C in water.[10,11] Hydrophilic acrylamide-based polymers and co-poymers such as NIPAM undergo phase transition or change in their size or volume upon increasing the temperature beyond LCST (**Figure 3.1**).[12] Several reports have indicated that the phase transitions in such polymeric solutions occur due to the reversible transition from hydrated to dehydrated states upon temperature variation.
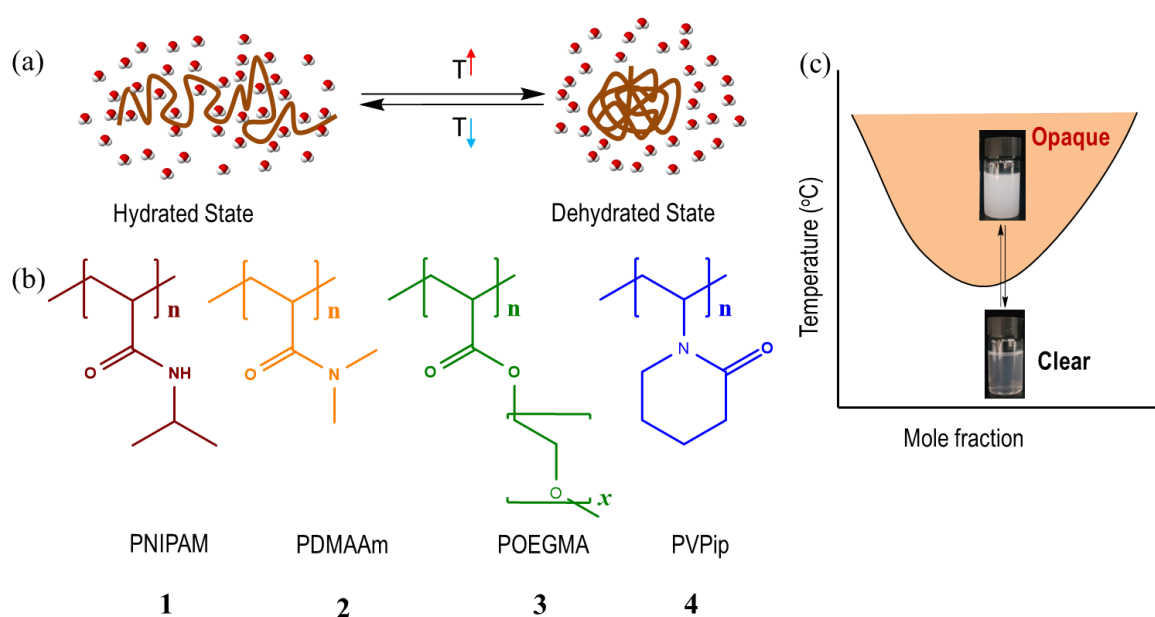
Figure 3.1. (a) A general schematic representation of the thermoresponsive phase transition of a polymeric solution. Phase transitions occur due to the reversible transition from hydrated state to dehydrated state upon temperature variations. **(b)** Chemical structures **1-4** of a few polymeric materials showing LCST phase transition. **(c)** Graphical representation of the opaque to clear transitions as a function of mole fraction. The insect shows photographs of PNIPAM **1** exhibiting an opaque to transparent switching in water.

Several polymers have been shown to exhibit LCST behavior. Ritter *et al*. have reported the thermoresponsive behavior of the host-guest complex of a co-polymer containing 2-methyacrylamido-carprolactum and *N,N*-dimethylacrylamide. Upon host-guest complexation *via* the addition of 1.5 equiv. of methylated-*β*–CD, the copolymer cloud point was increased to >50 °C (**Figure 3.2a**). Creation of such host-

guest assemblies to achieve thermoresponsive LCST phenomenon are extended to supramolecular systems such as *bis-p*-sulfonatocalix[4]arene based amphiphiles.[13]
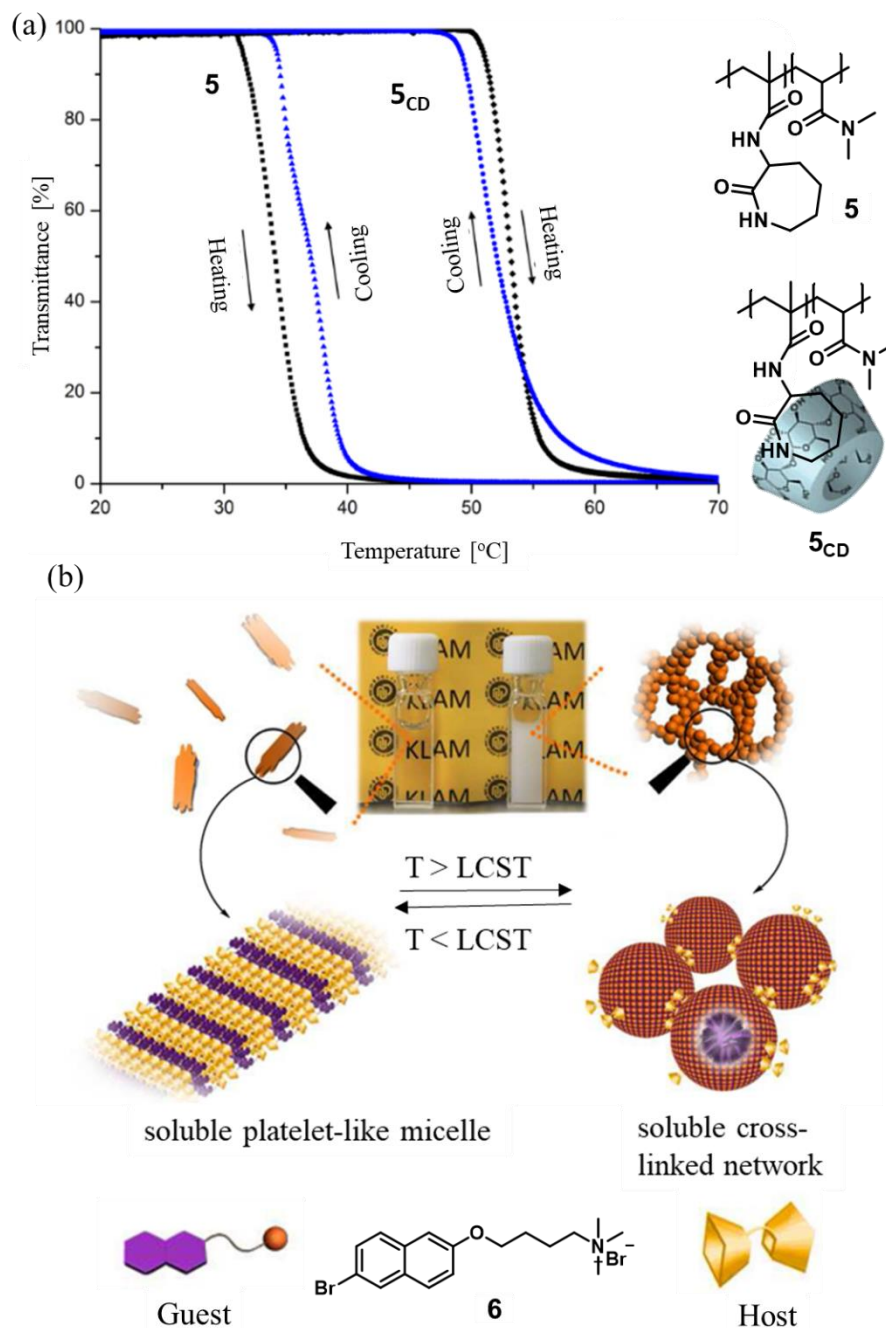
Figure 3.2. (a) Turbidity curves of polymer **5** in the presence and absence of β-CD. **(b)** A supramolecular amphiphilic system derived from the naphthalene derivative **6** and its LCST behavior based on an inclusion complex. The corresponding photographs of the opaque and transparent states are also shown.

In supramolecular systems, LCST phase transitions are usually observed due to their switching from water soluble assemblies to insoluble net-like cross-linked nanoparticles under applied temperature. Such phase transitions are generally regulated by multiple weak interactions such as hydrophilic and hydrophobic interactions, π−π stacking, and host−guest recognition. A hydrogel with LCST behavior was reported to provide a classical example for calixarene induced aggregation (CIA) and thermoresponsive self-assembled LCST systems.[14] Other examples of small molecule-based LCST systems, though rarely reported, include discotic molecules,[15] dendrimers,[16,17] supramolecular assemblies[18-20] and photoresponsive host-guest complexes (**Figure 3.2b**).[21] Stang and co-workers have observed coordination-driven self-assembly induced LCST phase transitions in an amphiphilic metallacyclic system. The metallacycle **7** showed good thermoresponsive behavior with a highly sensitive phase separation and excellent reversibility. Furthermore, the clouding point decreased with increasing metallacycle concentration and addition of K$^+$ (**Figure 3.3**).[22]
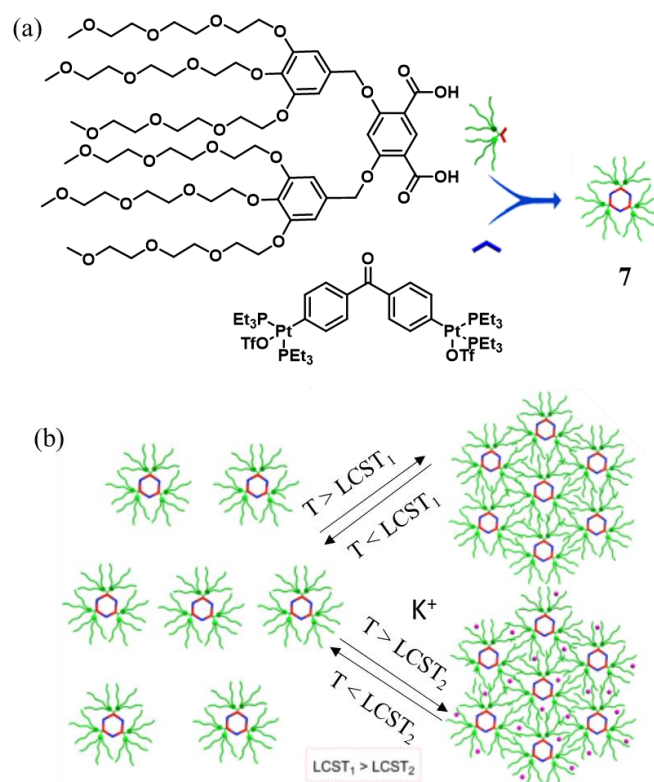
Figure 3.3. (a) Chemical structures of the components of the metallacycle **7** and **(b)** a schematic representation of the discrete LCST phase transition in the presence and absence of K$^+$.

Interestingly, Tang *et al.* have reported the thermoresponsive behavior of two stereogenic amphiphiles, *Z*-**8** and *E*-**8**, based on a tetraphenylethene core, that were isolated by HPLC. The isomer *Z*-**8** formed a vesicular morphology and its phase transition was easily visualized via an aggregation induced emission behavior. On the other hand, the isomer *E*-**8** formed micellar structures. Moreover, the amphiphile *Z*-**8** was found to uptake pyrene as guest molecules leading to a detectable change in its emission profile and resulted in a nanosheet like morphology (**Figure 3.4**).[23]
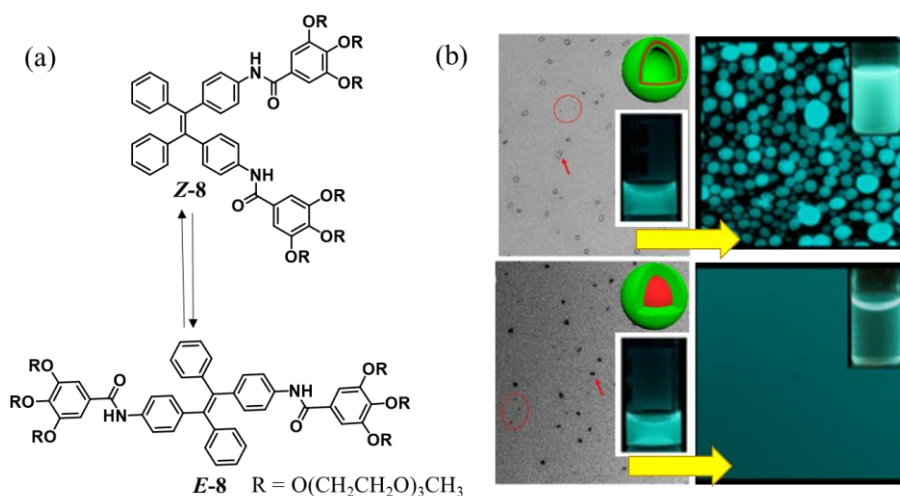
Figure 3.4. (a) Molecular structures of the amphiphilic isomers *Z*-**8** and *E*-**8** and **(b)** a schematic representation of their thermoresponsive LCST phase transition via the formation of particle and small micelle morphologies, respectively.

Current technologies for dynamic control of Solar Heat Gain (SHG) inside a built space via selectively allowing or blocking radiant heat requires high energy inputs. In addition, most of the available dynamic SHG control technologies are not cost-effective and hence have longer payback period preventing its large scale adoption in the building sector. Therefore, the development of low cost passive dynamic windows has gained much attention, as it offers the possibilities for easy integration into energy-efficient buildings with a considerably faster payback period.[24] In this context, LCST based materials possess huge potential due to their low cost of production, easy fabrication, and facile possibilities for integration into the existing glass-based building facades.[25]

In this context, Liu *et al.* have developed a passive dynamic system that switched its transparency, concomitant with a controlled transmission of solar radiation at temperatures near tropical temperature (32 ℃). Such dynamic systems are ideal for the design of energy efficient smart windows. Polymeric hydrogel micro particles with a defined hydrodynamic diameter ($H_D = 1388$ nm) at low temperature (25 ℃) allowed solar transmission. Upon increasing the temperature to 35 ℃, the particle size shrinked to 546 nm leading an opaque state and as a result, the windows were found to block >80% of the solar radiation (**Figure 3.5**).[26]
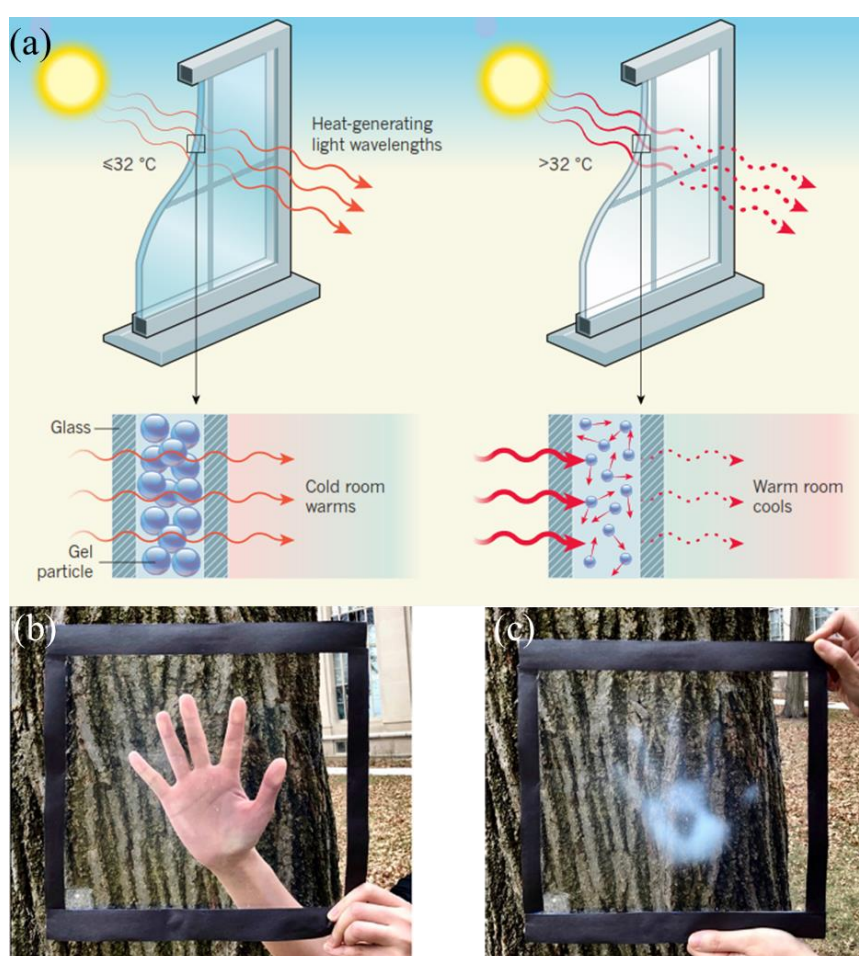
Figure 3.5. (a) An illustration of the control of solar light transmission via a temperature induced size distinction in thermoresponsive polymer microparticles. **(b,c)** The visual transition from transparent to opaque in the "palm-print" region, owing to the thermoresponsive nature of the polymer.

A smart window thermotropic composition by adjusting the LCST properties of *N*-isopropylacrylamide, *N,N*-methylenebis(acrylamide), ammonium persulfate and

N,N,N,N-tetramethylethylenediamine in water-glycol mixture for improving energy efficiency has been reported very recently. The LCST temperature was regulated by controlling the amount of glycol in deionized water.[27] A blend of two different polymer mixtures, poly-α-methylstyrene (PAMs) and polyvinyl methyl ether (PVMe) was also proposed as materials with a sharp temperature-dependent optical permeability.[28] A thermally programmable co-polymer system consisting of poly(*N*-isopropylacrylamide), poly(*N*-ethylacrylamide) or poly(*N,N*-dimethylacrylamide) was found to exhibit low temperature LCST behavior leading to a hydrophobic-to-hydrophilic transformation, wherein the acid-base properties of the system was found to be responsible for the phase change. The proposed application of this system involves the sequestration of gaseous CO_2.[29] Further, a smart window comprising of a thermo-responsive hydrogel that changed its transparency in response to temperature exposure via an LCST behavior has also been reported.[30]

Having mentioned that small molecules exhibiting LCST behavior are rarely found in scientific literature, molecules with inherent LCST behavior at ambient temperature, preferably in the range 25-30 °C, though they are of high demand for the development of smart windows, are even rarer. While several photoinduced processes have been exploited for tuning of LCST behavior,[31] photoinduced cycloadditions have never been considered for such property modulation. Therefore, we thought of exploring the potential of the classical Diels-Alder photocycloaddition to design new materials with intriguing properties. In Chapter 2, we have reported the selective [4 + 2] cycloaddition of a 9-phenylethynylanthracene derivative and its application in the construction of white OLEDs.[32] These studies prompted us to explore the potential of [4 + 2] photocycloaddition in other applications. To this end, we herein report the selective [4 + 2] photocycloaddition of an amphiphilic fluidic π–system **19** resulting in a bolaamphiphile **20** (**Scheme 3.1**), both exhibiting an LCST behavior within a temperature range of 20-35 °C. Liquid π–systems are an emerging class of soft materials for optoelectronic applications.[33] The amphiphilic molecule **19** with oligoethylene glycol (OEG)

chains exhibits an LCST behavior in a temperature range of 29-32 °C in water. This temperature depedent disparity in optical permeability is attributed to a dehydration assisted coil-globule transition. On the other hand, the [4 + 2] photocycloadduct **20**, which is a bolaamphiphile, exhibited LCST phase transition in 10% THF/water within a temperature range of 23-28 °C due to the formation of nano-to-micro sized spherical particles. Furthermore, we have exploited this LCST phase transition to fabricate smart windows by sandwiching their aqueous solutions between two parallel glass plates. Such an engineering using the amphiphile **19** could block >80% of solar transmission at temperatures above 32 °C, whereas below 29 °C, it allowed >92% visible light transmission. The use of the photoadduct **20** resulted in transparency below 24 °C and opacity above 27 °C. Such thermoresponsive behavior was found to be reversible over a number of cycles. As a proof-of-concept, we have further advanced the fabrication of dynamic windows by introducing a rotatable design that enabled us to achieve transparency even when the outdoor temperature was above its LCST.

3.3. Results and Discussion

3.3.1. Synthesis of Amphiphile 19 and Bolaamphiphile 20

We adopted a multistep synthetic strategy to synthesize the target molecule **19** as shown in **Scheme 3.1**.[34] The amphiphile **19** was synthesized by Sonogashira-Hagihara C-C coupling between 9-ethynylanthracene **17** and the amide **18** in THF/triethylamine mixture (1:1) using PdCl₂(PPh₃)₂/CuI as catalyst. The precursors **17** and **18** were synthesized using previously reported procedures.[34] All the intermediates and final compound were characterized by various spectroscopic and spectrometric analyses.
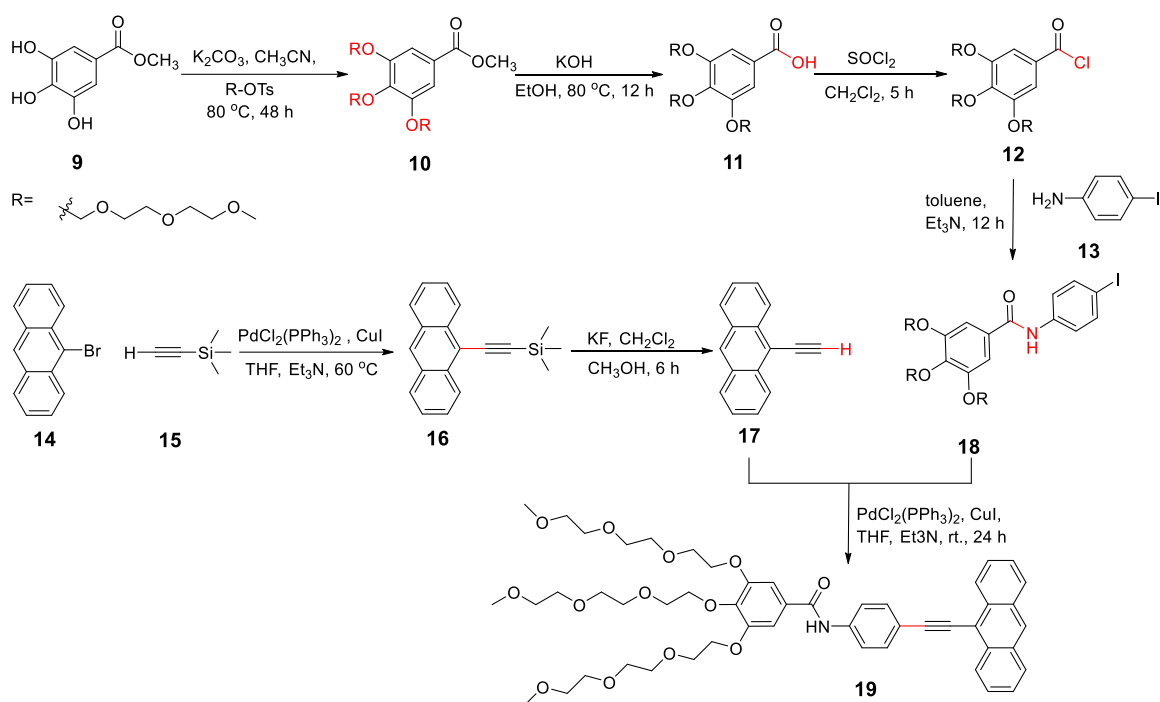
Scheme. 3.1. Synthesis of the amphiphile **19**.

The structure of compound **19** was elucidated by the analysis of its ^{1}H NMR spectrum (CDCl$_3$, 500 MHz, 25 °C) as shown in **Figure 3.6**. The amide proton, H$_h$ was found to resonate as a broad singlet at 8.80 ppm. Two of the anthracene protons, H$_b$ and H$_a$, appeared at 8.67 (doublet) and 8.43 (singlet) ppm, respectively. The H$_c$ H$_d$ and H$_e$ protons appeared respectively at 8.03 ppm (doublet), 7.77 ppm (doublet) and 8.02 ppm (doublet). The peaks corresponding to the phenyl protons (H$_g$, H$_f$) ortho to the triple bond were found to appear as two multiplets between 7.62 and 7.50 ppm. The phenyl protons H$_i$, belonging to the second benzene ring were found to have a chemical shift of 7.28 ppm and appeared as a singlet. The remaining glycol protons appeared as characteristic peaks resonating in the range 4.25-3.33 ppm. ^{13}C NMR spectrum was found to correlate well with the expected structure of compound **19**. HRMS further corroborated the existence of a chemical species corresponding to the expected structure of compound **19** (calcd. mass for the molecular formula of **19**: 883.4143, experimentally found: 884.4244 [M+H]$^+$, 906.4059 [M+Na]$^+$). The complete characterization data is provided in the experimental section.
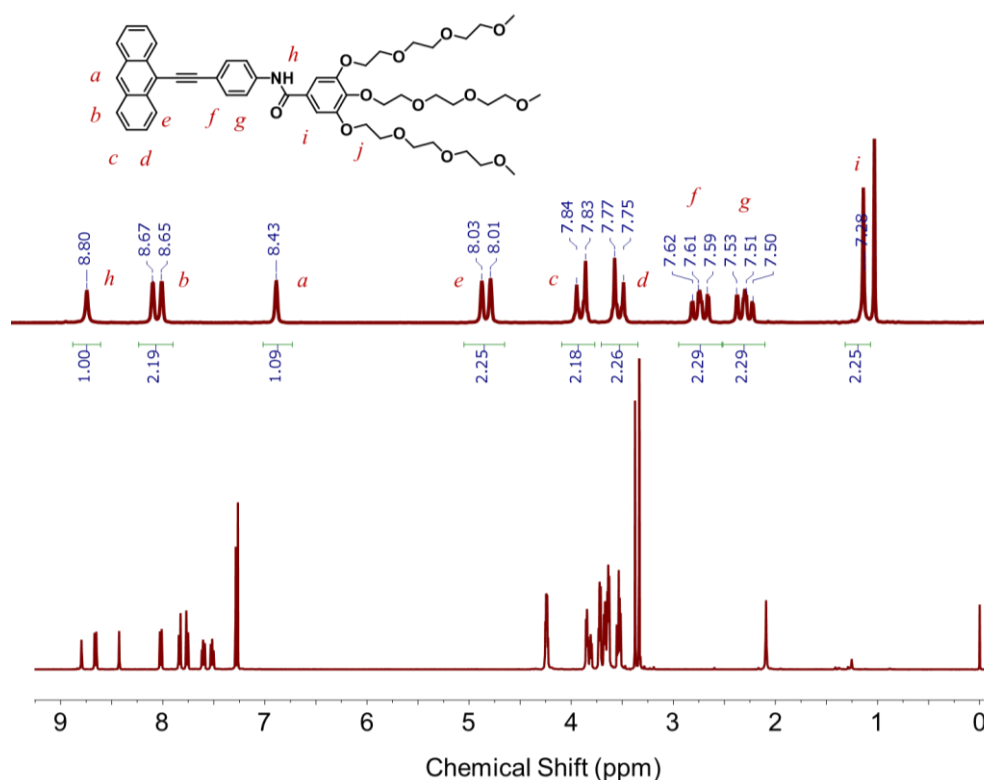
Figure 3.6. ¹H NMR spectrum in CDCl₃ (500 MHz, 25 °C) and the chemical structure of compound **19**. The protons are labelled in red (*a-i*). The middle panel shows the expanded region of the spectrum corresponding to the aromatic protons.

The amphiphile **19** was dissolved in oxygen free toluene in a quartz vessel and irradiated for 20 h with UV light (λ_{max} = 365 nm) to obtain the photoadduct **20** in 70% yield. (**Scheme 3.2**). Formation of the *anti*-[4 + 2] cycloaddition product was confirmed by ¹H NMR and NOESY spectroscopy. The ¹H NMR spectrum of **20** showed the appearance of a new peak at 5.74 ppm that was assigned to the dearomatized proton (red), that is spatially close (< 4.5 Å) to the proton indicated in green (**Figure 3.7**). MALDI-TOF analysis of the photoirradiated product **20** confirmed the existence of a chemical species of molecular mass 1789.48, that correlates to the corresponding [4 + 2] cycloadduct ([M+Na]⁺). Formation of the [4 + 2] adduct indicates that the bimolecular Diels-Alder reaction occurred between the C≡C bond (dienophile) of one molecule and the anthracene (diene) ring of another molecule.
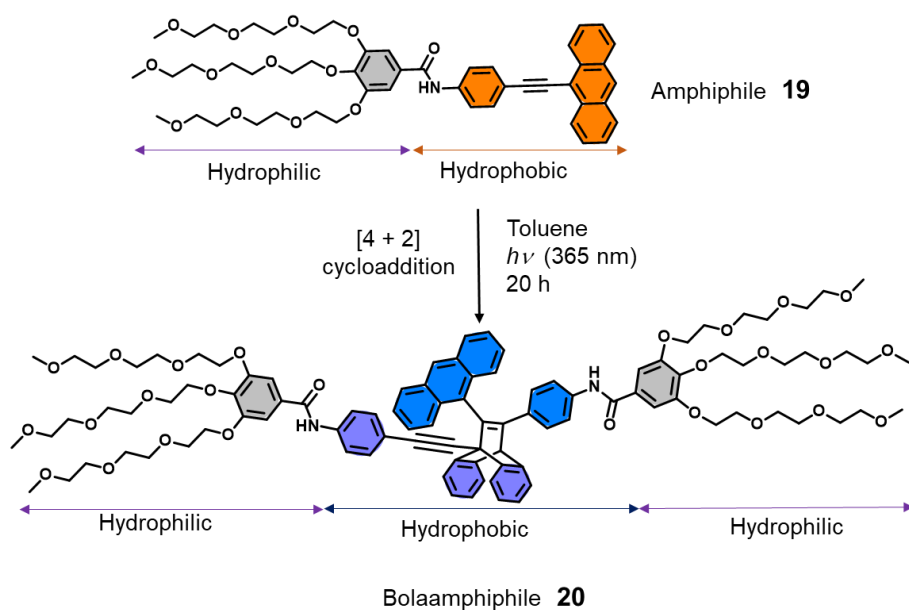
Scheme 3.2. Light induced conversion of the amphiphile **19** to the bolaamphiphile **20** via a bimolecular [4 + 2] Diels-Alder photocycloaddition.
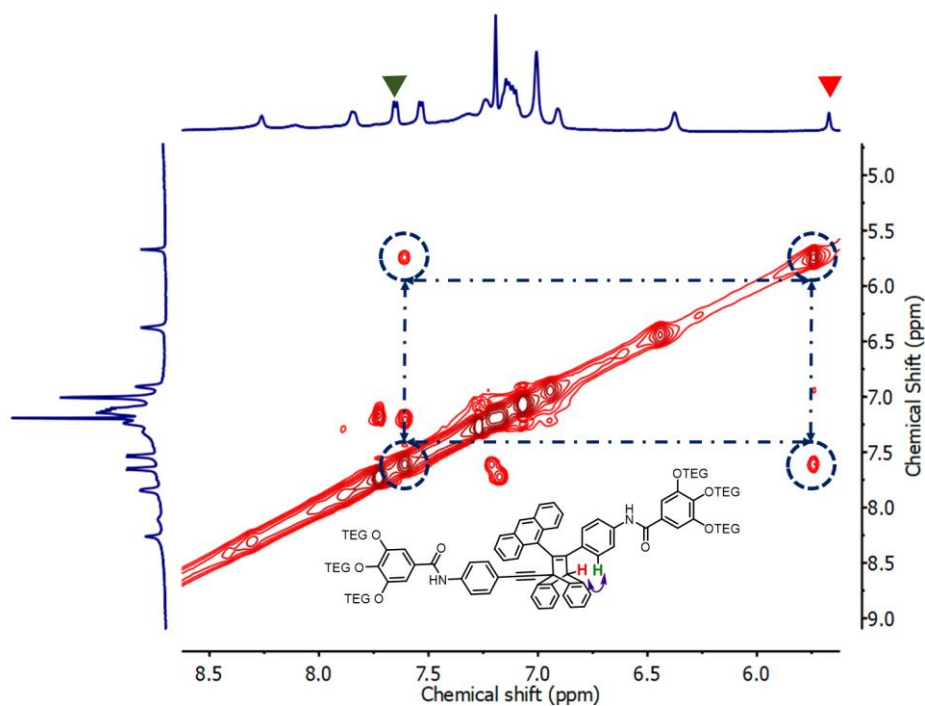
Figure 3.7. 2D NOESY spectrum of the bolaamphiphile **20** in CDCl₃, indicating special interactions between protons indicated in red and that indicated in green, confirming the formation of the *anti*-[4 + 2] cycloaddition product.

3.3.2. Thermal and Spectroscopic Characterization

In the solvent-free state, the amphiphile **19** and the bolamphiphile **20** were found to exist as sticky liquids (**Figure 3.8a**). Differential scanning calorimetry (DSC) thermogram showed a glass transition at 160 °C for the amphiphile **19** whereas that for the bolamphiphile **20** was found to be 159 °C (**Figure 3.8b**).
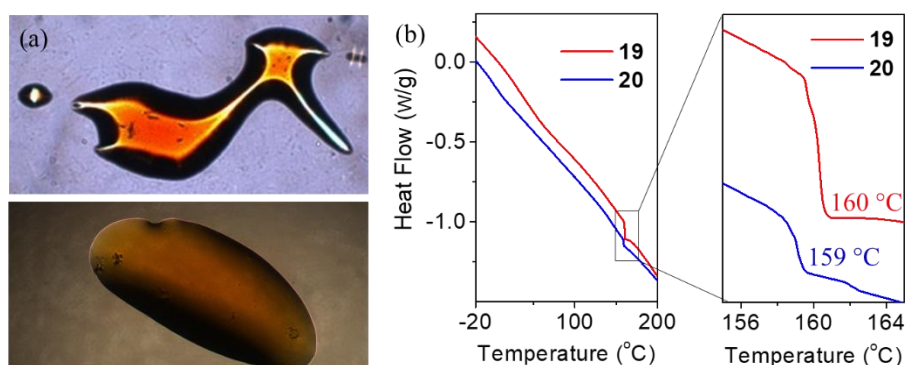
Figure 3.8. (a) Photographs of **19** (top) and **20** (bottom), exhibiting their solvent-free fluid states. **(b)** DSC thermograms showing the glass transition (Tg) of **19** at 160 °C (red) and **20** at 159 °C (blue). An expanded version of the DSC thermogram is shown on the right.

In THF, the absorption spectrum of compound **19** (c = 2.5 x 10^{-5} M) showed the characteristic vibronic structure of anthracene with absorption bands at 365, 387, 406 and 429 nm (**Figure 3.9a**). A hypsochromic shift of 34 nm (from 429 nm to 395 nm) was observed in the absorption spectrum of compound **20** (c = 2.5 x 10^{-5} M) in THF and was composed of its structural vibronic bands appeared similar to that of an isolated anthracene moiety 354, 374, and 395 nm (**Figure 3.9b**). The emission spectrum of compound **19** (c = 2.5 x 10^{-5} M) in THF showed peaks at 440, 464, 496 and 530 nm corresponding to the molecularly dissolved species (**Figure 3.9a**). The fluorescence spectrum of compound **20** (c = 2.5 x 10^{-5} M, THF) showed a broad peak with a maximum at λ = 439 nm (**Figure 3.9b**).
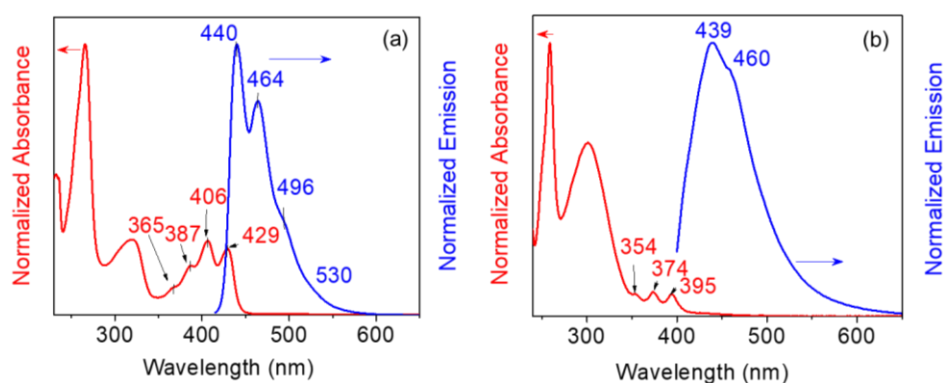
Figure 3.9. Normalized absorption (red) and emission (blue) spectra of **(a)** compound **19** and **(b)** compound **20** in THF (c = 2.5 x 10^{-5} M). The corresponding peak maxima (nm) are also marked.

3.3.3. LCST Phase Transition of the Amphiphile 19

While preparing the aqueous solutions of the amphiphile **19** and the bolaamphiphile **20** for photophysical studies, we observed a reversible, temperature dependent phase transition between transparent and opaque states. For instance, the transparent aqueous solution of **19** appeared as pale yellow, below 32 °C and became cloudy above 32 °C (**Figure 3.10a**). Realizing this behavior as an LCST phenomenon, we performed a detailed investigation of the phase changes occurring during this transparency switching. The thermoresponsive behavior of an aqueous solution of the amphiphile **19** (0.25 mM) was confirmed by the temperature dependent differences in scattering intensity at 500 nm (**Figure 3.10b**). The scattering intensity increased with increase in concentration and changes were predominant for a 5 mM solution at 30-32 °C. The heating and cooling curves showed a thermal hysteresis of 4.1 °C during the LCST phase transition process (**Figure 3.10c**) and was found to be reversible with no sign of fatigue over several cycles (**Figure 3.10d**).
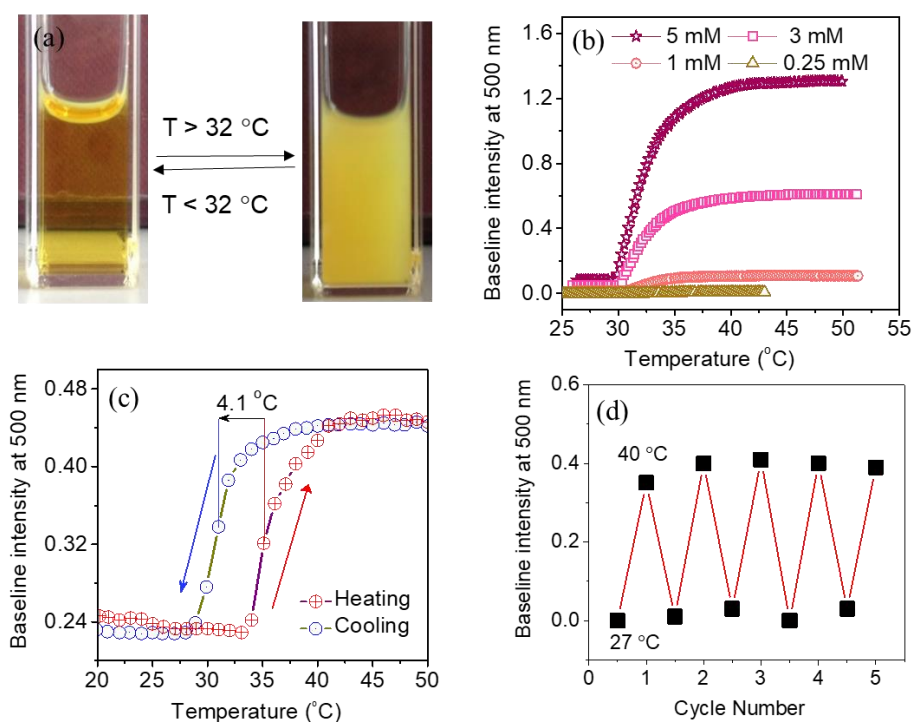
Figure 3.10. (a) Photographs showing the change in the physical appearance of an aqueous solution of compound **19** before and after phase transition at 32 °C (c = 5 x 10^{-3} M). **(b)** Scattering intensities showing the phase change of compound **19** as a function of temperature at various concentrations. **(c)** Scattering intensity during the heating and cooling cycles of an aqueous solution of compound **19** (c = 0.1 mM) showing the hysteresis and reversibility. **(d)** Change in scatteing intensity for multiple cycles between 27 °C and 40 °C (c = 1 x 10^{-4} M).

A gradual decrease in T_{cloud} point was observed with increase in concentration of the compound **19** in water (**Figure 3.11a**). Any point in the colored part of the plot of T_{cloud} *vs* concentration indicates the prevalence of a clear solution. Crossing the *tie* line at a constant concentration results in turbidity. The transmittance was found to decrease considerably in response to a slight change in temperature around T_{cloud}. DLS analysis of the aqueous solution of compound **19** below its LCST revealed the coexistance of very small (~10 nm) and large aggregates (~400 nm). Upon heating the solution to 40 °C, the average hydrodynamic diameter was increased to ~760 nm with an increased scattering intensity (**Figure 3.11b**).
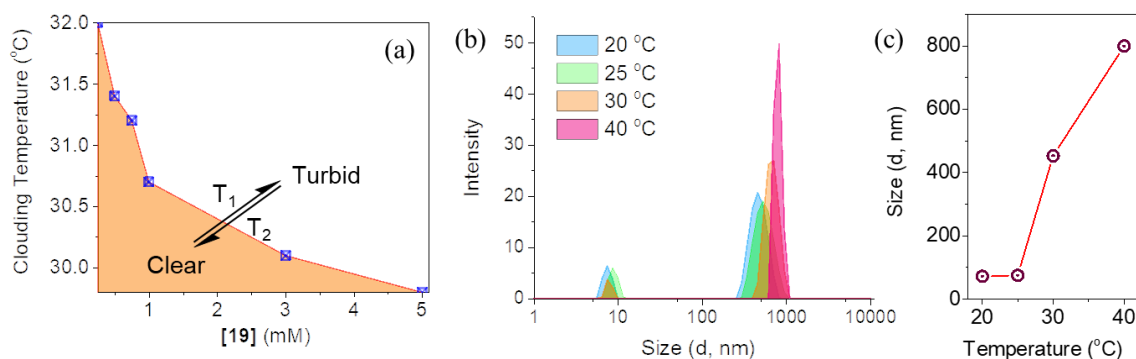
Figure 3.11. (a) Variation of the clouding temperature with concentration of compound **19** in water. **(b)** Variable temperature DLS measurement (intensity vs size, c = 1 mM) of an aqueous solution of compound **19** and **(c)** the corresponding plot of average particle size vs temperature.

3.3.4. LCST Phase Transitions of the Bolaamphiphile 20

The photochemical conversion of the amphiphile **19** to the bolaamphiphile **20** and the subsequent increase in the number of glycol chains influenced the assembly of the π–core, resulting in the modulation of its LCST. At a constant concentration of the compound **20** in water, the cloud formation was accelerated by the addition of a small percentage of THF (up to 10%). The opacity in 9:1 water-THF mixture was found to increase by twenty fold, as compared to that in water (**Figure 3.12a,b**). The light scattering intensity at 500 nm was found to increase with increase in concentration whereas the T_{cloud} was significantly reduced to 25 °C at a concentration of 100 μM (**Figure 3.12c**). Moreover, the bolaamphiphile **20** showed an LCST transition at relatively lower concentrations when compared to that of the amphiphile **19** and the T_{cloud} was found to be in the range of 23-28 °C, which is one of the lowest values reported for any LCST system. (**Figure 3.12d**). As observed for the parent compound **19**, a clear solution of compound **20** was found to exist at any point in the colored part of the plot of T_{cloud} *vs* concentration and turbidity emerged upon crossing the *tie* line at a constant concentration. The transmittance was also found to be highly sensitive to slight changes in temperature around T_{cloud}.
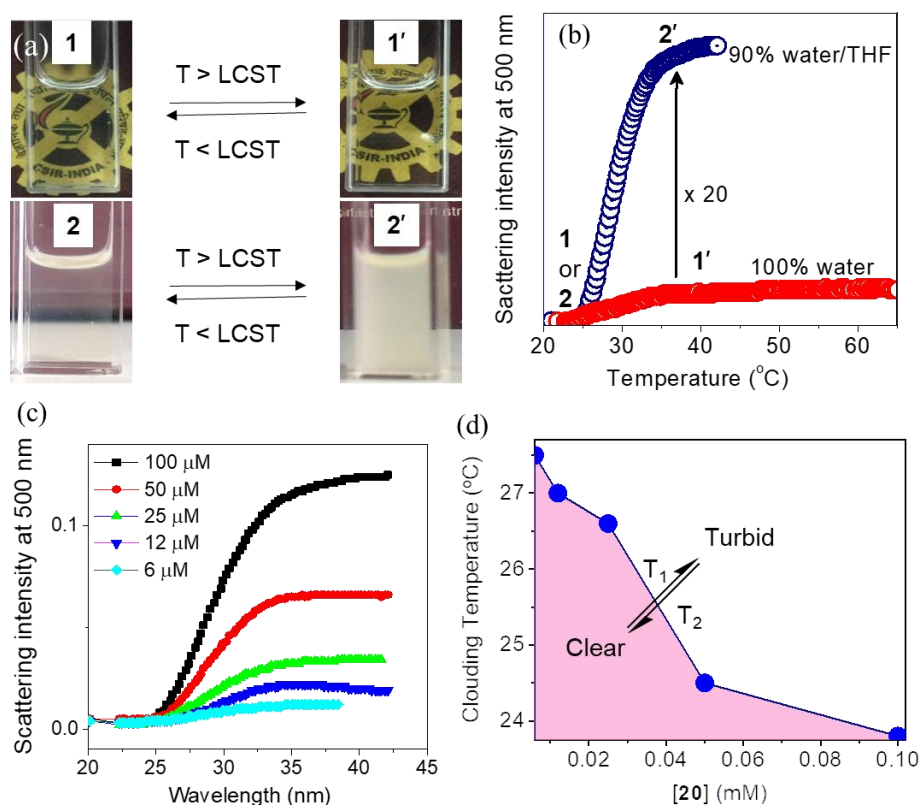
Figure 3.12. (a) Photographs showing the difference in phase transitions and opaqueness of a solution of compound **20** in water (bottom) and 10% THF-water (top). **(b)** Temperature dependent variations in scattering intensity (500 nm) for a solution of compound **20** in water (red) and 10% THF-water (blue). **(c)** Temperature dependent scattering intensity variations at 500 nm for a 10% THF-water solution of compound **20** at various concentrations (6-100 μM). **(d)** Variation of the clouding temperature with concentration of compound **20** in 10% THF-water.

Similar to the parent compound **19**, a thermal hysteresis was observed between heating and cooling cycles of the compound **20**, indicating the reversible behavior of the system. However, the hysteresis (2.53 °C) of the bolaamphiphile **20** was relatively narrow in comparison to that of the compound **19** (4.1 °C), which is indicative of a faster switching between the transparent and opaque states (**Figure 3.13a**). DLS measurements suggested a sudden increase in particle size above the T_{cloud} is most likely the reason behind turbidity. The particle size was found to increase by 141 fold at 30 °C (mean diameter, 848.5 nm) in a 10% THF-water mixture, when compared to that at 15 °C (mean diameter, 6 nm, **Figure 3.13b**).

However, in pure water, only ~8 fold increase in particle size was observed, corroborating an inefficient LCST transition.
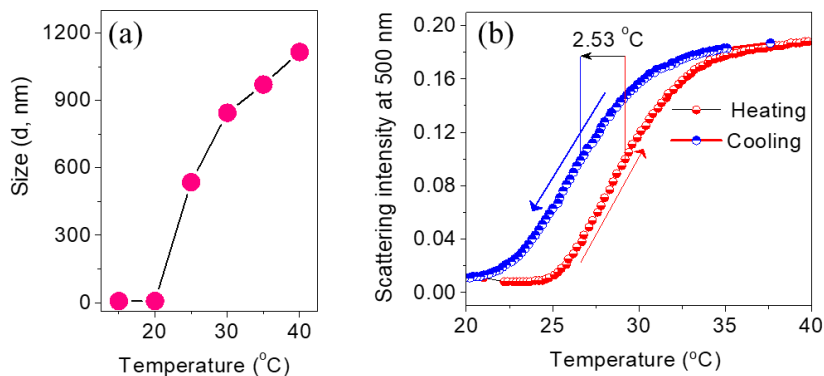
Figure 3.13. (a) Variable temperature DLS measurement showing the particle size variation in a 10% THF-water solution of compound **20**. **(b)** Heating and cooling cycles of a 10% THF-water solution of compound **20** showing the hysteresis and reversibility.

3.3.5. Structural Changes during LCST Transition

The LCST behavior of compound **19** is believed to originate from the spatial arrangement of the monomeric species leading to aggregation in water. The hydrophobic cores are most likely positioned away from the aqueous environment via π−π stacking, simultaneous with the exposure of the glycol chains to form strong H-bonds with water molecules. Thermally reversible perturbation of H-bonds between water molecules and glycol chains facilitate the hydrophobic part of the molecules to come closer and form globular structures leading to light scattering and opacity.[1,35] Below the cloud point (T_{cloud}), non-covalent interactions between the glycol chains of compound **19** and water molecules are predominant, whereas above the T_{cloud}, dehydration of glycol chains results in the creation of a hydrophobic pocket, leading to larger spherical aggregates. However, the morphological disparities during the LCST phase transition could not be imaged using microscopic techniques, since both the systems are fluidic in their solvent-free states. Therefore, we relied on dynamic light scattering (DLS) experiments to determine the size and structure of the supramolecular aggregates.[36] The correlation co-efficient decay time for an aqueous solution of compound **19** is longer at low temperature than that at

higher temperatures and was not found to be sigmoidal in nature (**Figure 3.14a**). This observation is indicative of the non-spherical nature of the molecular assembly below LCST, leading to the possible formation of fibril-like supramolecular aggregates at low temperature.[37] At 35 °C, the plot of the DLS correlation coefficient with time exhibited a sigmoidal decay, indicating that the aggregates transformed into larger spherical particles which was confirmed by particle size measurements via DLS (**Figure 3.11b,c**).
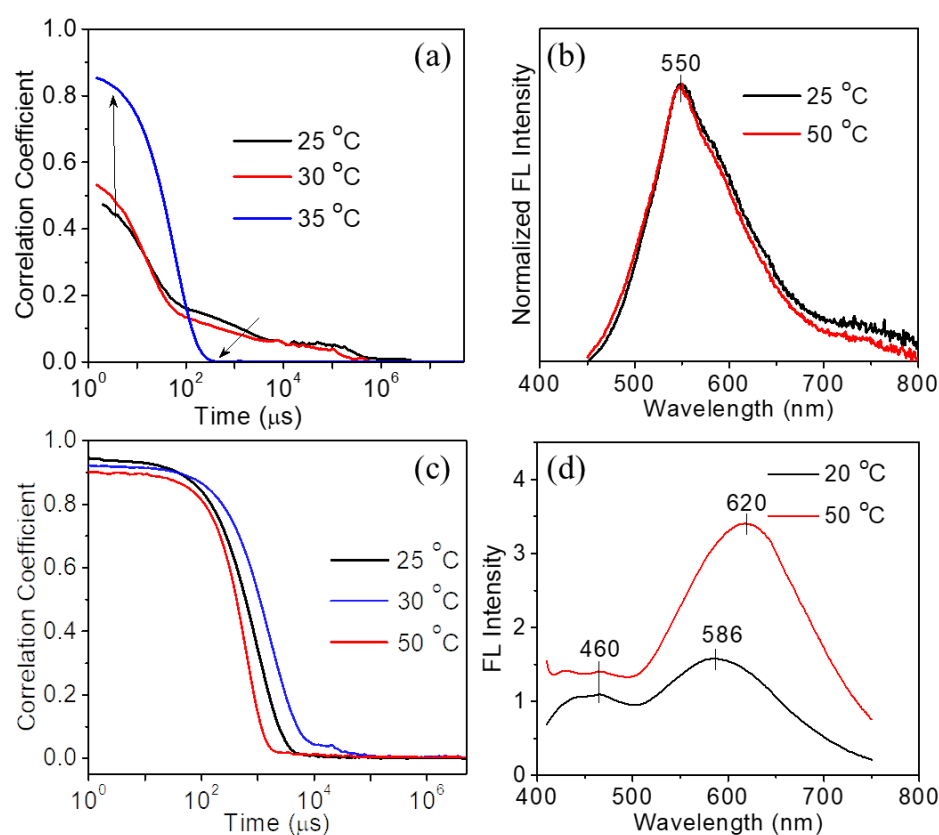
Figure 3.14. DLS correlation co-efficient decay profile with time for **(a)** the amphiphile 1**9** and **(c)** the bolaamphiphile **20**. The emission profiles (c = 1 x 10^{-4} M) of **(b)** **19** and **(d)** **20** above and below LCST. The experiments were performed using a water solution of compound **19** and a 10% THF-water solution of compound **20**.

On the other hand, a 10% water-THF solution of compound **20** exhibited a sigmoidal correlation co-efficient decay with time, irrespective of the temperature of the solution, indicating the presence of spherical particles below and above its LCST (**Figure 3.14c**). The observed dimension of the low-temperature aggregates (6 nm)

can be attributed to hydrated lower order aggregates comprising of a few molecules. Upon increasing the applied temperature, the smaller spherical aggregates grew into larger sphereical aggregates with a mean diameter of 848.5 nm at 30 °C (**Figure 3.13b**).

Emission spectra obtained below and above the LCST for an aqueous solution of compound **19** (c = 1 x 10^{-4} M) and 10% THF-water solution of compound **20** (c = 1 x 10^{-4} M) provided an indirect evidence for the nature of molecular aggregates present in the two phases. Below and above LCST, an aqueous solution of compound **20** (c = 2.5 x 10^{-5} M) exhibited a 225 fold decrease in the monomeric emission intensity (THF, c = 2.5 x 10^{-5} M) along with a bathochromic shift of λ_{max} to 550 nm due to molecular aggregation. The fluorescence life time decay profile confirmed that the emission at 550 nm originate from the excimer formation with a τ value of 13.42 ns and comparably low quantum yield (**Table 3.1**). At this point, it is worth mentioning that anthracene excimers are reported only in rare cases.[38] Above LCST, the solution did not exhibit any change in the emission profile corroborating the retention of the packing of the π−core before and after clouding (**Figure 3.14b**). On the other hand, the weak fluorescence spectra of compound **20** in 10% THF-water at 20 °C (below LCST) showed a broad excimer emission at 586 nm and at 50 °C (above LCST), with an increase in intensity with a bathochromic shift of 34 nm (**Figure 3.14d**).

Table.3.1 Emission properties, quantum yeild and fluorescence life-time decay profile of compound **19** in THF and water

Solvent	λ_{em} [nm]	Φ_f	τ_1 [ns]	A_1 [%]	τ_2 [ns]	A_2 [%]
THF	440	0.72	2.7	100	--	--
Water	550	0.038	3.9	41.77	13.42	58.23

The π−π interaction between the anthracene moieties in the self-assembled state of compound **19** was further confirmed by absorption band corresponds to ^1B_b

transition of anthracene core around 240-260 nm in THF and water. The absorption band of compound **19** was found to be broadened upon increasing the water content, whereas that of the bolaamphiphile **20** was not affected to a large extent (**Figure 3.15**).
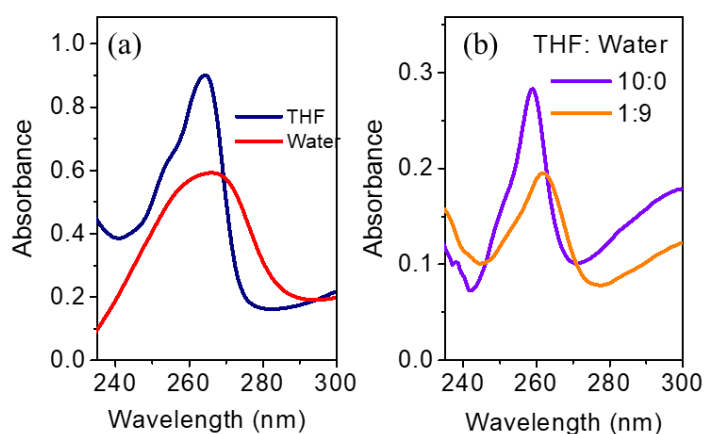
Figure 3.15. Comparison of the absorption profiles of **(a)** compound **19** in THF and water, and **(b)** compound **20** in THF:water in the range 230-300 nm.

Based on DLS and photophysical investigations, a plausible mechanism of the LCST phase transition of the amphilphile **19** and the bolaamphile **20** and the associated cloud formation is shown in **Figure 3.16**. In water, the amphiphile **19** formed aggregates in which the hydrophobic core was hidden and the hydrophilic side chains were exposed, resulting in fibrous assemblies below its LCST (**Figure 3.16a**, State I). However above its LCST, the fibrillar assemblies transformed into globular structures as a result of the dehydration of the fibrils without any major change in the overall molecular packing as evident from the fluorescence spectra (**Figure 3.16a**, State II). On the other hand, the bolaamhiphile **20** formed smaller aggregates in THF-water mixture below its LCST (**Figure 3.16b**, State I). Upon increasing the temperature above its LCST, the smaller aggregates coalesced to form large spherical aggregates as evident from the DLS analysis. As the particles grew in size, the local concentration and the tight packing of the chromophore increased leading to a corresponding increase in the intensity of the excimer emission with a concomitant red-shift (**Figure 3.16b**, State II).

113

(a)

$T > LCST_1$

$T < LCST_1$
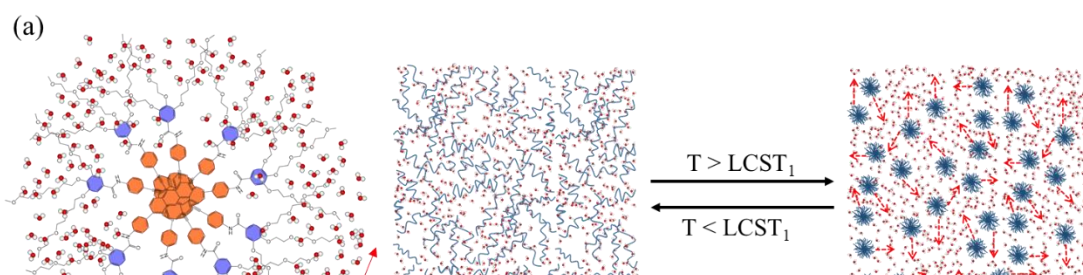
Figure 3.16. Schematic representation of a plausible mechanism for the LCST phase transition of **(a)** compound **19** in water due to the transformation of the hydrated fibrils to dehydrated globular assembly and **(b)** compound **20** in 10% THF-water, wherein the discrete hydrated molecules get transformed into larger spherical aggregates.

3.3.6. Modulated Transmittance of Solar Radiation

With an objective of developing energy efficient windows for dynamic modulation of heat and light transmission, we further obtained the visible, NIR and IR transmission profiles of the water solution of compound **19** and 10% THF-water solution of compound **20** in response to applied temperature. It was observed that the solutions of both compounds **19** and **20** were transparent in the whole range of interest (250-2500 nm) below their LCST temperature (**Figure 3.17**). Upon increase in temperature, the solutions gradually turned opaque and solar radiation was blocked. Such transitions were found to be reversible for a number of cycles. Careful manipulation of the controllable visible-NIR-IR profiles of such systems is expected to provide a strategy for energy efficiency in indoor environment via dynamic

modulation of heat and light transmission, wherein the temperature dependent transparency of window directly correlates to the amount of energy required for indoor lighting and maintaining indoor temperature.
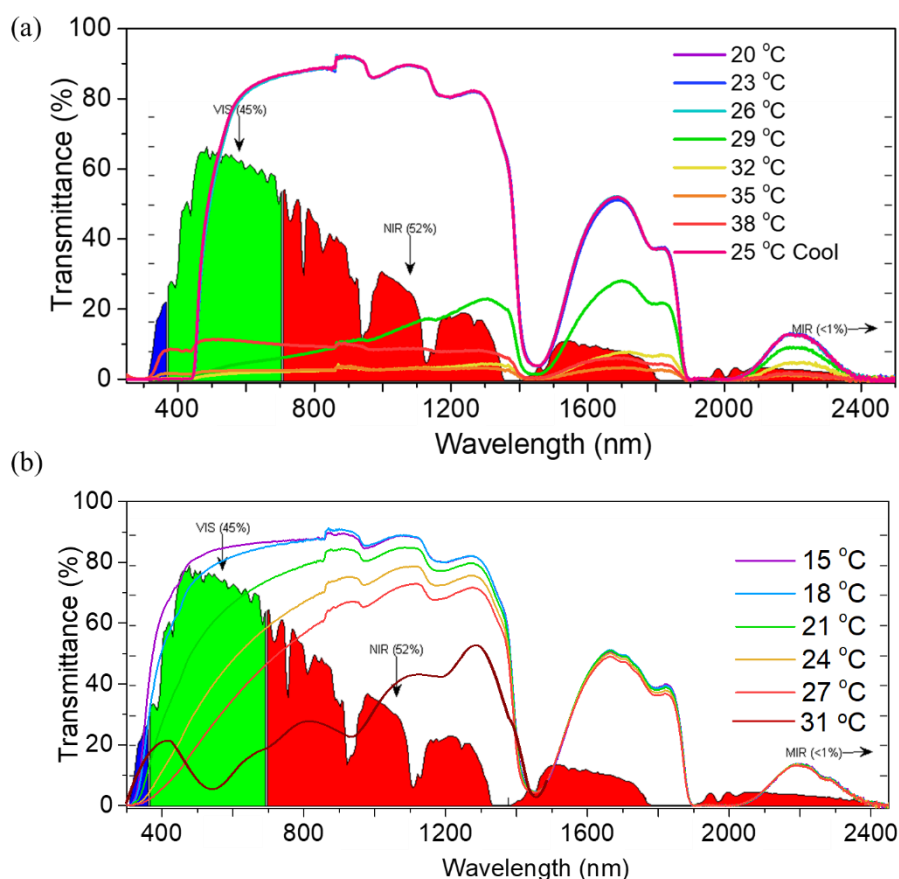
Figure 3.17. The modulation of solar light transmission in the temperature dependent states of **(a)** the amphiphile **19** in water and **(b)** the bolaamphiphile **20** in 10% THF-water mixture

3.3.7. Transmission Modulated Dynamic Window Prototypes and Thermal Imaging

As indicated in the previous sections, an aqueous solution of the amphiphile **19** was found to exhibit a reversible LCST behavior between 27 °C and 32 °C, a temperature range that is very attractive for regulated heat/light transmission. This observation motivated us to design and fabricate proof-of-concept smart window prototypes using an aqueous solution of molecule **19**. The solution was sandwiched between two parallel glass plates of size 10 cm × 10 cm and sealed. The fabricated dynamic

window rendered a transparent yellow color in the light transmission mode (T < 30 °C) and an opaque yellow shade above 30 °C with an almost complete blockage of light. This switching in opacity below and above the LCST was also readily observed in both indoor and outdoor conditions. For instance, with temperature below 27 °C inside an air-conditioned room, the prototype maintained its transparency and switched to the opaque state upon exposure to an outdoor temperature above 32 °C (**Figure 3.17**).
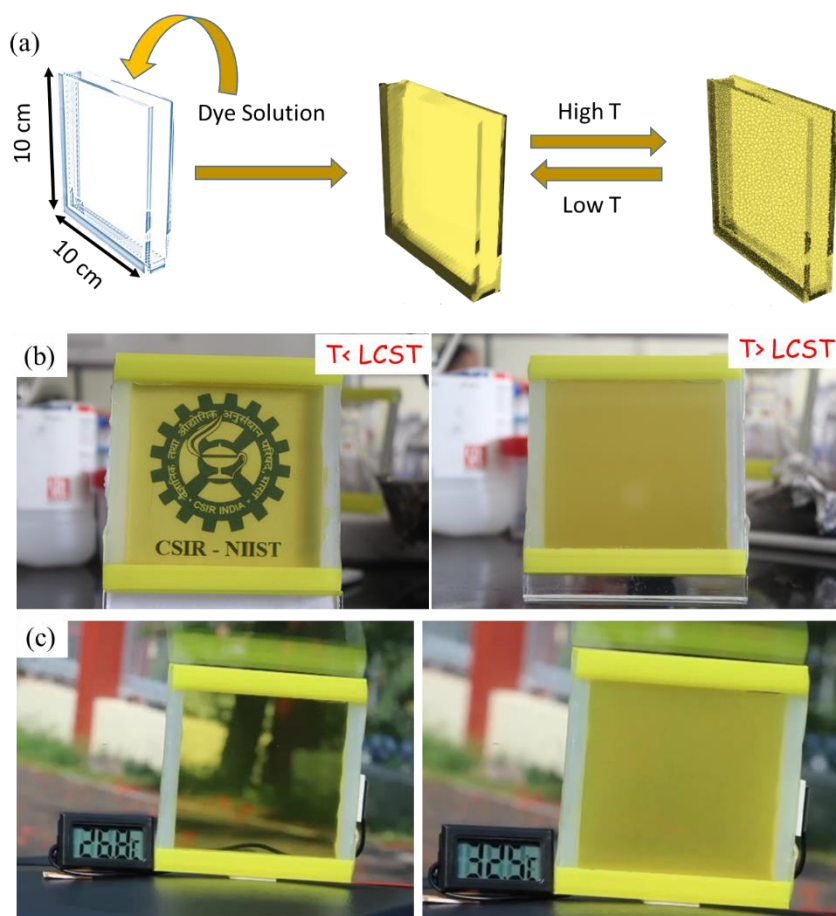
Figure 3.17. (a) The design principles behind the fabrication of smart windows using an aqueous solution of the amphiphile **19**. **(b)** An illustration of the stable switched states of the dynamic window (10 cm × 10 cm) at temperature < LCST (left), and temperature > LCST (right), and a 10 cm × 10 cm prototype showing **(c)** transparency at cold (26.8 °C, left) and opacity at hot (32.5 °C, right) temperatures.

Furthermore, facile color tunability can be rendered to the dynamic windows *via* the addition of water soluble dyes such as 'Methylene Blue' for green coloration and 'Rhodamine B' for red coloration at defined weight percentages, thereby adding to to the aesthetics of the installations. Interestingly, the addition of such water soluble dyes at a particular wt% did not alter the LCST phase transition and light/heat transmission behavior of the active compound. Such multi-component systems allow access to the generation of color tunable LCST switching of optical transparency (**Figure 3.18**).
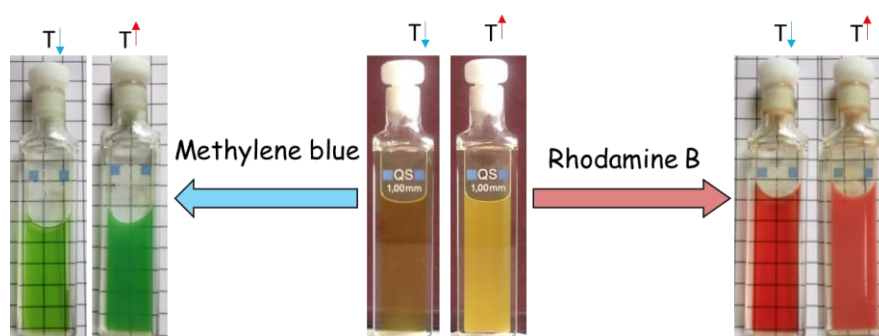
Figure 3.18. The color tunability of the thermoresponsive solutions of the compound **19** with the addition of water soluble dyes such as Methylene Blue for green (left) and Rhodamine B for red (right) opacity switching.

In order to investigate the surface temperature variations of the dynamic window prototypes during their LCST phase transitions, we mapped their temperature profiles via thermal imaging. During the transition from clear to opaque states, an increase in surface temperature was observed. The mapped surface temperatures were found to be comparable to the LCST temperature (**Figure 3.19**).

3.3.8. Rotatable Smart Windows

Depending upon the geographical location and seasonal variations, the energy demand to achieve a comfortable room temperature in response to heating/cooling will vary in the range of 25-32 °C. Hence, enabling active control for both radiative and conductive heat transfer is of utmost importance for reducing the heating/cooling energy demands. Energy efficiency in such environments can be

achieved via different approaches: (a) by reducing the conductive heat loss from indoor to outdoor and (b) by dynamic solar heat regulation. To minimize heat loss via conduction, insulating glass-based transparent windows/facades are currently preferred, as it renders visual comfort and meets the requirement for energy-efficient daylight modulation. However, the blockage of radiative heat transfer using insulating glass is challenging, and leads to an increased cooling energy load.
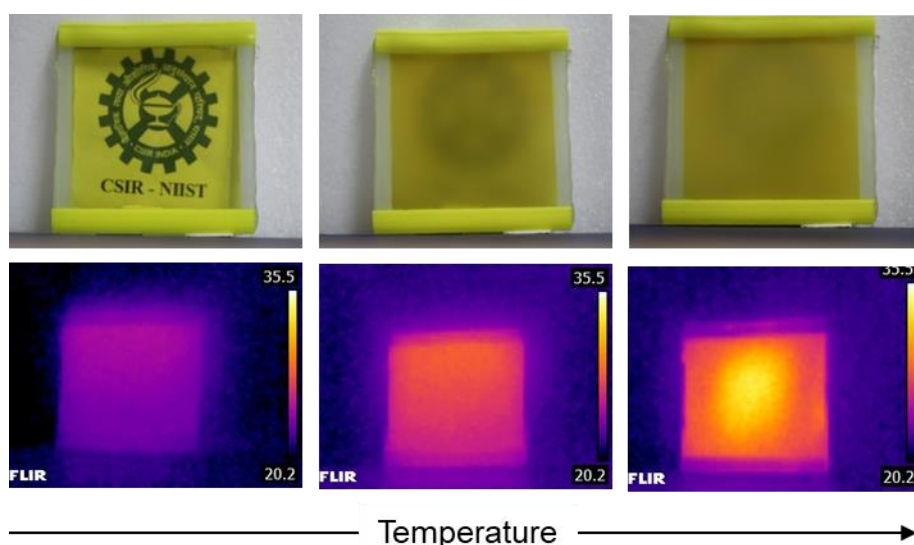
Figure 3.19. Visible images (top) and the corresponding thermal mapping (bottom) of a 10 cm × 10 cm dynamic window prototype fabricated from the aqueous solution of the amphiphile **19** at different stages of phase transitions (below LCST: left, above LCST: right, and an intermediate stage: middle). The direction of increase in temperature is represented by the arrow.

In order to achieve active energy management, we further designed a rotatable dynamic window that addresses the specific demands for visual comfort, daylight regulation, and radiative heating. The dynamic window prototypes fabricated from the aqueous solution of the molecule **19** using a simple sandwich-type architecture did not allow for transparency above its LCST temperature (>30 °C). However, the rotatable design provided the opportunity to have a transparent window even though the outdoor temperature was > 30 °C with a simultaneous blocking of conductive heat flow from outdoor to indoor. Depending on the requirement, the user can rotate the window 180° vertically/horizontally to switch the transparency. The rotatable window consists of four parallel glass panels, designed in such a way that one of the

118

two chambers bordered by these 4 glass panels is filled with the thermoresponsive aqueous solution, and other one is air filled and sealed. In order to achieve transparency when the indoor temperature is below the LCST and outdoor temperature is above the LCST of the compound **19**, the window was rotated such that the chamber filled with the thermoresponsive aqueous solution faced indoors. The air-gap in the design offered thermal insulation from the outside environment, thereby preventing conductive heat transfer and at the same time allowing visible light transmission through the window (**Figure 3.20a**). To block the radiative heat from outdoors, the window may be rotated 180º, resulting in the exposure of the thermoresponsive solution to the outdoor temperature, which is above the LCST temperature, triggering a transparent to opaque transition, thereby blocking the transmission of solar radiation. (**Figure 3.20b**). The indoor temperature under both the aforesaid conditions remained constant, irrespective of the outdoor temperature, as evident from the thermal mapping. Thus, by adopting a rotatable smart window design, indoor energy efficiency can be achieved *via* the active modulation of heat and light transmission. The temperature-dependent switching of the dynamic window effectively manages the energy demands for indoor lighting and maintaining indoor temperature as well as enable need based privacy, simultaneous with added aesthetics of the architecture.

3.4. Conclusion

In conclusion, a fluidic π−system comprising of an anthracene moiety coupled with self-assembling motifs via a triple bond upon photoirradiation in toluene resulted in [4 + 2] cycloaddition, facilitating an amphiphile-to-bolaamphiphile transition. The starting amphiphile and the final bolaamphiphile (cycloadduct) showed distinct LCST phase transitions within ambient temperatures and excellent thermal reversibility. However, for the bolaamphiphile, small amount of a co-solvent (10% THF in water) was required to achieve optimum LCST phase transitions. The amphiphile showed LCST phase transition due to a fibril-to-globule transformation between its hydrated and dehydrated states.[39] However, in the case of the

bolaamphiphile, turbidity arose via the growth of initially formed small aggregates to higher order spherical particles. Further, the amphiphile was used in the development of dynamic window prototypes, that could effectively block solar transmittance and ensure need based privacy upon demand. We believe that the developments made in this study will contribute to the design of novel stimuli-responsive materials with controlled light transmission, particularly useful for dynamic windows leading to efficient energy management and utilization.
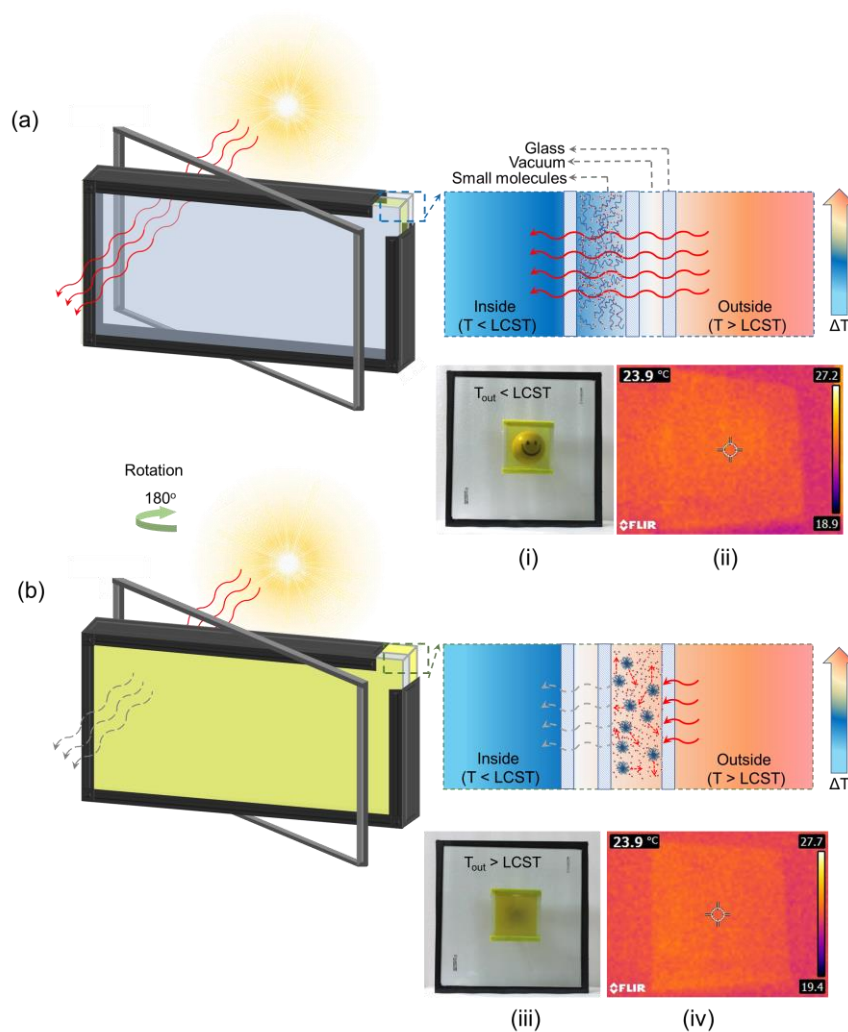
Figure 3.20. (a,b) Schematic representation (left) of rotatable insulating window design for active switching of light and heat transmittance. Corresponding visible and thermal images of the window before (i,ii) and after (iii,iv) LCST phase transitions are provided in the right panels. The surface temperatures indicated in the thermal images represent the indoor temperature, that remained constant even when the outside temperature is greater than LCST.

3.5. Experimental Section

3.5.1. Materials and Methods

Differential Scanning Calorimetry (DSC): DSC analyses were carried out with a TA analysis instrument at a temperature range of -60 ℃ to 300 ℃ under N_2 atmosphere and at atmospheric pressure.

Dynamic Light Scattering (DLS): DLS analyses were carried out with a Zetasizer Nano S from Malvern Instruments at 25℃. 10^{-3} M solutions of the compound **19** in water and **20** in 10% THF-water were prepared. The sample was injected and the readings were taken at an interval of 10 min. for one hour. The average hydrodynamic radii was calculated from Stork-Einstein equation ($R_H = k_B T/(6\pi\eta D)$). 'D' is translational diffusion coefficient [m²/s]. k_B = Boltzmann constant [m²kg/Ks²], T = Temperature [K], η = viscosity [Pa.s], R_H = Hydrodynamic radius [m]. All solutions used for detecting hydrodynamic diameter by DLS were passed through Millipore filters with a pore size of 0.22 μm to remove any dust particles.

Preparation of LCST Solutions: Compound **19** in the required concentration was added to Millipore filtered water purched with nitrogen for 10-15 min. The solution was then kept in cold water bath (<20 ℃) and gently shaken to ensure homogeniety. The solution was sealed and kept at a temperature < 22 ℃. Similar experimental procedure was used for the molecule **20**, but using a 10% THF-water mixture.

Preparation of 10 cm × 10 cm Glass Window Prototypes: The set-up consists of two glass plates, each of size 10 cm × 10 cm and thickness of 2.8 mm. The glass plates were sealed with an internal spacing of 1 mm, using a UV-epoxy resin. An aqueous solution of **19** (18 mL, 22 mM) was injected into the system and was sealed further to obtain the window prototypes.

Development of Rotatable Smart Windows: The rotatable smart window was fabricated by stiching the previously mentioned 100 cm^2 prototypes to a sealed insulating glass unit (IGU) having an air gap (12 cm × 12 cm × 6 mm, **Figure 3.21**). The assembled window structure was attached to a wooden box with a horizontally rotable screw. The wooden box was sealed from every side to restrict any heat leakage. The temperature inside the wooden chamber was maintained at 22-24 °C.
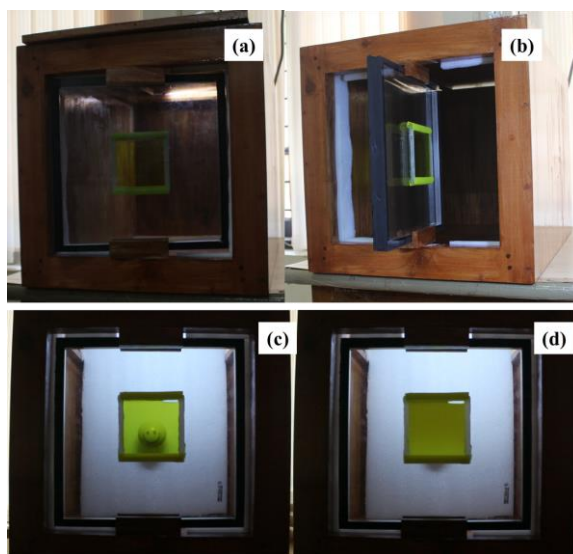
Figure 3.21. Rotatable smart window in (**a,b**) closed and open state, respectively. (**c**) Image of a clear state when the solution containing glass panel projected inside the wooden box. (**d**) Image of the an opaque state when the the solution containing panel was projected outside. As the temperature outside was higher than the LCST, opacity resulted on blocking the visibility.

3.5.2. Synthesis and Characterization

Synthesis of the Amphiphile 19

The aryl halide **18** (1.94 g, 0.80 mmol), bis(triphenylphosphine)palladium (II) dichloride (115 mg, 10 mol%), and copper (I) iodide (90 mg, 10 mol%) were added to an oven-dried two-neck round bottom flask equipped with a magnetic stirring bar. The round bottom flask was then sealed with a rubber septum, evacuated and filled with argon three times. Degassed triethylamine (10 mL) was added followed by degassed THF (10 mL). After stirring for 5 min. at room temperature, 9-ethynylanthracene **17** (0.405 g, 0.96 mmol) dissolved in degassed

trimethylamine/THF (10 mL, 1:1 v/v) was added and the reaction mixture was stirred at room temperature until the completion of the reaction was confirmed by TLC. The reaction mixture was then extracted using chloroform and was washed with dilute hydrochloric acid. The combined organic extracts was washed with brine, dried over anhydrous sodium sulphate and evaporated under reduced pressure. The crude product was then purified by column chromatography on silica gel (120 mesh) using chloroform/methanol (95:5) as eluent. Yield: 69%

^{1}H NMR (500 MHz, CDCl$_3$): δ = 8.80 (s, 1H), 8.67 (d, J = 9.5 Hz, 2H), 8.43 (s, 1H), 8.02 (d, J = 8.5 Hz, 2H), 7.84 (d, J = 8.5 Hz, 2H), 7.77 (d, J = 9 Hz, 2H), 7.62-7.59 (m, 2H), 7.53-7.50 (m, 2H), 7.28 (d, J = 14.5 Hz, 2H), 4.24-4.22 (m, 6H), 3.87-3.80 (m, 6H), 3.73-3.71 (m, 6H), 3.67-3.63 (m, 12H), 3.55-3.52 (m, 6H), 3.36 (s, 3H), 3.33 (s, 6H) ppm.

^{13}C NMR (125 MHz, CDCl$_3$): δ = 165.51, 152.50, 142.13, 138.86, 134.16, 132.55, 132.37, 131.23, 129.92, 128.71, 127.54, 127.25, 126.82, 126.58, 125.71, 120.21, 119.07, 117.46, 108.16, 100.83, 85.98, 77.29, 77.04, 76.79, 72.41, 71.95, 71.90, 70.67, 70.58, 70.52, 70.41, 69.88, 69.26, 59.03, 58.97 ppm.

HRMS: calcd. for C$_{50}$H$_{61}$NO$_{13}$ 883.4100, found: 884.4244 [M+H]$^+$, 906.4059 [M+Na]$^+$

Synthesis of the Bolaamphiphile 20

Compound **19** (15.0 mg, 16.9 mmol) was dissolved in oxygen free toluene (3 mL) in a quartz cuvette and irradiated for 20 h with UV light (365 nm). The crude mixture was then purified on silica-gel using chloroform:methanol (95:5) as eluent. Yield = 10.8 mg, 70%.

^{1}H NMR (500 MHz, CDCl$_3$): δ = 8.69 (s, 1H), 8.49 (d, J = 8.6 Hz, 2H), 8.31 (d, J = 8.2 Hz, 2H), 7.73 (d , J = 8.5 Hz, 4H), 7.62 (d, J = 5 Hz, 2H), 7.48-7.43 (m, 4H),

7.27 (s, 2H), 7.23-7.15 (m, 5H), 7.02 (s, 1H), 6.94 (s, 1H), 6.44 (br s, 2H), 5.74 (s, 1H) 4.16-4.04 (m, 12H), 3.76-3.48 (m, 48H), 3.41-3.21 (m, 18H) ppm.

^{13}C-NMR (125 Hz, CDCl$_3$): δ = 165.39, 152.42, 152.32, 148.42, 145.40, 144.73, 143.97, 131.95, 131.39, 130.56, 128.38, 126.83, 125.57, 125.25, 125.14, 125.02, 122.73, 107.60, 91.06, 84.26, 70.64, 59.05, 58.95, 58.89, 58.36, 56.26, 29.67 ppm.

MALDI-TOF: calcd. for C$_{100}$H$_{122}$N$_2$O$_{26}$ 1766.83 found: 1789.48 [M+Na]$^+$

3.6. References

(1) de la Rosa, V.; Woisel, P.; Hoogenboom R. *Materials Today* **2016**, *19*, 44-55.

(2) Kanaoka, S.; Yagi, N.; Fukuyama, Y.; Aoshima, S.; Tsunoyama, H.; Tsukuda, T.; Sakurai, H. *J. Am. Chem. Soc*. **2007**, *129*, 12060.

(3) Bergbreiter, D. E.; Case, B. L.; Liu, Y.-S.; Caraway, *J. W. Macromolecules,* **1998**, *31*, 6053.

(4) Kabanov, A. V.; Vinogradov, S. V. *Angew. Chem., Int. Ed*. **2009**, *48*, 5418.

(5) Yamaguchi, T.; Ito, T.; Sato, T.; Shinbo, T.; Nakao, S.-i. *J. Am. Chem. Soc.* **1999**, *121*, 4078.

(6) Uchiyama, S.; Kawai, N.; Prasanna de Silva, A.; Iwai, K. *J. Am. Chem. Soc.* **2004**, *126*, 3032.

(7) Pasparakis, G.; Cockayne, A.; Alexander, C. *J. Am. Chem. Soc*. **2007**, *129*, 11014.

(8) Ionov, L.; Diez, S. *J. Am. Chem. Soc*. **2009**, *131*, 13315.

(9) Koopmans, C.; Ritter, H. *J. Am. Chem. Soc*. **2007**, *129*, 3502.

(10) Ono, Y.; Shikata, T. *J. Am. Chem. Soc*. **2006**, *128*, 10030.

(11) Lutz, J.-F.; Akdemir, Ö.; Hoth, A. *J. Am. Chem. Soc*. **2006**, *128*, 13046.

(12) Schild H. G. *Polym. Sci*. **1992**, *17*, 163.

(13) Burkhart, A.; Ritter, H. *Beilstein J. Org. Chem*. **2014**, *10*, 1951

(14) Yao, X.; Wang, X.; Tao Jiang, T.; Xiang Ma, X.; Tian, H.; *Langmuir*, **2015**, *51*, 13647.

(15) Richards, G.J.; Labuta, J.; Hill, J. P.; Mori, T.; Ariga, K.; *J. Phys. Chem. Lett.*, **2010**, *1*, 1336.

(16) Aathimanikandan, S. V.; Savariar, E. N.; Thayumanavan S. *J. Am. Chem. Soc.*, **2005**, *127*, 14922.

(17) Fuller, J. M.; Raghupathi, K. R.; Ramireddy, R. R.; Subrahmanyam, A. V.; Yesilyurt, V.; Thayumanavan, S. *J. Am. Chem. Soc.* **2013**, *135*, 8947.

(18) Lee, S.; Lee, J.-S.; Lee, C. H.; Jung, Y.-S.; Kim, J.-M. *Langmuir* **2011**, *27*, 1560.

(19) Hirose, T.; Matsuda, K.; Irie, M. *J. Org. Chem.* **2006**, *71*, 7499.

(20) Betancourt, J. E.; Rivera, J. M.. *J. Am. Chem. Soc.* **2009**, *131*, 16666.

(21) Ogoshi, T.; Kida, K.; Yamagishi, T.-a. *J. Am. Chem. Soc.* **2012**, *134*, 20146.

(22) Wei, P.; Cook, T. R.; Yan, X.; Huang, F.; Stang, P. J. *J. Am. Chem. Soc.* **2014**, *136*, 15497.

(23) Peng, H.-Q.; Liu, B.; Wei, P.; Zhang, P.; Zhang, H.; Zhang, J.; Li, K.; Li, Y.; Cheng, Y.; Lam, J. W. Y.; Zhang, W.; Lee, C.-S.; Tang, B. Z. *ACS Nano*, **2019**, *13*, 839.

(24) Baetens, R.; Jelle, B. P. ; Gustavan, A. *Sol. Energy Mater. Sol. Cells,* **2019**, *94*, 87–105.

(25) Serpe, M. J. *Nature*, **2019**, *565*, 438.

(26) Li, X.-H.; Liu, C.; Feng, S.-P.; Fang, N. X.; *Joule*, **2019**, *3*, 290.

(27) Lee, *et al.* Thermotrophic composition for smart window for controlling phase transition temperature Repub. Korean Kongkae Taeho Kongbo, KR 2019060304A, **2019**.

(28) Siol *et al.*, Polymer Mixtures with Lower Critical Solution Temperature (LCST) Behavior, US 5430104 A, **1995**

(29) van Gough, *et al.* Programmable pH Buffers, US 9550168 B2, **2017**.

(30) Smart Window Comprising Temperature-Sensitive Hydrogel Containing Photothermal Conversion Material and Method for Manufacturing the Same, WO 2015130012 Al, **2015**.

(31) (a) Plamper, F. A.; Schmalz, A.; Ballauff, M.; Muller, A. H. E. *J. Am. Chem. Soc.* **2007**, *129*, 14538. (b) Ogoshi, T. Kida, K. Yamagishi, T.-a. *J. Am. Chem. Soc.* **2012***, 134,* 20146.

(32) Das, S.; Okamura, N.; Yagi, S.; Ajayaghosh, A. *J. Am. Chem. Soc.* **2019**, *141*, 5635.

(33) Ghosh, A.; Nakanishi, T. *Chem. Commun.* **2017**, *53*, 10344.

(34) Thirumalai, R.; Mukhopadhyay, R.; Praveen, V.; Ajayaghosh, A. *Sci. Rep.*, **2015**, 9842.

(35) Li, S.; Liu, K.; Kuang, G.; Masuda, T.; Zhang, A. *Macromolecules* **2014**, *47*, 3288.

(36) Korevaar, P. A.; Newcomb, C. J.; Meijer, E. W.; Stupp, S. I. *J. Am. Chem. Soc.* **2014**, *136*, 8540.

(37) Kiyonaka, S.; Sugiyasu, K.; Shinkai, S.; Hamachi I. *J. Am. Chem. Soc.* **2002**, *124*, 10954.

(38) (a) Moore, G. F. *Nature* **1966**, *212*, 1452–1453. (b) Sagara Y. Kato T. *Angew. Chem. Int Ed.* **2011**, *123*, 9294.

(39) Heyda, J.; Muzdalo, A.; Dzubiella J. *Macromolecules* **2013**, *46*, 1231.

Thermally Assisted Supramolecular Film Formation within a Monophasic Solvent Medium
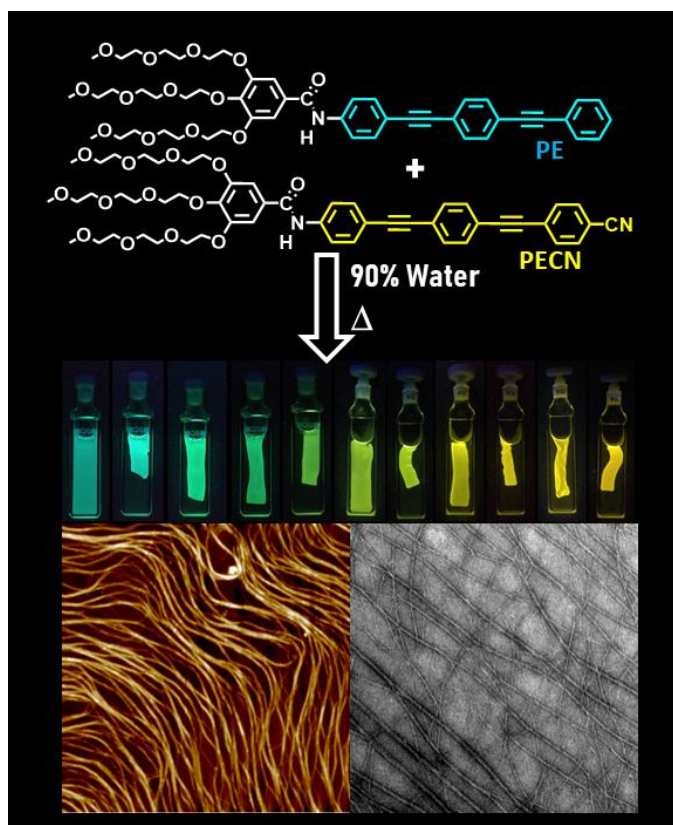
4.1. Abstract

Despite decades of intense investigations, feasible strategies towards the creation of free-standing organic films are confined to solvent evaporation or chemical or physical processes at interfaces. Formation of an organic film within a single phase solvent medium is hard to achieve and still remains elusive. Herein, we exploited a thermoresponsive supramolecular co-polymerization approach to achieve film formation in an aqueous medium comprising of a completely miscible monophasic water/THF mixture. By thermally manipulating solvent-molecule interactions via changes in amphiphilicity and dipole-dipole interactions, the supramolecular co-assembly of oligo(phenyleneethynylene) amphiphiles resulted in free-standing films

in (9:1 Water-THF), mediated by a coalescence process. Morphological investigations suggested that the films were composed of 1D tubular networks. Thermally assisted ejection of water molecules from the initially formed molecular assembly leads to the formation of cross-linked tubular fibers, resulting in the formation of free-standing films. This could be a rare example of an entropy-driven supramolecular co-polymerization of a two-component π-system leading to the formation of free-standing macroscopic organic films with variable emission profiles.

4.2. Introduction

Crystallization is fundamentally a dynamic self-assembly process, where the self-assembling molecules/atoms periodically extend over a long range in a controlled manner within a solvent medium.[1] Engineering of the crystallization processes have been primarily focussed on obtaining a thermodynamically stable structure under controlled environmental conditions.[2-3] The process is mainly governed by the interfacial chemical potential of the crystal and liquid interface.[4] There has been a long-standing curiosity to realize crystallization under non-equilibrium conditions in a monophasic medium. Understanding the nucleation and growth mechanism leading to crystal formation has recently been of prime significance.[5] Lee and co-workers have investigated the complicated process of crystallization of a simple salt, (KH_2PO_4).[6,7] It was observed that high concentration of KH_2PO_4 initially resulted in a metastable crystal before reaching its thermodynamically stable crystal at room temperature. However, a less concentrated solution resulted in different localized structures, which directly transformed into the stable crystalline phase (**Figure 4.1**).

On the other hand, studies on the kinetic aspects of crystal growth of metal-organic frameworks and other self-assembled structures have gained momentous attention in recent years.[8] For instance, Maspoch and co-workers have investigated in detail, the non-classical crystal growth process involving MOFs in microfluidic devices (**Figure 4.2a**).
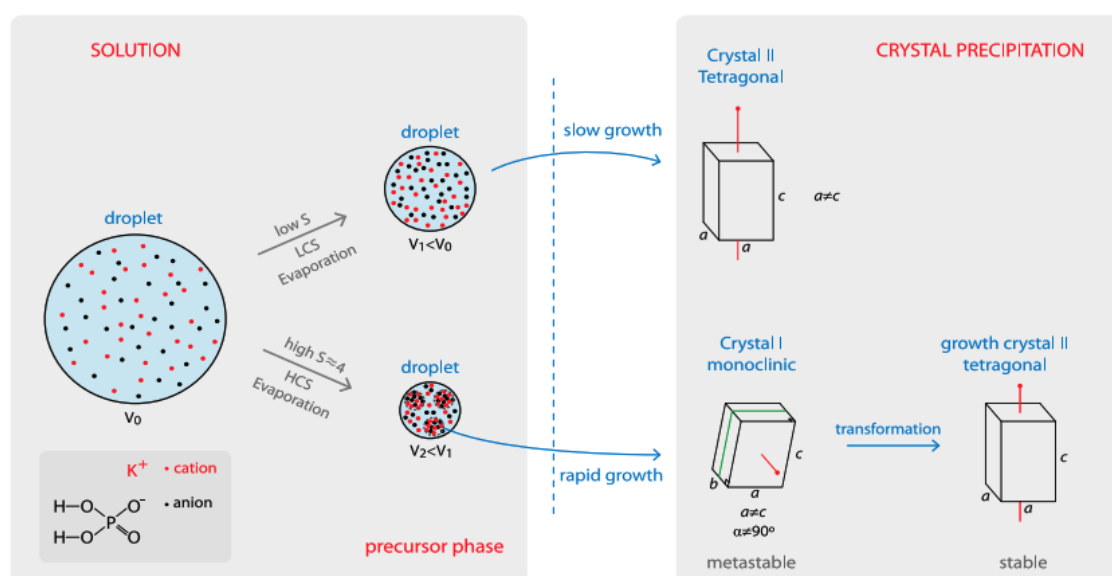
Figure 4.1. The pathway complexity of KH_2PO_4 crystallization at different concentrations. Normal crystallization at low concentration is shown and a three-step nucleation process, starting with a precursor phase, a metastable phase and ending with stable tetragonal crystal structure at high concentration are also shown.[7]

It has been demonstrated for the first time, that concentration gradient plays a significant role in controlling the crystallization process under microfluidic environments, thereby enabling the formation of out-of-equilibrium crystals.[9] XRD patterns corroborated a similar structural identity of these crystals as compared to those synthesized using conventional methods (**Figure 4.2b**). TEM images further confirmed the evolution of crystal growth as trapped crystalline phases ranging from needles to hollow frames to plate-like crystals (**Figure 4.2c,d**).

Akin to crystallization, film growth is also a multi-step process.[10] Though highly interesting for several applications, formation of organic macroscopic films from solution is basically confined to the controlled evaporation of solvents or interfacial processes. In the solvent evaporation technique, a film is formed *via* multiple steps involving particle ordering, deformation, and coalescence, whereas chemical modifications and reactions facilitate film formation at a solid-liquid, liquid-liquid or liquid-air interface.[11] Organic solvent based paint and coating formulations form films upon solvent evaporation (**Figure 4.3a**).[12,13] The advantage of using organic

solvents is that they plasticize the polymer particles by reducing the particle shear modulus.[14] Consequently a facile viscous deformation of particles takes place and a mechanically strong film is formed at ambient conditions.
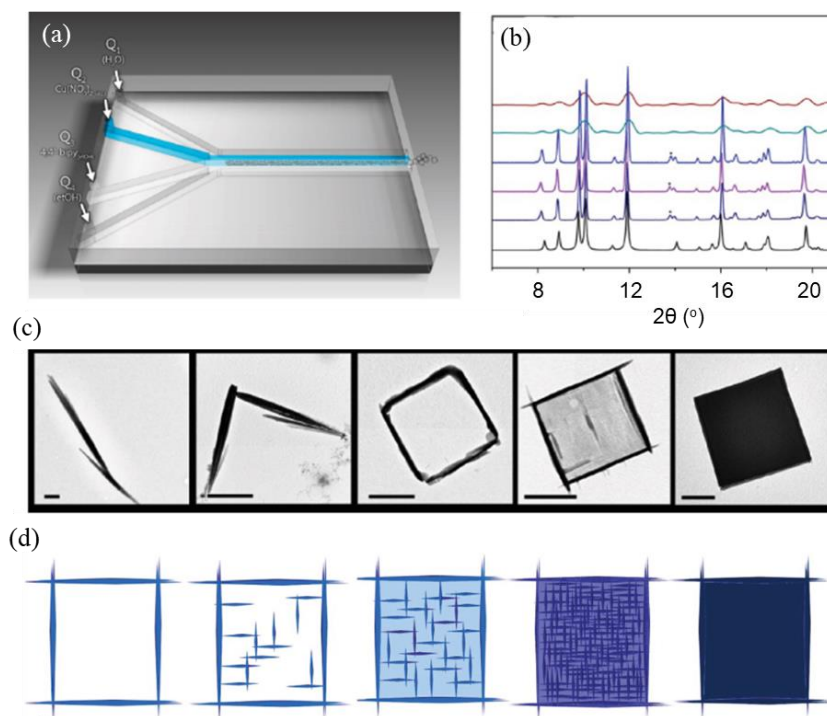
Figure 4.2. (a) A schematic representation of the microfluidic device. **(b)** XRD patterns of the crystals: simulated (black), and synthesized at a flow rate ratio (FRR) of 0.1 (dark blue), 1 (violet), 2 (blue), 4 (green), and 5 (red). **(c)** TEM images of crystals fabricated in the microfluidic device at different FRR (from left to right: FRR 5, 4, 2, 1 and 0.1). Scale bar = 1 µm. **(d)** An illustration of the progressive filling of the internal area of the hollow frames depicting the crystal growth process.

Nevertheless, such self-assembly and particle ordering is not limited to paint or latex particles. Controlled formation of superstructures has been reported for several organic (Eg: polystyrene, acrylates) and inorganic substances (Eg: silica).[15,16,17] For instance, ordered three dimensional superstructures in the millimetre regime was reported by Maspoch *et al.* via solvent evaporation on a clean glass surface.[18] When a colloidal solution of the metal organic framework, ZIF-8 was drop cast on a substrate, the nanocrystals organised themselves into three dimensional superstructures upon drying at 65 °C (**Figure 4.3b**).
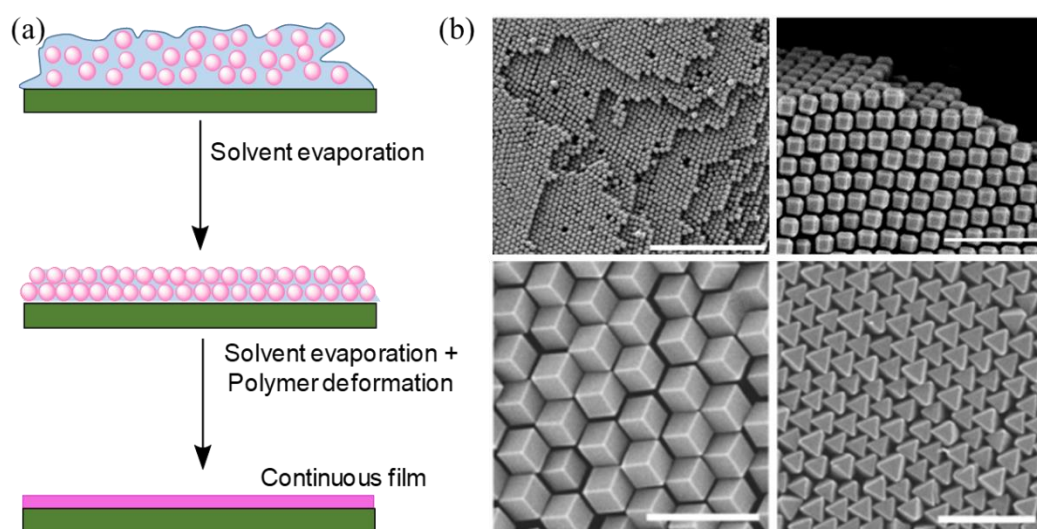
Figure 4.3. (a) A schematic representation of the steps involved in solvent evaporation mediated film formation. **(b)** SEM images showing the 3D superstructure formation of ZIF-8 nanocrystals via heat induced solvent evaporation. Scale bar = 10 μm (top left), 1 μm (all others).

Organic nanocrystals of aromatic π–systems such as perylene diimides **1-4** have been reported to form free-standing crystalline films upon filtration (**Figure 4.4**). The nanostructured films were shown to have good mechanical strength and thermal stability. These films with a non-linear optical response were further demonstrated to have applications as ultrafiltration membranes owing to their controllable porosity.[19]

1: R = H, **2**: R = Me, **3**: R = NO$_2$ **4**
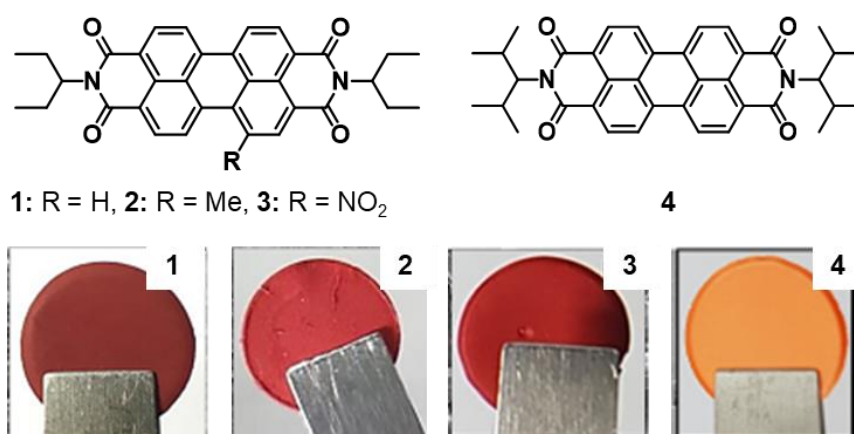
Figure 4.4. Chemical structures of the PDI derivatives **1-4** and photographs of the corresponding free-standing films obtained *via* the filtration of their aged nanocrystal solutions.

Self-assembly at air/liquid[20] or liquid/liquid interface is yet another strategy widely employed for film formation via interfacial processes.[21,22] The process of film formation at an air/liquid interface is popularly known as Langmuir-Blodgett (L-B) method.[23] Amphiphiles with a polar head group remain well organised on the surface of a polar solvent like water, whereas their hydrophobic subunits would be projected away so as to minimize the interactions with water. Formation of a monolayer amphiphilic assembly on the surface of water reduces surface tension and the film is referred to as an LB film. LB method has been extensively used to fabricate ordered 2D membranes. For instance, Lai *et al.* have reported the fabrication of a membrane 2D based on a covalent organic framework (COF) **5** using LB method. The membrane was found to be highly crystalline and was formed by a layer-by-layer assembly under LB conditions (**Figure 4.5**). The membranes exhibited excellent molecular sieving properties with onset-cut off between 600-900 Da. Moreover, the well-ordered thermally stable crystalline membrane exhibited better solvent permeability than its amorphous counterpart.[24]

Figure 4.5. (a) Chemical structures of the precursors (left) and the COF **5** (right). **(b)** A schematic representation of the LB method for film formation at the air-water interface.

Films are also formed at a liquid-liquid interface via chemical reactions or non-covalent modifications (**Figure 4.6a**).[25] Exploiting the donor-acceptor interactions between the molec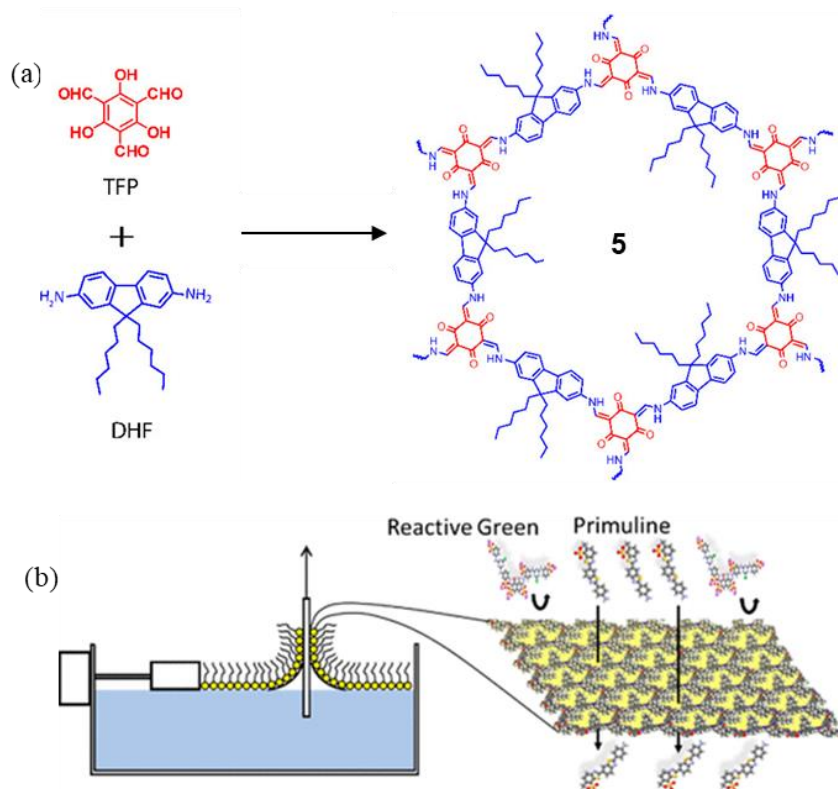ules **6** and **7** and their inclusion complexation with cucurbit[8]uril, Fang and co-workers have successfully prepared monolayers of a 2D supramolecular organic framework (SOF) (**Figure 4.6b**).[26] At the liquid-liquid interface, the SOF formed free-standing large area films with a hexagonal layered arrangement and excellent homogeneity and mechanical strength.
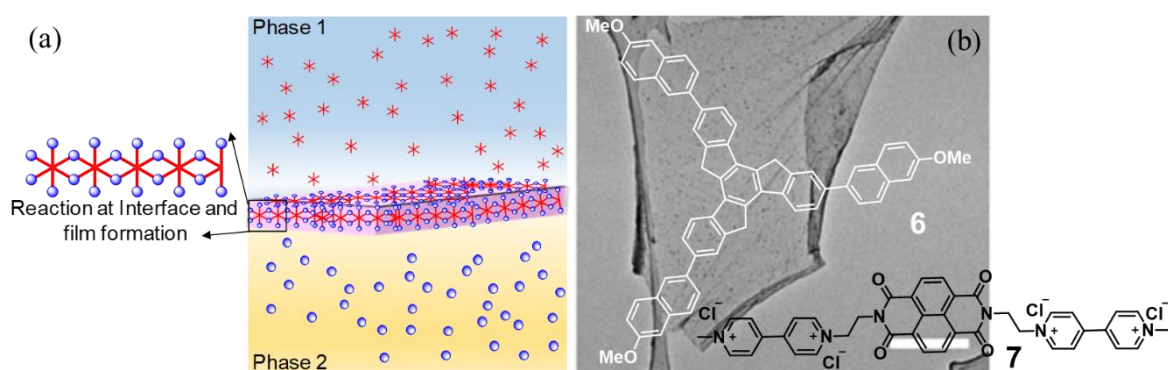
Figure 4.6. (a) An illustration of the 2D growth of supramolecular networks in a biphasic solvent interface via coordination, supramolecular H-bonding or host-guest interactions. **(b)** TEM image of the 2D monolayer film formed by the donor **6** and the acceptor **7** via inclusion complexation of the D-A adduct with CB[8] at the liquid-liquid interface.

Interfacial chemical reactions involving polymerizing units are also reported to form films or 2D sheet like structures.[27] Although several strategies for crystallization and film formation are well-established, the evolution of freestanding films in a monophasic solvent medium is rather poorly understood. In this context, Hamachi and co-workers have demonstrated a reversible solvent expelled supramolecular assembly of a pH responsive hydrogel. Upon protonation, the hydrogel showed a reversible shrinkage or swelling unlike other reported supramolecular hydrogels, that displayed simple sol-gel transitions with changes in pH (**Figure 4.7**). Protonation induced expulsion of solvent in these hydrogels allowed the formation of an opaque film-like soft material (**Figure 4.7b top**).[28]
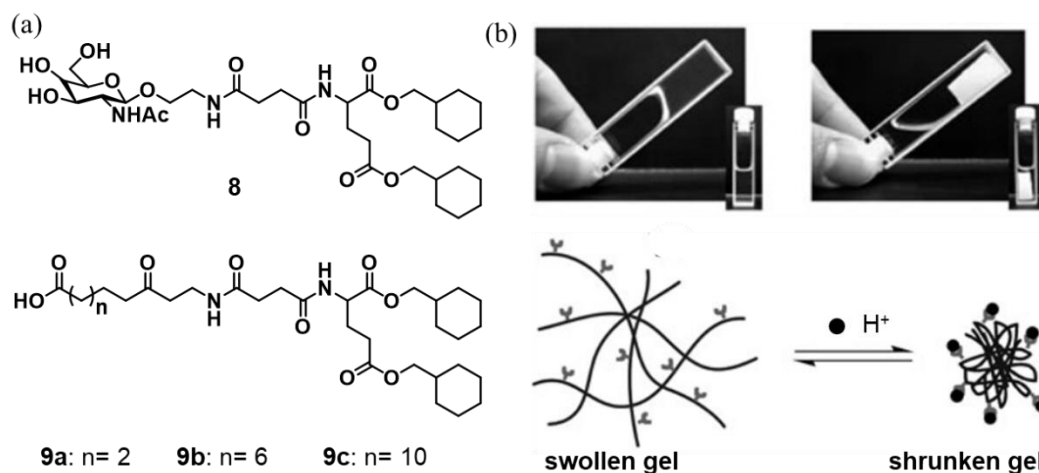
Figure. 4.7. (a) Chemical structures of the gelators **8-9** and **(b)** the protonation induced reversible switching of the hydrogel between its swollen and shrunken states. The photographs (top) of the swollen and shrunken gel and the corresponding mechanism (bottom) are shown.

Herein, we report the formation of free-standing films synchronized with supramolecular polymerization, utilizing lower critical solution temperature (LCST) phase transitions of two amphiphiles in a monophasic solvent medium (**Scheme 4.1**). This strategy provides a novel route to fabricate free-standing macroscopic films in a monophasic solvent, that makes it unique compared to existing film processing techniques. We envisage that the realization of macroscopic films via thermally assisted self-assembly processes in a single phase solvent would open up new opportunities for further developments in thin film processing and supramolecular chemistry of stimuli-responsive smart materials, the understanding of phase transitions involving polymeric solutions, and controlling chemical processes leading to the elucidation of complex structural components in biology.

The formation of the freestanding film was achieved using a co-assembly process between of two amphiphilic molecules **PE** and **PECN**, with the application of heat as an external stimulus. One of the amphiphiles **PECN** is a cyano derivative that possesses a permanent dipole moment. A completely miscible solvent mixture of water and tetrahydrofuran (9:1 v/v) was used, wherein discrete supramolecular assemblies of the amphiphiles were found to be dispersed. Typically, a preformed

assembly was prepared by adding water to the THF solution of **PE** and **PECN** (water:THF = 9:1).
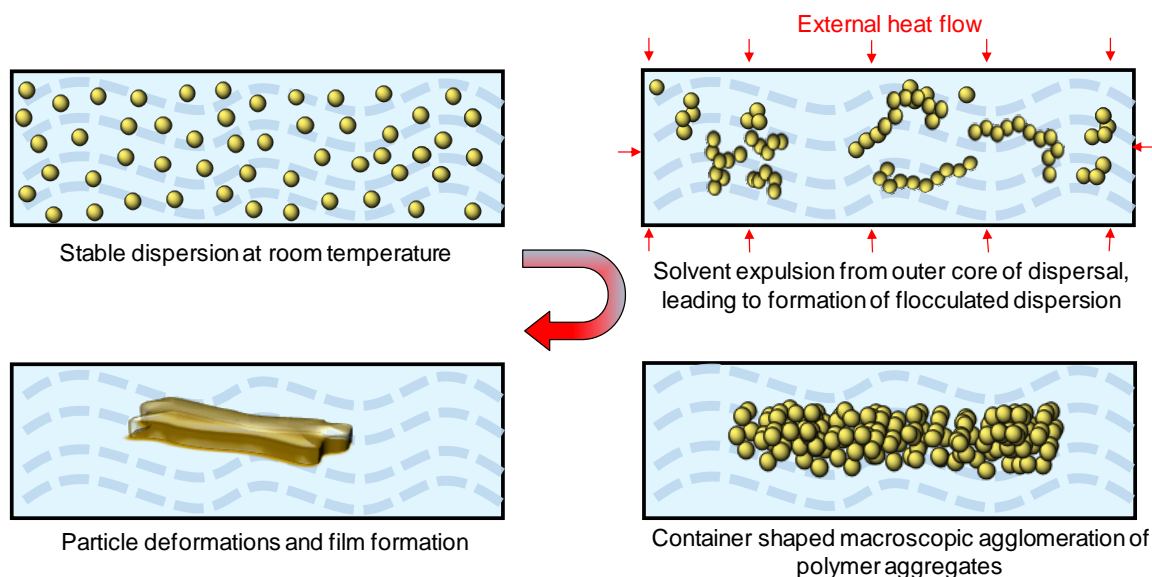
Scheme 4.1. A schematic representation of the proposed approach to create a free-standing macroscopic film within a monophasic solvent system via controlled manipulation of the molecular level interactions between the solvent and the aggregated amphiphiles.

While the amphiphile **PE** alone did not form any macroscopic film via hierarchical self-assembly at varying concentrations and temperatures, film formation was observed upon mixing **PE** with **PECN** in varied proportions ranging from 9:1 to 0:10, under gentle heating. Monodispersed co-assemblies were observed irrespective of the ratio of **PE** and **PECN** and macroscopic free-standing films were formed under the application of a thermal stimulus. With increasing amounts of **PECN** in the co-assembly, the critical film forming temperature also increased. For instance, while a 9:1 **PE:PECN** co-assembly formed a film at 49.7 °C, a 2:8 mixture required a temperature of 61 °C for effective film formation. Morphological studies revealed that monodispersed nanostructures formed at room temperature under the influence of higher temperatures, got transformed to hierarchical micrometer sized films. However, their emission profiles were found to be identical, that is indicative of an unaltered molecular arrangement with disparities in morphologies.

4.3. Results and Discussion

4.3.1. Synthesis of the Amphiphiles PE and PECN

We have adopted a multistep strategy to synthesize the target molecules **PE** and **PECN** (**Scheme 4.2**). The synthesis of **PE** was previously reported from our group[29] and **PECN** was synthesized using a similar strategy involving the Sonogashira-Hagihara cross-coupling between the acetylene derivative **15** and 4-iodobenzonitrile **16** under inert conditions, in 68% yield. All the intermediates and final compounds were purified and then characterized by nuclear magnetic resonance spectroscopy (NMR) and high–resolution mass spectrometry (HRMS).
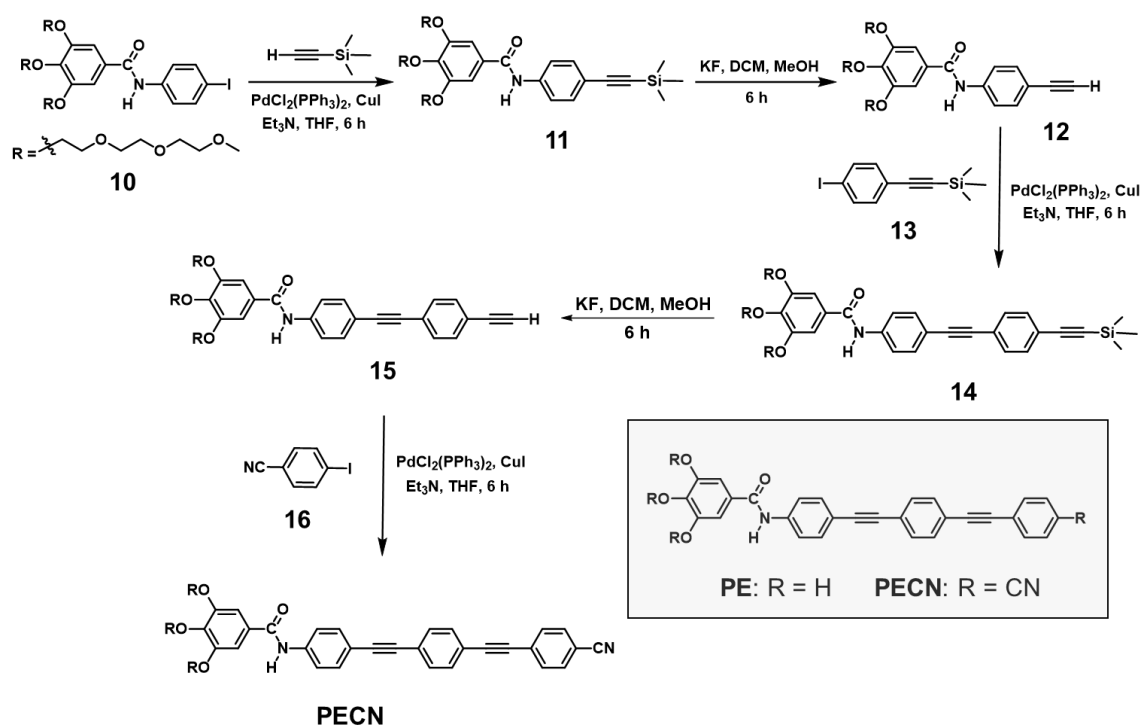
Scheme 4.2. Synthetic protocol adopted for the synthesis of the amphiphile **PECN**. **PE** was synthesized using a previously reported procedure.[29]

The characterization data obtained for **PE** was identical to those already reported.[29] ^{1}H NMR of **PECN** in CDCl$_3$ (25 °C, 500 MHz, **Figure 4.8**) featured the most de-shielded amide proton H$_g$ at 8.85 ppm (singlet). The phenyl protons ortho to the cyano group H$_a$ were found to resonate at 7.74 ppm and those *meta* to the cyano

group appeared at 7.65 ppm. Other aromatic protons (H$_c$, H$_d$, H$_e$ and H$_f$) of the OPE core were observed between 7.62 and 7.27 ppm. The glycol protons appeared between 4.27 and 3.24 ppm. ^{13}C NMR spectrum (CDCl$_3$, 25 °C, 125 MHz) further corroborated the expected chemical structure of **PECN**. High resolution mass spectrum of **PECN** unanimously confirmed the chemical structure of **PECN** with an [M+Na]$^+$ peak at 930.80. The detailed characterization data is presented in the experimental section.
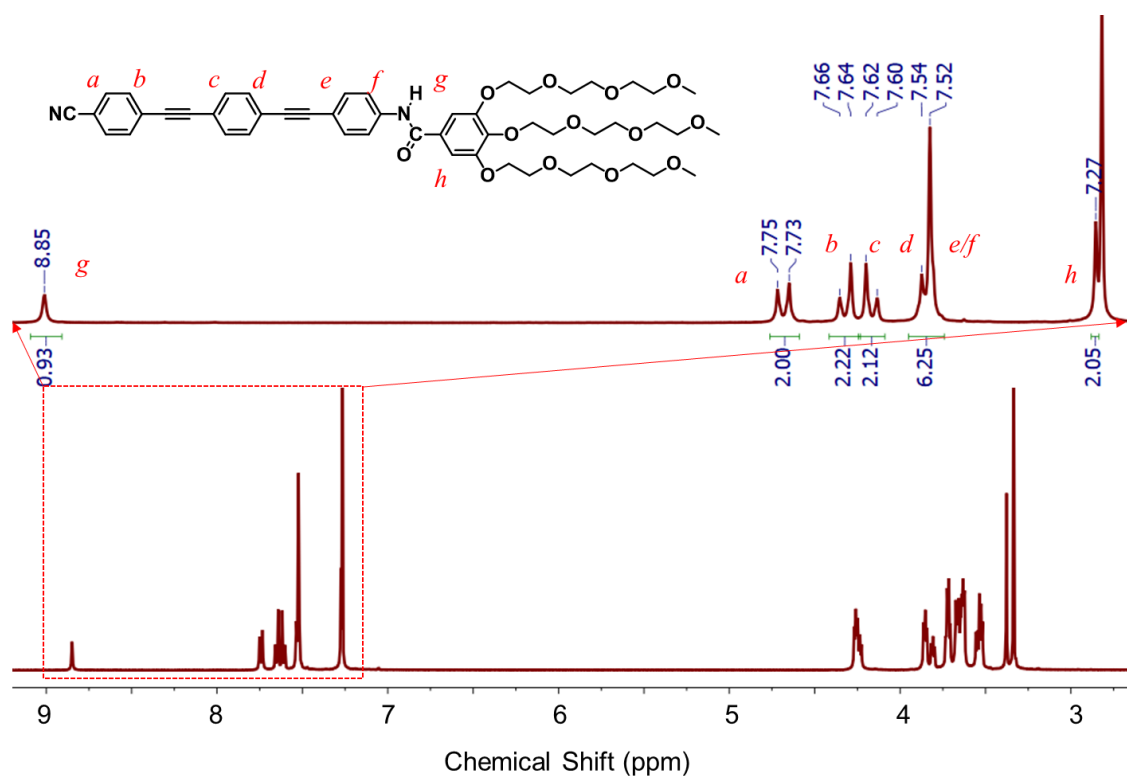
Figure. 4.8. ^{1}H NMR spectrum of **PECN** in CDCl$_3$ (500 MHz, 25 °C) and the chemical shift assignment corresponding to the chemical structure of **PECN**. An expanded spectrum (7-9 ppm) is also shown.

4.3.2. Design Strategies of PE and PECN

Both the amphiphiles **PE** and **PECN** feature hydrophobic polyethyleneglycol chains, connected to an extended aromatic π−core through an amide bond. The molecule **PECN** has a polar cyano group covalently attached to the extended π−core that differentiates it from the molecule **PE**. The amide group and the aromatic core are envisioned to facilitate intramolecular non-covalent interactions such H-bonding

and π–stacking respectively, that in turn leads to supramolecular polymerization of the amphiphiles in an aqueous medium (**Scheme. 4.3**).
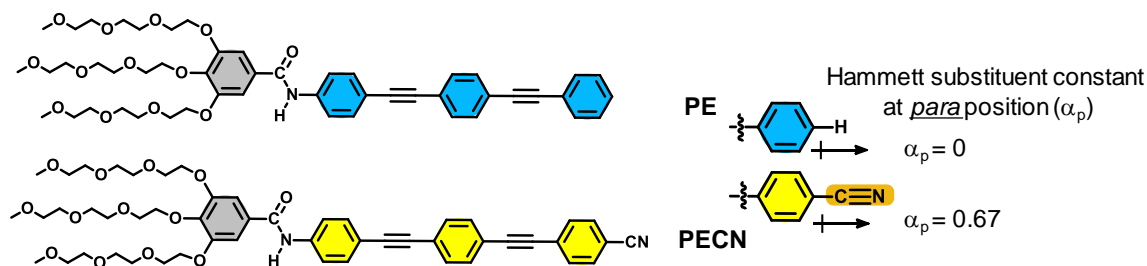
Scheme. 4.3. Molecular structures of the amphiphile **PE** (top) and **PECN** (bottom). Incorporation of the cyano group (Hammett *para*-substitution constant = 0.67) ascribes a permanent dipole moment to **PECN**.

The presence of cyano group (Hammett *para*-substitution constant $\alpha_p = 0.67$)[30] induces a permanent dipole moment to **PECN**, thereby facilitating the amphiphile to self-assemble into highly thermostable supramolecular aggregates via dipole-dipole interactions[31] in addition to H-bonding and π–stacking.[32] Inspired by our previous studies, it was expected that both molecules may exhibit LCST characteristics in water. Subsequent temperature dependent morphological changes, for instance, from fibrillary or cylindrical structures to globular or spherical structures, may follow the LCST phase transitions. However, due to the presence of a polar cyano group in **PECN**, the resulting dipole-dipole interactions may further facilitate the alignment of the initially formed supramolecular polymers, thereby leading to detectable deviations from the normal LCST pathways. Moreover, it would be of interest to follow the supramolecular assembly pathways for the mixtures of **PE** and **PECN** at different molar ratios, that may provide unprecedented opportunities to control and manipulate their morphological features.

4.3.3. Mole Fraction Variable Matrix Assembly and Film Formation

Since **PE** alone was not found to result in the formation of films and in view of the above design strategies, we decided to adopt a variable mole fraction mixing strategy of **PE** and **PECN** to evaluate their macroscopic film forming properties within a

single phase solvent medium (10% THF-water) at a constant total concentration of **PE** + **PECN** ($c = 1 \times 10^{-4}$ M), inside a tightly closed 1 mm rectangular cuvette. Upon application of temperature, film formation was observed in all cases except for the single component assembly of **PE** (**PE:PECN** = 10:0). All the films were found to be stable for several weeks at room temperature and retained their original size/shape and the emission of films could be directly correlated to the amounts of **PE** and **PECN** in the mixture (**Figure. 4.9**).
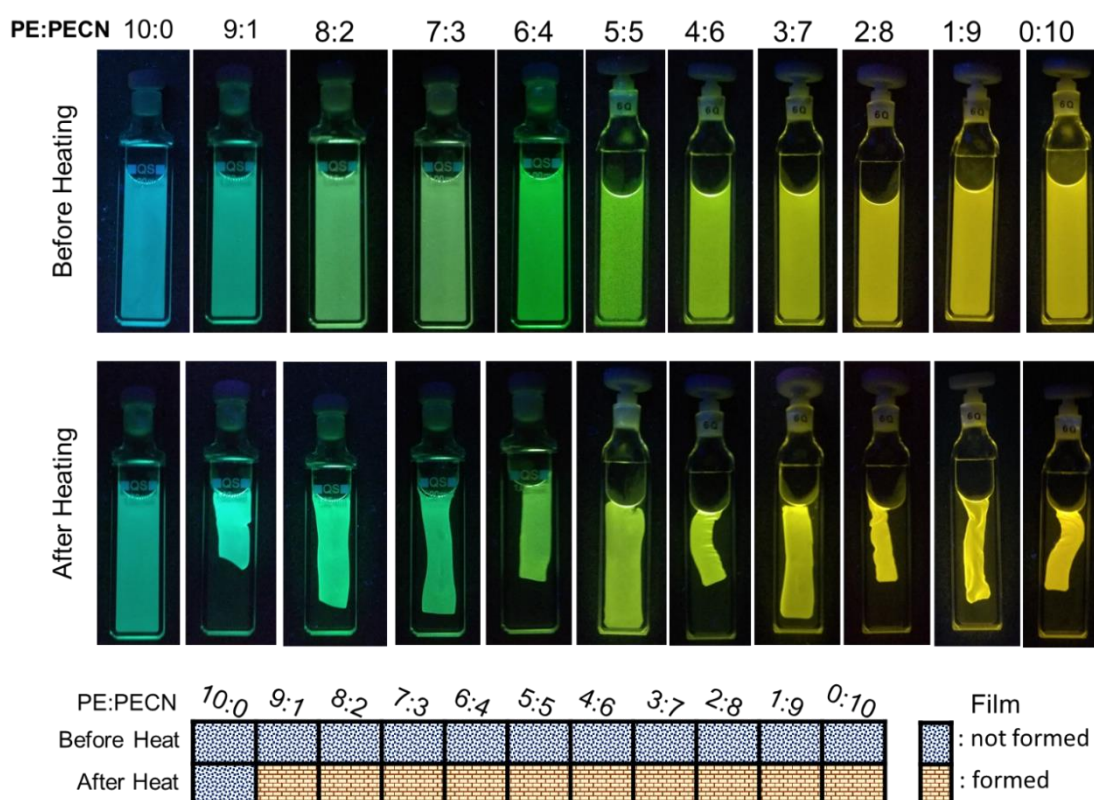
Figure 4.9. Variable mole fraction mixing of **PE:PECN** (total concentration = 1 x 10^{-4} M) in 10% THF-water. The film formation was observed upon heating to the tightly closed cuvettes containing a mixture of **PE:PECN** except for the single component system (**PE:PECN** = 10:0). The photographs of the cuvettes under 365 nm light before (top) and after heating (bottom) and the cases of film formation (bottom) are shown.

4.3.4. Spectroscopic Investigations

UV-vis spectra of the monodispersed co-assemblies at room temperature before film formation revealed a bathochromic shift in the absorption maximum with increasing

amounts of **PECN**, and were found to be in between the individual absorption maxima of **PE** (λ_{max} = 324 nm, 100% **PE**) and **PECN** (λ_{max} = 342 nm, 100% **PECN**) in 10% THF-water. Simultaneous with the shift in λ_{max}, an increase in the intensity of the band at 297 nm was also observed (**Figure 4.10a**). Absence of a distinct absorption band for the co-assembly that is different from the individual bands of **PE** and **PECN** neglects the possibilities for self-sorting in these supramolecular architectures. To further confirm that the assemblies are not self-sorted, we recorded the emission profiles by exciting at their respective absorption maxima (**Figure 4.10b**). It was observed that the emission maximum also shifted to longer wavelengths, with **PE** featuring a cyan emission (λ_{max} = 485 nm, Stokes shift = 10240 cm^{-1}) and **PECN** having a yellowish emission with high Stokes shifts (λ_{max} = 575 nm, Stokes shift = 11848.5 cm^{-1}). As expected, all the co-assemblies exhibited a broad emission maximum that shifted bathochromically with increasing amounts of **PECN** (**Figure 4.10b,c**). A plot of Stokes shift *vs* the mole fraction of **PECN** for all the co-assemblies exhibited a linear relationship with an average Stokes shift of 11523.95 cm^{-1} per mole fraction (**Figure 4.10d**). This trend in the shifts of absorption and emission maxima (1.8 nm and 8 nm respectively per mole fraction of **PECN**), and Stokes shift (98.13 cm^{-1} per mole fraction) is indicative of the significance of the amount of **PECN** in the co-assembly. A large Stokes shift, whereby self-quenching can be minimized, is highly advantageous for better bioimaging and accurate colour mapping with high colour contrast.[33]

To achieve the objective of obtaining macroscopic hierarchical supramolecular films within monophasic solvent system, we exploited the well-established relationship between temperature and solubility or hydrated/dehydrated states of an amphiphilic assembly in water. Lower Critical Solution Temperature (LCST) phase transitions have been shown to play a decisive role in controlling the assembly process in such thermoresponsive systems.[34] Further ordering of the **PE**-**PECN** self-assembled structures, driven by LCST phase transitions under the influence of applied temperature, provides a novel strategy for macroscopic film formation with

excellent control, in a monophasic solvent system. It was observed that, in the presence of an external heat supply, all the co-assemblies of **PE:PECN** started forming flocculated nanostructures. Finally, a film composed of coagulated micrometer long supramolecular structures was observed within the solvent system (**Figure 4.9**). The photographs were taken after cooling the solution to 22 °C and keeping the films submerged for 24 h. In fact, the free-floating films inside a closed cuvette was found to be stable for several weeks.
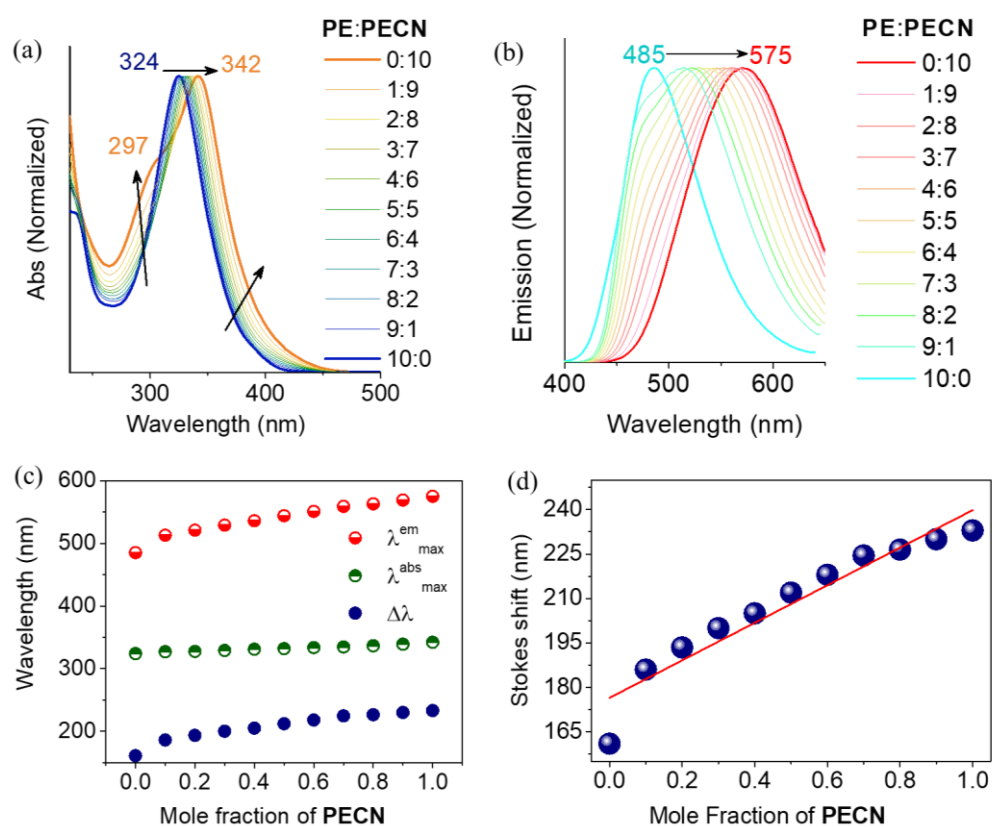
Figure 4.10. Normalized absorbance **(a)**, and emission **(b)** of the self-assembled mixtures of **PE** and **PECN** (10:0 – 0:10) in 10% THF-water (total concentration = 0.1 mM, 22 °C). **(c)** Variation of absorption maximum (green), emission maximum (red) and stokes shift (blue) with increasing mole fraction of **PECN**. **(d)** A plot of Stokes shift *vs* the mole fraction of **PECN** exhibiting a linear relationship.

A minimum of 5% PECN is required to obtain a stable film. Notably, the temperature required for film formation varies with the amount of **PECN** present in the mixture. With the increasing amounts of **PECN** in the co-assembly, higher

temperature was required to obtain stable films (**Figure 4.11a**). Following the change in absorbance at λ_{onset} (*via* Mie scattering) with varying temperature, it was observed that the co-assembly of a 9:1 mixture of **PE**-**PECN** formed a film at 49.7 °C. However, in the absence of **PE** (**PE:PECN** = 0:10) the film formation was found to start at 59.6 °C (**Figure 4.11b**).
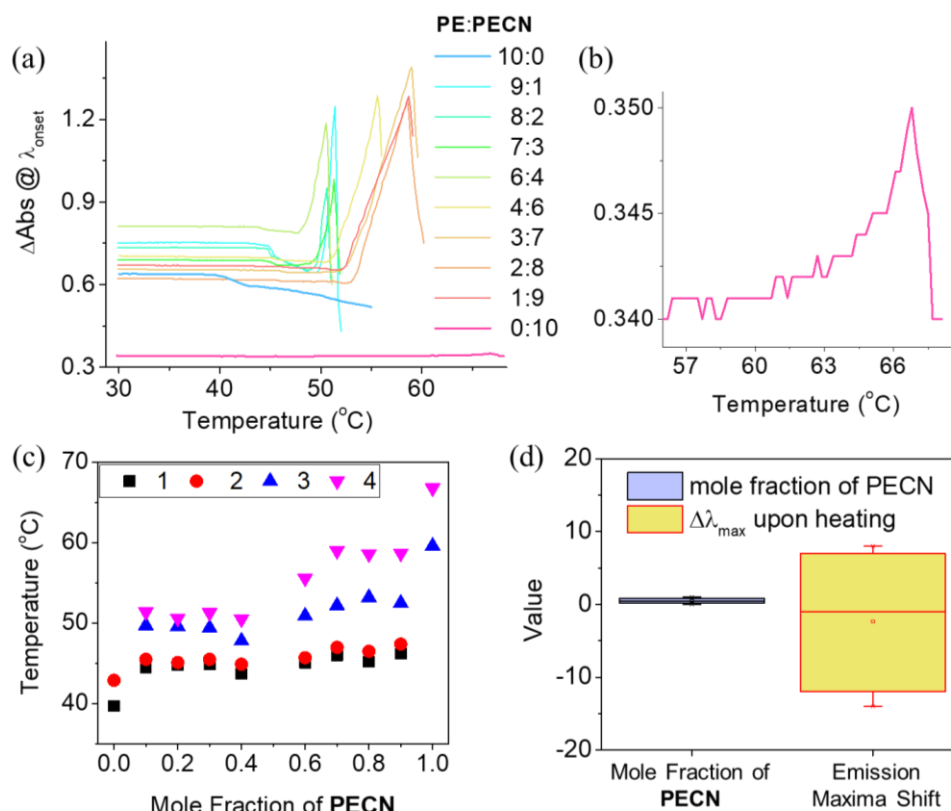
Figure 4.11. (a) Plot of change in absorption at λ_{onset} (via Mie scattering) vs applied temperature of the **PE**-**PECN** co-assemblies. **(b)** The enlarged area of the plot of change in absorption at λ_{onset} vs applied temperature for an assembly of **PECN** alone (**PE:PECN** = 0:10). **(c)** Film formation monitored via absorption changes for different mole fraction of **PECN** depicted as a plot of temperature vs mole fraction of **PECN**. The black squares represent the deformation temperature (temperature at which the deformation of the aggregates started), the red circles represent the temperature up to which the deformation process continued, the blue triangles represent the temperature at which film formation was observed and the pink triangles represent the temperature at which the film stayed within the path-length of incident light (After this temperature, the films shrunk and floated away from the incident light). **(d)** Changes in the mole fraction and its respective emission maxima shift before and after heating.

Heating a solution of PE alone in 10% THF-water (**PE:PECN** =10:0) resulted in the emission changed from cyan (485 nm) to blue (410 nm) and traced back its original colour (cyan) reversibly upon cooling. However, the Mie scattering increased during heating, which implies an increase in the particle size, simultaneous with deformation at the molecular level (**Figure 4.11d**). As observed for the co-assemblies at room temperature, the emission maxima of the films were broad and shifted to longer wavelengths with increasing amounts of **PECN** (**Figure 4.12**).

From DLS measurements, the hydrodynamic diameter of the self-assembled aggregates of both **PE** (**Figure 4.13a,d**) and **PECN** (**Figure 4.13c,d**) in 10% THF-water increased continuously with increasing temperature, whereas the co-assemblies of **PE**:**PECN** did not show any logical relationship between applied temperature and particle size as film formation via particle coalescence was observed. An example of **PE:PECN** (8:2 ratio) is shown in **Figure 4.13b,d**.
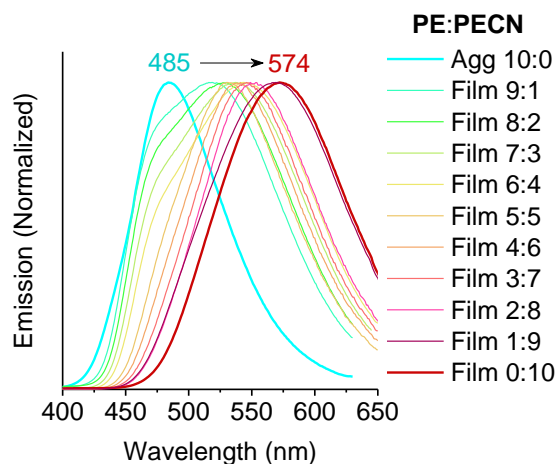
Figure 4.12. Emission profiles of the self-assembled aggregates and films (as indicated) of **PE** and **PECN** (10:0 – 0:10) in 10% THF-water (total concentration = 1 x 10^{-4} M).

As expected, the correlation co-efficient decay profile for the self-assembled aggregates of both **PE** (**Figure 4.14a**) and **PECN** (**Figure 4.14c**) in 10% THF-water was nearly sigmodal irrespective to temperature changes. This observation indicates the presence of spherical aggregates in these systems, though film formation is observed for **PECN** at high temperatures. However, **PE:PECN** mixtures at other ratios exhibited a rather non-sigmoidal correlation co-efficient decay profiles,

indicating the formation of films without the presence any spherical aggregates. An example of **PE:PECN** = 8:2 ratio is shown in **Figure 4.14b**.
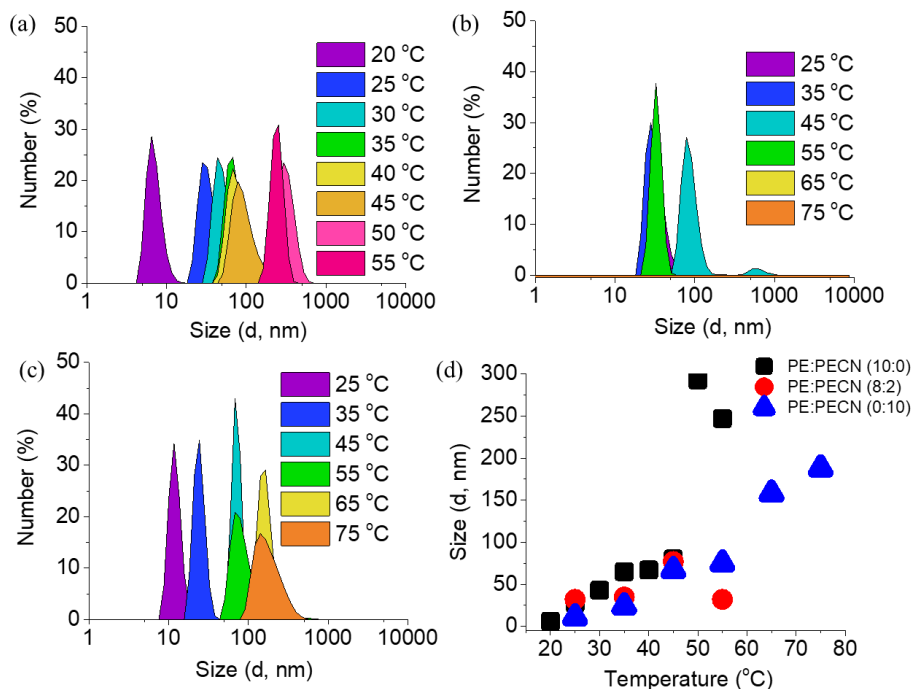
Figure 4.13. Temperature variable Dynamic Light Scattering measurements showing the size distribution plots (number *vs* size) of **(a) PE** only **(b) PE:PECN** (8:2) **(c) PECN** only and **(d)** plots of the obtained particle size vs temperature for **a-c**.
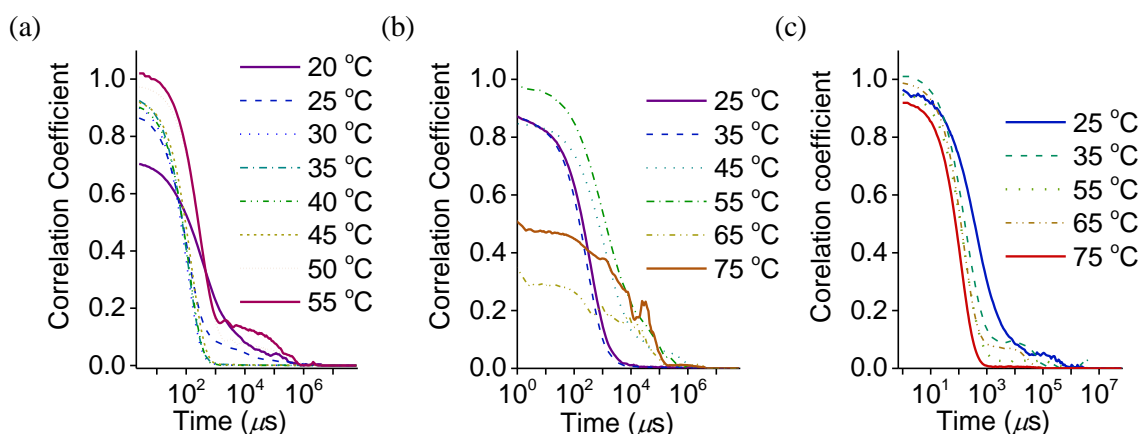
Figure 4.14. Temperature variable Dynamic Light Scattering correlation co-efficient decay profile for **(a) PE** alone, **(b)** 8: 2 **PE:PECN** and **(c) PECN** alone (c = 1 x 10^{-5} M) in 10% THF-water mixture.

To get better insights into the temperature induced changes in the photophysical properties of the co-assemblies during their transformation from aggregates to films, their fluorescence life time decay profiles were obtained. Transformation of the

monodispersed aggregates to the respective macroscopic films did not affect the shape of the emission spectra of the co-assemblies of **PE**-**PECN**. However, a slight shift in their emission maxima (±7 nm) was observed (**Figure 4.12**), which is a significantly smaller effect when compared to their Stokes shifts (**Figure 4.10c,d**). A similar effect was observed in life time decay profiles. **PE** was found to be weakly emissive in its monomeric state, whereas **PECN** showed a blue emission with a lifetime decay of 0.54 ns. The life time decay of all the co-assemblies are from multi-emissive species with one of them being an eximeric emission with a life time value >20 ns even after the film formation (**Figure 4.15**, **Tables 4.1, 4.2**). These data suggest that the supramolecular organization of the emissive part of amphiphiles **PE** and **PECN** remain mostly unaltered during the thermally assisted phase transitions.
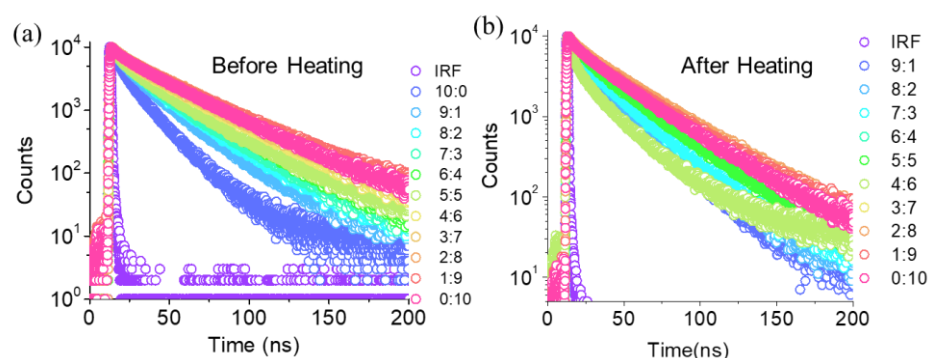
Figure 4.15. Fluorescence lifetime decay profiles of **PE:PECN** mixture in 10% THF-water mixture **(a)** before and **(b)** after heating.

Therefore, we propose that no significant correlation exists in the chromophore-to-chromophore packing during the thermoresponsive transformation of the hierarchical assembly. Film formation is essentially a macroscopic transformation, where the π–core packing remains more or less same before and after heating.

4.3.5. Shape Influenced Growth of Superstructures

An interesting observation during the film formation involving **PE** and **PECN** in different ratios was that, the hierarchical superstructure is influenced by the shape of the container used. **Figure 4.16** shows the photographs of the films formed in containers of different shapes, when viewed under UV light illumination. For

instance, in a thin cuvette, thin elongated films were formed, whereas, the formation of a thick film was observed within a rectangular cuvette. The use of an NMR tube led to the formation of a rod-shaped structure, however, inside a test tube, a thicker elongated film with curved edges was formed. Thus, a templating effect of the shape of the container was obviously reflected in the nature of the superstructures/films formed. Over-heating the films caused them to shrink in size, most likely due to solvent expulsion, without detectable changes in their shape. The shrunk film neither returned to its original position nor got dismantled or precipitated even after prolonged storage. This study provides the first instance of robust macroscopic film formation in a monophasic solvent medium based on a non-covalent supramolecular system.

Table 4.1. Summary of the fluorescence lifetime decay of **PE:PECN** aggregates in 10% THF-water at 22 ^{o}C (before heat stimulation).

Agg PE:PECN	τ_1 [ns]	A_1 [%]	τ_2 [ns]	A_2 [%]	τ_3 [ns]	A_3 [%]	$\langle\tau_{av}\rangle$ [ns]	χ^2
10:00	7.57	34.82	17.78	58.95	1.31	6.24	7.90	1.17
9:1	13.23	40.6	26.59	53.73	2.74	5.68	13.98	1.07
8:2	13.54	34.3	28.99	61.3	2.52	4.39	15.66	1.08
7:3	12.60	28.57	30.27	67.17	2.26	4.26	15.71	1.07
6:4	12.74	22.98	31.83	73.46	2.23	3.56	17.52	1.08
5:5	11.609	21.95	32.31	74.06	2.05	3.99	16.32	1.07
4:6	17.31	20.18	35.99	76.14	3.37	3.67	22.88	1.08
3:7	18.41	21.81	37.84	75.03	2.97	3.16	23.64	1.10
2:8	18.20	13.01	38.27	84.41	3.40	2.58	27.19	0.99
1:9	24.08	29.96	41.53	67.33	3.24	2.72	27.00	1.06
0:10	19.25	18.34	37.32	79.0	2.76	2.66	24.80	1.09
PE$_{mono}$	0.79 [ps]	100	--	--	--	--	0.79 [ps]	1.91
PECN$_{mono}$	0.54	100	--	--	--	--	0.54	1.00

4.3.6. Mechanistic Understanding of the Film Formation

To a have a better understanding of the mechanism behind film formation, we carefully followed the temperature dependent changes in their absorbance and linear dichroism profiles.

Table 4.2. Summary of the fluorescence lifetime decay of **PE:PECN** films in 10% THF-water at 22 °C (after heat stimulation).

| Film PE:PECN	τ_1 [ns]	A_1 [%]	τ_2 [ns]	A_2 [%]	τ_3 [ns]	A_3 [%]	$\langle\tau_{av}\rangle$ [ns]	χ^2
$10:0_{agg}$	7.57	34.82	17.78	58.95	1.31	6.24	7.90	1.17
9:1	13.74	40.42	27.42	54.63	2.78	4.96	14.90	1.04
8:2	13.39	35.56	29.10	59.49	2.52	4.95	15.01	1.13
7:3	12.54	26.71	30.60	68.74	2.41	4.54	15.97	1.09
6:4	13.85	22.54	32.53	73.64	2.51	3.82	18.49	1.07
5:5	13.13	19.27	33.76	77.88	2.17	2.86	19.66	1.06
4:6	6.59	24.02	25.91	70.26	0.55	5.72	5.97	1.20
3:7	7.27	16.28	28.98	81.04	0.28	2.68	6.88	1.19
2:8	14.75	9.41	37.93	88.68	2.76	1.91	27.28	1.01
1:9	7.81	7.57	36.42	91.3	0.38	1.14	15.48	1.14
0:10	13.44	12.46	35.75	85.31	1.99	2.23	22.58	1.01
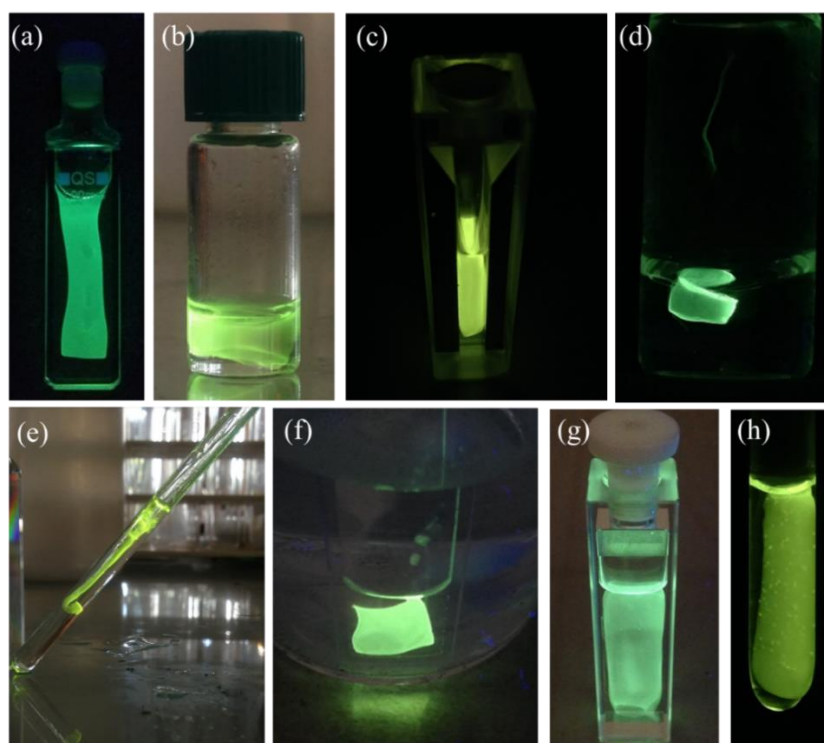
Figure 4.16. Photographs (under UV light) showing the templated formation of the superstructures inside **(a)** a 1 mm cuvette, **(b)** a cylindrical vial, **(c)** a 1 mL rectangular cuvette, **(d)** a larger vial, **(e)** an NMR tube, **(f)** a 1 mm Cuvette with small quantity of **PE:PECN** aggregates **(g)** a 1 cm cuvette and **(h)** a tube.

Temperature controlled variations in the intensity of absorption at the λ_{max} of **PE** (10:0) and **PE**: **PECN** (9:1) in 10% THF-water showed a major distinguishable spectral behaviour. (**Figure 4.17**). Upon heating a solution of **PE**, the optical density (OD) was found to remain unchanged with increase in temperature up to 39.9 °C (1′, **Figure 4.17**). Above 39.9 °C, a sharp decay of OD at 324 nm was observed up to 42.6 °C, followed by a slow decay until 55 °C (2′, **Figure 4.17**). However, the Mie scattering intensity increases and decreases reversibly as a response to heat. In the case of **PE: PECN** at a ratio of 9:1, the OD remained unchanged up to 44.5 °C (1, **Figure 4.17**) followed by dip between 45-49.7 °C (2, **Figure 4.17**). A sudden increase in absorbance within a short temperature range (49.7 - 51.4 °C) indicates the formation of the film (3, **Figure 4.17**). Subsequent sudden drop in the OD represents the shrinkage of film, wherein the incident light was not falling on the film anymore. Therefore, absorbance (i.e scattering intensity) reduced drastically (4, **Figure 4.17**).
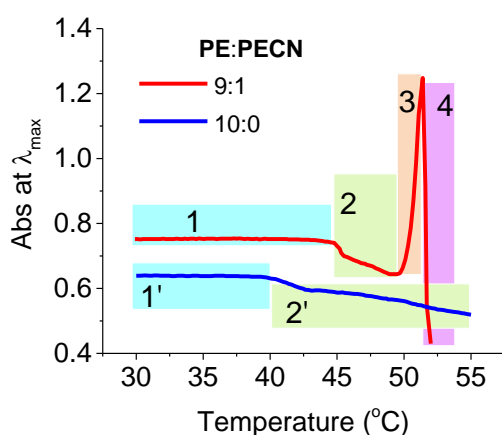
Figure 4.17. Temperature dependent absorbance changes at λ_{max} for the composition **PE:PECN** (9:1, red) and **PE** alone (blue) at a concentration of 1×10^{-4} M in 10% THF-water mixture. Region 1: minimal changes in the absorbance intensity upon heating; Region 2: Deformation of molecular arrangement started upon heating resulting in reduction in intensity; Region 3: Film formation leading to increased light scattering; Region 4: Shrinkage of films leading to deviation from the light path and hence a sharp decrease in absorbance.

The co-assembly with other combinations of **PE:PECN** followed nearly the same thermoresponsive absorbance change except in the case of **PECN** alone. The

transformation of monodispersed aggregates to the films occurred after a lag phase corresponding to the deformation process of the aggregates of **PE:PECN**. The lag phase may be dependent on the rate of water expulsion and subsequent formation of flocculated aggregates. Nevertheless, no films were formed in the case of **PE** alone. We infer that external heating altered the hydrophilicity balance of the monodispersed aggregates to form hydrophobic flocculated nanostructures leading to the finally observed large hierarchical superstructures. Similar rationale can be extended to other ratios of **PE**-**PECN** and **PECN** alone.

4.3.7. Linear Dichroism (LD)

Linear dichroism (LD) spectroscopy analysis provides valuable information on the structural orientation of assembled chromophores within a supramolecular system.[35] Therefore, we recorded the changes in linear dichroism for **PE**-**PECN** mixtures in solution state upon heating from room temperature to the corresponding film forming temperature (T_{film}). The LD measurements of **PE** and **PECN** mixtures with different combinations in 10% THF-water ($c = 1 \times 10^{-4}$ M) exhibited significant positive LD signals indicating greater parallel ($A\parallel$) absorption of the polarized light than perpendicular ($A\perp$). The observed higher parallel absorption of the polarized light is most likely due to the predominant parallel orientation of the transition dipole moment with respect to the film formation direction.[36] Thus, the films obtained upon heating in an aqueous medium arose from a unidirectional orientation of the chromophores (**Figure 4.18a**).[37]

Strong LD responses were obtained for the film-forming combinations of **PE**:**PECN** co-assemblies. However, the LD value for the pure aggregates of **PE** (ΔOD = 3 x 10⁻³) was rather low. While the spectral profile for the assemblies of **PE** alone displayed a slight increment at $\lambda_{max} = 324$ nm with increase in temperature, the rest of the combinations of **PE**-**PECN** exhibited a strong increment at the absorption maxima upon heating. These LD spectral features are, however, inconsistent with our claim that **PECN** bearing a cyano group could contribute to induce anisotropy

in the system leading to the formation of stable films and superstructures. It has already been shown that cyano group is capable of inducing chromophoric orientation in the supramolecular assemblies via strong dipole correlation effects.[32] The amphiphile **PE**, that is devoid of any –CN group, did not form any such superstructure. Pure aggregates of **PE** are less ordered where compared to that of the co-assemblies of **PE** and **PECN**.
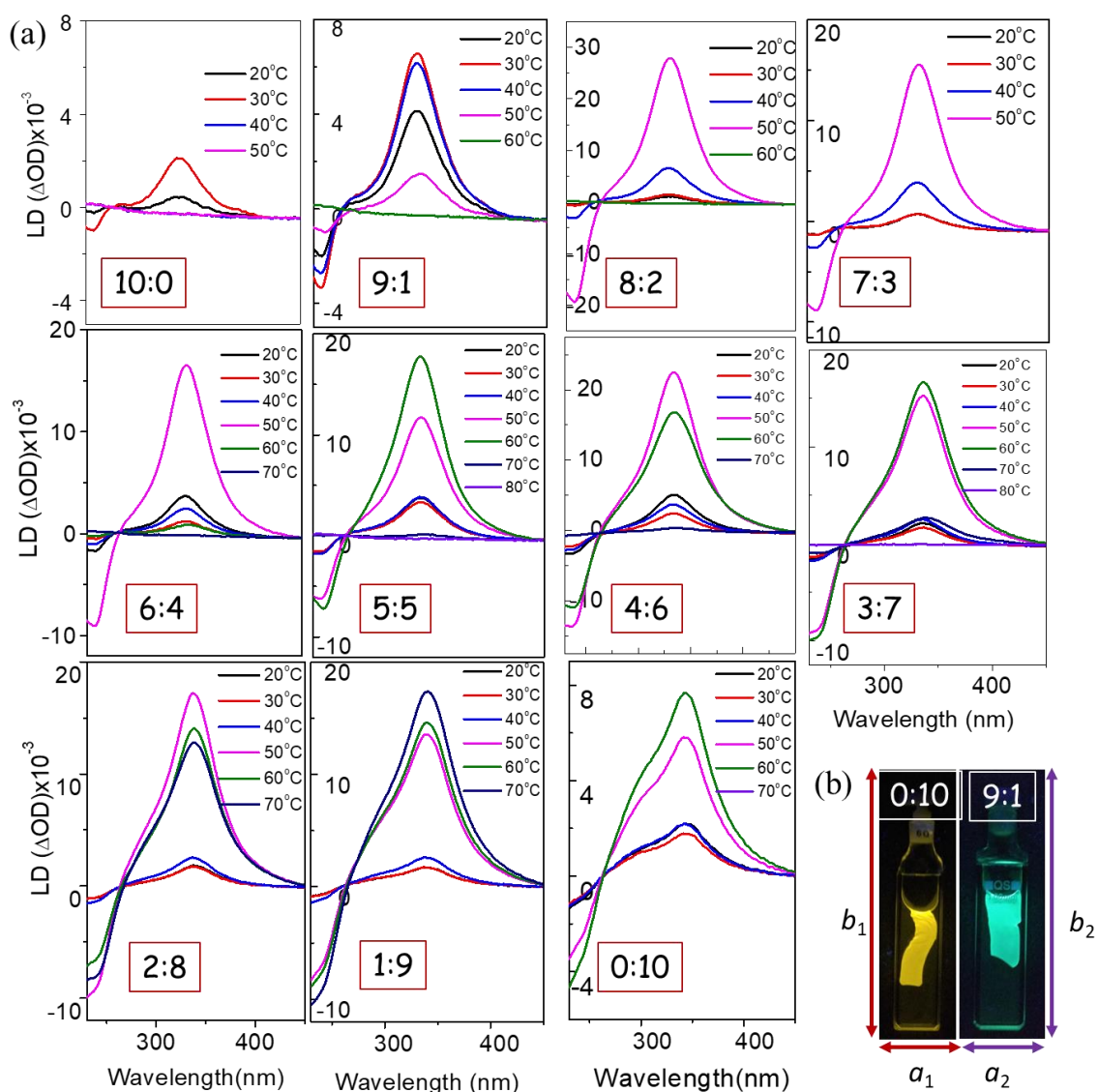

Figure 4.18. (a) Temperature variable linear dichroism of **PE:PECN** co-assemblies in 10% THF-water solution (constant total concentration, $c = 1 \times 10^{-4}$ M) obtained using a 1 mm path length cuvette. The ratio of **PE:PECN** is shown in each spectrum. **(b)** The assignment of longitudinal and perpendicular axes for the cuvettes containing the films of **PE:PECN** mixtures.

The films obtained from the co-assemblies of **PE** and **PECN** consist of tubular structures oriented in a direction parallel to the film (mostly along the b_2 axis). However, a pure **PECN** film consists of small spherical aggregates randomly organized in both directions (a_1 and b_1) (**Figure 4.18b**).

4.3.8. Morphological Analysis

The self-assembly of amphiphiles **PE** and **PECN** individually in 10% THF-water resulted in spherical aggregates of varying size (20-50 nm). However, upon heating, the aggregates of **PE** transformed into larger ill-defined structures, whereas those of **PECN** transformed into macroscopic films via the coalescing of the initially formed particles. Scanning Electron Microscopy (SEM) images revealed the initial formation of spherical aggregates of **PE** in 10% THF-water (**Figure 4.19a**), that flocculated upon heating leading to an ill-defined morphology (**Figure 4.19b,c**). PECN also formed spherical structures initially at room temperature (**Figure 4.19d**), which then fused to form film like superstructures upon heating (**Figure 4.19e,f**). The co-assemblies of **PE** and **PECN** at varying molar ratios formed films upon heating. (**Figure 4.19g-i**). As indicated in the previous sections, dynamic light scattering (DLS) measurements further support these observations (**Figures 4.13, 4.14**).

The films obtained via the thermal stimulation of **PE:PECN** co-assemblies were further examined by TEM and AFM (**Figures 4.20, 4.21**). The co-assembly of **PE** and **PECN** at different molar ratios form network-like structures with high aspect ratio (**Figure 4.20**). These nanofibers with diameter 10-30 nm, were several micrometres long and were found distributed throughout. The fibril-like morphologies were not very evident from the SEM images due to the coating of the surfaces with gold and due to the higher concentration of solution used for drop-casting. It was observed from the TEM images that increasing concentration of **PECN** leads to the formation of more particle like features in the film (**Figure**

4.21d) as opposed to fibril-like morphologies (**Figure 4.21a-c**) at lower concentrations.
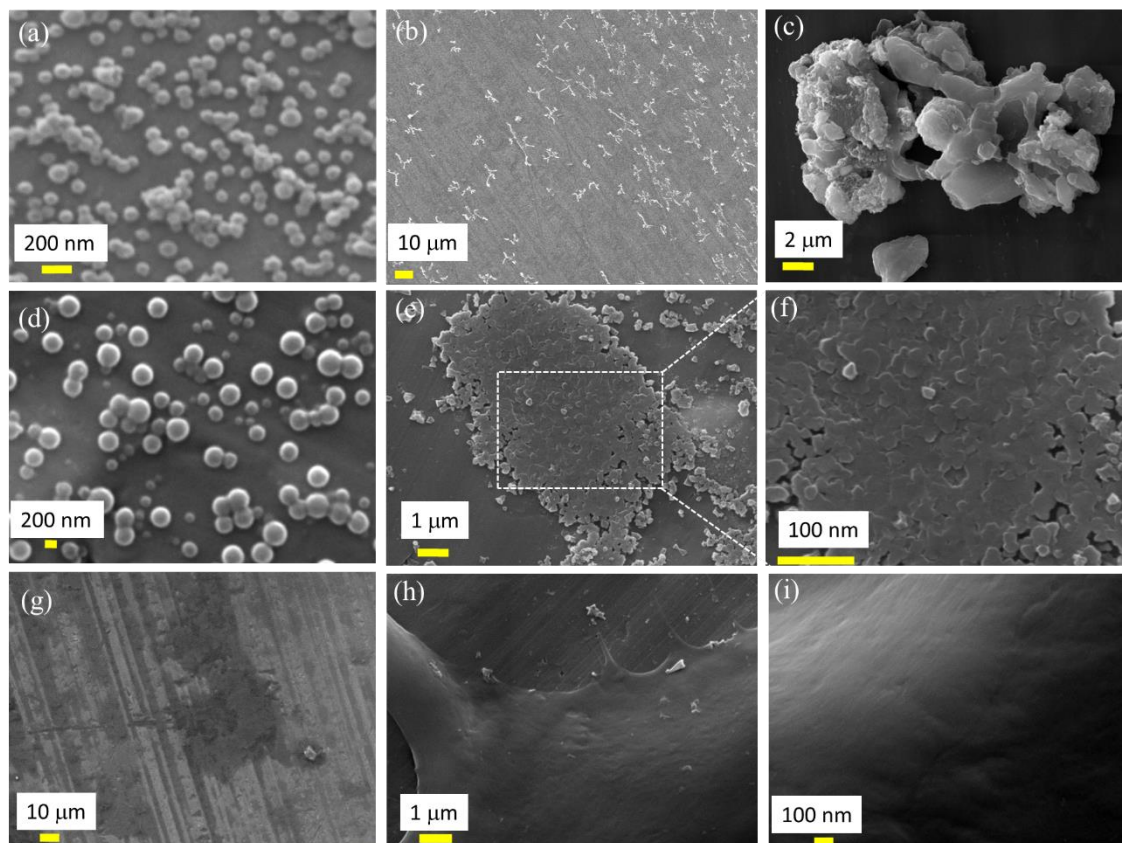
Figure 4.19. SEM Images of the supramolecular assemblies obtained from a 10% THF-water solution of **PE (a)** before and **(b,c)** after heating. **(d)** SEM Images of the supramolecular assemblies obtained from a 10% THF-water solution of **PECN (d)** before and **(e,f)** after heating. The film was obtained via the coalescence of small aggregates. A zoomed-in image of the selected area of **(e)** is shown in **(f)**. SEM Images of the supramolecular assemblies obtained from a 10% THF-water solution of **PE**: **PECN** (1:1) mixture **(g)** before and **(h,i)** after heating demonstrating the film formation.

The formation of the film is a macroscopic transformation wherein the molecular level chromophoric interactions are believed to be unaltered upon heating, as indicated by the emission profiles that remain the same before and after heating (**Figure 4.10c**). In contrast to the **PECN** film that follows a particle deformation pathway followed by coalescence of the initial spherical aggregates, the co-assembly of **PE** and **PECN** initially formed lamellar type aggregates with a height of ~3 nm.

Upon heating, these aggregates transformed into hollow nanofibers. Expulsion of water from the amphiphilic lamellar assembly and balancing the thermal energy, these lamellar aggregates are believed to be transformed into tubular nanofibers and formed aligned network-like structures.
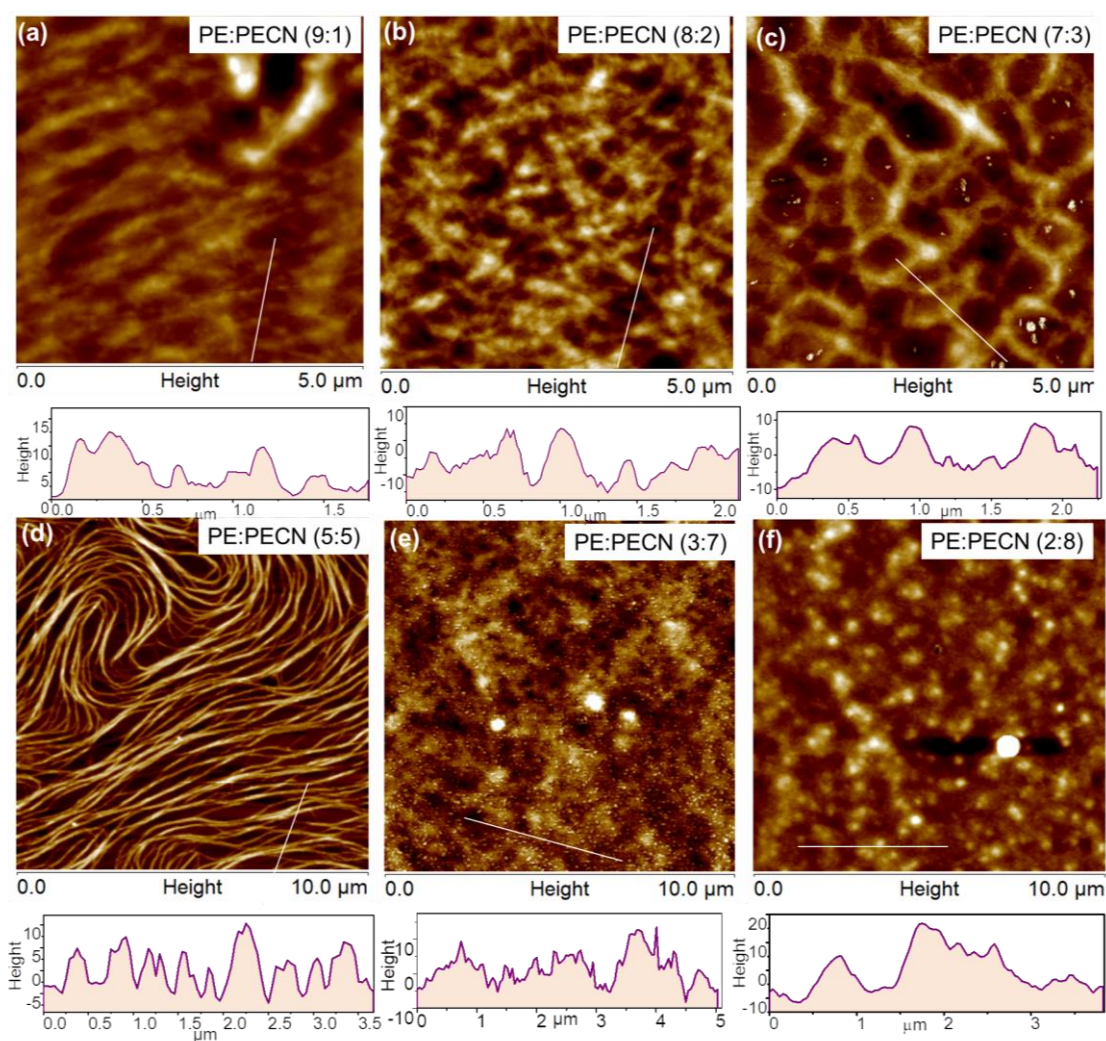
Figure 4.20. AFM images (top) and the corresponding height profiles (bottom) of the films formed by a mixture of **PE-PECN** at ratios of **(a)** 9:1, **(b)** 8:2, **(c)** 7:3, **(d)** 5:5, **(e)** 3:7, and **(f)** 2:8.

4.3.9. Molecular Organization in the Macroscopic Films

AFM image of a 7:3 mixture of **PE:PECN** drop cast on a mica substrate before forming the film is shown in **Figure 4.22a**. A continuous fractured 2D layer was

observed over a large area. The typical length of the sheets was found to exceed several hundreds of micrometers.
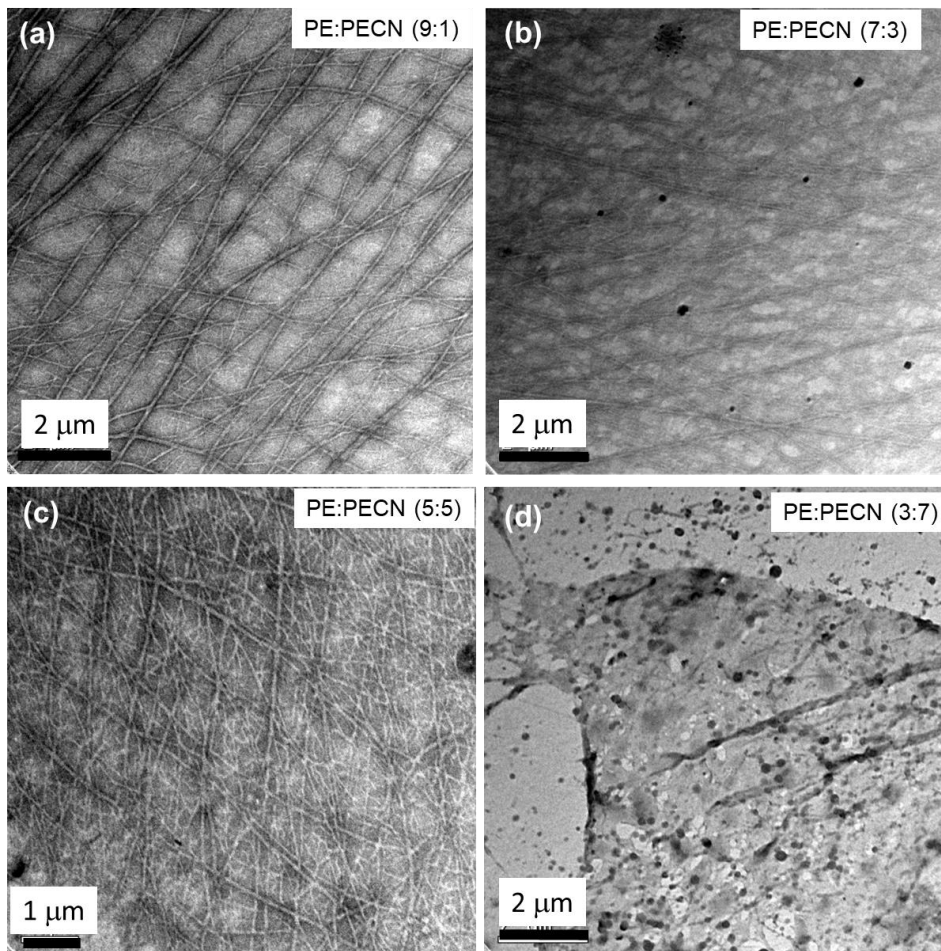
Figure 4.21. TEM images of the films formed by a mixture of **PE-PECN** at ratios of **(a)** 9:1, **(b)** 8:2, **(c)** 7:3, **(d)** 5:5 and **(e)** 3:7.

The formation of robust and free-standing flat nanostructures is more favorable within the bulk solution due to favorable interactions with water. The AFM height profile of the zoomed-in area (**Figure 4.22b**) revealed planar sheets with an average thickness of 2.91 nm, which matches well with the height of a single layer (**Figure 4.22c**). Molecular organization inside the sheet can be estimated from the length of the **PE** and **PECN** molecules. The amphiphiles **PE** and **PECN** possess rigid molecular cores of lengths 2.65 nm and 2.81 nm respectively (**Figure 4.22d**).
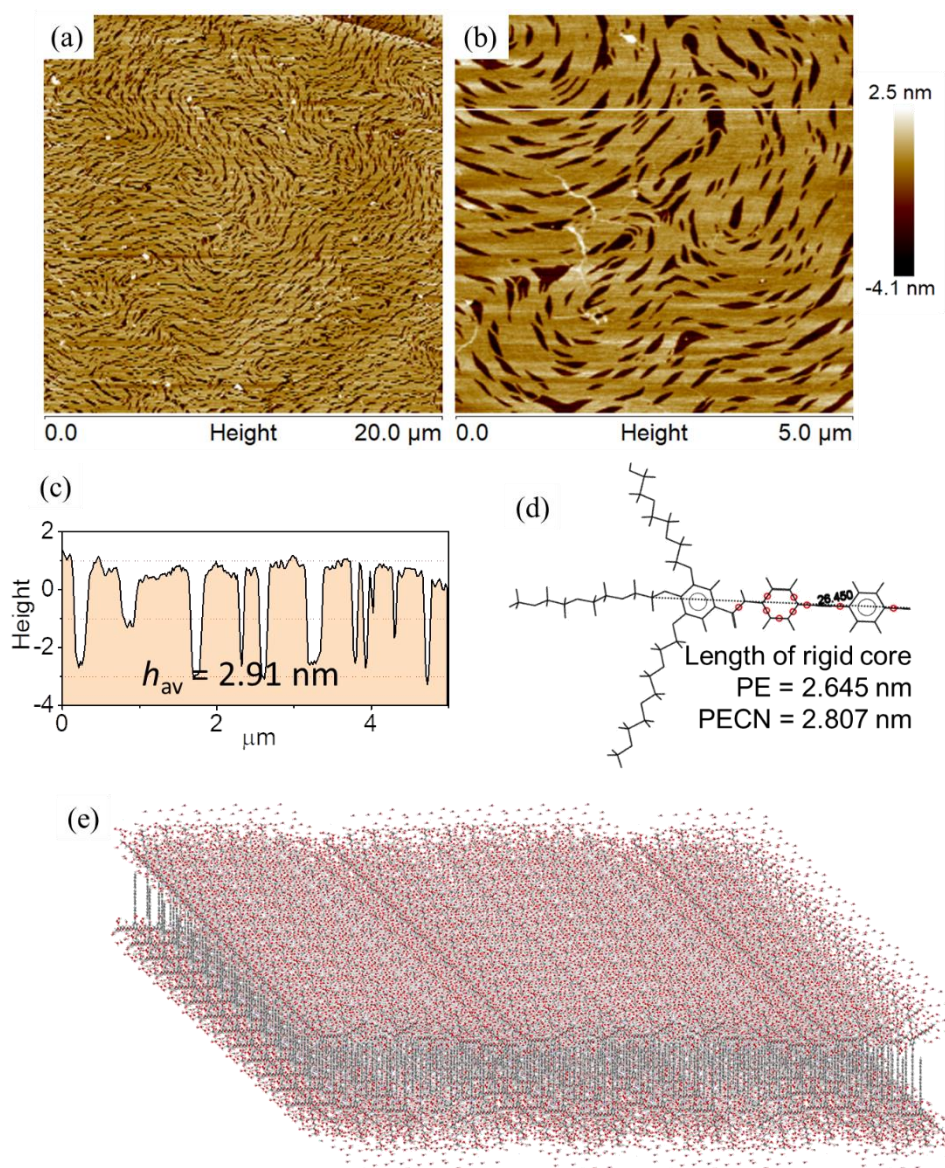
Figure 4.22. (a) AFM image of **PE:PECN** (7:3) co-assembly on a hydrophilic mica substrate at room temperature before forming the film. **(b)** Zoomed-in image of an area from **(a)**. **(c)** AFM height profile of the marked area in **(b)** having an average height of 2.91 nm. **(d)** Molecular structure showing the length of the rigid cores of **PE** and **PECN**. **(e)** A schematic representation of the co-assembly having an anti-parallel arrangement of **PE** and **PECN**.

In water, such a layered superstructure will be free-standing only if the outer surface of sheets remain hydrophilic and water accessible. Considering such a situation, an *anti*-parallel arrangement of **PE-PECN** molecules is highly favorable where hydrophobic cores are hidden inside (**Figure 4.22e**). In contrast with individual **PE** and **PECN** aggregates, the co-assembly provides lamellar type morphology, even

with a minimum percentage of **PECN** (10%) as the co-monomer or dopant to induce a local dipole moment into the **PE:PECN** nano-assembly. Such an induced dipole environment favors an *anti*-parallel organization to nullify the local area dipolar effects.

4.3.10. Effect of Temperature in Molecular Organization

In order to elucidate why the **PE:PECN** sheets with a lamellar-type arrangement irreversibly transformed into tubular structures upon heating to form a stable free-standing film in a bulk monophasic solvent medium, we hypothesized the role of temperature induced variation in chemical potentials of H-bonded water molecules and bulk water molecules at the interface of the hydrophilic segment of the well-dispersed aggregates at room temperature. The solvent system used can be considered to exist in a liquid-liquid equilibrium that comprises two liquid layers: the bulk water molecules [noted as A_1 (nH$_2$O) and D_1 (nH$_2$O)) and the H-bonded water molecules (noted as B_1 (mH$_2$O) and C_1 (mH$_2$O)].

At lower temperatures, the system fulfilled the thermodynamic requirements for equilibrium: the chemical potential of B_1(mH$_2$O) molecules at the interface, μ_{B1} is equal to that of A_1 (nH$_2$O) in the bulk, μ_{A1}, and therefore $\mu_{A1} - \mu_{B1} = 0$. Similarly, for the other interface of the formed sheets, $\mu_{C1} - \mu_{D1} = 0$. The potential difference of both sides could be equal or indistinguishable, such that $\mu_{A1} - \mu_{B1} = \mu_{C1} - \mu_{D1}$. Hydrated states of **PE** or **PECN** are in *anti*-parallel arrangement and well fitted with the 2D layered assembly (**Figure 4.23a**). During directional heat flow from walls of the cuvette to the bulk solution, one side of the sheets gets heated up preferentially. As a result, the water expulsion and folding of glycol chains starts from the heated surface of these supramolecular sheets due to the breakage of H-bonding between water and glycol chains, thereby disturbing the equilibrium between bulk water molecules and H-bonded water molecules (**Figure 4.23b**).

Thus, the heated surface becomes comparatively hydrophobic and its solvent accessible area gets reduced, leading to a convex structure that upon folding forms

the tubular structures to balance the temperature effect (**Figure 4.24**). As the sheets were found to be several hundreds of micrometers long and uniformly dispersed over whole volume, an elongated film is envisioned to form inside the cuvette. Further heating leads to the shrinkage of the macroscopic film via solvent exclusion. Such fine tuning of thermoresponsive interfacial chemical equilibrium in a supramolecular amphiphilic assembly can open up new ways to prepare uniform macroscopic films within a monophasic solvent medium.
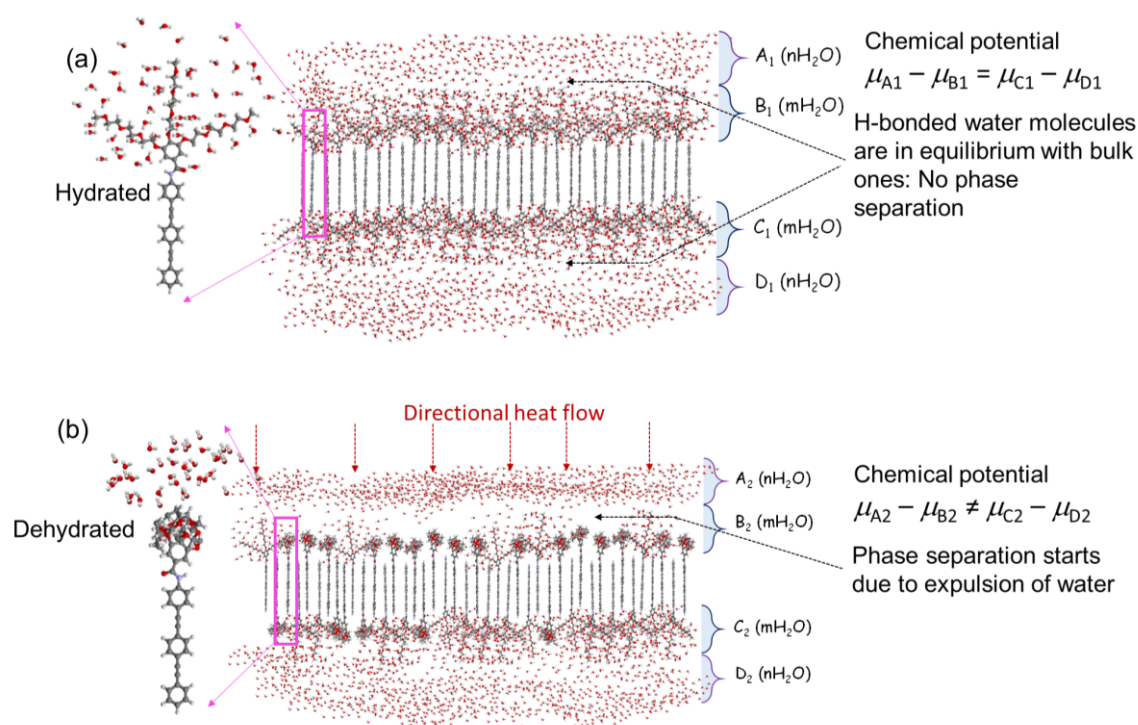
Figure 4.23. (a) Hydrated state of the supramolecular sheets and their indistinguishable interfacial chemical potential difference between H-bonded water and bulk water molecules. **(b)** Preferential heat flow to the one side of the layered structures that disturbed the chemical equilibrium between H-bonded and bulk water molecules at the interface and expulsion of water molecules from hydrated glycol chains.

4.4. Conclusion

In conclusion, a unique strategy to prepare macroscopic free-standing films of organic molecules with a monophasic solvent medium is described. The amphiphilic molecular assemblies underwent a balancing of hydrophobic-hydrophilic, dipolar-

dipolar, and other non-covalent intermolecular interactions via a thermal stimulus. As a result, a hierarchical film was obtained by coalescence of the initially formed spherical structures. The supramolecular co-polymerization of monomers having non-polar and polar aromatic cores attached to a hydrophilic group exhibiting LCST behaviour is the key to the formation of the free-standing films.
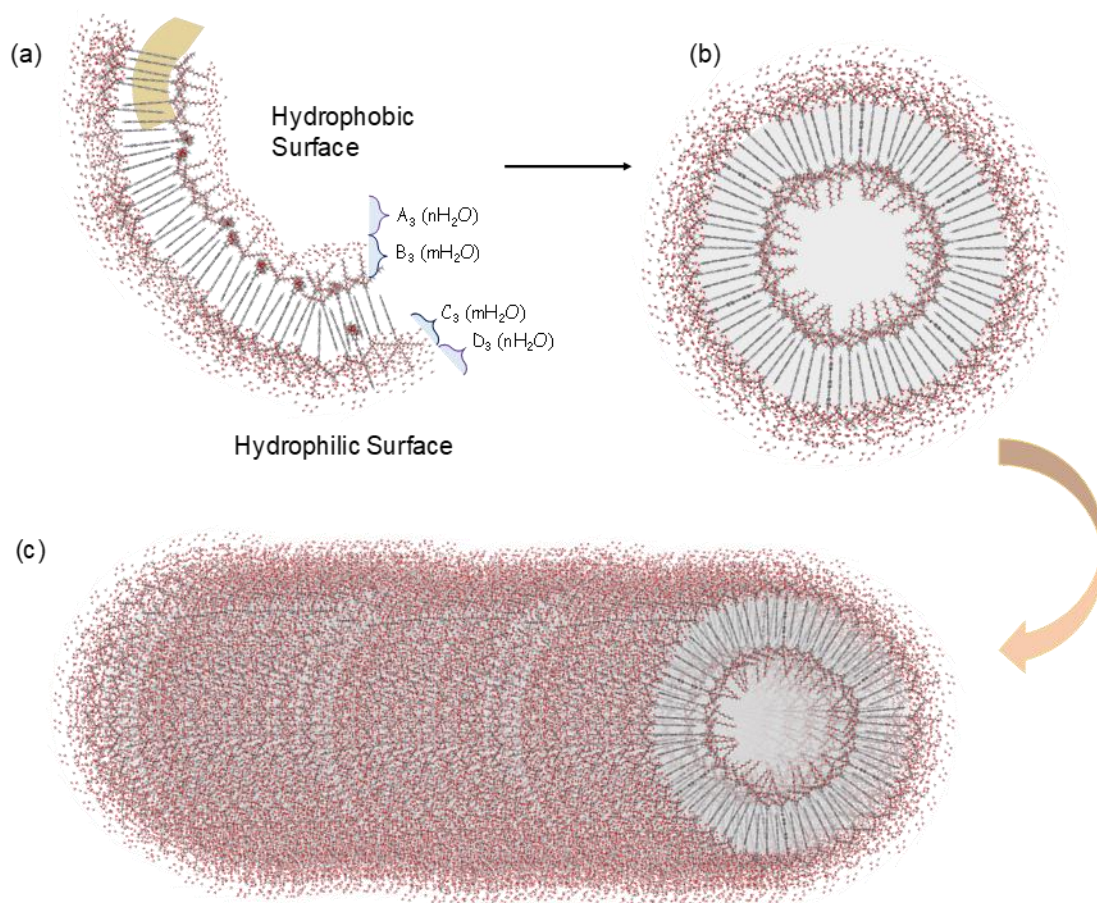
Figure 4.24. (a) Water expulsion from the heated surface of the 2D sheets (see **Figures 4.22e, 4.23**) and the resultant volume disparities between hydrated and dehydrated surfaces leading to a curvature of the surface. **(b,c)** The convex surface thus formed undergoes coiling to form tubular structures leading to extended networks and film formation.

The fluorescence of the resultant film could be varied by changing the molar ratio of the molecular components. While there are many examples for the formation of organic free-standing films at the air-solvent or solvent-solvent interfaces, the

present work could be the first example for the formation of films within a miscible monophasic solvent system.

4.5. Experimental Section

4.5.1. Materials and Methods

Linear Dichroism (LD) Measurement: LD experiments were performed on a JASCO 810 spectrometer using a quartz cuvette of 1 mm path length. The LD spectra were recorded as ΔOD ($A_{\parallel} - A\perp$) at variable temperatures and were processed by subtraction of the non–rotating baseline spectra. The temperature of the solutions was controlled using an attached Peltier thermostat. The solutions of **PE: PECN** were prepared at least 10 h prior to the measurement and kept at 20-25 ºC.

Scanning Electron Microscope (SEM): SEM images were obtained using a Zeiss EVO 18 cryo SEM Special Edn. equipped with a variable pressure detector working at 20–30 kV. The images were obtained by transferring solvent immersed film over a freshly cleaved mica substrate, attached to the SEM stub followed by drying under vacuum.

Dynamic Light Scattering (DLS) Measurements: For DLS measurements, all **PE: PECN** samples (c = 1 x 10^{-5} M) were prepared in 10% tetrahydrofuran (THF)-water (Milli–Q deionized water and filtered through 0.22 μm PVDF filter. Temperature variable particle size measurements were performed on DLS instrument (Malvern Instruments Limited, Model No:- ZEN 3600, Serial No:- 1026421) equipped with a solid-state laser operating at 532 nm. The scattered light intensity was collect at angles (θ) ranging from 30 to 100°, and around over 2 runs of 14 seconds per angle.

Time-Correlated Single-Photon Counting (TCSPC) Measurements: The measurements were performed on a DeltaFlex(TM), Horiba Jobin Yvon IBH

Ltd System (Serial No:- 14094), armed with a laser excitation source operating at 331 nm. All **PE**: **PECN** mixtures (c = 1 x 10^{-4} M) were taken in a 1 mm quartz cuvette and measured before and after film formation. The film formation was carried out externally and measurements were done at room temperature.

General Procedure to Prepare PE: PECN Mixtures of Different Compositions: From individual monomeric stock solutions of **PE** and **PECN** in THF (c = 1.0×10^{-2} M), the mixtures were prepared by mixing **PE** and **PECN** in varying ratios of 10:0, 9:1, 8:2, 7:3, 6:4, 5:5, 4:6, 3:7, 2:8, 1:9, 0:10 so that the total concentration and volume remained constant (c = 1.0 x 10^{-4}, 1 mL). The aggregates were preserved at ~22 °C in closed and air-tight vials. Required dilutions were achieved diluting into 10% THF-water mixture.

General Procedure for the Preparation of Films from PE:PECN Mixtures: A mixture of **PE**:**PECN** (as required) was taken in 10% THF-water in a container of the preferred shape and size. The closed containers were then immersed into a temperature-controlled water bath. The temperature of the water bath was slowly increased to the required film forming temperature of **PE-PECN** at a controlled heating rate of ~2 °C/min. The films formed were confirmed visually under 356 nm light. However, further increase in the water-bath temperature beyond the film forming temperature, resulted in the shrinkage of the films. Rapid and non-uniform heating, either using a hot-air gun or by direct immersion into a pre-heated water-bath, is not recommended for film formation at any concertation or composition of **PE-PECN** mixtures.

General Procedure of Sample Preparation for AFM and TEM Analyses: A pre-formed **PE**: **PECN** film in its solution was gently shaken for 1 min and diluted 10× with 10% THF-water. The aliquot was drop cast either over freshly peeled mica sheet for AFM measurements or on carbon coated TEM grids for TEM analysis. The samples were dried by slow evaporation followed by vacuum at room temperature prior to the measurements.

4.5.2. Synthesis and Characterization

Synthesis of the amphiphiles PE and PECN

PE was prepared as per a reported procedure in 69% yield.[29] For the preparation of **PECN**, compound **16** (0.5 g, 1.67 mmol), Pd(PPh$_3$)$_2$Cl$_2$ (0.1 g, 0.17 mmol) and CuI (0.03 g, 0.1 mmol) were added to an oven dried two neck round bottom flask purged with argon. Degassed trimethylamine - THF (20 mL, 1:1 v/v) was added under a flow of argon. Compound **15** (0.2 g, 2.0 mmol) was then added to the reaction mixture and stirred at room temperature under an argon atmosphere for 12 h. After completion of reaction, chloroform (50 mL) and 10% HCl were added and stirred for 15 min. The organic layer was washed with water and brine and then dried over anhydrous sodium sulphate. After the removal of the solvent, the residue was purified by silica gel column chromatography using 5% methanol/chloroform as eluent. Yield = 68%

^{1}H–NMR (500 MHz, CDCl$_3$): δ = 8.85 (s, 1H, N–H), 8.75–8.73 (d, J = 10 Hz, 2H, Ar–H), 7.66–7.64 (m, 2H, Ar–H), 7.62–7.60 (m, 2H, Ar–H), 7.54–7.52 (m, 6H, Ar–H), 7.27 (s, 2H, Ar–H), 4.26-4.22 (m, 6H), 3.86-3.84 (t, J = 5 Hz, 4H), 3.81-3.79 (t, J = 5 Hz, 2H), 3.73-3.70 (m, 6H), 3.67-3.65 (m, 6H), 3.64-3.62 (m, 6H), 3.55-3.51 (m, 6H), 3.37 (s, 3H), 3.33 (s, 6H) ppm.

^{13}C–NMR (125 MHz, CDCl$_3$): δ = 165.5, 152.4, 142.1, 132.3, 132.1, 131.7, 131.5, 129.8, 128, 124.3, 121.7, 119.9, 111.6, 108.2, 93.5, 92.1, 89.1, 88.2, 71.9, 70.3, 69.2, 58.8 ppm.

HRMS: calcd. for C$_{51}$H$_{60}$N$_2$O$_{13}$ 908.4100, found: 930.8000 [M+Na]$^+$

4.6. References

(1) Walton A. G. *Science*, **1965**, *148*, 601.

(2) ten Wolde P. R.; Frenkel, D. *Science*, **1997**, *277*, 1975.

(3) Turnbull, D. *Physics of Non-Crystalline Solids*, ed Prins J. A. (North-Holland, Amsterdam) **1964**.

(4) Spaepen F. *Acta Metall.* **1975**, *23*, 729.

(5) Erdemir, D.; Lee, A. Y. Myerson A. S. *Acc. Chem. Res.* **2009**, *42*, 621.

(6) Lee, S.; Wi, S. H.; Jo, W.; Cho, Y. C.; Lee, H. H.; Jeong, S.-Y.; Kim, Y.-II, Lee, G. W. *Proc. Natl. Acad. Sci.* **2016**, *113*, 13618.

(7) Bonn, D.; Shahidzadeh, N. *Proc. Natl. Acad. Sci.* **2016**, *113*, 13551.

(8) Hollingsworth, M. D. *Science* **2002**, *295*, 2410.

(9) Rubio-Martinez, M.; Imaz, I.; Domingo, N.; Abrishamkar, A.; Mayor, T. S.; Rossi, R. M.; Carbonell, C.; deMello, A. J.; Amabilino, D. B.; Maspoch, D.; Puigmartí-Luis, J. *Adv. Mater.* **2016**, *28*, 8150.

(10) (a) Keddie, J. L. *Materl. Sci. Eng.* **1997**, *21*, 101. (b) Visschers, M.; Laven, J.; German, A. L. *Prog. Org. Coat.*, **1997**, *30*, 39.

(11) Dobler, F.; Holl, Y. *Trend. Poly. Sci.*, **1996**, *4*, 145.

(12) Winnik. M. A. *Curr. Opin. Colloid Interface Sci.*, **1997**, *2*,192.

(13) Wang, Y.; Winnik, M. A. *Macromolecules*, 1990, 23, 4731.

(14) Johnson, S. B.; Russel, A. S.; Scales, P. *Colloid and Surfaces* **1998**, *141*, 119.

(15) von Freymann, G.; Kitaev, V.; Lotsch, B. V.; Ozin, G. A. *Chem. Soc. Rev.* **2013**, *42*, 2528.

(16) Wong, S.; Kitaev V.; Ozin, G. A. *J. Am. Chem. Soc.* **2003**, *125* , 15589.

(17) von Freymann, G.; John, S.; Kitaev V.; Ozin, G. A. *Adv. Mater.* **2005**, *17*, 1273.

(18) Avci, C.; Imaz, I.; Carné-Sánchez, A.; Pariente, J. A.; Tasios, N.; Perez-Carvajal, J.; Alonso, M. I.; Blanco, A.; Dijkstra, M.; Lopez, C.; Maspoch, D. *Nat. Chem.* **2018**, *10*, 78.

(19) Wolf, T.; Niazov-Elkan, A.; Sui, X. M.; Weissman, H.; Bronshtein, I.; Raphael, M.; Wagner, H. D.; Rybtchinski, B. *J. Am. Chem. Soc.* **2018**, *140*, *14*, 4761.

(20) Kuzmenko, I.; Rapaport, H.; Kjaer, K.; Als-Nielsen, J.; Weissbuch, I.; Lahav, M.; Leiserowitz, L. *Chem. Rev.* **2001**, *101*, 1659.

(21) Robertson, E. J.; Battigelli, A.; Proulx, C.; Mannige, R. V.; Haxton, T. K.; Yun, L.; Whitelam, S.; Zuckermann, R. N. *Acc. Chem. Res.* **2016**, *49*, 379.

(22) Sakakibara, K.; Hill, J. P.; Ariga, K. *Small* **2011**, *7*, 1288.

(23) Eliash, R.; Weissbuch, I.; Weygand, M. J.; Kjaer, K.; Leiserowitz, L.; Lahav, M. *J. Phys. Chem. B* **2004**, *108*, 7228.

(24) Shinde, D. B.; Sheng, G.; Li, X.; Ostwal, M.; Emwas, A.-H.; Huang, K.-W.; Lai, Z. *J. Am. Chem. Soc.* **2018**, *140*, 14342.

(25) (a) Edler, K. J.; Yang, B. *Chem. Soc. Rev*. **2013**, *42*, 3765. (b) Rahim, M. A.; Kristufek, S. L.; Pan, S.; Richardson, J. J.; Caruso, F. *Angew. Chem. Int. Ed.* **2018**, *57*, 2. (c) Sakata, J. K.; Dwoskin, A. D.; Vigorita, J. L.; Spain, E. M. *J. Phys. Chem. B* **2005**, *109*, *1*, 138.

(26) Pfeffermann, M.; Dong, R.; Graf, R.; Zajaczkowski, W.; Gorelik, T.; Pisula, W.; Narita, A.; Mullen, K.; Feng, X. *J. Am. Chem. Soc.* **2015**, *137*, 14525.

(27) Wang, L.; Sahabudeen, H.; Zhang, T.; Dong, R.; *npj 2D Mater Appl*, **2018**, *2*, 26.

(28) Zhou, S.-L.; Matsumoto, S.; Tian, H.-D.; Yamane, H.; Ojida, A.; Kiyonaka, S.; Hamachi, I. *Chem. Eur. J.* **2005**, *11*, 1130.

(29) Thirumalai, R.; Mukhopadhyay, R.; Praveen, V.; Ajayaghosh, A. *Sci. Rep.*, **2015**, 9842.

(30) Hansch, C.; Leo, A.; Taft, R. W. *Chem. Rev.* **1991**, *2*, 165.

(31) Atwood, J. L.; Barbour, L. J.; Hardie, M. J.; Raston, C. L. *Coor. Chem. Rev.* **2001**, *222*, 3.

(32) Moradi, M.; Opara, N. L.; Tulli, L. G.; Wackerlin, C.; Dalgrna, S. J.; Teat, S. J.; Baljozovic, M.; Popova, O.; van Genderen, E.; Kleibert, A.; Stahlberg, H.; Abrahams, J. P.; Padeste, C.; Corvini, P. F.-X.; Jung, T. A.; Shahgaldian, P. *Sci. Adv.* **2019**, *5*, eaav4489.

(33) (a) Haidekker, M. A., Brady, T. P., Lichlyter, D. & Theodorakis, E. A. *Bioorg. Chem.* **2005**, *33*, 415. (b) Bochkov, A. Y.; Akchurin, I. O.; Dyachenko, O. A.; Traven, V. F. *Chem. Commun.* **2013**, *49*, 11653.

(34) Kim, H.-J.; Kim, T.; Lee, M. *Acc. Chem. Res.* **2011**, *44*, *1*, 72.

(35) Hicks, M. R.; Kowalski, J.; Rodger, A. *Chem. Soc. Rev.* **2010**, *39*, 3380.

(36) Bell, O. A.; Wu, G.; Haataja, J. S.; Brömmel, F.; Fey, N.; Seddon, A. M.; Harniman, R. L.; Richardson, R. M.; Ikkala, O.; Zhang, X.; Faul, C. F. J. *J. Am. Chem. Soc.* **2015**, *137*, 142.

(37) Sakakibara, K.; Chithra, P.; Das, B.; Mori, T.; Akada, M.; Labuta, J.; Tsuruoka, T.; Maji, S.; Furumi, S.; Shrestha, L. K.; Hill, J. P.; Acharya, S.; Ariga, K.; Ajayaghosh, A. *J. Am. Chem. Soc.* **2014**, *136*, 8548.

List of Publications and Patents from the Thesis

1. Supramolecular Gel Phase Controlled [4 + 2] Diels–Alder Photocycloaddition for Electroplex Mediated White Electroluminescence: **Satyajit Das**, Naoki Okamura, Shigeyuki Yagi, and Ayyappanpillai Ajayaghosh: *J. Am. Chem. Soc.*, **2019**, *141*, 5635–5639.

2. Thermoresponsive Molecules for Controlled Heat and Light Transmission Windows and Applications Thereof: Ayyappanpillai Ajayaghosh, **Satyajit Das**, Soman Suraj, Asok Adersh, Shankar Pooppanal Sreejith: (Indian Patent Application No:- **201911052506**; Patent Cooperation Treaty (PCT) Application, **2019** and manuscript under preparation).

3. Thermally Assisted Supramolecular Film Formation within a Monophasic Solvent Medium. **Satyajit Das**, Rajasekaran Thirumalai, and Ayyappanpillai Ajayaghosh (Manuscript under preparation)

List of Publications from Other Related Works

4. A Hybrid Organogel of a Low Band Gap Diketopyrrolopyrrole with PC71BM: Phase Separated Morphology and Enhanced Photoconductivity: Samrat Ghosh, **Satyajit Das** Akinori Saeki, Vakayil K. Praveen, Shu Seki, Ayyappanpillai Ajayaghosh: *ChemNanoMat* **2018**, *4*, 831–836.

5. Stimuli-responsive Supramolecular Gels - Chapter 7: Rakesh K. Mishra, **Satyajit Das**, Balaraman Vedhanarayanan, Gourab Das, Vakayil K. Praveen and Ayyappanpillai Ajayaghosh; **2018** Print ISBN:978-1-78801-111-2: https://doi.org/10.1039/9781788013147-00190.

List of Conference Presentations

1. **Satyajit Das**, Naoki Okamura, Shigeyuki Yagi, and Ayyappanpillai Ajayaghosh; Structural Tuning Bandgap, Photoluminescence, Self-assembly and Electroluminescence Properties of Ethynylanthracence by Photoactive

Diels-Alder Reaction; CSMAT-2017 Munnar, Kerala, March 9-11, 2017. (Poster presentation)

2. **<u>Satyajit Das</u>**, and Ayyappanpillai Ajayaghosh; Thermo-photo Responsive Supramolecular Assembly in Aqueous Medium; 8th East Asia Symposium on Functional Dyes and Advanced Materials held at CSIR-NIIST, Thiruvananthapuram, Kerala, September 20-22, 2017. (Poster presentation)

3. **<u>Satyajit Das</u>**, Naoki Okamura, Shigeyuki Yagi, and Ayyappanpillai Ajayaghosh; Supramolecular [4 + 2] Cycloadduct of an Organogelator exhibits Electroplex Mediated White Light Emission, 14th JNC Research Conference on Chemistry of Materials held at Thiruvananthapuram, Kerala, October 03-05, 2018 (Poster Presentation)

4. **<u>Satyajit Das</u>**, Manuraj Mohan, Rakhi Raghavan Baby and Ayyappanpillai Ajayaghosh; Fabrication of High Frequency Electrochemical Capacitor from Bio-waste Eggshell and CNTs; Polymer Conference for Young Researchers (PCYR-2018), held at CSIR-NIIST, November 17th, 2018, Thiruvananthapuram, Kerala. (Poster Presentation)

5. **<u>Satyajit Das</u>**, Anagha Jose, Rajasekaran Thirumalai, and Ayyappanpillai Ajayaghosh; Constructing Out-of-Equilibrium Molecular Assemblies; International Conference on Polymer Science and Technology (MACRO-2018), held at IISER Pune Maharashtra, December 19-22, 2018. (Poster Presentation)

6. **<u>Satyajit Das</u>**, Naoki Okamura, Shigeyuki Yagi, and Ayyappanpillai Ajayaghosh; Controlled [4+2] Photocycloaddition at Gel Phase and Electroplex Mediated White Light Emission; 24th CRSI National Symposium in Chemistry held at CSIR-Central Leather Research Institute and Indian Institute of Technology Madras, Chennai, 7 – 10th February 2019. (Poster Presentation)

7. **<u>Satyajit Das</u>**, Naoki Okamura, Shigeyuki Yagi, and Ayyappanpillai Ajayaghosh; Supramolecular [4+2] Cycloadduct of an Organogelator Exhibits Electroplex Mediated White Light Emission; CSIR-Inter-

Institutional Student Conferences on Sustainable Chemistry for Health, Environment and Materials (Su-Chem-Yuva-2019) held at CSIR-IICT Hyderabad during July 24-26, 2019. (Best Oral Presentation)

8. **Satyajit Das**, and Ayyappanpillai Ajayaghosh; LCST Modification of Amphiphilic π-Systems by Photocycloaddition for Controlled Transmission of Solar Radiation; 15th JNC Research Conference on Chemistry of Materials held at Thiruvananthapuram, Kerala, September 30-October 03, 2019. (Oral Presentation)

9. **Satyajit Das**, and Ayyappanpillai Ajayaghosh; LCST Modification of Amphiphilic π-Systems by Photocycloaddition for Controlled Transmission of Solar Radiation; International Conference on Advanced Functional Materials held at CSIR-NIIST, Thiruvananthapuram, Kerala, December 9-10, 2019. (Oral Presentation).